Multiscale topology optimization of solid and fluid structures

Andreasen, Casper Schousboe

Publication date:
2011

Document Version
Publisher's PDF, also known as Version of record

Multiscale topology optimization of solid and fluid structures

PhD Thesis

$$(EIv'')'' = q - \rho A\ddot{v}$$

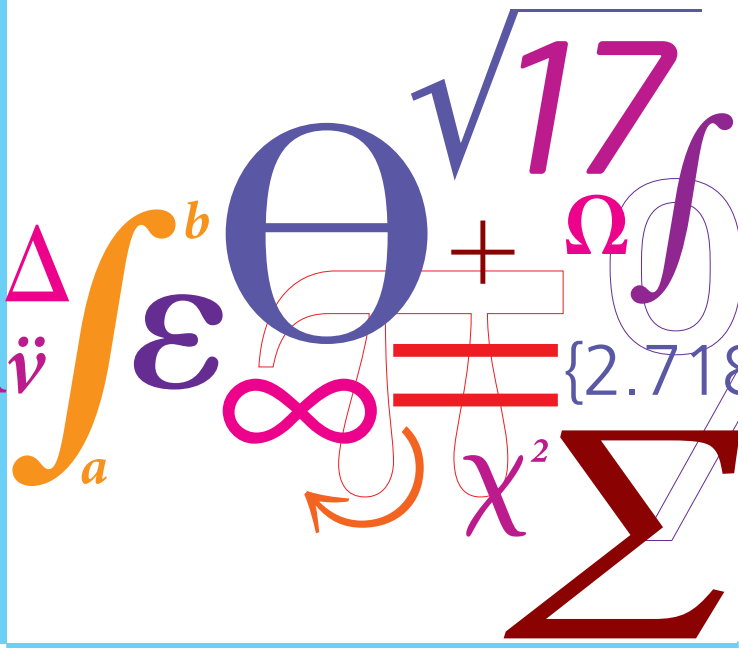

Casper Schousboe Andreasen
DCAMM Special Report No. S131
May 2011

DTU Mechanical Engineering
Department of Mechanical Engineering

Multiscale topology optimization of solid and fluid structures

by

Casper Schousboe Andreasen

DEPT. OF MECHANICAL ENGINEERING
Solid Mechanics

TECHNICAL UNIVERSITY OF DENMARK

Title of the thesis:
Multiscale topology optimization of solid and fluid structures

Ph.D. student:
Casper Schousboe Andreasen
E-mail: csan@mek.dtu.dk

Supervisor:
Ole Sigmund
E-mail: sigmund@mek.dtu.dk

Address:
Department of Mechanical Engineering, Solid Mechanics
Technical University of Denmark
Nils Koppels Allé, Building 404, 2800 Kgs. Lyngby, Denmark

DCAMM Special Report no. S131
ISBN 978-87-90416-59-1

Preface

This thesis is submitted in partial fulfillment of the requirements for obtaining the degree of Ph.D. in mechanical engineering at the Technical University of Denmark (DTU). The Ph.D. project was funded by the Danish Agency for Science, Technology and Innovation and carried out at the Department of Mechanical Engineering, Solid Mechanics, at DTU in the period March 1^{st} 2008 - May 9^{th} 2011. Supervisor on the project was Professor Dr.Techn. Ole Sigmund, Department of Mechanical Engineering.

I am very grateful to my supervisor for his inspiring support and always taking his time to discuss the work and the results during the project. I would also like to thank Professor Dr.Techn. Martin P. Bendsøe, who was my co-supervisor until January 1^{st} 2009, for our many good discussions on the homogenization theory.

The project was initiated in a collaboration between DTU and the Technical University in Munich, Chair of Structural Analysis, where I spent the fall of 2009. I would like to express my gratitude towards Martin Herrenbrück, Önay Can, Professor R. Lackner and Professor K.U. Bletzinger for creating a warm atmosphere and their willingness to discuss the project during my stay.

I am thankful to Professor Krister Svanberg at Royal Institute of Technology, Sweden, who has granted me permission to use his MMA-implementation. Thanks to my colleagues in the TopOpt Group and the other Ph.D.-students at Section for Solid Mechanics for creating an educative and inspiring working environment.

Finally, I would like to express my sincere thanks to my wife Susanne and my son Anton for their support and patience during the project.

Kgs. Lyngby, May 9^{th} 2011.

Casper Schousboe Andreasen

Resumé (in Danish)

Denne afhandling omhandler brugen af topologioptimeringsmetoden på multiskalaproblemer særligt fluid-struktur-interaktionsproblemer. Ved brug af multiskalametoder udvikles og separeres ligevægtsligningerne, Navier-Cauchy og de inkompressible Navier-Stokes ligninger, hvilket resulterer i et sæt mikro- og makroligninger til modellering af interaktionen.

Topologioptimeringsmetoden benyttes til materialedesign med henblik på at optimere trykkoblingen i porøse materialer. Endvidere vises det, ved kombination af materialedesign og makroskopisk modellering, at materialers mikrostruktur kan optimeres i forhold til brugsskala-egenskaberne. En poroelastisk aktuator bestående af to væskefyldte porøse materialer er optimeret med denne fremgangsmåde.

Baseret på homogenisering af en fastlagt mikrostrukturtopologi genereres materialeinterpolationsfunktioner til brug i materialedistributionsproblemer i væskefyldte poroelastiske strukturer. Topologioptimering er benyttet til optimeringen af en stødabsorberende struktur og til fluid-struktur-interaktionen på et tryksat låg.

En tredje anvendelse omhandler alene væskestrømningen i en mikrofluidblander. Opblandingen af et transporteret medie er optimeret ved hjælp af topologioptimering og det vises at de optimerede designs har geometriske elementer, så som skrå riller og sildeben, der også benyttes i litteraturen.

For at kunne sikre producerebarheden af de optimerede designs er en ny parametrisering foreslået. Den tillader støbe/fræse bearbejdning og sikrer et binært design. Metoden er succesfuldt benyttet til mikroblander design.

Abstract

This thesis considers the application of the topology optimization method to multiscale problems, specifically the fluid-structure interaction problem. By multiple-scale methods the governing equations, the Navier-Cauchy and the incompressible Navier-Stokes equations are expanded and separated leaving a set of micro- and macroscale equations for the interaction modeling.

The topology optimization method is applied to the material design in order to optimize the pressure coupling properties of porous materials. Furthermore, by combining both the material design and the macroscopic modeling, it is shown that the material microstructure can be optimized with respect to application scale properties. A poroelastic actuator consisting of two saturated porous materials is optimized using this approach.

Based on the homogenization of a fixed microstructure topology, material design interpolation functions are obtained for use in material distribution problems of a saturated poroelastic structure. Topology optimization is applied for the optimization of an impact absorbing structure and the fluid-structure-interaction of a pressurized lid.

A third application considers the pure fluid flow in a microfluidic mixer. The mixing of a transported matter is optimized by means of topology optimization and it is shown that the optimized designs contain geometric elements such as slanted grooves and staggered herringbones also used in the literature.

To ensure the manufacturability of the topology optimized designs a new explicit parametrization is proposed. It allows for casting/milling type manufacturing and ensures a binary design. The method is successfully applied to micromixer design.

Publications

The following publications are part of the thesis

[P1] C.S. Andreasen, O. Sigmund, Saturated poroelastic actuators generated by topology optimization, *Structural and Multidisciplinary Optimization*, 2011; **43**:693-706

[P2] C.S. Andreasen, O. Sigmund, Multiscale optimization of poroelastic actuators, *Smart Materials & Structures*, To be submitted

[P3] C.S. Andreasen, O. Sigmund, Topology optimization of fluid-structure-interaction problems using the Biot consolidation equations, *Computer Methods in Applied Mechanics and Engineering*, To be submitted

[P4] C.S. Andreasen, A.R. Gersborg, O. Sigmund, Topology optimization of microfluidic mixers, *International Journal of Numerical Methods in Fluids*, 2009; **61**:498-513

[P5] A.R. Gersborg, C.S. Andreasen, An explicit parameterization for casting constraints in gradient driven topology optimization, *Structural and Multidisciplinary Optimization*, Published online 2011

Contents

Chapter 1
Introduction

1.1 Motivation

Most man-made and biological materials contain multiple scales in which one or more different material constituents create microstructures at different length scales. The biological materials (bone, wood, etc.) are very often highly hierarchical with several levels of microstructure optimized over time for mechanical or transport properties. This ingenuity of enhancing the materials by changing the microstructure is very appealing in material sciences.

During the last decades the field of multiscale modeling has expanded heavily as the developments within scientific computing have provided much larger and faster computers. This means that more details can be included in the models yielding a better prediction of, and a larger insight into, the material and structural behavior. This, of course, also makes it possible to design lighter, stronger and more advanced products.

A natural extension to the modeling is therefore to apply optimization in order to obtain better materials and structures for use in modern products. New ideas for material development and larger insight into the mechanics can be gained trough multiscale optimization. This potentially leads to highly customized material structures that might have very intricate designs. However, modern production methods allow, to a large extend, the generation of such advanced materials through e.g. additive manufacturing techniques such as Stereolithography (SLA), Selective Laser Sintering (SLS) or 3D printing using ink-jet techniques.

It is the aim of this thesis to extend and apply the topology optimization method to the fluid-structure interaction problems within saturated porous materials and structures made of such materials. This includes both material scale optimization, application scale optimization and a combination of both. Furthermore, some attention will be given to the optimization of microfluidic mixers and the manufacturability of optimized designs.

1.2 Structure of the thesis

The thesis presents the work done during the Ph.D. study and constitutes a summary of the results in papers [P1-5]. The first three chapters contain this general introduction, an introduction to the modeling and an introduction to topology optimization, respectively. This is followed by a one chapter summary for each paper and finalized by some concluding remarks in the last chapter. A more detailed outline of each chapter is given in the following:

Chapter 2 presents a general introduction to multiscale modeling. This includes scale

definitions and the methods that are applied in order to achieve the multiscale equations for fluid-structure interaction problems.

The topology optimization method and the developments towards multiscale topology optimization is introduced in chapter 3. The different equations that are used for the modeling are presented along with the design interpolation, which is needed for applying topology optimization. Furthermore, an introduction to adjoint sensitivity analysis is given and the gradient-based topology optimization procedure is outlined.

In chapter 4 the results from [P1] are presented which deal with the optimization of the material microstructure for a poroelastic material used in a pressure driven actuator. The work focuses on the pressure coupling between the fluid and the solid. Under the assumption that an increase in pressure coupling will also increase the macroscopic deflection, the pressure coupling is maximized by altering the microstructure.

The aforementioned assumption is investigated further in chapter 5 which presents the results from [P2] where a two-scale model is applied to the optimization of a poroelastic actuator. By the introduction of a two-scale model, the objective can be defined on the application scale while the optimization concerns the underlying material microstructure. This makes it possible to tailor the material microstructure for the specific application. It is seen that the material stiffness has an important role when optimizing a saturated pressure-driven poroelastic actuator.

The material distribution problem in a saturated poroelastic medium is considered in chapter 6 which summarizes the results of [P3]. The optimization is done on the macroscopic level by varying the density of the material while keeping the microstructure topology fixed. Homogenization of the material microstructure is used in order to obtain the design interpolation schemes necessary for the optimization. Even though the inertia effects are neglected the problem is transient due to the coupling between fluid flow and solid deformations.

The results of [P4] which presents a method for optimizing microfluidic mixers are summarized in chapter 7. This multiphysics problem is a combination of fluid flow and transport. The transport is convection dominated which means that the fluid flow has a large influence on the mixing and by altering the flow path, the mixing of the transported matter can be greatly improved. Microfluidic mixers are usually very small and in order to manufacture these devices it is of great importance to impose certain constraints on the design.

Manufacturability is the theme of chapter 8 that summarizes the results from [P5] in which a method is presented for ensuring the manufacturability of topology optimized designs. The method ensures manufacturability for casting/milling type processing by the introduction of a new parametrization. The method is also applied to the design of a microfluidic mixer.

Finally the thesis is concluded in chapter 9 which also includes some remarks on future work and extensions.

Chapter 2
Multiscale modeling of fluid-structure interaction

In this chapter the fluid-structure interaction as it appears in a saturated periodic poroelastic material is presented. Most materials in nature are not solid but porous at one or more scales. One example of this is the human bone and tissue that have several scales of microstructure. In order to make appropriate models of the deformation of bones or tissue during e.g. exercise, a great level of detail is needed. However, it is impossible to capture all scales into one model, as this would contain too much information. Instead, a multiscale model can be applied in which the effective properties of each scale can be used at the higher level. Some of the scales in human bone is illustrated in the figure below.

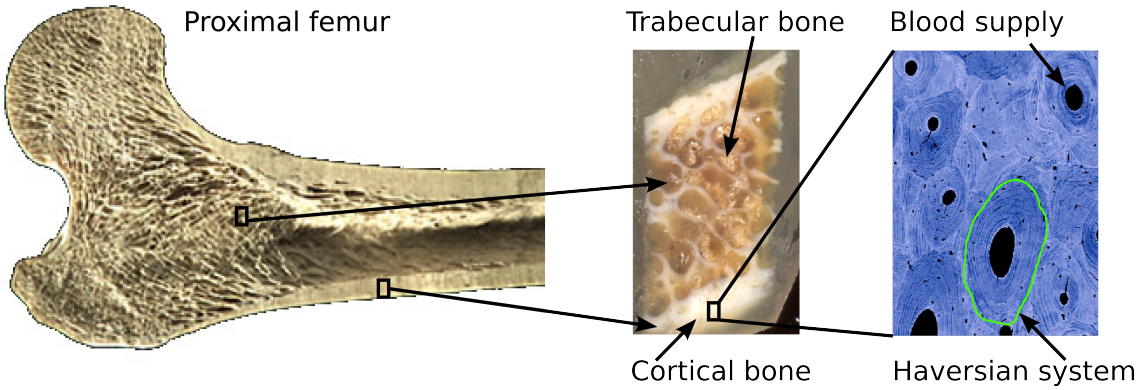

Figure 2.1 Illustration of multiple scales in human bone. Left: Proximal femur, Center: bone sample from pelvic bone (hip), Right: Magnification of cortical bone. Pictures from *http://depts.washington.edu/bonebio/ASBMRed/ASBMRed.html*

Multiscale methods can be applied to a large range of different physics and biomechanics problems is just one class of problems which contains fluid-saturated porous materials. During the twentieth century much work has been conducted in order to develop macroscopic descriptions for the multi-scale phenomena in the interaction between water and soil. Fillunger (1913) and von Terzaghi (1923) developed some of the early phenomenologically based models of soil-liquid interaction. Biot (1941, 1955) derived the poroelastic consolidation theory for saturated elastic soils, that is still used today, without any microstructure considerations. This model couples the deformation of the solid skeleton and the Darcy flow of the saturating fluid. The method was further developed for dynamic problems in Biot (1956a,b).

Many different multiscale methods exist (see e.g. Berryman (2005)) and much effort has been put into the characterization of heterogeneous materials in terms of structure

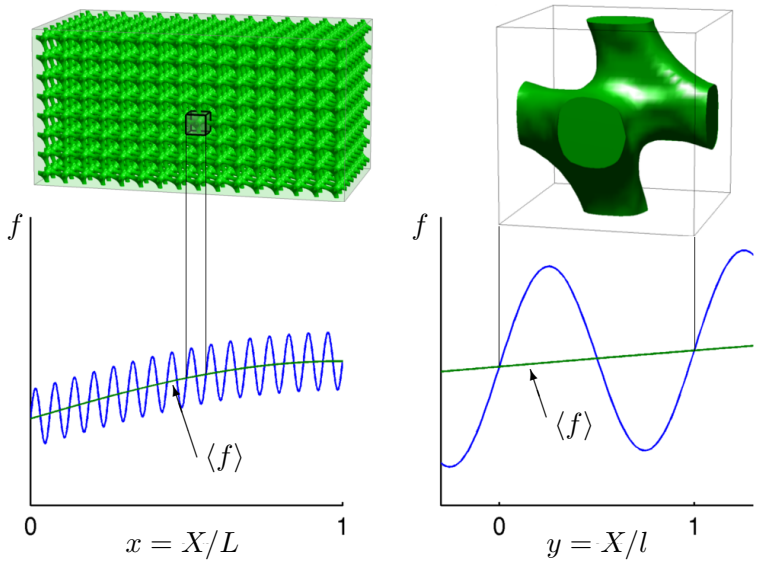

Figure 2.2 Illustration of the two scales along with the global and local variation of a function. x and y are the nondimensionalized macro and micro coordinates. The function f is an arbitrary function and $\langle f \rangle$ denotes the volume average of f.

and effective properties. A general introduction to the various material characterization methods is given by Torquato (2002).

2.1 Two scale asymptotic expansion

In this thesis, the focus is on homogenization using multiple-scales expansion as it is described in Bensoussan et al. (1978) and Sanchez-Palencia (1980). The basic concept of the method is the assumption that the variation of e.g. the displacement along a structure, can be seen as a superposition of scale related displacements. This assumption allows for the scales to be separated such that the local and global variations can be computed independently. This makes it possible to compute effective (homogenized) material properties for a representative volume element of the material and to use these in the modeling of the structure. Figure 2.2 illustrates the concept. The main structure shown to the left has a periodic microstructure and has an average behavior e.g. deflection given by the green line with local periodic oscillations illustrated by the blue line.

Due to the periodicity of the material microstructure it is possible to define a representative volume element, which in this case is the periodic unit cell shown to the right along with its oscillating signal. The macroscopic length scale is denoted L and the microscopic l. If the ratio between these two is a sufficiently small number $\epsilon = l/L \to 0$ then it is possible to expand and separate the different scales of the problem and assume that they do not influence each other. The resulting scales will therefore be a *slowly* vary-

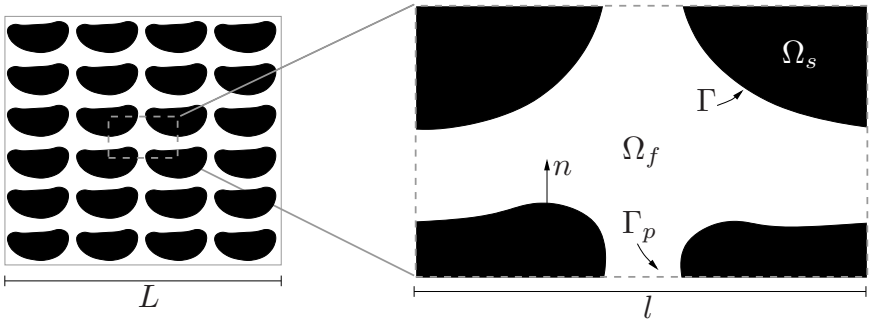

Figure 2.3 Sketch of the fluid-structure interaction problem in a periodic porous material showing material ensemble and a representative volume element (periodic unit cell). L and l are the characteristic lengths of the macro and micro scale, respectively.

ing macroscale $\mathbf{x}$ and a *faster* microscale $\mathbf{y} = \epsilon^{-1}\mathbf{x}$. In the following the subscript X denotes that the operator works on the original problem while x and y denotes that the operator is defined on the nondimensionalized macro and micro-scale, respectively.

2.2 The fluid-structure interaction problem

The homogenization of the fluid-structure interaction problem in e.g. soils (Auriault and Sanchez-Palencia, 1977; Sanchez-Palencia, 1980; Auriault et al., 2009) potentially leads to three different models depending on the material properties: a two phase model, an elastic model and a viscoelastic model of which the first is equivalent to that of Biot and is the most commonly used. It is also the model used in this work and it is applied to static and quasi-static problems. In the following, the multiscale equations used in papers [P1-3] are outlined. The details of the expansion and separation are given in Appendix A.

The fluid-structure interaction problem in a periodic porous material is illustrated in figure 2.3. The solid skeleton (black) have pores that are saturated with fluid (white) which together occupy the complete unit-cell. The two domains of the problem are governed by different partial differential equations namely; the Navier-Cauchy equation within the solid material Ω_s and the incompressible Navier-Stokes equation for the Newtonian fluid in Ω_f. At the interface between solid and fluid a no-slip condition is applied to the fluid flow and continuity in the stresses are assumed. The governing equations yield

$$\nabla_X \cdot \boldsymbol{\sigma}_s = \rho_s \frac{\partial^2 \mathbf{u}}{\partial t^2} \quad \text{where} \quad \boldsymbol{\sigma}_s = \mathbf{C} : \boldsymbol{\varepsilon}_X(\mathbf{u}) \quad \text{in } \Omega_s \tag{2.1}$$

$$\nabla_X \cdot \boldsymbol{\sigma}_f = \rho_f \left(\frac{\partial \mathbf{v}}{\partial t} + (\mathbf{v}\nabla_X) \cdot \mathbf{v} \right) \quad \text{where} \quad \boldsymbol{\sigma}_f = 2\mu\boldsymbol{\varepsilon}_X(\mathbf{v}) - p\mathbf{I} \quad \text{in } \Omega_f \tag{2.2}$$

$$\nabla_X \cdot \mathbf{v} = 0 \quad \text{in } \Omega_f \tag{2.3}$$

$$(\boldsymbol{\sigma}_s - \boldsymbol{\sigma}_f)\mathbf{n} = 0 \quad \text{on } \Gamma \tag{2.4}$$

$$\dot{\mathbf{u}} - \mathbf{v} = 0 \quad \text{on } \Gamma \tag{2.5}$$

where $\mathbf{u}$ is the solid deformation and $\dot{\mathbf{u}}$ and $\mathbf{v}$ are the solid and fluid velocity, respectively. The properties of the fluid is given by the fluid density ρ_f and the viscosity μ while the solid density is given by ρ_s and it stiffness by the tensor $\mathbf{C}$. The interface between solid and fluid is denoted Γ and the normal $\mathbf{n}$ points into the fluid domain. $\boldsymbol{\varepsilon}_X(\mathbf{u})$ is the linear infinitesimal strain defined as

$$\boldsymbol{\varepsilon}_X(\mathbf{u}) = \frac{1}{2}\left(\nabla_X \mathbf{u} + (\nabla_X \mathbf{u})^T\right) \tag{2.6}$$

Equations (2.1)-(2.5) model the full dynamic behavior of the interaction problem; however, some simplifications are made in order to apply the multiscale method to the problems considered in this thesis. The problem is assumed quasi-static and hence the inertia terms in both the fluid and the solid equations can be neglected. Furthermore, the flow is assumed so slow that the influence from convection is vanishing. The system then reduces to a homogeneous version of the previous equations

$$\nabla_X \cdot \boldsymbol{\sigma}_s = 0 \quad \Rightarrow \quad \nabla_X \cdot (\mathbf{C} : \boldsymbol{\varepsilon}_X(\mathbf{u})) = 0 \quad \text{in } \Omega_s \tag{2.7}$$

$$\nabla_X \cdot \boldsymbol{\sigma}_f = 0 \quad \Rightarrow \quad \nabla_X \cdot (2\mu\boldsymbol{\varepsilon}_X(\mathbf{v}) - p\mathbf{I}) = 0 \quad \text{in } \Omega_f \tag{2.8}$$

$$\nabla_X \cdot \mathbf{v} = 0 \quad \text{in } \Omega_f \tag{2.9}$$

$$(\boldsymbol{\sigma}_s - \boldsymbol{\sigma}_f)\mathbf{n} = 0 \quad \text{on } \Gamma \tag{2.10}$$

$$\dot{\mathbf{u}} - \mathbf{v} = 0 \quad \text{on } \Gamma \tag{2.11}$$

These linearized equations are the foundation for the multiscale analysis. The ratio between the pressure and the viscous terms in the Stokes equation (2.8) is of great importance in the following expansion of the equation system. The ratio is given by

$$\mathcal{Q} = \frac{|\nabla_X p|}{|\mu \nabla_X^2 \mathbf{v}|} \tag{2.12}$$

and depending on the order of $\mathcal{Q}$ either of the following macroscopic descriptions is obtained

$\mathcal{Q} = \mathcal{O}(\epsilon^{-2})$**:** a diphasic description similar to that of Biot

$\mathcal{Q} = \mathcal{O}(\epsilon^{-1})$**:** a monophasic elastic description

$\mathcal{Q} = \mathcal{O}(\epsilon^{0})$**:** a monophasic viscoelastic description

while orders below is equivalent to having an empty porous matrix and orders above are non-homogenizable i.e. the scales cannot be separated and no macroscopically equivalent description exists. It is the first diphasic description that forms the basis for this work. The procedure for obtaining the multiscale equations is first to expand the state variables and insert those into the governing equations. Assuming $\mathcal{Q} = \mathcal{O}(\epsilon^{-2})$ and considering nondimensionalized versions of equations (2.7), (2.8), (2.9) and the interface conditions

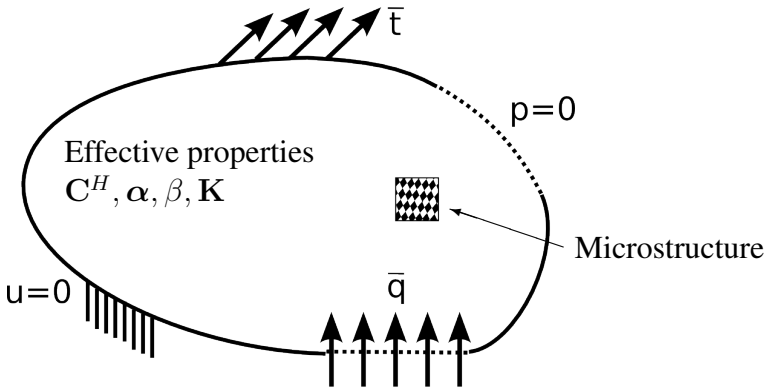

Figure 2.4 Illustration of the macroscopic boundary value problem and its boundary conditions.

(2.10),(2.11). The variables are then expanded by the asymptotic expansion

$$\mathbf{u}(\mathbf{x},\mathbf{y},t) = \mathbf{u}^{(0)}(\mathbf{x},\mathbf{y},t) + \epsilon\mathbf{u}^{(1)}(\mathbf{x},\mathbf{y},t) + \dots \tag{2.13}$$

$$\mathbf{v}(\mathbf{x},\mathbf{y},t) = \mathbf{v}^{(0)}(\mathbf{x},\mathbf{y},t) + \epsilon\mathbf{v}^{(1)}(\mathbf{x},\mathbf{y},t) + \dots \tag{2.14}$$

$$p(\mathbf{x},\mathbf{y},t) = p^{(0)}(\mathbf{x},\mathbf{y},t) + \epsilon p^{(1)}(\mathbf{x},\mathbf{y},t) + \dots \tag{2.15}$$

where $\mathbf{y} = \epsilon^{-1}\mathbf{x}$ and the expanded variables $\mathbf{u}^{(i)}$, $\mathbf{v}^{(i)}$ and $p^{(i)}$ are Ω-periodic in $\mathbf{y}$. By inserting the expanded variables and separating the scales, two sets of equations are obtained namely; one set describing the macroscopic behavior of the system and another describing the microscopic. The details are shown in Appendix A that follows the expansion and separation procedure from Auriault et al. (2009).

2.2.1 The macroscopic equations

The resulting macroscopic model is also known as the Biot consolidation equations that were shown by Biot (1941) and were derived using a phenomenological approach. The macro model formulation is also named the mixed stiffness formulation (Wang, 2000) due to the choice of state variables, namely the strains (displacements) and the pressure. A sketch of the boundary value problem along with the applicable boundary conditions is shown in figure 2.4. The macroscopic equations yield

Find $\mathbf{u} \in \mathcal{V}^3$ and $p \in \mathcal{P}$ such that

$$\int_V \varepsilon_{ij}(\hat{\mathbf{u}}) C^H_{ijlm} \varepsilon_{lm}(\mathbf{u})\,\mathrm{d}V - \int_V \varepsilon_{ij}(\hat{\mathbf{u}})\alpha_{ij} p\,\mathrm{d}V = \int_{A_t} \hat{u}_i \bar{t}_i\,\mathrm{d}A \qquad \forall \hat{\mathbf{u}} \in \mathcal{V}^3_0 \tag{2.16}$$

$$\int_V \alpha_{ij}\varepsilon_{ij}(\dot{\mathbf{u}})\hat{p}\,\mathrm{d}V + \int_V \beta\hat{p}\dot{p}\,\mathrm{d}V + \int_V \hat{p}_{,i}\frac{K_{ij}}{\mu}p_{,j}\,\mathrm{d}V = -\int_{A_v} \hat{p}\bar{q}\,\mathrm{d}A \quad \forall \hat{p} \in \mathcal{P}_0 \tag{2.17}$$

where the upper equation resembles the principle of virtual work for a linear elastic solid with an additional pressure dependent body force. The lower equation is the seepage equation with corrector terms for the change in pore volume that describes the Darcy flow

within the porous material. The material parameters $\mathbf{C}^H$, $\boldsymbol{\alpha}$, β and $\mathbf{K}$ are all determined by the microscale equations which are presented in the next section. The traction $\bar{\mathbf{t}}$ is acting on a part of the solid boundary, A_t and $\bar{q}$ is a prescribed fluid flux into the domain at A_v.

2.2.2 The microscopic equations

Several microscale equations appear that are all defined in a unit-cell having periodic boundary conditions, as this periodicity is a prerequisite for the multiscale procedure. The microscale equations are necessary for the homogenization of material properties. These properties are the effective material stiffness tensor $\mathbf{C}^H$, the pressure coupling tensor $\boldsymbol{\alpha}$, which transfers the pore pressure into solid stress, the microstructure compressibility β and the fluid permeability $\mathbf{K}$. By solving the microscale equations, the effective properties can be obtained by integration over the volume.

Effective elastic properties

First the properties of the elastic skeleton are computed. The microscale equations yield

Find $\boldsymbol{\xi}^{kh} \in \mathcal{V}^3$ and $\boldsymbol{\eta} \in \mathcal{V}^3$ such that

$$\int_{\Omega_s} \varepsilon_{ij}(\hat{\mathbf{u}}) c_{ijlm} \varepsilon_{lm}(\boldsymbol{\xi}^{kh}) \,\mathrm{d}\Omega = \int_{\Omega_s} \varepsilon_{ij}(\hat{\mathbf{u}}) c_{ijlm} \bar{\varepsilon}^{kh}_{lm} \,\mathrm{d}\Omega \qquad \forall \hat{\mathbf{u}} \in \mathcal{V}^3_0 \tag{2.18}$$

$$\int_{\Omega_s} \varepsilon_{ij}(\hat{\mathbf{u}}) c_{ijlm} \varepsilon_{lm}(\boldsymbol{\eta}) \,\mathrm{d}\Omega = \int_{\Omega_s} \varepsilon_{ij}(\hat{\mathbf{u}}) \delta_{ij} \,\mathrm{d}\Omega \qquad \forall \hat{\mathbf{u}} \in \mathcal{V}^3_0 \tag{2.19}$$

where $\bar{\varepsilon}^{kh}_{lm}$ is a second order tensor with the only non-zero entry $\bar{\varepsilon}^{kh}_{kh} = 1$ and c_{ijlm} is the nondimensional stiffness tensor of the basis material ($c_{ijlm} = C_{ijlm}/c^*$). Equation (2.18) contains six boundary value problems due to k and h taking up the values from one to three and considering the symmetry of the elastic material tensor. Equation (2.19) contains just a single problem. The effective elastic properties can then be evaluated using the solutions $\boldsymbol{\xi}^{kh}$ and $\boldsymbol{\eta}$. The homogenized stiffness tensor is given by the volume average

$$C^H_{ijkh} = \frac{c^*}{|\Omega|} \int_{\Omega_s} c_{ijkh} + c_{ijlm} \varepsilon_{lm}(\boldsymbol{\xi}^{kh}) \,\mathrm{d}\Omega \tag{2.20}$$

The pressure coupling tensor $\boldsymbol{\alpha}$, also known as the *Biot-Willis* coefficient (Biot and Willis, 1957), can be computed using either of the two solutions as

$$\alpha_{ij} = \phi \delta_{ij} + \frac{1}{|\Omega|} \int_{\Omega_s} c_{ijlm} \varepsilon_{lm}(\boldsymbol{\eta}) \,\mathrm{d}\Omega, \qquad \alpha_{ij} = \phi \delta_{ij} - \frac{1}{|\Omega|} \int_{\Omega_s} \xi^{ij}_{p,p} \,\mathrm{d}\Omega \tag{2.21}$$

where ϕ is the porosity. The microstructure compressibility, or the constrained specific

storage[1], is computed as

$$\beta = \frac{1}{|\Omega| K_b^*} \int_{\Omega_s} \eta_{p,p} \, \mathrm{d}\Omega \tag{2.22}$$

where K_b^* is the bulk modulus of the basis material. It should be noted that if the basis material is isotropic then the solution for $\boldsymbol{\eta}$ is redundant as $\boldsymbol{\alpha}$ and β can be computed from the homogenized stiffness tensor $\mathbf{C}^H$ by

$$\alpha_{ij} = \delta_{ij} - \frac{C^H_{pqij}\delta_{pq}}{3\lambda + 2G} \tag{2.23}$$

$$\beta = \frac{1}{3\lambda + 2G} \left(3(1-\phi) - \frac{C^H_{ppjj}}{3\lambda + 2G} \right) \tag{2.24}$$

where $\lambda = E\nu/[(1+\nu)(1-2\nu)]$ and $G = E/[2(1+\nu)]$ are the Lamé coefficients for the basis material with Young's modulus E and Poisson's ratio ν. For macroscopically isotropic materials, the fraction in the $\boldsymbol{\alpha}$ computation reduces to the ratio between the bulk modulus of the composite and the basis material. This means that the pressure coupling approaches unity if an incompressible material is used.

Effective fluid properties

The flow inside the porous microstructure is given by Stokes equation assuming incompressibility which is reflected in the microscale flow equations i.e.

Find $\mathbf{v}^k \in \mathcal{W}^3$ and $\theta^k \in \mathcal{P}$ such that

$$\int_{\Omega_f} \hat{v}_{i,j} v^k_{i,j} \, \mathrm{d}\Omega - \int_{\Omega_f} \hat{v}_{i,i} \theta^k \, \mathrm{d}\Omega = \int_{\Omega_f} \hat{v}_i \delta_{ik} \, \mathrm{d}\Omega \qquad \forall \hat{\mathbf{v}} \in \mathcal{W}^3_0 \tag{2.25}$$

$$\int_{\Omega_f} \hat{\theta} v^k_{i,i} \, \mathrm{d}\Omega = 0 \qquad \forall \hat{\theta} \in \mathcal{P} \tag{2.26}$$

in which $\mathbf{v}^k$ is the velocity field and θ^k is the pressure field. It is noted that the equations describe three distinct boundary value problems corresponding to an imposed flow in the three coordinate directions. The permeability tensor can be computed as the volumetric average of the flow velocity as

$$\kappa_{ik} = \frac{1}{|\Omega|} \int_{\Omega_f} v^k_i \, \mathrm{d}\Omega \tag{2.27}$$

Contrary to the elastic properties where the size of the microstructure does not matter the permeability is scale related. The permeability should, prior to insertion in equation (2.17), be scaled according to the unit-cell size l as $\mathbf{K} = l^2 \boldsymbol{\kappa}$.

[1] In poromechanics the constrained specific storage usually considers a slightly compressible fluid, in this case this will change to $\beta_{tot} = \beta + \phi/K_f$ (Auriault et al., 2009), where K_f is the bulk modulus of the fluid.

Effective properties

In order to exemplify the behavior of the effective parameters for a varying density, successive homogenizations of a fixed microstructure topology with varying cross-section width is performed. The microstructure is a grid-type microstructure and is visualized in figure 2.5. By varying the width w of the solid cross section, the relative density, $\rho = 3w^2 - 2w^3$, is also varied and relations between density and the homogenized properties are established.

The effective stiffness properties are plotted in figure 2.6 by means of normalized stiffness matrix entries e.g $\tilde{C}_{1111} = C^H_{1111}/C_{1111}$. It is important to observe that the stiffness is not a linear function, but rather a power function, of the density.

In figure 2.7 the pressure coupling coefficient α ($\boldsymbol{\alpha} = \alpha\mathbf{I}$ for cubic symmetry) and microstructure compressibility β are plotted. The pressure coupling is large when the density is low while the coupling is zero for the total solid material. The β parameter is zero for both total solid and total absence of material. The physical interpretation of the parameter can be stated as *the ratio of increment in fluid content to the change in pore pressure for a constant volumetric strain*(Wang, 2000). For the limit of an empty microstructure there will solely be incompressible fluid inside the unit-cell and hence β approaches zero. When the unit-cell is solid only, there is no room for fluid and β will again approach zero.

The homogenized values for the permeability are shown in figure 2.8. It should be noted that the ordinate is logarithmic and that the permeability of the structure varies with several orders of magnitude. In principle the permeability is infinite at $\rho = 0$ and zero at $\rho = 1$; however, due to the final discretization of the microstructure the limits are not investigated further.

2.3 The Brinkman equation

Elaborating further on the porous flow model in a homogenization context, it can be shown that the Brinkman equation (Brinkman, 1947) that models the transition flow from porous to free media can be obtained using the same homogenization method as for obtaining the Darcy flow law if just an additional corrector term is included(Lévy, 1983; Auriault et al., 2005). However, it is beyond the scope of this work to follow the derivation. The Brinkman equation, assuming an isotropic permeability K, yields

Find $v_i \in \mathcal{W}$ and $p \in \mathcal{P}$ such that

$$\int_{\Omega_f} \mu \hat{v}_{i,j} v_{i,j} \, \mathrm{d}\Omega - \int_{\Omega_f} \hat{v}_{i,i} p \, \mathrm{d}\Omega + \int_{\Omega_f} \hat{v}_i \frac{\mu}{K} v_i \, \mathrm{d}\Omega = 0 \qquad \forall \hat{v}_i \in \mathcal{W}_0 \tag{2.28}$$

from which it is seen that when the permeability is infinite (free flow) the Stokes equations are resembled. If the permeability is very low one might think that Darcy's law is obtained in the limit; however, as the viscous term is not interpolated it is persistent and the equation models the porous flow in a different way. The physical validity and limited

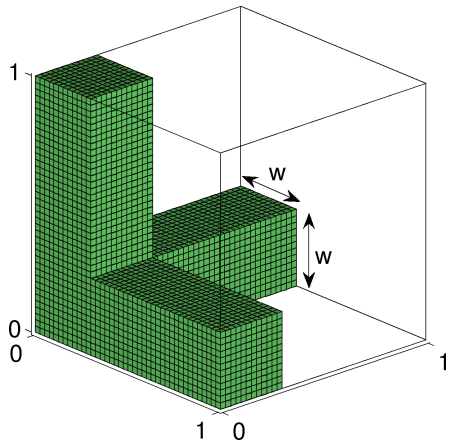

Figure 2.5 Homogenized microstructure topology, here shown for $w = 0.3$. Periodic boundary conditions are applied and a single corner node is fixed to prevent rigid body motion. The procedure is used and further described in [P3].

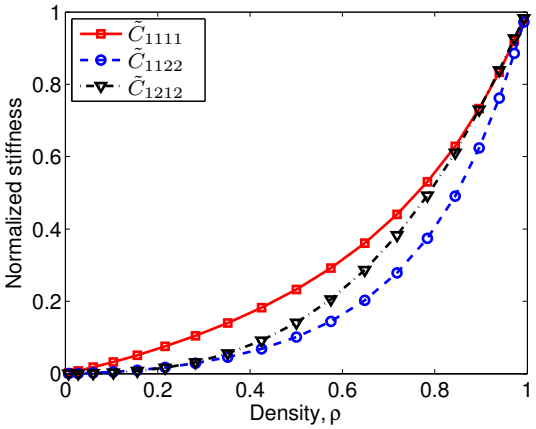

Figure 2.6 Effective stiffness parameters nondimensionalized by the corresponding entries from the stiffness matrix of the basis material.

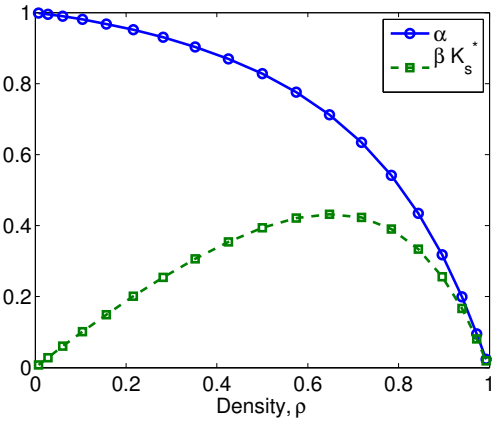

Figure 2.7 Homogenization based values for pressure coupling α and normalized compressibility βK_s^* using equation (2.23) and (2.24). For a cubic symmetric microstructure the pressure coupling tensor can be represented by a scalar $\boldsymbol{\alpha} = \alpha \mathbf{I}$

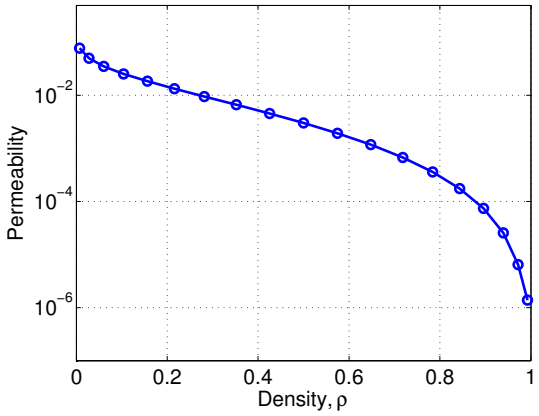

Figure 2.8 Homogenized permeability of microstructure for varying density. In principle there should be vertical asymptotes at both $\rho = 0$ and $\rho = 1$.

applicability of modeling porous flow by the Brinkman equation is discussed in Auriault (2009). However, in this thesis the Brinkman equation is used for modeling the transition flow where the flow in the low permeability areas is of less interest.

Chapter 3
Topology optimization applied to multiscale problems and flows

Topology optimization is one of several approaches for systematically improving the design of a general structure. Roughly, the different methods can be classified as: Sizing; in which the sizes of the members in a given structure are modified. Shape; in which the shape of the design is considered by moving / altering the boundary and Topology; in which material or no material is distributed within a fixed domain such that a new topology can appear. This fact, that the topology is free to change, is a great advantage in the optimization of materials and structures.

The topology optimization method, as it is applied most frequently, uses the so-called density method. This means that the design domain, visualized as a digital picture, is divided into a number of design elements, pixels. Each design element, or pixel, can then take a density between 0 and 1 representing the relative density of material. For a given design the boundary between material and void is usually well defined, however this strict partitioning of the domain is relaxed in topology optimization in such a way, that the design variables can take intermediate values. This corresponds in the image analogy to transform from black-white into grayscale. During optimization, intermediate densities are allowed and upon convergence, the picture should again be black-white. Choosing a proper interpolation function for the involved physical parameters will most often result in a black-white design.

The optimization procedure is an iterative process in which an initial design is given e.g. a random distribution. The corresponding state equations are solved and the sensitivity for each design variable is computed. Using a suitable optimization algorithm for solving Non Linear Programs (NLP), here the Method of Moving Asymptotes (MMA), the design is updated and a new iteration is initiated.

The development of the topology optimization method and its application to areas related to the subject of this thesis will be presented next. Furthermore, the methods and concepts used in this work will be introduced.

3.1 Literature review

Topology optimization has its offspring in the homogenization theory (Bensoussan et al., 1978) for linear elastic materials. The initial idea was to use the homogenization of a unit-cell in order to derive material properties for use in a structural problem. By choosing a simple geometry for the unit-cell design i.e. a unit square with a square hole, the material can be characterized by the length of the square and additionally the rotation of the material. In order to limit the number of homogenization procedures a final number

of different unit cells were analyzed and the values for intermediate square sizes were interpolated. The method was first presented in the seminal paper by Bendsøe and Kikuchi (1988) and elaborated further on in Suzuki and Kikuchi (1991).

The introduction of the SIMP interpolation (Bendsøe, 1989; Zhou and Rozvany, 1991) an acronym for Solid Isotropic Material with Penalization simplified the material interpolation greatly. However, in the beginning the physical interpretation of the microstructures related to the SIMP interpolation were less obvious but this was revisited in Bendsøe and Sigmund (1999). The interpolation introduces a single variable interpretation of the material in each material point. The SIMP scheme is a power law, which suffers from the fact that it has no sensitivity for void elements. This deficit is circumvented by the introduction of RAMP (Stolpe and Svanberg, 2001) (Rational Approximation of Material Properties) which is used for most designs in this thesis.

Already from the first papers on the topology optimization method it is evident that the optimized designs suffer from numerical artifacts such as mesh dependency and checkerboard patterns that introduce artificial stiffness. By applying a heuristic filter on the sensitivities, Sigmund (1994a) avoids the checkerboard patterns. Further methods for avoiding the numerical artifacts are discussed in Sigmund and Petersson (1998) and Sigmund (2007). The sensitivity filter works well within elastic problems; however, a more versatile method is presented in Bruns and Tortorelli (2001) which filters the densities. A thorough mathematically description is given in Bourdin (2001). With the density filter, intermediate density elements appear in the final design, which is unfavorable. Several filters have been proposed to deal with this issue as well as the challenge of imposing a minimum length scale and robustness in the design. A survey is given in Sigmund (2007).

In the following subsections the developments within areas that relate to the optimization presented in this thesis are reviewed.

3.1.1 Microscale - Material optimization

The applications and developments within material optimization are numerous. Much work has been dedicated to the material characterization based on variational bounds and self-consistent estimates. The developments presented here are all material designs based on topology optimization.

Materials with prescribed material parameters using inverse homogenization for truss-like structures were optimized in Sigmund (1994b, 1995). The concept was extended for continuum structures in order to optimize materials with extreme thermal expansion coefficients in Sigmund and Torquato (1996, 1997). The elastic properties such as the bulk modulus were maximized in Sigmund (1999, 2000) subject to constraints on the conductivity while elastic design using multiple phases was considered in Gibiansky and Sigmund (2000). The permeability of a porous material were optimized in Guest and Prévost (2007) while the pareto-optimality of permeability and stiffness were investigated in Jung and Torquato (2005) and Guest and Prévost (2006).

The design of elastic materials have a close connection to bone remodeling and scaf-

fold engineering (Bagge, 2000; Hollister et al., 2002; Lin et al., 2004) in which similar methods have been applied.

The stability of topology optimized structures were investigated in Neves et al. (1995) and applied for material optimization by penalization of highly localized buckling modes in Neves et al. (2002).

3.1.2 Multiscale

Most applications of the topology optimization method use the density approach e.g. the SIMP interpolation scheme as a material indicator. However, the seminal paper Bendsøe and Kikuchi (1988) uses a homogenization approach to derive the material properties. These are obtained by homogenizing a fixed topology microstructure for a varying density; however, in practice a final number of homogenization is performed and the properties are interpolated. By considering this homogenization as a material design problem, a full two-scale model appears. Such a hierarchical multiscale optimization model is presented in Rodrigues et al. (2002). It includes sequential optimization of the material microstructure and the material distribution problem. The final macrostructure will most unlikely be completely binary as the gray elements are representative for an optimized porous microstructure. The method has been implemented for bone reanalysis in Coelho et al. (2008, 2009). Furthermore, it was also used for extending transient thermal problems (Turteltaub, 2001) into hierarchical optimization problems (Guedes et al., 2006).

A slightly different approach using interpolation schemes at both the macro and the micro scale was introduced in Liu et al. (2008) for compliance optimization and in Nui et al. (2008) for fundamental frequency optimization. A two-scale method for optimizing the structural compliance subject to a seepage constraint was presented in Xu and Cheng (2010).

Free material optimization (FMO) introduced in Bendsøe et al. (1994) is another approach to multiscale optimization as it concerns the distribution of material parameters rather than densities allowing for anisotropic materials. However, the method itself does not consider the material designs or composite layups that are needed.

3.1.3 Fluid optimization

Topology optimization has also successfully been applied to flow problems with vanishing to moderate Reynolds numbers. The seminal paper by Borrvall and Petersson (2003) concerns Stokes flow, in which lubrication theory motivates use of the Brinkman equation to interpolate between flow and non-flow regions. A large-scale 3D approach was presented in Aage et al. (2008). In Gersborg-Hansen et al. (2005); Olesen et al. (2006) the flow modeling was extended to moderate Reynolds numbers governed by the Navier-Stokes equation. The limits on the permeability applied in the Brinkman equation were investigated by Evgrafov (2006). Another interpolation approach is taken in Guest and Prévost (2007) in which the interpolation is between the Darcy and the Stokes equations. In the limit of a 0-1 solution the difference between the two methods is vanishing. A

Darcy-Stokes interpolation is also used in Wiker et al. (2007) where the viscosity is also interpolated.

As topology optimization was first presented for structural optimization problems the finite element method is an obvious method of discretization. Within fluid mechanics, the finite volume method is popular and Othmer (2008) presents an implementation for commercial CFD programs. In Pingen et al. (2007) the lattice boltzmann method was used for the modeling while Evgrafov et al. (2008) presents an implementation using kinetic gas theory.

Topology optimization of the fluid-structure interaction problem is difficult as both the fluid and the solid need to be represented in the monolithic representation. In Yoon (2010) such a coupling is introduced however, the designs and applications are limited. Another approach is taken in Kreissl et al. (2010) where flexible microfluidic devices are optimized.

Related to the flow problems is that of scalar transport. This could either be the concentration of some matter or simply temperature. In Gersborg-Hansen (2007) a coupled transport problem in a microfluidic channel is optimized with respect to mixing and in Okkels and Bruus (2007) a catalytic reactor is optimized for increased reaction rate.

3.2 Introduction to topology optimization

In the following subsections, the application of topology optimization to the topics covered in this thesis is explained.

3.2.1 Elasticity

The design interpolation schemes used in topology optimization are generally based on the homogenization method as mentioned previously. For the application in linear elasticity, the first interpolation scheme introduced was SIMP (Bendsøe, 1989) which is essentially a power law

$$E(\rho) = \rho^p E_0 \tag{3.1}$$

where p is a penalization power and E_0 is the stiffness of the solid elastic material. The interpolation is between void and elastic material and the scheme is widely used in the community though it has some deficits. As the void material naturally has no stiffness the governing equations become singular in this limit. This, however, can be cured by introducing a very low artificial stiffness for the void material. Another deficit and the main reason for using of the RAMP interpolation (Stolpe and Svanberg, 2001) in this thesis is that the sensitivity for void elements is zero. This might influence the change in topology, as new isles of material cannot appear on their own; they need to emerge from an existing solid/porous region. The RAMP interpolation used for the material is

$$E(\rho) = \left(E_{min} + \frac{\rho(1 - E_{min})}{1 + p(1 - \rho)} \right) E_0 \tag{3.2}$$

in which $E_0 E_{min}$ is the stiffness of void and p is a penalty factor. For $p = 0$ it reduces to a linear interpolation between two materials.

3.2.2 Flow - Brinkmann

Flow problems are usually modeled by the Navier-Stokes equations. Compared to the equations for linear elasticity it is not as obvious where to introduce the interpolation. Relying on the linear elastic case it is most obvious to interpolate the viscosity, as the diffusion term of the Navier-Stokes equations look similar. This idea was tested in Gersborg-Hansen (2007) with limited success. A less intuitive but much more robust method was presented in Borrvall and Petersson (2003) which was motivated by Couette flow (flow in the narrow gap between two plates). The equation that was employed was the Brinkman equation (Brinkman, 1947) which models flow in porous media with larger obstacles than that of the Darcy equation. With the Brinkman equation, the regularization of the flow is done through the variation of the permeability term. From a numerical point of view, it is simply a penalization of the flow velocity.

For the flow problems an interpolation scheme is proposed by Borrvall and Petersson (2003) which at first sight seems to share structure with the RAMP scheme

$$\zeta(\rho) = \zeta_{max} + (\zeta_{min} - \zeta_{max})(1 - \rho)\frac{1 + q}{(1 - \rho) + q} \tag{3.3}$$

where ζ is the inverse permeability and q is a penalization factor. However, for a penalty parameter $q = 1/p$ it is in fact the RAMP scheme. The limit ζ_{max} is determined such that the fluid flow velocity in the dense porous media is of negligible magnitude and ζ_{min} is typically zero such that the Brinkman term vanishes and the Stokes equation is obtained.

3.2.3 Poroelasticity

Having introduced these two interpolation schemes, the frame for the topology optimization is set. The papers [P1,P2,P4,P5] all use the density method for the optimization. However, in [P3] we return to the method presented in the seminal paper by Bendsøe and Kikuchi (1988), and apply this to the poroelastic equations. This means that for a fixed microstructure topology the homogenization of the elastic and flow properties for a number of different densities, related to the width of a structure, are evaluated and afterwards interpolated. The microstructure topology is that of a cross with a square cross section. This type of topology is cubic symmetric as it looks the same from each side of the unit cell and in an ensemble of unit-cells it yields a grid. This makes it possible to characterize the elastic properties by three values and the permeability by a single value.

3.3 Optimization and numerical procedure

In this section, a brief introduction will be given to the optimization algorithm; however, the focus is on the procedure rather than the underlying theorems.

The optimization problems solved in this thesis can all be cast in the form of a general optimization problem

$$\left.\begin{array}{lll} \min\limits_{\boldsymbol{\rho}\in\mathbb{R}^N} & f_0(\boldsymbol{\rho},\mathbf{x}) & \text{Objective function} \\ \text{subject to} & \mathbf{A}(\boldsymbol{\rho})\mathbf{x}=\mathbf{b}(\boldsymbol{\rho}) & \text{State equations} \\ & f_i(\boldsymbol{\rho},\mathbf{x})<0 \quad \text{for } i=1,...,M & \text{Inequality constraints} \\ & 0\leq\rho_e\leq 1, \quad \text{for } e=1,...,N & \text{Box constraints} \end{array}\right\} \tag{3.4}$$

where M is the number of inequality constraints and N is the number of design variables. There are two different ways to approach this optimization problem. The first is often referred to as the nested approach as the state problem is solved during objective evaluation and the state variables are not a part of the design variables. The second procedure is named SAND (Simultaneous Analysis and Design) in which the state variables are a subset of the optimization variables. The advantage of the nested approach is that existing solution procedures can easily be integrated into the optimization scheme and that the equality constraints related to the state problem can be left out of the optimization problem.

The solutions of the optimization problems in this thesis have all been obtained using the MMA implementation by Svanberg (1987). However during the research other methods have been applied for comparison, these includes GCMMA (Globally Convergent version of Method of Moving Asymptotes,Svanberg (2001)), IPOPT (Interior Point OPTimizer, Wächter and Biegler (2006)) and SNOPT (Sparse Non-linear OPTimizer, Gill et.al) which are all based on solving convex approximations of the nonlinear program. The optimizers were all implemented for the mixer problem [P4] but no explicit comparison study was conducted. In general it is the authors experience that MMA is the most efficient optimizer for topology optimization problems with a few constraints. The handling of infeasible constraints seems to be more efficient in (GC)MMA compared to IPOPT. Furthermore, the objective initially decrease at a faster rate but the total number of function evaluations might be the same. The implementation of SNOPT was targeted the handling of many linear manufacturing constraints; however, the method of [P5] is a more efficient choice. For brevity only MMA will be given further attention.

The basic concept behind the MMA is that a general non-linear optimization problem can be approximated locally by a convex problem. The approximating function is generated using two hyperbolic functions and has two vertical asymptotes for each design variable which are adjusted during the optimization. At every optimization step this approximation is generated and solved by a primal-dual solver. This procedure is repeated until convergence, which in this thesis as in many other applications of the topology optimization method is interpreted as a sufficiently small change in the design in two sequent iterations e.g. $\|\boldsymbol{\rho}^k-\boldsymbol{\rho}^{k+1}\|_\infty<0.01$.

An overview of the procedure for a general topology optimization problem using a density based filter can be given as

1. Initialize
2. For $k = 1$ to k_{max}
   (a) Filter densities $\tilde{\boldsymbol{\rho}}^k = \mathcal{F}(\boldsymbol{\rho}^k)$
   (b) Solve state problem(s), compute f_0, f_i,
   (c) Solve adjoint problem(s) and compute sensitivities, $\frac{\mathrm{d}f_0}{\mathrm{d}\tilde{\boldsymbol{\rho}}^k}, \frac{\mathrm{d}f_i}{\mathrm{d}\tilde{\boldsymbol{\rho}}^k}$
   (d) Update sensitivities, $\frac{\mathrm{d}f_0}{\mathrm{d}\boldsymbol{\rho}^k} = \frac{\mathrm{d}f_0}{\mathrm{d}\tilde{\boldsymbol{\rho}}^k}\frac{\mathrm{d}\tilde{\boldsymbol{\rho}}}{\mathrm{d}\boldsymbol{\rho}}$, $\frac{\mathrm{d}f_i}{\mathrm{d}\boldsymbol{\rho}^k} = \frac{\mathrm{d}f_i}{\mathrm{d}\tilde{\boldsymbol{\rho}}^k}\frac{\mathrm{d}\tilde{\boldsymbol{\rho}}}{\mathrm{d}\boldsymbol{\rho}}$
   (e) Compute $\boldsymbol{\rho}^{k+1}$ using MMA
   (f) Break if $\|\boldsymbol{\rho}^k - \boldsymbol{\rho}^{k+1}\|_\infty < 0.01$
3. Post process

The numerical implementation of the optimization procedure is written in a framework of Comsol Multiphysics and Matlab where the FEM problems are solved within Comsol and the optimization is handled by a Matlab code elaborating on the MMA implementation by Svanberg (1987).

3.3.1 Filtering

The optimized designs presented in this thesis are all, except [P4], regularized by the application of a density filter (Bruns and Tortorelli, 2001; Bourdin, 2001). In comparison to filters in image processing, the density filter is similar to the blur operation. It is applied to avoid single node hinges and checkerboard patterns. The filter is easily implemented and performs well for a not too large filter neighborhood; however, if speed is an issue a PDE-filter approach can be used (Lazarov and Sigmund, 2011). For a filter with radius R the filtered density of an element e can be computed as

$$\tilde{\rho}_e = \mathcal{F}(\rho_e) = \frac{\sum\limits_{i \in N_e} w(\mathbf{x}_i, \mathbf{x}_e) v_i \rho_i}{\sum\limits_{i \in N_e} w(\mathbf{x}_i, \mathbf{x}_e) v_i}, \qquad N_e = \{i \mid \|\mathbf{x}_i - \mathbf{x}_e\| < R\} \tag{3.5}$$

where $\mathbf{x}_e$ is the spatial coordinate of element e, $w(\mathbf{x}_i, \mathbf{x}_e) = R - \|\mathbf{x}_i - \mathbf{x}_e\|$ is the linear weighting function and v_i is the element volume. The chain rule used to update the sensitivities can be stated as

$$\frac{\mathrm{d}f_0}{\mathrm{d}\rho_e} = \sum_{i \in N_e} \frac{\mathrm{d}f_0}{\mathrm{d}\tilde{\rho}_i} \frac{w(\mathbf{x}_e, \mathbf{x}_i) v_e}{\sum\limits_{j \in N_i} w(\mathbf{x}_j, \mathbf{x}_i) v_j} \tag{3.6}$$

which means that not only is the weighting of the neighboring elements involved but also the weighting of their neighbors.

3.3.2 Sensitivity analysis

One of the main advantages of the topology optimization method is that there is no need for internal boundary representation. This is obtained by casting the equations in a monolithic form and the sensitivities are then related to the elements instead of explicit boundaries. In general, every finite element in the design domain has its own density leading to potentially very many design variables requiring an efficient technique for computing the sensitivities. For simple design problems containing a few design variables, the finite difference approach, requiring one state evaluation per design variable, would be a feasible choice. However, this is rarely the case in topology optimization and therefore the adjoint method is most often applied (see e.g. Michaleris et al. (1994)). A brief outline of the procedure is

1. Construct the augmented Lagrangian $\mathcal{L}$ (objective function plus the residual of the state equations multiplied by the adjoint variable λ)

2. Differentiate $\mathcal{L}$ with respect to the design variables,

3. Collect and equate to zero the terms that depend on the derivative of the state variables and solve this adjoint problem.

4. Compute the sensitivity by inserting the obtained adjoint variable λ in the remaining terms.

For the general problem stated in equation (3.4) the adjoint sensitivity is given by first constructing the Lagrangian $\mathcal{L}$:

$$\mathcal{L} = f_0(\boldsymbol{\rho}, \mathbf{x}) + \boldsymbol{\lambda}^T(\mathbf{b}(\boldsymbol{\rho}) - \mathbf{A}(\boldsymbol{\rho})\mathbf{x}) \tag{3.7}$$

then differentiate by the design variables and apply the chain rule

$$\frac{\mathrm{d}\mathcal{L}}{\mathrm{d}\boldsymbol{\rho}} = \frac{\partial f_0}{\partial \boldsymbol{\rho}} + \boldsymbol{\lambda}^T\left(\frac{\partial \mathbf{b}}{\partial \boldsymbol{\rho}} - \frac{\partial \mathbf{A}}{\partial \boldsymbol{\rho}}\mathbf{x}\right) + \underbrace{\frac{\partial f_0}{\partial \mathbf{x}}\frac{\mathrm{d}\mathbf{x}}{\mathrm{d}\boldsymbol{\rho}} - \boldsymbol{\lambda}^T\mathbf{A}\frac{\mathrm{d}\mathbf{x}}{\mathrm{d}\boldsymbol{\rho}}}_{*} \tag{3.8}$$

Now, by letting the terms that depend directly on the derivative of the state variable equate to zero, the calculation of this quantity can be avoided. Instead the * marked terms form the adjoint problem

$$\mathbf{A}^T\boldsymbol{\lambda} = \left(\frac{\partial f_0}{\partial \mathbf{x}}\right)^T \tag{3.9}$$

The adjoint problem is very similar to the original problem and for symmetric problems, such as elasticity, the system matrix $\mathbf{A}$ and its factorization can be reused in the solution of the adjoint problem. For problems involving convection, $\mathbf{A}$ is generally non-symmetric

and a new matrix must be assembled and factorized. After obtaining the adjoint variable the sensitivities can be computed by the expression

$$\frac{\mathrm{d}f_0}{\mathrm{d}\boldsymbol{\rho}} = \frac{\mathrm{d}\mathcal{L}}{\mathrm{d}\boldsymbol{\rho}} = \frac{\partial f_0}{\partial \boldsymbol{\rho}} + \boldsymbol{\lambda}^T \left(\frac{\partial \mathbf{b}}{\partial \boldsymbol{\rho}} - \frac{\partial \mathbf{A}}{\partial \boldsymbol{\rho}} \mathbf{x} \right) \tag{3.10}$$

In the case of transient optimization problems, the present method is also applicable but the derivations are lengthier. Therefore the reader is referred to [P3] for the transient version as it only applies to the problems solved therein.

For some optimization problems the adjoint variable shows up to be identical to the original state solution $\mathbf{x}$ (or $-\mathbf{x}$) which makes it possible to compute the sensitivities by the state solution only, i.e. self-adjoint problems. This is the case for e.g. minimum compliance problems in linear elasticity and heat conduction but also the case for homogenization of the elastic stiffness and the permeability tensors. Most often, a volume constraint is imposed on the topology optimization problem and as this is a linear function of the design variables, the sensitivities are easily computed using standard differential calculus and by applying the chain-rule (3.6).

Chapter 4
Material optimization - micro scale modeling [P1]

This chapter investigates the optimization of the fluid-structure interaction in a saturated periodic porous media. The pressure coupling properties of a porous media change with its microstructure topology and this is utilized in the design of a material for use in a poroelastic actuator. The material design is optimized by applying topology optimization and the objective is to increase the shear coupling properties.

4.1 Method

Many hi-tech applications rely on adaptive materials, such as piezoelectric materials, for use in e.g. small actuators used in linear stepper motors. Such small motors are used in the auto-focus unit of modern digital cameras and as the driving mechanism in atomic force microscopes. Inspired by such applications it is interesting to develop a solid-fluid mechanical counterpart. This can be achieved by applying topology optimization to the material design used for an actuator. Figure 4.1 shows a sketch of an actuator made from two porous materials. The actuator is fixed at the left face through which it is also loaded by a fluid pressure. The dark gray material has a high stiffness and a high permeability and serves as a foundation for the actuator. The light gray material is the optimized porous material. The objective for the optimization is to make the right face of the actuator deflect or deform as much as possible.

In order to simplify the study it is assumed that the macroscopic deflection is closely

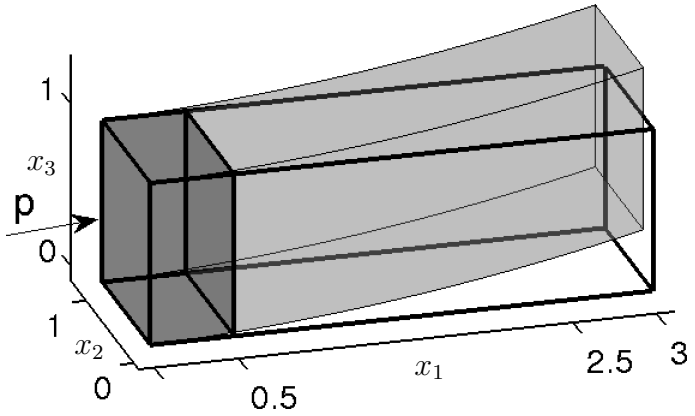

Figure 4.1 Slab of porous material in a deformed state. In the left dark gray domain, an isotropic material with relatively high stiffness and permeability is modeled. In the right light gray domain the optimized material is modeled. Left face is fixed and loaded by a fluid pressure p. All other faces are sealed.

related to the pressure coupling tensor as the actuator is loaded by an internal pressure. This motivates to focus on the microstructure and the effective parameters alone. As a second step the the optimized material is used in the actuator configuration and the deflection is evaluated.

The objective in this microstructure optimization is to maximize the shear pressure coupling properties of a saturated porous elastic material. This is done by introducing an interpolation of the stiffness in the unit-cell, as described in section 3.2.1, and by solving the homogenization equations (Section 2.2.2 and Appendix A). The solution of the homogenization is a displacement field[1] $\boldsymbol{\eta}$ from which the objective can be computed

$$\Phi = \int_\Omega \alpha_{12} + \alpha_{13} + \alpha_{23} \, \mathrm{d}\Omega \tag{4.1}$$

$$\text{where} \quad \alpha_{ij} = \frac{1}{|\Omega|} \int_\Omega (1-\rho)\delta_{ij} + E_{ijlm}(\rho)\varepsilon_{lm}(\boldsymbol{\eta}) \, \mathrm{d}\Omega \tag{4.2}$$

In order to ensure stability of the material microstructure a set of stiffness constraints is imposed. The stiffness is quantified by the directional elastic modulus and the constraints prescribe that the ratio between the homogenized and the basis material stiffness needs to be above a specified value. Furthermore, a permeability constraint is added to ensure that it is actually an open cell structure such that the structure can be loaded internally by pressurizing the saturating fluid.

4.2 Results

The results of three different optimization runs are presented; one with a volume constraint only, one with an additional constraint on the stiffness and finally one where also the permeability is constrained. Figure 4.2 shows the optimization process when the only constraint is on the solid volume fraction, here set to 50% of the design domain. It is seen that the optimized microstructure consists of inclined planes with their normal aligned to the diagonal of the unit-cell. It is also evident from the optimization history that it is within the first 100 iterations that the topology changes hereafter the optimization only concerns details in the design.

Figure 4.3 shows the optimized design when a stiffness of at least 10% relative to the basis material is required. It is seen that the planes are now connected which ensures stability in the microstructure as the planes cannot move freely anymore. Comparing the objective with the previous design, it is seen that the performance is lower; however, a material without stiffness cannot be used.

The designs with inclined planes allow a fluid flow along the planes, however if the actuator in figure 4.1 is made from these materials and the planes are considered impermeable then only the very first part of the actuator can actually be pressurized as the cells are not connected. In order to alleviate this shortcomming a constraint on the permeability of the microstructure is added. In figure 4.4 the optimized material microstructure for

[1] For consistency with Chapter 2 $\boldsymbol{\eta}$ is used even though in [P1] the corresponding solution is denoted $\boldsymbol{\xi}$

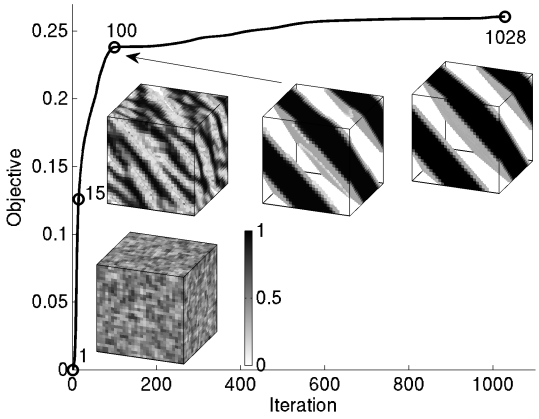

Figure 4.2 Iteration history for the maximization of the shear coupling properties subject to a volume constraint of 50%. A density filter of 1.4 element size was used. 30^3 elements. $\Phi_{final} = 0.2610$

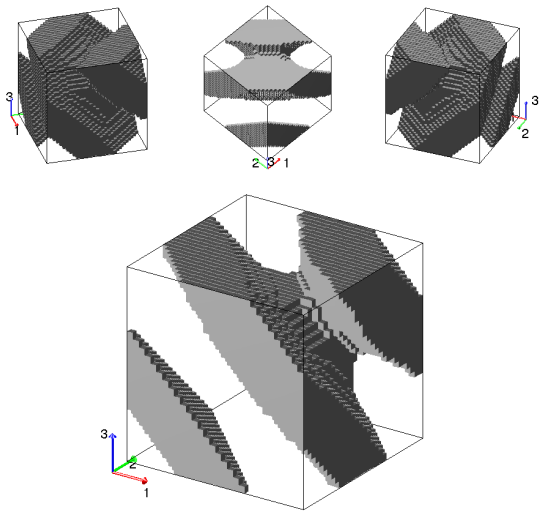

Figure 4.3 Optimized microstructure with at least 10% stiffness in each coordinate direction and 50% solid volume fraction. $\Phi_{final} = 0.2138$

such a material is shown. It is seen that the topology has changed such that the planes now have *holes* through them in which the fluid can propagate and hence pressurize the whole actuator. The objective on the other hand is of course also influenced by this constraint as the addition of holes in the inclined planes of the microstructure naturally decrease the shear coupling performance.

In order to give a better impression of the material structure a super-cell containing 27 unit-cells is shown in figure 4.5. The inclining of the unit-cell structure is visible as is the fluid connectivity among the cells.

The materials are all optimized for their effective parameters and it interesting to test whether their macroscopic performance is as expected. The effective parameters from the material shown in figure 4.4 are used in the actuator of figure 4.1. When pressurized it deflects and the resulting deformation is shown in figure 4.6 while the deformation of the right face is plotted in figure 4.7. It is seen that the actuator upon pressurization has a positive deflection in all directions, as it was intended. The right face of the actuator also dilates slightly.

Exemplified by this material optimization for use in a poroelastic actuator it is shown that the macroscopic behavior of a periodic poroelastic material can be changed such that adaptive structures can be made. A natural extension is to consider the performance of the actuator with the material embedded and optimize this directly. This approach is discussed in the next chapter.

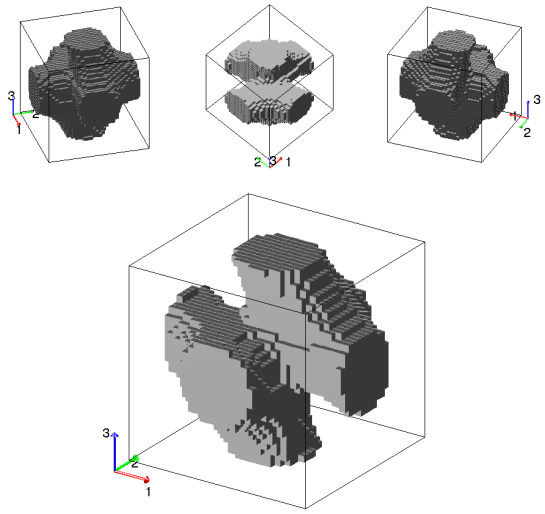

Figure 4.4 Topology for optimized pressure shear coupling, imposing constraints both on the stiffness (10% of base material) and on the permeability. $\Phi_{final} = 0.0479$

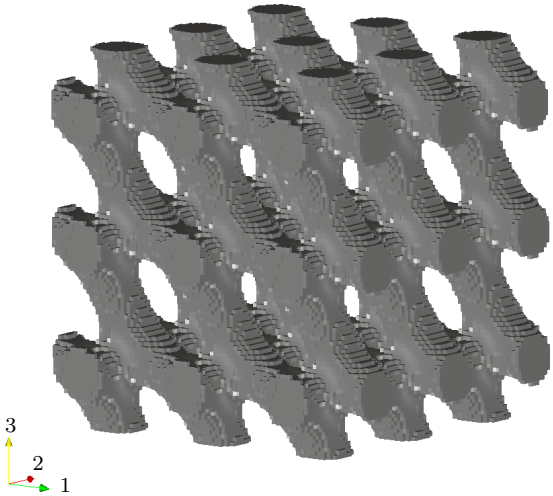

Figure 4.5 Super-cell containing $3 \times 3 \times 3$ unit-cells of the optimized material from figure 4.4. The connection among the cells is clear and the inclined planes for converting pressure to shear stress are visible.

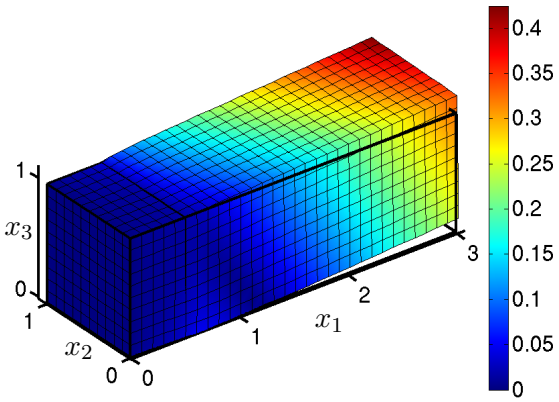

Figure 4.6 Deformation of the actuator using the maximized shear α microstructure material from figure 4.4. Colored by the cross section deformation ($\sqrt{u_2^2 + u_3^2}$).

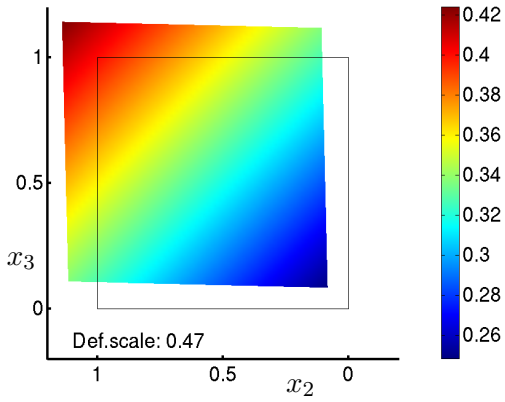

Figure 4.7 Deformation of the right face of the actuator. The pressure loading makes the actuator end translate and deform slightly. Colored by the cross section deformation ($\sqrt{u_2^2 + u_3^2}$).

Chapter 5
Material optimization - two scale approach [P2]

In this chapter, the results from [P2] are presented which covers material optimization with respect to application scale performance. The method is a natural extension to the approach presented in the previous chapter as the optimized material is analyzed and optimized in a specific application and not *just* for e.g. increased pressure coupling. Topology optimization is applied at the material scale and a fixed number of materials are optimized, in this case two.

5.1 Method

The application in which an optimized poroelastic material could be embedded is a linear motor with bi-morph actuators. The working principle of such a motor is illustrated in figure 5.1 below. Usually the actuators in linear motors are made from piezoelectric mate-

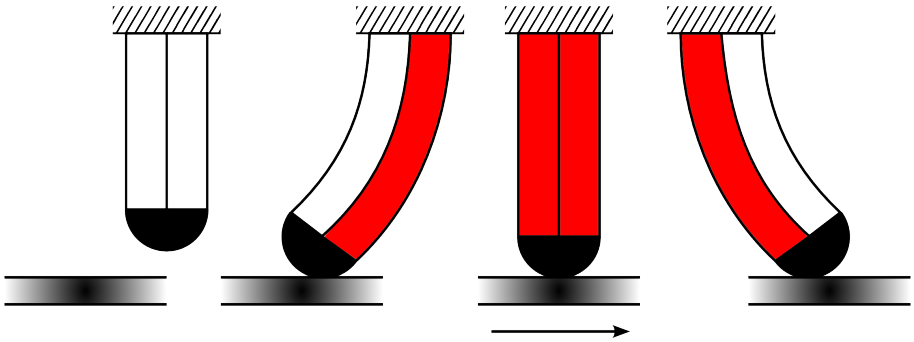

Figure 5.1 Working principle of a linear motor based on a bi-morph actuator. Step 1: Actuator is unloaded. Step 2: The right material elongates and *grips* the rod. Step 3: The left material elongates increasingly while the right material retracts which makes the rod move. Step 4: The left material is now elongated alone and the rod has moved towards right.

rials, which extend by applying a voltage. However, this might also be an application for a poroelastic actuator where applying a pressure to the saturating fluid will make it deform. Such actuators and linear motors might be applicable in non-electronics environments.

In the optimization, only the actuator is considered and the macro problem is shown in figure 5.2. The actuator consists of two fluid saturated and individually sealed porous slabs, which are assembled with a half cylinder of a solid material. At the nose line of the actuator a set of line-springs are added for the purpose of optimization. By adding these springs, it is possible to ensure that the optimized actuator is capable of applying a force to the actuated specimen, e.g. the rod, c.f. compliant mechanism design in Sigmund (1997). The actuator is fixed at the left face.

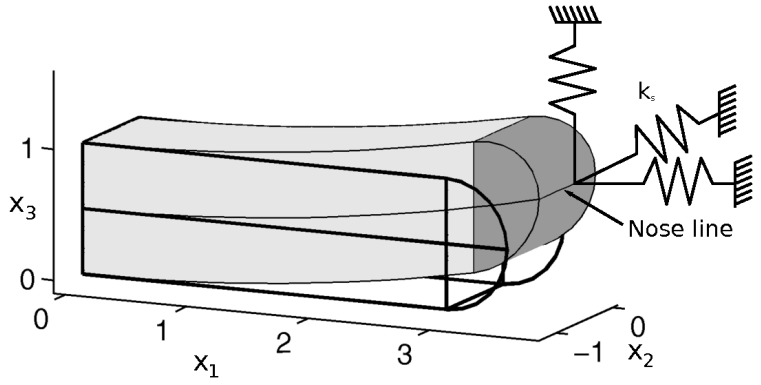

Figure 5.2 Actuator problem; two individually sealed porous slabs (light grey) assembled with a half cylinder of a stiffer elastic material (dark). Initial and deformed geometry are shown. Line springs are attached to the nose line of the actuator.

The operation of a linear motor, and thereby the actuator, is of course transient, however to simplify the optimization task only two states will be considered for the optimization, namely when either of the two porous slabs are pressurized. It is assumed that the permeability of the material microstructure is sufficiently large such that a pressure change propagates fast, hence the pressure can be assumed uniform and the transients can be neglected.

The objective is to maximize the vertical deflection of the nose-line in both the positive and negative direction. The optimization problem can, due to the two load cases denoted by superscripts, be formulated as the following min-max optimization problem:

$$\left.\begin{aligned}
\min_{\boldsymbol{\rho}\in\mathbb{R}^N} \quad & \max\left\{u_3^{(1)}, -u_3^{(2)}\right\} \\
\text{s.t.} \quad & \text{Macro equation} \\
& \text{Micro equations} \\
& \sum_{e=1}^{N_1} v_e\rho_e - \gamma_1 V_0 \leq 0, \\
& \sum_{e=N_1+1}^{N_2} v_e\rho_e - \gamma_2 V_0 \leq 0, \\
& g_i \leq 0 \\
& 0 \leq \rho_e \leq 1, \qquad\qquad \text{for } e = 1, ..., N
\end{aligned}\right\} \tag{5.1}$$

where u_3 denotes the deflection in the 3rd direction integrated along the nose line. $N = N_1 + N_2$ is the number of elements (total and in each material), γ is the allowed solid volume fraction for each material, v_e is the element volume and V_0 is the total volume of the unit-cell. g_i denotes a set of inequality constraints which will be introduced later.

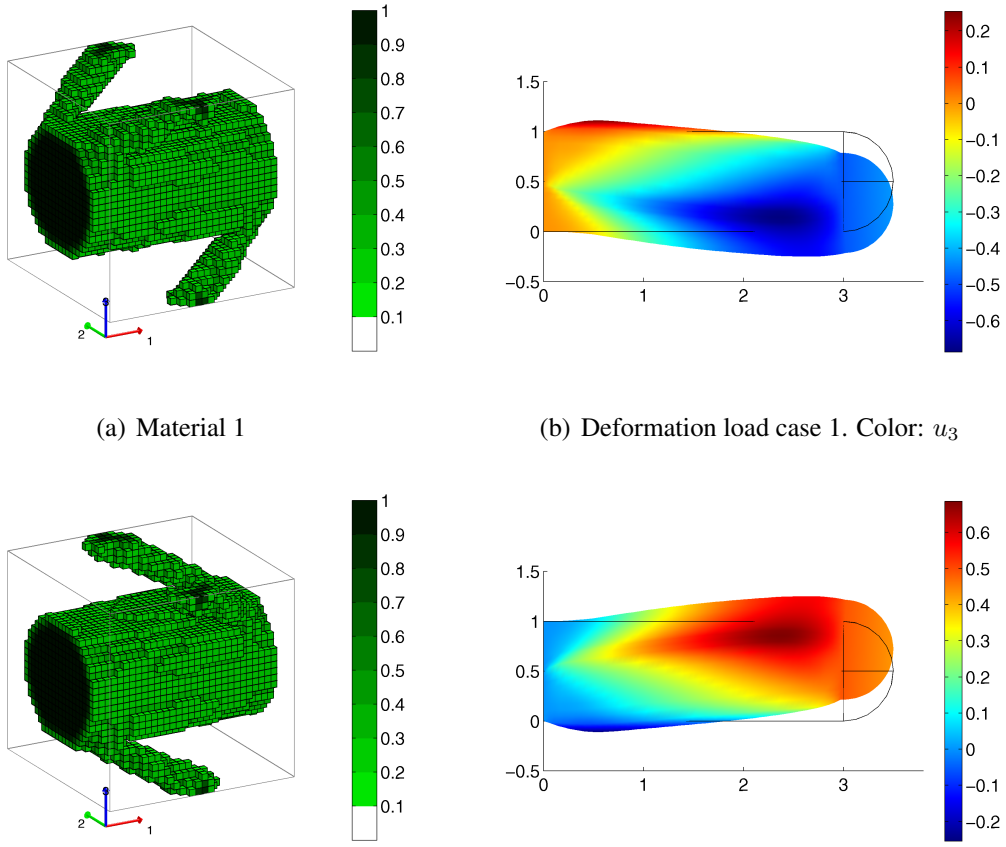

(a) Material 1

(b) Deformation load case 1. Color: u_3

(c) Material 2

(d) Deformation load case 2. Color: u_3

Figure 5.3 Optimized material configuration and deflections for each of the two load cases. Optimized with spring stiffness $k = 10^{-3}$ and pressure $p = 10^{-3}$. Same deformation scaling applies to both plots. $\Phi_{final} = max\{-u_3^{(1)}, u_3^{(2)}\} = 0.424$

5.2 Results

In this section, the results of two optimization runs are presented. The first is for an actuator, which is optimized for the transversal deflection without any considerations of the extension while the second requires the deflection to be as large as the extension.

In figure 5.3 the optimized materials and the deformed states are shown for the first problem. The initial design was a solid cross structure, which yields a perfect grid when the unit-cells are repeated. From 5.3(a) and 5.3(c), it is seen that the optimized material has a main beam in the 1st direction (along the actuator) while the connections in the 2nd and 3rd direction are thin and inclined. This results in a low transversal stiffness of the material. No explicit symmetry constraint is enforced but starting with a symmetric initial design and optimizing using a symmetric objective function does not leave any motivation to the optimizer to make two different designs except the mirroring. From

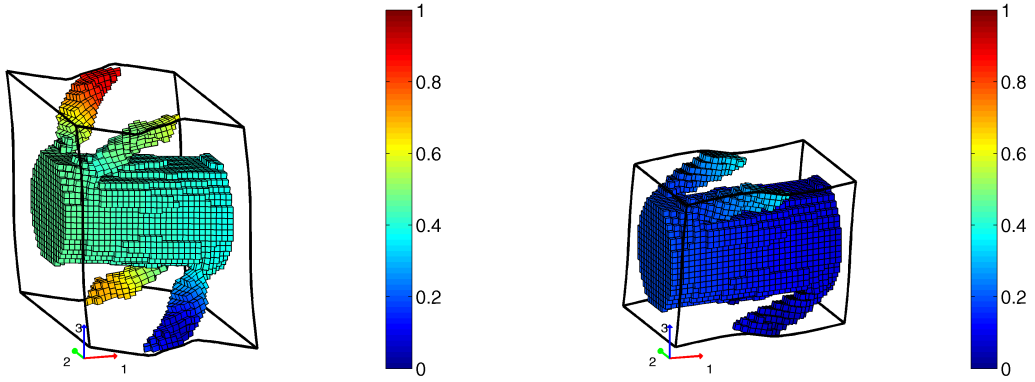

Figure 5.4 Deformed unit cell for the material at $\mathbf{x}_{up} = (1.5, -0.5, 0.75)$ for each load case. Color shows the deformation vector sum ($\sqrt{u_1^2 + u_2^2 + u_3^2}$). The deformations are scaled by a factor 0.5.

figure 5.3(b) and 5.3(d) the deformed actuator can be observed. It is seen that the vertical deflection is dominating the deformation. The upper and lower boundaries are nearly straight which might indicate that the shear strain is important. This could be linked to the low transversal stiffness of the materials together with the pressure coupling, which will make the actuator deflect.

As the link between the micro and macro scale is rigorous it is also of interest to inspect the microstructure during the deformation. The deformed unit-cell in a single point $\mathbf{x}_{up} = (1.5, -0.5, 0.75)$ is shown in figure 5.4. It is seen that upon pressurization the material extends in the 3rd direction while it is compressed when the other material is pressurized. This is also seen in figure 5.3.

Deflection/extension constraints

The previous actuator shown in figure 5.3 performs very well with respect to transversal deflection for which the design was optimized. However in order to use the actuator in e.g. a linear motor an extension is also required. This can be ensured by adding a set of constraints that restricts the ratio of the extension and the deflection to be approximately one. The constraints are given by

$$g_1 = (-u_3^{(1)}/u_1^{(1)} - 1)^2 - \epsilon \leq 0 \tag{5.2}$$

$$g_2 = (u_3^{(2)}/u_1^{(2)} - 1)^2 - \epsilon \leq 0 \tag{5.3}$$

where ϵ is a small number (here $\epsilon = 0.01$).

Considering these restrictions the material design changes. As the material design is symmetric, only the upper material and the first load case are shown in figure 5.5. It is clearly seen that the actuator now also extends. In comparison to the deformations of the

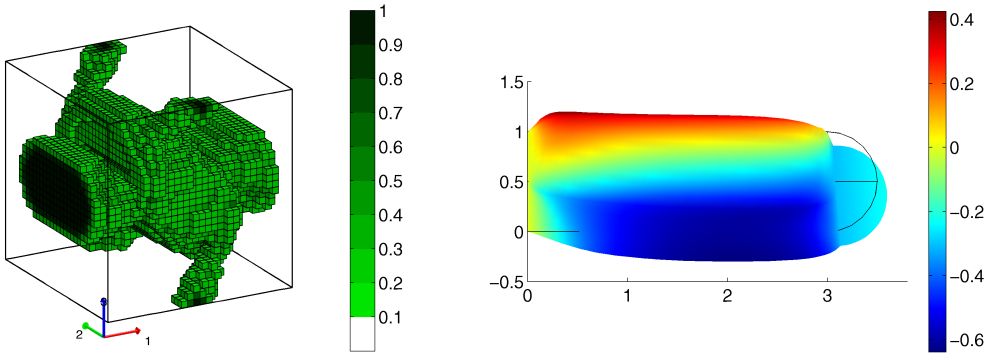

(a) Material 1

(b) Deformation load case 1. Color: u_3

Figure 5.5 Optimized material configuration and deflections for each of the two load cases. A set of constraints ensure that the extension-deflection ratio is approximately one. Optimized with spring stiffness $k = 10^{-3}$ and pressure $p = 10^{-3}$. $\Phi_{final} = max\{-u_3^{(1)}, u_3^{(2)}\} = 0.226$

previous actuator, it seems to bend slightly more based on the inclining of the interface between the slabs and the half cylinder.

Final material designs

In order to give a better impression of the resulting material microstructure the unit-cells for each of the optimized materials (upper material) are smoothed and repeated. These material super cells are shown in figure 5.6.

This method for designing materials embedded in a specific application makes it possible to design materials optimized for very specific purposes. The procedure could be further extended by allowing more materials, maybe even consider hierarchical optimization, and by re-introducing the flow and transient aspects of the problem. The idea of optimizing the material distribution in the transient consolidation problem is followed in the next chapter using a fixed microstructure topology.

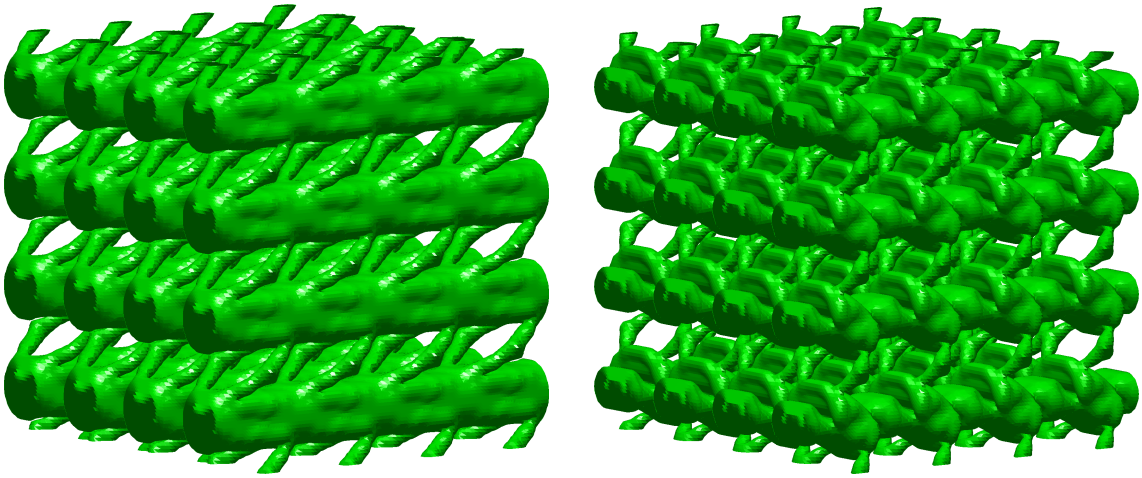

Figure 5.6 Smoothed and repeated unit cells for the optimized material 1 shown in figure 5.3(a) and 5.5(a)

Chapter 6
Topology optimization using a saturated poroelastic media [P3]

In this chapter, the material distribution problem in a saturated poroelastic structure using a fixed microstructure topology is presented. Whereas the papers [P1-2] deal with the material optimization this paper assumes a certain microstructure topology and uses the homogenized material properties in order to make an interpolation scheme which is linked to the microscale. This approach was also taken in the seminal paper on topology optimization by Bendsøe and Kikuchi (1988).

6.1 Method

In this section the Biot consolidation equations are used for the modeling and optimization of saturated poroelastic structures. The problems are transient such that the fluid structure interaction is active; however, slow enough to ignore the inertia terms. The method is not linked to any specific application but may be used for the optimization of an absorber mechanism that utilizes energy dissipation from the fluid flow resistance. It could also be the optimization of the more explicit fluid-structure interaction problem of an object in a pipe or the pressure loading of a structure.

The basic idea behind the homogenization approach to topology optimization is to base the interpolation schemes on homogenization results. In this case a grid-type microstructure is chosen which in the unit-cell representation is a solid cross as illustrated in figure 6.1.

By varying the cross-section width w and homogenizing the microstructure a relation between the density $\rho = 3w^2 - 2w^3$ and the stiffness $\mathbf{C}^H$, pressure coupling $\boldsymbol{\alpha}$, compressibility β and permeability $\mathbf{K}$ can be established. These relations are shown in figures 6.2, 6.3 and 6.4 and are used as design interpolation functions in the material distribution problem. The microstructure is orthotropic with cubic symmetry and hence characterized by three unique material parameters, in this case represented by three entries from the stiffness matrix. The stiffness interpolation is based on the RAMP and SIMP schemes introduced in chapter 3. The interpolation of the permeability is based on the empirical Kozeny-Carman relation (Carman, 1937). It is based on the topology of the microstructure, in this case simplified to unidirectional square pipes, and modified slightly to fit the homogenized values.

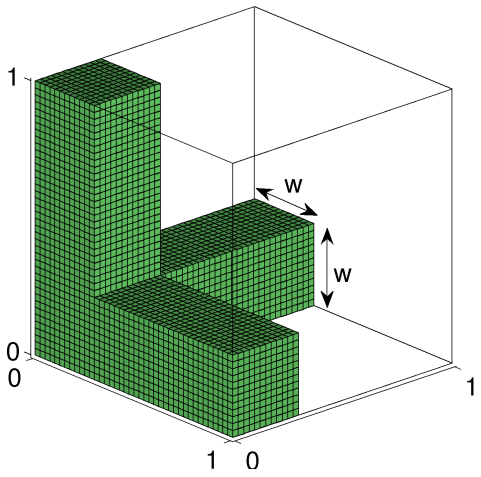

Figure 6.1 Grid-type microstructure topology studied for obtaining the interpolation schemes. Discretized by 40^3 1st order elements for the homogenization of stiffness and permeability. Periodic boundary conditions are applied and a single corner node is fixed to prevent rigid body motion.

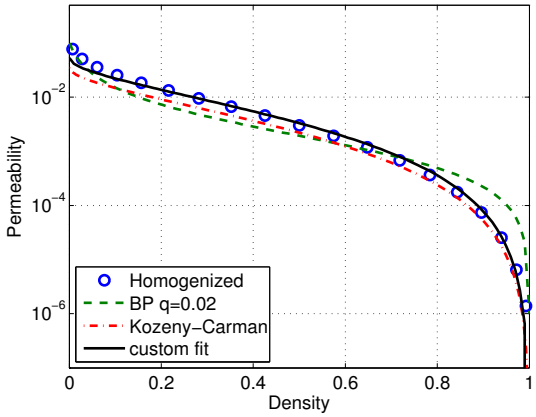

Figure 6.2 Homogenization results for the permeability along with 3 interpolations. BP refers to Borrvall and Petersson (2003). Kozeny-Carman is an empirical relation, here for square pipes of same cross-section width and a modified version.

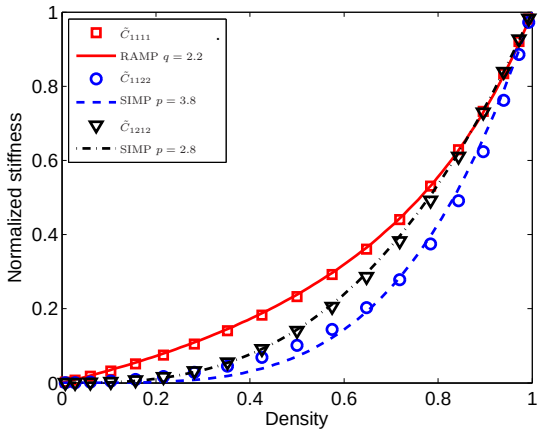

Figure 6.3 Homogenized stiffness tensor entries and fits based on SIMP and RAMP. The microstructure exhibits cubic symmetry and can be described by three independent variables.

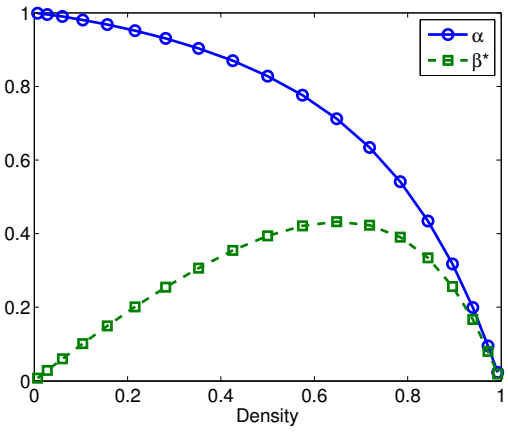

Figure 6.4 Pressure coupling and compressibility which have been computed from the homogenized stiffness tensor.

Optimization

The optimization problem can be cast into a general formulation of a non-linear program

$$\min_{\boldsymbol{\rho}\in\mathbb{R}^N} \quad f_0(\boldsymbol{\rho}, \mathbf{u}, \mathbf{p}) \tag{6.1}$$

$$\text{s.t.} \quad \mathbf{r}(\boldsymbol{\rho}, \mathbf{u}(t), \mathbf{p}(t), \dot{\mathbf{u}}(t), \dot{\mathbf{p}}(t)) = 0 \tag{6.2}$$

$$\frac{1}{V_0}\sum_{e=1}^{N} \rho_e v_e - \gamma \leq 0 \tag{6.3}$$

$$\varrho \leq \rho_e \leq \bar{\rho} \qquad \text{for } e = 1, \ldots, N \tag{6.4}$$

where $\mathbf{r}$ is the residual of the state equations, γ is the allowed solid volume fraction, N is the number of design variables and $(\varrho, \bar{\rho}) = (0.01, 0.99)$ are the limits for the design variables. These values are chosen such that the material will never be either solid or fluid as the interpolation of the permeability in the pure fluid limit is problematic. From a physical point of view, the permeability in the pure fluid case is infinite and this is not covered by the method. Opposed to topology optimization problems in general, the scope of this study is not necessarily to end up in a black-white design as the intermediate design values have a clear interpretation.

6.2 Results

A potential application could be in the design of an absorber mechanism where the energy dissipation is due to the flow resistance. For such an application the deformation path is of interest. Here the rectangular semi-sealed bed shown in figure 6.5 is considered. The left, right and bottom boundaries are fixed. The top boundary is divided into an impermeable loaded center part ($\bar{t} = 0.01C_{1111}$) and two outer permeable parts ($p = 0$). The objective

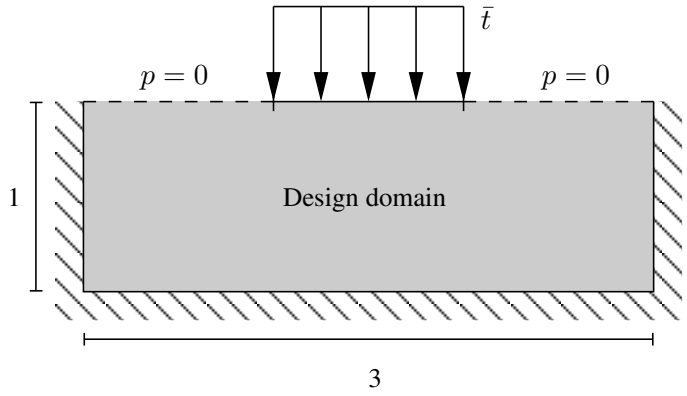

Figure 6.5 Computational domain and boundary conditions for the optimization of an absorber mechanism. The top boundary is divided into a loaded impermeable center part and two permeable (p=0) parts. The remaining boundaries are impermeable and displacements are fixed.

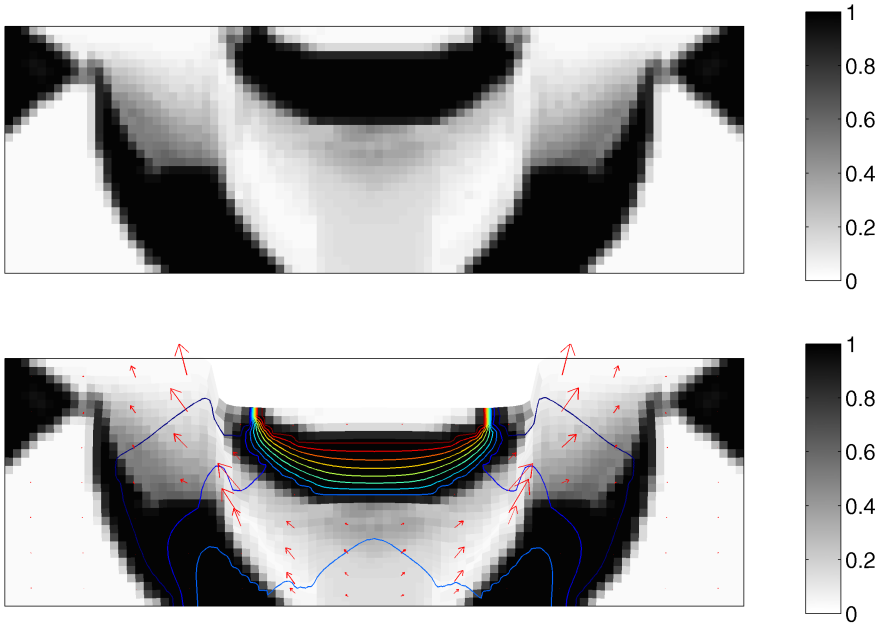

Figure 6.6 Optimized material distribution for the absorber problem using a simulation time of $100s$ and the predefined curve $u_2^* = 10^{-3}(t^2 - 200t)$. The lower figure shows the deformed state and the pressure contours along with indicators of flow direction. Mesh 90×30 square $\mathrm{u}_2\mathrm{p}_1$ elements.

is to minimize the difference between a prescribed deflection and the actual deflection

$$f_0 = \int_0^T \int_{\Gamma_t} (u_2^* - u_2)^2 \, \mathrm{d}\Gamma \, \mathrm{d}t \tag{6.5}$$

The interplay between stiffness, loading and permeability determines the consolidation time which influences the optimized designs. If the microstructure size is very small the permeability is small and the structure will therefore not consolidate within the simulation time. Increasing the unit-cell size and thereby the permeability tends to introduce more a entangled design such that the fluid needs to travel for a longer distance in order to fit to the prescribed time-deflection curve and consolidate around $t = 100s$. Figure 6.6 shows the optimized design for $E = 10^6 Pa$, $\nu = 0.3$, $l = 10^{-3}m$ and $\mu = 0.1Pa \cdot s$ using a simulation time of $100s$ and the prescribed deflection curve $u_2^* = 10^{-3}(t^2 - 200t)$. It should be noted that the loading is ramped used a smoothed Heaviside function such that the structure is only fully loaded after $5s$. Both the undeformed and the deformed structure is plotted and it is seen that the center part of the domain moves downward like a piston when loaded. This pressurizes the fluid underneath and it is squeezed out through the cavities.

The initial material distribution is uniform with density $\rho = 0.5$ and no constraint is imposed on the solid volume fraction during optimization. In order to give an impression of the evolution of the design, four design snapshots along with their respective deflection

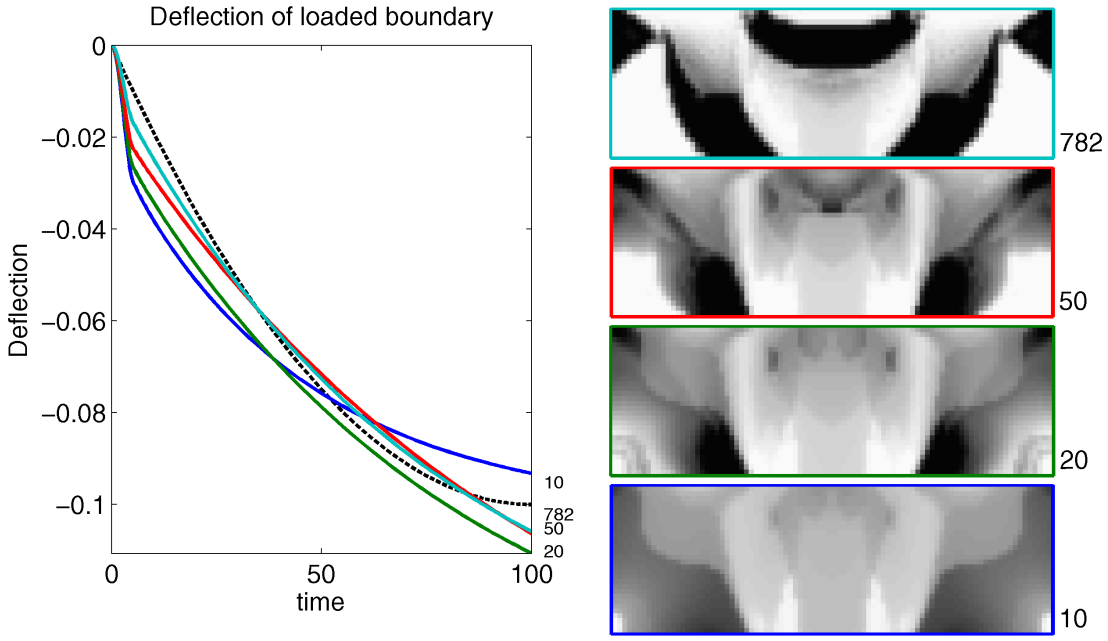

Figure 6.7 Optimization history for the optimization of the absorber problem. The predefined curve $u_2^* = 10^{-3}(t^2 - 200t)$ and the deflection curves of the loaded boundary are compared to the left while the corresponding four designs are shown to the right.

curves are shown in figure 6.7. It is seen that even though the curve approaches the predefined it is not possible to match the two exactly. It is furthermore evident that not much improvement is achieved from iteration 50 to 782 where the optimization process was considered converged.

Internally pressurized lid

Another example, in which the loading is induced by a pressure, is that of an internally pressurized lid, see figure 6.8(a). A similar problem was presented in Sigmund and Clausen (2007) which motivated the use of the mixed formulation for solving pressure loading problems. The design domain is loaded by a fluid which is present in a small domain below the design domain and fluid is allowed to enter through the lower horizontal boundary. The lower part of the vertical sides are fixed and the remaining boundary is free to move and is permeable (p=0).

The resulting topology from an optimization using steady-state modeling is shown in figure 6.8(b). It is seen that the structure is an arch just as obtained in Sigmund and Clausen (2007) however, the final material distribution is not completely black-white. Some low-density material is present underneath the arch. Low density material is also deformed by the fluid and hence these intermediate densities lowers the compliance. The steady-state design is compared to two transient optimization results with the same or smaller microstructure size shown in figure 6.8(c) and 6.8(d). The microstructure size used in figure 6.8(b) and figure 6.8(c) is the same and it is so large that the structure in the

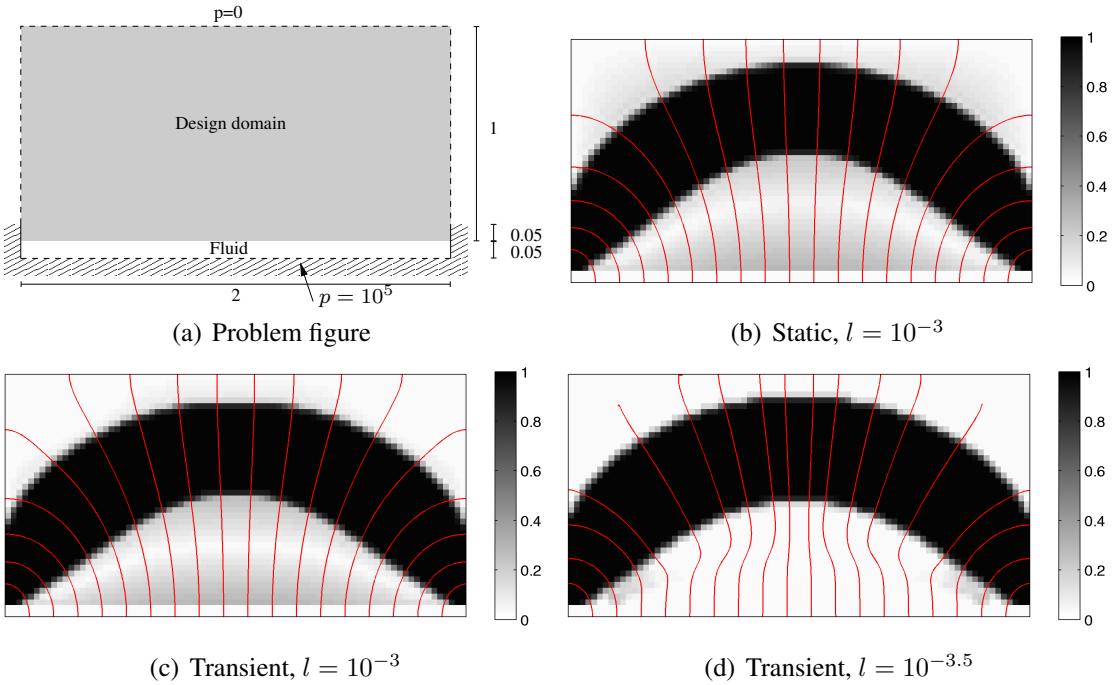

(a) Problem figure

(b) Static, $l = 10^{-3}$

(c) Transient, $l = 10^{-3}$

(d) Transient, $l = 10^{-3.5}$

Figure 6.8 *Problem figure:* The design domain is fixed at the lower part of the vertical boundaries and loaded by the fluid entering through the lower boundary. The remaining boundary is free and permeable (p=0). The bottom part of the domain is fixed fluid domain. *Optimized designs:* Minimum compliance design with basis material parameters: $E = 10^6 Pa$, $\nu = 0.3$, $\mu = 1 Pa \cdot s$ and a varying microstructure size and fixed time of $100s$. Mesh 80×40 square u_2p_1 elements. Streamlines are also plotted.

transient case consolidates within the simulation time. This, of course, is also reflected in the designs which are similar. When the microstructure is decreased, the permeability is also decreased and the simulation time is not long enough to make the structure consolidate. This is reflected in the design, figure 6.8(d), that does not have intermediate density material underneath the arch. This is due to the undeveloped fluid flow which induce less interaction with the low density material. The streamlines of the flow are also shown in the figures and it is seen that the fluid penetrates the *solid* material as it has a finite permeability.

The results confirm that the method can be used for the optimization of fluid-structure interaction problems in porous media. For the two problems shown it was not allowed to distribute full solid or fluid; however, these limits might be interesting to investigate further in order to approach interaction problems which are not embedded into a poroelastic medium.

Chapter 7
Optimization of a microfluidic mixer [P4]

The application of topology optimization as a systematic approach to the design of static microfluidic mixers is presented in this chapter. The mixing of transported matter in laminar low Reynolds number flows is difficult when the solute has a low diffusivity (i.e. the transport is convection dominated) as the mixing that naturally occurs in turbulent flows are missing due to the absence of spontaneous velocity fluctuations. This applies to the microfluidic devices and mixers used in e.g. lab-on-a-chip products for the medical industry. Traditionally the design of these mixers are based on an imprinted geometry in the bottom of a pipe e.g. slanted grooves, staggered herringbones or zig-zag walls, which alters the fluid path and thereby increase the mixing by inducing a more or less chaotic motion. This great variety of designs, from which not all can be optimal, call for a systematic approach in order to obtain an optimized design.

The optimization procedure relies on the flow model introduced in Borrvall and Petersson (2003) and Gersborg-Hansen et al. (2005) with an additional coupled transport equation as it was presented in Gersborg-Hansen (2007) for a 2D problem.

7.1 Method

The microfluidic flows are naturally assumed to be micro scale and therefore laminar. As the flow speed is also low in comparison to the speed of sound, the fluid can also be assumed incompressible. In order to model non-flow regions within the computational domain a porosity term $\alpha(\xi)\mathbf{u}$ is added to the steady state Navier-Stokes equation. This term resides from the Brinkman equation, which models the transitional flow from Darcy

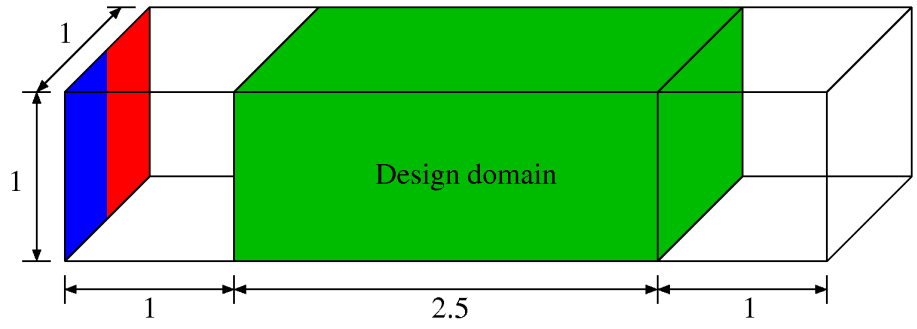

Figure 7.1 Pipe with square cross section having outer measures $1 \times 1 \times 4.5$ and a design domain of length 2.5 in order to avoid influence from boundary conditions on the design. Parabolic inflow profile to the left with a Heaviside concentration distribution. No-slip at horizontal faces and free outlet at the right vertical face.

flow in porous media to the Stokes flow in free fluid. Due to the incompressibility of the fluid, the continuity condition must also hold. The modeling equations yield

$$-\nabla\cdot(\mu(\nabla\mathbf{u}+(\nabla\mathbf{u})^T)-\mathbf{I}p)+\mathbf{u}\cdot\rho\nabla\mathbf{u}+\alpha(\xi)\mathbf{u}=\mathbf{0} \qquad \text{in } \Omega \tag{7.1}$$

$$-\nabla\cdot\mathbf{u}=0 \qquad \text{in } \Omega \tag{7.2}$$

where α is the porosity field, ξ is the spatially varying design variable field, $\mathbf{u}$ is the velocity field, p is the pressure and $\mathbf{I}$ the identity tensor. μ is the viscosity and ρ is the mass density, which both are considered constant. Figure 7.1 shows a design problem with in- and outlet domains and a design domain. In the in- and outlet the porosity term is zero mimicking a free flow but in the design domain the design field ξ is varying spatially and gives the possibility to model either no-flow (extremely slow porous flow, large α, $\xi=0$) or free flow (zero α, $\xi=1$) without having to impose explicit boundary conditions.

Additional to the flow problem a scalar transport problem is solved using the convection from the flow. The convection-diffusion problem yields

$$\mathbf{u}\cdot\nabla\phi-\frac{1}{Pe}\nabla^2\phi=0 \qquad \text{in } \Omega \tag{7.3}$$

where ϕ is the concentration of the matter, $Pe=Ud_h/D$ is the Péclet number with U being a reference velocity (here mean velocity), D is the diffusivity and d_h the hydraulic diameter. The hydraulic diameter is given by $d_h=4\mathcal{A}/\mathcal{O}$ where $\mathcal{A}$ is the cross section area and $\mathcal{O}$ is the circumference. For low Pe numbers the diffusive properties of the solute are dominating and the mixing occurs very quickly. However, for large Pe numbers, the diffusion is low and the flow needs to convect the solute to improve the mixing.

A one-way coupling is assumed such that the flow equations (7.1)-(7.2) are independent of the concentration ϕ governed by equation (7.3).

In order to model the flow and transport using 1st order finite elements a Galerkin Least Squares (GLS) stabilization scheme (Hughes and Franca, 1987) is added to the flow problem to avoid pressure oscillations. As the transport is convection dominated a Streamline Upwind Petrov-Galerkin (SUPG) scheme (Brooks and Hughes, 1982) is imposed on the transport problem in order to avoid oscillations in the concentration field.

Optimization

The optimization problem for the microfluidic mixer problem shown in figure 7.1 can be stated as

$$\min_{\boldsymbol{\xi}\in\mathbb{R}^n} \quad \Phi=\frac{1}{\langle\phi\rangle_{\text{in}}^2\int_{\Gamma_{\text{out}}}\mathrm{d}\Gamma}\int_{\Gamma_{\text{out}}}(\phi-\langle\phi\rangle_{\text{in}})^2\,\mathrm{d}\Gamma \tag{7.4}$$

$$\text{s.t.} \quad \text{Governing equations (7.1), (7.2), (7.3)}$$

$$\Delta p\le\beta\Delta p_{\text{ref}}$$

$$\alpha_e(\xi_e)=\overline{\alpha}+(\underline{\alpha}-\overline{\alpha})\xi_e\frac{1+q}{\xi_e+q} \qquad \text{for } e=1,...,n$$

$$0\le\xi_e\le 1 \qquad \text{for } e=1,...,n$$

where $\boldsymbol{\xi} \in \mathbb{R}^n$ is a vector of element design variables, n is the number of elements and Φ is the cost function which measures the mixing performance. The mixing performance is here defined as the difference between the concentration at the outlet and the average inlet concentration $\langle\phi\rangle_{\text{in}} = \int_{\Gamma_{\text{in}}} \phi \, \mathrm{d}\Gamma / \int_{\Gamma_{\text{in}}} \mathrm{d}\Gamma$. Normalizing this with respect to the average inlet concentration an ideal mixer will have the performance $\Phi_{\text{ideal}} = 0$ due to conservation of mass while the absence of mixing yield $\Phi = 1$. The allowed pressure drop with respect to a reference configuration (empty pipe) is controlled by β in order to avoid a very entangled flow-path as this yields good mixing but have a huge pressure drop and thereby a large cost.

7.2 Results

The optimization problem is shown in figure 7.1 and consists of an inlet, a design domain and an outlet. The in- and outlet are included in order to avoid influence from the boundary conditions on the design. The flow enters at the left face and has a prescribed parabolic velocity profile and a discontinuous concentration distribution (0-2). The right face has a prescribed pressure $p = 0$ mimicking a free outflow. The convection is assumed negligible hence, the linear Stokes flow is considered.

Optimizing the mixer and allowing a pressure drop of 2.5 in comparison to an empty pipe yields a design as shown in figure 7.2. The mixing performance is visualized by the concentration field from which the folding and stretching of the fluid is apparent. The obtained design has several guiding vanes that make the fluid move such that the high-low concentration interface is stretched as much as possible in order to enlarge the mixing.

The performance of the mixer is increased from $\Phi_{ref} = 0.6786$ to $\Phi_{final} = 0.2051$ in comparison to a empty pipe. This is a mixing improvement of 70% obtained by the cost of a 2.5 times larger pressure drop. The improved performance is clear, however the design of the mixer might be difficult to realize in a lab-on-a-chip application due to the intricate design which have overhangs and do not comply with usual manufacturing techniques for microfluidic systems. The obtained design is a proof of concept and a more simple design is considered next.

Micromixer with bottom layer design

A more directly applicable design is obtained by changing the problem setting to that shown in figure 7.3 where the pipe length is heavily increased and the design domain is restricted to the bottom of the channel. Mixers of this kind are found in the literature with different kind of patterns in the bottom, including slanted grooves and herring bones(Stroock et al., 2002) while other designs combine patterns along the top and bottom (Yang et al., 2007).

The problem considered corresponds to the first section of the staggered herringbone mixer in Stroock et al. (2002). The optimized mixer using a Reynolds number of $Re = \rho U d_h/\mu = 0.01$ and a Peclet number of $Pe = 2000$ is seen in figure 7.4 along with a visualization of the concentration field along the flow direction. By applying topology

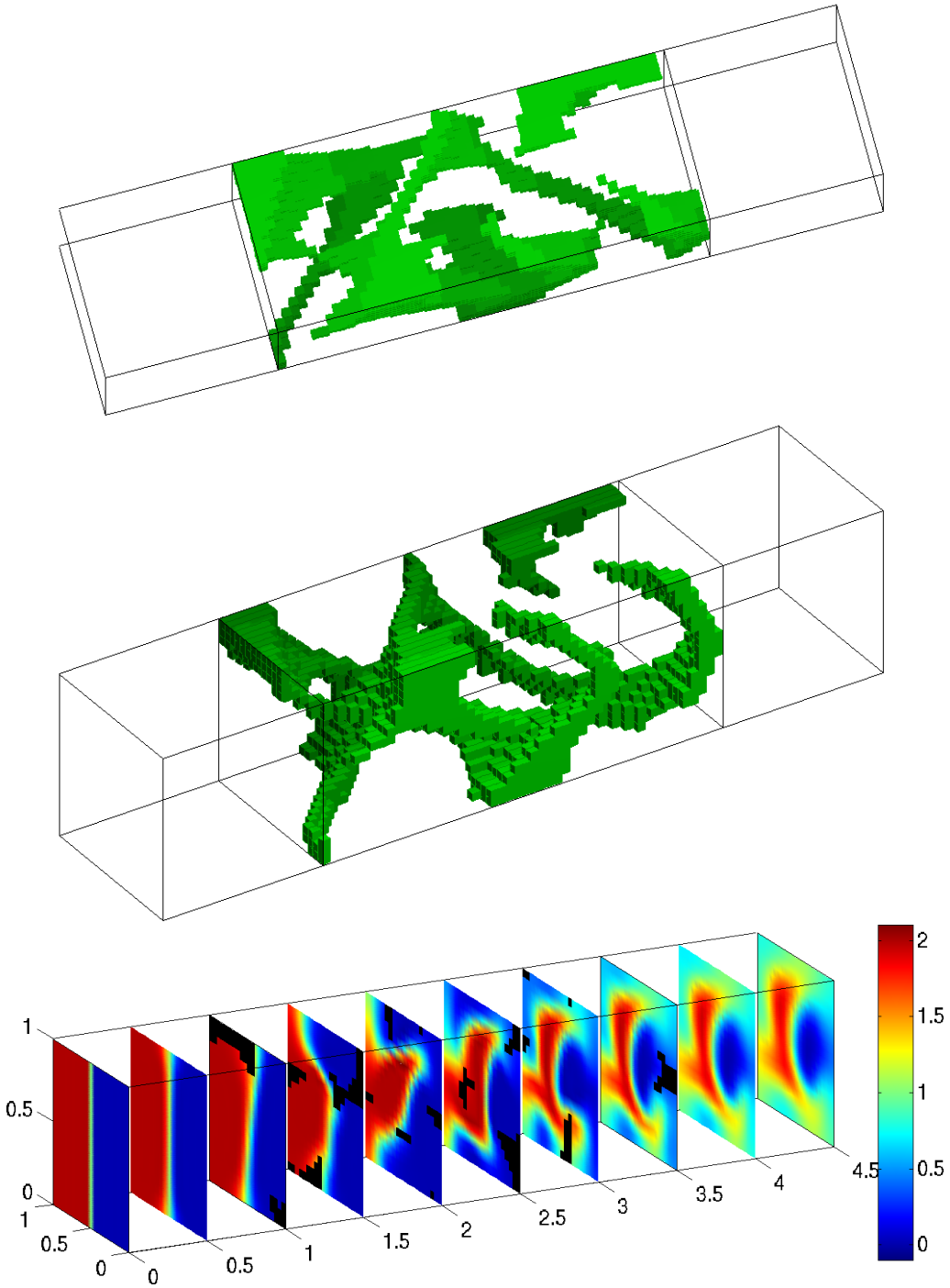

Figure 7.2 Optimized design for Stokes flow ($\rho = 0, \mu = 1$) with $Pe = 1000$ in the square cross sectioned pipe. Final objective $\Phi_{final} = 0.2051$, reference objective $\Phi_{empty} = 0.6786$. Allowed pressure drop $\beta = 2.5$. *Top and center*: Design variables plotted with threshold $\xi < 0.5$, colored by depth. 20000 ($20 \times 20 \times 50$) design variables. *Bottom*: Concentration ϕ in several cross sections along the flow. Solid material ($\xi < 0.5$) in the cross sections is colored black.

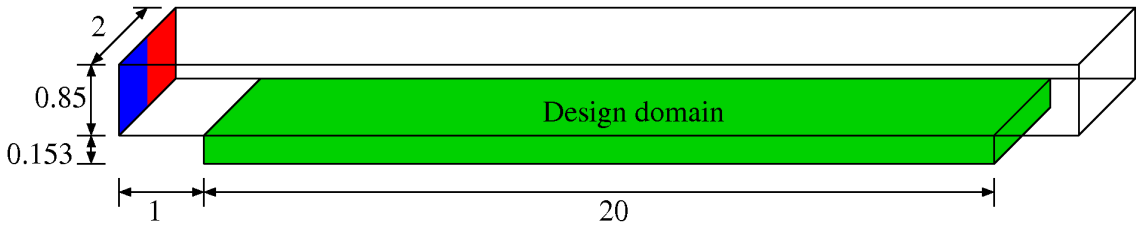

Figure 7.3 Problem figure showing the reference micro mixer. The inlet velocity profile is parabolic in order to mimic fully developed laminar flow and the concentration profile is a Heaviside function. The right vertical face has $p = 0$ to model a free outlet. The design domain (green) is for the reference filled with material with a low permeability.

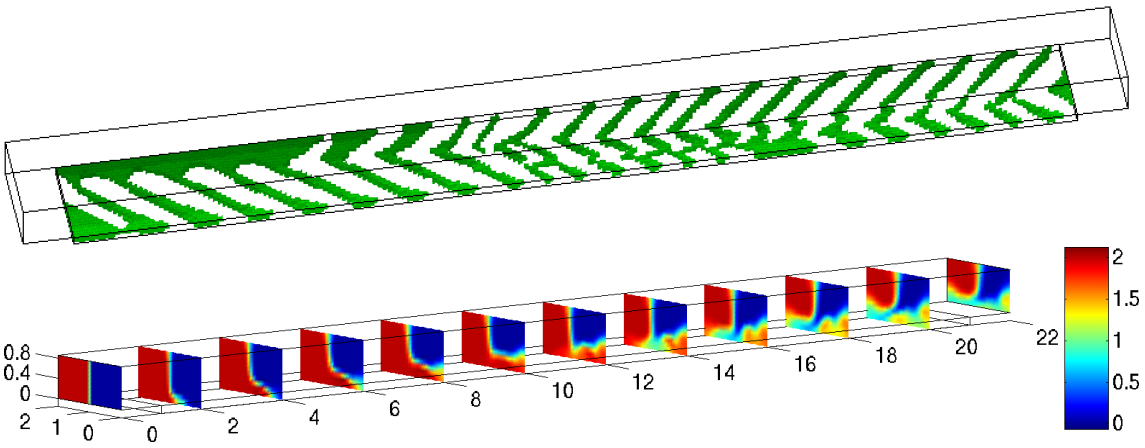

Figure 7.4 Optimized topology for the micro mixer with bottom layer design domain having $Re = 0.01$, $Pe = 2000$. Optimized performance $\Phi_{final} = 0.5594$. *Top*: Design variables thresholded by $\xi < 0.5$ and colored by depth. 11520 design variables($240 \times 24 \times 2$) in the bottom layer. *Bottom*: Concentration ϕ plotted in several cross sections along the mixer.

optimization the mixing was improved by 31% (from $\Phi_{ref} = 0.8114$ to $\Phi_{final} = 0.5594$) by a 1.27 fold pressure drop increase in comparison to a mixer with a solid bottom.

The mixer length is due to computational limitations only the same size as the first segment of that in the reference. Comparing the performance the reference performs better but the resolution of the present model is not capable of resolving the same amount of details. However inspecting the topology of the optimized design it is seen that it actually combines the slanted grooves and the staggered herringbones as optimal geometric shapes for use in microfluidic mixers. Opposed to optimization based on groove size or groove distance variation this method provides a new configuration with grooves and herringbones.

Chapter 8
Manufacturability of topology optimized designs [P5]

In this chapter, a method for ensuring the manufacturability of topology-optimized designs is presented. Most optimized designs include holes or cavities with overhangs, which can be difficult to manufacture using e.g. milling or casting processes. In an industrial context, it is important to ensure that the obtained designs can be manufactured. The two main competitors on the market for commercial topology optimization codes, Tosca Structure from FE-Design and OptiStruct from Altair Engineering, each have a method to ensure manufacturability. However not much have been published about the imposed methods or their implementation. In [P5] a method is developed in which the parameterization of the domain is changed in order to ensure manufacturability and binary designs.

The basis for the method is to change the parameterization such that the problem is manufacturable per definition regardless of the design variable values. Usually the design parametrization used in topology optimization is comparable to the pixels in a digital image, which are allowed to vary individually. By introducing a mapping function, a complete row or column of pixels can be related to a single design value. In this way, the number of design variables reduce drastically and the density distribution along the strip of elements can be computed by an analytic expression. This mapping of elements is cast in a format similar to that of the density filter often used in topology optimization.

8.1 Method

The minimum compliance problem of the MBB beam in figure 8.1 is chosen as a reference problem as the resulting topology is well known in the topology optimization community. The optimization problem with an imposed filter can be stated as

$$\min_{\boldsymbol{\rho}\in\mathbb{R}^m} \quad c = \mathbf{u}^T\mathbf{f} \tag{8.1a}$$

$$\text{subject to} \quad \widetilde{\boldsymbol{\rho}} = \mathcal{F}(\boldsymbol{\rho}), \qquad \widetilde{\boldsymbol{\rho}} \in \mathbb{R}^n \tag{8.1b}$$

$$\mathbf{K}(\widetilde{\boldsymbol{\rho}})\mathbf{u} = \mathbf{f} \tag{8.1c}$$

$$g \leq 0 \tag{8.1d}$$

$$0 \leq \rho_i \leq 1 \text{ for } i = 1, ..., m \tag{8.1e}$$

where $\boldsymbol{\rho}$ is a vector with m design variables and c is the compliance measure computed by the solid displacement $\mathbf{u}$ and the load $\mathbf{f}$. $\mathcal{F}(\boldsymbol{\rho})$ is the filter operation, $\mathbf{K}(\widetilde{\boldsymbol{\rho}})$ is the design dependent stiffness matrix and g denotes a general inequality constraint, here the volume constraint. Usually the number of design variables m is the same as the number of physical design variables n, where $\widetilde{\boldsymbol{\rho}}$ are the physical design variables, however this is not a requirement.

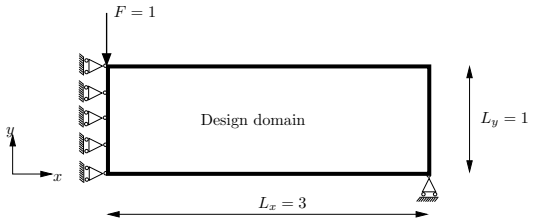

Figure 8.1 Boundary conditions for the MBB problem. The x displacement is fixed at the left side of the domain and the y displacement is fixed in the lower right corner. A unit load is applied in the upper left corner and the aspect ratio of the design domain is $L_x/L_y = 3$.

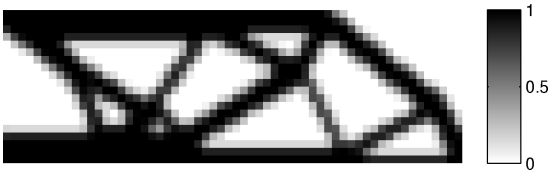

Figure 8.2 Optimized topology design for the MBB problem on a 60×20 mesh with a volume constraint of 50%, the density filter with radius 1.4 element side length. The graybar shows the value of the physical density $\widetilde{\rho}$, $c = 2.16 \cdot 10^2$.

For the standard MBB problem, the optimized design is shown in figure 8.2. It is clearly seen that the manufacturing of such a part needs to be perpendicular to the design plane. In order to ensure in-plane manufacturability a casting plane is defined. For a 2D problem, it collapses to a line, here aligned with the left vertical boundary of the design domain. The physical design variables $\widetilde{\boldsymbol{\rho}}$ are mapped to strips of elements, which are given by a single design value per row $\boldsymbol{\rho}$. This mapping is visualized in figure 8.3.

When the mapping is established, it is important to choose a proper function to describe the transition from solid to void elements. As holes or cavities cannot be allowed, the function should be monotone and as the final solution of the optimization problem should be binary, a Heaviside function is preferred

$$H(t) = \begin{cases} 1, & t \leq 0 \\ 0, & t > 0 \end{cases}, \qquad t \in \mathbb{R} \tag{8.2}$$

However, in order to be applied in a continuous optimization problem this is approximated by a smooth Heaviside function. Letting the non-dimensional x-coordinate of a design element be given by $s(x) = x/L_x$ and the design variable be ρ_j, indicating the solid void interface location, then the physical density of any element in the j'th row can be

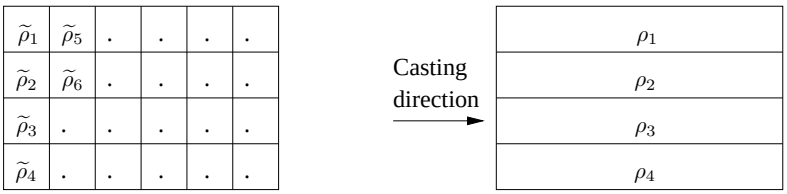

Figure 8.3 Left: Standard design parametrization, one design variable per element. Right: New casting parametrization. One design variable defines the densities in a row of elements in the casting direction.

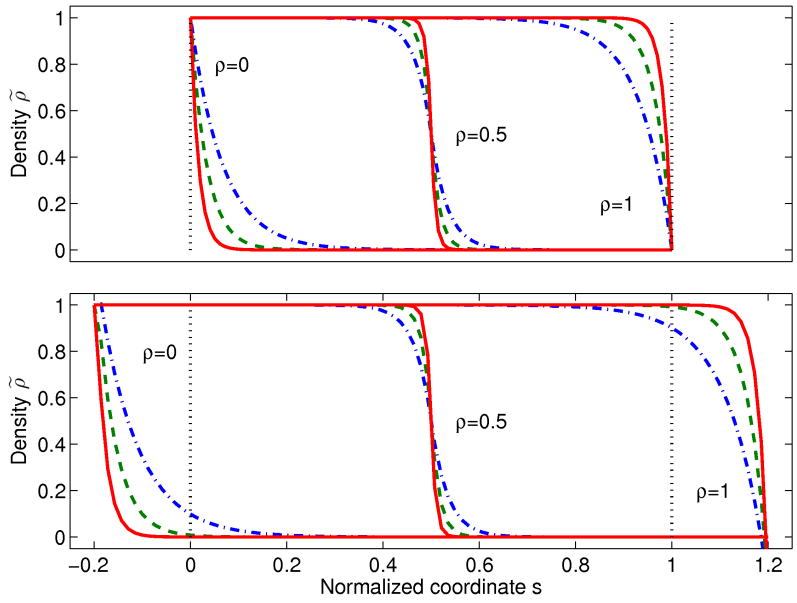

Figure 8.4 Step function parameterization cf. equation (8.4) shown for $\rho = \{0, 0.5, 1\}$ and with varying steepness $\beta = \{15, 30, 60\}$ indicated by {.-, - -, –}, respectively. $s = x/L_x$ is the normalized x-coordinate and $\widetilde{\rho}$ is the physical density. *Top*: Using the definition in equation (8.3). *Bottom*: The definition using a stretched variable cf. equation (8.5) with $b = 0.2$ and $a = 1.2$.

computed as

$$\widetilde{\rho}(x) = H_s(s(x), \rho_j; \beta) \tag{8.3}$$

with $H_s(s(x), \rho_j; \beta)$ given by

$$\left.\begin{array}{l} \textbf{If} \quad \rho_j \leq s(x) \\ \quad H_s = 1 - \rho_j[e^{-\beta(1-s(x)/\rho_j)} - (1 - s(x)/\rho_j)\, e^{-\beta}] \\ \textbf{else} \\ \quad H_s = 1 - (1 - \rho_j)\,[\,1 - e^{-\beta(s(x)-\rho_j)/(1-\rho_j)} \\ \qquad\qquad + (s(x) - \rho_j)\, e^{-\beta}/(1 - \rho_j)] - \rho_j \end{array}\right\} \tag{8.4}$$

where $\beta > 0$ controls the steepness of the approximation (Xu and Cheng, 2010). The function is plotted in figure 8.4 (top) for three different design values and three different steepness-values β. From the figure it is seen that for the limit densities $\rho = 0$ and $\rho = 1$ the physical density is fixed to 1 and 0, respectively. For general applicability of the parameterization, this feature should be removed such that the elements near the boundary can be either solid or void. This is done by the introduction of a stretched variable $\widehat{\rho}$ which stretches the mapping function relative to the normalized coordinate $s(x)$ as seen in figure 8.4 (bottom).

The procedure for computing the physical density $\widetilde{\rho}(x_i, y_j)$ of every element is

$$\left.\begin{array}{l} \text{1. Compute the normalized } x\text{-coordinate} \\ \quad s_i = x_i / L_x \\ \text{2. Compute the stretched variable} \\ \quad \widehat{\rho} = (a+b)\rho(y_j) - b, \quad b < a,\ \widehat{\rho} \in [-b; a] \\ \text{3. Compute the density of the element} \\ \quad \widetilde{\rho}\,(x_i, y_j) = H_s(s_i, \widehat{\rho}; \beta) \end{array}\right\} \tag{8.5}$$

where a and b are determined such that the density of the elements near the boundary can be both solid and void. Further details on the choice of parameters are given in [P5].

The implementation of the parameterization can be cast as a filter, which is denoted $\widetilde{\boldsymbol{\rho}} = \mathcal{H}\,(\boldsymbol{\rho})$. In order to avoid most numerical difficulties when approximating a discontinuous function a continuation of the β parameter is applied to the optimization routine.

Furthermore, the standard density filter is applied in order to avoid checkerboard patterns (abrupt changes in the density) in the y-direction. Hence the physical densities are computed as $\widetilde{\boldsymbol{\rho}} = \mathcal{F}\,(\mathcal{H}\,(\boldsymbol{\rho}))$.

8.2 Results

The MBB problem is optimized using the proposed parameterization ensuring a manufacturable design in the x-direction. The optimized design can be seen in figure 8.5 and is indeed manufacturable. The design differs much from the original design as no void can be placed inside the structure. The objective is worse than that of the original problem, almost 3 times larger, however this is expected since the optimizer can no longer place material along the upper and lower boundary hence, increase the bending stiffness. Instead, the structure resembles the optimal thickness distribution of a solid beam (Pedersen and Pedersen, 2009) which it is compared to in figure 8.6. It is seen that the distribution only deviates slightly from the analytical result obtained for slender beams. A solid connection from the load application point to the structure is seen at the left boundary, which is necessary to transfer the load.

Figure 8.5 Optimized design for the MBB problem subject to a 50% volume constraint and the parameterization $\widetilde{\rho} = \mathcal{F}\,(\mathcal{H}\,(\rho))$ cf. equation (8.5). The value of $\widetilde{\rho}$ is displayed in the graybar. Continuation on $\beta = \{15, 30, 35, 40\}$ is performed. 480×160 elements obtained in 34 iterations with $c = 6.15 \cdot 10^2$. The constraint g is negative and of the order $10^{-5} - 10^{-4}$.

Figure 8.6 Comparison of the design in figure 8.5 with an analytic estimate of the height (white line) given by $h(x) = 0.43\sqrt{L_x - x}$. The estimate is obtained using Bernoulli-Euler beam theory (Pedersen and Pedersen, 2009) and a surprisingly good agreement with the design is observed despite the aspect ratio of $L_x/L_y = 3$.

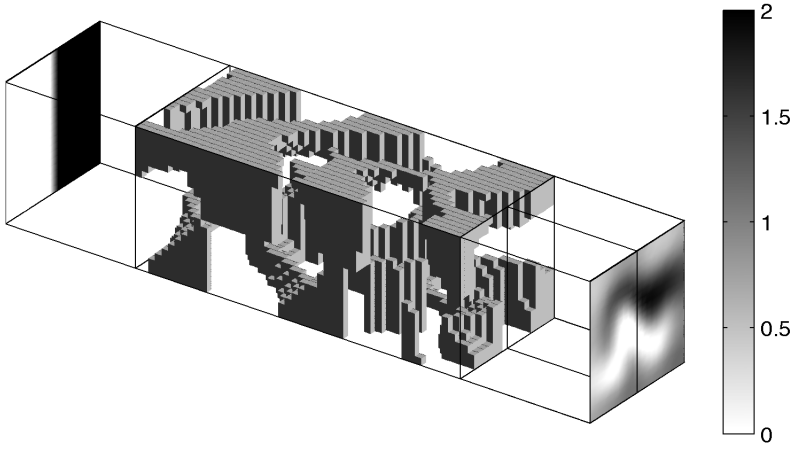

Figure 8.7 Inline microfluidic mixer optimized using the explicit parameterization. Left face: Fully developed velocity profile and discontinuous concentration profile. Right face: Free outlet conditions (zero pressure) and concentration profile cf. graybar. Creeping flow conditions and convection dominated transport. Allowed pressure drop is 5 times the one for a corresponding empty pipe. $\Phi_{final} = 0.1631$

Application to mixer design

In the previous chapter, topology optimized microfluidic mixers were designed. The obtained design for the inline mixer was rather intricate with internal guiding vanes that are difficult to manufacture. The explicit parameterization is therefore applied to this design problem. Assuming that a microfluidic mixer can be assembled from two separately machined parts a casting plane is defined as a horizontal plane at $z = 0.5$. This reduces the number of design variables from 20,000 to 2,000 and the optimization is rerun allowing a slightly larger pressure drop along the mixer. As flow problems are not prone to checkerboard problems the physical densities are computed directly from the parameterization $\widetilde{\boldsymbol{\rho}} = \mathcal{H}(\boldsymbol{\rho})$ and the optimized design is seen in figure 8.7.

It is clearly seen that the solid elements are connected to either the upper or the lower face as prescribed. No overhangs exist and the casting plane is clearly visible. The in-

crease in allowed pressure drop is necessary as the performance decrease when restrictions are imposed on the design.

The proposed explicit Heaviside parameterization provides a way of obtaining manufacturable designs in gradient-based topology optimization at a small coding effort and without the need of solving any extra equation systems. This option is useful as a mean to reduce the complexity of the topology e.g. when collaborating with experimentalists.

Chapter 9
Conclusion

This thesis presents the application of the topology optimization method to the design of saturated porous materials and structures made of such materials. The optimization of the pressure coupling properties is an extension of the existing material design optimization and allows for the design of pressure actuated porous materials. A methodology for a multiscale approach to the optimization of poroelastic actuators is also presented, which allows the material design to be coupled to the application scale performance. Even though the method is presented for only two porous materials in an actuator, the method could potentially be applied for the design of materials composed of several different constituents for use in e.g. artificial tissue and bone or energy absorbing mechanisms. Furthermore, the optimization of material distribution in a saturated porous media using the consolidation equations is considered. Despite the quasi-static assumption it is demonstrated that optimized saturated poroelastic structures can be used in absorbing mechanisms and for the design optimization of transient fluid-structure interaction problems.

Micromixer design can also be improved by the topology optimization method. The design problem of a microfluidic mixer is difficult as it is often only possible to alter either top or bottom profile of the mixer. By restricting the design freedom, optimized designs that include well known design elements, such as slanted grooves and herringbones, are obtained. The comparison of performance of the optimized design with reference designs is difficult as the models suffer from coarse discretizations which does not allow a comparable level of detail.

Design manufacturability needs to be considered when the often intricate optimized designs should be produced. The proposed manufacturability parameterization ensures that the designs can be manufactured using casting/milling type processing. It is demonstrated on the common topology optimization problem, the MBB problem, and successfully applied to the design of a microfluidic mixer.

The simulation of both the transient problems and some of the 3D homogenization problems were conducted using the Comsol Multiphysics environment, a finite element based program, which allows the user to either work with predefined physics modes or to implement their own partial differential equations. The program is flexible and new ideas can quickly be implemented however, with the topology optimization of the 3D and transient problems shown in this thesis the limit for the problem size is reached.

Future work and extensions

Within the application of topology optimization to the saturated poroelastic structures the extension into a true multiscale optimization i.e. an hierarchal approach, combining the

ideas from [P2] and [P3] would be very interesting. The approach would be related to that of Rodrigues et al. (2002) and Coelho et al. (2008) but computationally heavier, due to internal flow and time dependency. Such an extension requires a fully parallel platform for the computations as this involves the solution and optimization of many homogenization problems as well as transient topology optimization. A suitable platform would be the TopOpt groups parallel C++ framework DFEM.

The inclusion of the inertia terms in the multiple-scales procedure is another interesting extension. This would make it possible to simulate the dynamics of the porous media, either as an extension to the transient modeling in [P3] or by assuming time harmonic vibrations. The damping or energy dissipating properties of saturated porous materials could then be optimized for use in e.g. dampers or impact absorbers.

The optimization of microfluidic mixers could also benefit from a parallel implementation as the resolution could be increased and a fair comparison between the optimized and reference performance could be made. Furthermore, it might be possible to design the complete micro mixer and not only a single section. However, a repeated analysis, coupling the outlet of one section to the inlet of the next, using sections with the same design might also be interesting.

In general it would be interesting to manufacture and test some of the optimized materials and structures in order to gain a larger insight into the limitations of the employed physical models. The manufacturing of the optimized designs might also enlighten other manufacturability issues that need to be considered.

References

Aage, N., Poulsen, T., Gersborg-Hansen, A. and Sigmund, O. (2008). Topology optimization of large scale Stokes flow problems. *Structural and Multidisciplinary Optimization*, 35:175–180.

Auriault, J.L. and Sanchez-Palencia, E. (1977). Study of macroscopic behavior of a deformable saturated porous-medium. *Journal De Mecanique*, 16(4):575–603.

Auriault, J.L. (2009). On the domain of validity of Brinkman´s equation. *Transport in Porous Media*, 79:215–223.

Auriault, J.L., Boutin, C. and Geindreau, C. (2009). *Homogenization of Coupled Phenomena in Heterogeneous Media*. ISTE Ltd and John Wiley & Sons Inc.

Auriault, J.L., Geindreau, C. and Boutin, C. (2005). Filtration law in porous media with poor separation of scales. *Transport in Porous Media*, 60:89–108.

Bagge, M. (2000). A model of bone adaptation as an optimization process. *Journal of Biomechanics*, 33(11):1349–1357.

Bendsøe, M.P. (1989). Optimal shape design as a material distribution problem. *Structural and Multidisciplinary Optimization*, 1:193–202.

Bendsøe, M.P., Guedes, J.M., Haber, R.B., Pedersen, P. and Taylor, J.E. (1994). An analytical model to predict optimal material properties in the context of optimal structural design. *Journal of Applied Mechanics*, 61(4):930–937.

Bendsøe, M.P. and Sigmund, O. (1999). Material interpolation schemes in topology optimization. *Archive of Applied Mechanics*, 69:635–654.

Bendsøe, M.P. and Kikuchi, N. (1988). Generating optimal topologies in structural design using a homogenization method. *Computer Methods in Applied Mechanics and Engineering*, 71(2):197–224.

Bensoussan, A., Lions, J. and Papanicolaou, G. (1978). *Asymptotic Analysis for Periodic Structures*. North-Holland Pub. Co.

Berryman, J.G. (2005). Comparison of upscaling methods in poroelasticity and its generalizations. *Journal of Engineering Mechanics*, 131(9):928–936.

Biot, M.A. (1955). Theory of elasticity and consolidation for a porous anisotropic solid. *Journal of Applied Physics*, 26(2):182–185.

Biot, M.A. (1956a). Theory of propagation of elastic waves in a fluid-saturated porous solid. I. low-frequency range. *The Journal of the Acoustical Society of America*, 28(2):168–178.

Biot, M.A. (1956b). Theory of propagation of elastic waves in a fluid-saturated porous solid. II. higher frequency range. *Journal of the Acoustical Society of America*, 28(2):179–191.

Biot, M.A. and Willis, D.G. (1957). The elastic coefficients of the theory of consolidation. *Journal of Applied Mechanics*, pages 594–601.

Biot, M.A. (1941). General theory of three-dimensional consolidation. *Journal of Applied Physics*, 12(2):155–164.

Borrvall, T. and Petersson, J. (2003). Topology optimization of fluids in Stokes flow. *International Journal for Numerical Methods in Fluids*, 41(1):77–107.

Bourdin, B. (2001). Filters in topology optimization. *International Journal for Numerical Methods in Engineering*, 50:2143–2158.

Brinkman, H.C. (1947). A calculation of the viscous force exerted by a flowing fluid on a dense swarm of particles. *Applied Scientific Research Section A-mechanics Heat Chemical Engineering Mathematical Methods*, 1(1):27–34.

Brooks, A.N. and Hughes, T.J.R. (1982). Streamline upwind petrov-galerkin formulations for convection dominated flows with particular emphasis on the incompressible navier-stokes equations. *Computer Methods in Applied Mechanics and Engineering*, 32(1-3):199–259.

Bruns, T. and Tortorelli, D. (2001). Topology optimization of non-linear elastic structures and compliant mechanisms. *Computer Methods in Applied Mechanics and Engineering*, 190:3443–3459.

Carman, P. (1937). Fluid flow through granular beds. *Transactions, Institution of Chemical Engineers, London*, 15:150–166.

Coelho, P.G., Fernandes, P.R., Guedes, J.M. and Rodrigues, H.C. (2008). A hierarchical model for concurrent material and topology optimisation of three-dimensional structures. *Structural and Multidisciplinary Optimization*, 35(2):107–115.

Coelho, P.G., Fernandes, P.R., Rodrigues, H.C., Cardoso, J.B. and Guedes, J.M. (2009). Numerical modeling of bone tissue adaptation-a hierarchical approach for bone apparent density and trabecular structure. *Journal of Biomechanics*, 42(7):830–837.

Evgrafov, A. (2006). Topology optimization of slightly compressible fluids. *Zammzeitschrift Fur Angewandte Mathematik Und Mechanik*, 86(1):46–62.

Evgrafov, A., Pingen, G. and Maute, K. (2008). Topology optimization of fluid domains: kinetic theory approach. *Zamm-zeitschrift Fur Angewandte Mathematik Und Mechanik*, 88(2):129–141.

Fillunger, P. (1913). Der Auftrieb in Talsperren. *Österr. Wochenzeitschrift für den öffentl. Baudienst.*, I. II. III:532–552, 522–556, 567–570.

Gersborg-Hansen, A., Sigmund, O. and Haber, R. (2005). Topology optimization of channel flow problems. *Structural and Multidisciplinary Optimization*, 30:181–192.

Gersborg-Hansen, A. (2007). *Topology optimization of flow problems*. Ph.D. thesis, DCAMM, Department of Mathematics, Department of Mechanical Engineering, Technical University of Denmark.

Gibiansky, L.V. and Sigmund, O. (2000). Multiphase composites with extremal bulk modulus. *Journal of the Mechanics and Physics of Solids*, 48(3):461–498.

Guedes, J., Lubrano, E., Rodrigues, H. and Turteltaub, S. (2006). Hierarchical optimization of material and structure for thermal transient problems. In M.P. Bendsøe, N. Olhoff and O. Sigmund, editors, *IUTAM Symposium on Topological Design Optimization of Structures, Machines and Materials*, volume 137 of *Solid Mechanics and Its Applications*, pages 527–536. Springer Netherlands.

Guest, J.K. and Prévost, J.H. (2006). Optimizing multifunctional materials: Design of microstructures for maximized stiffness and fluid permeability. *International Journal of Solids and Structures*, 43(22-23):7028–7047.

Guest, J.K. and Prévost, J.H. (2007). Design of maximum permeability material structures. *Computer Methods in Applied Mechanics and Engineering*, 196(4-6):1006–1017.

Hollister, S.J., Maddox, R.D. and Taboas, J.M. (2002). Optimal design and fabrication of scaffolds to mimic tissue properties and satisfy biological constraints. *Biomaterials*, 23(20):4095–4103.

Hughes, T.J.R. and Franca, L.P. (1987). A new finite element formulation for computational fluid dynamics: VII. the Stokes problem with various well-posed boundary conditions: Symmetric formulations that converge for all velocity/pressure spaces. *Computer Methods in Applied Mechanics and Engineering*, 65(1):85–96.

Jung, Y. and Torquato, S. (2005). Fluid permeabilities of triply periodic minimal surfaces. *Phys. Rev. E*, 72(5):056319–.

Kreissl, S., Pingen, G., Evgrafov, A. and Maute, K. (2010). Topology optimization of flexible micro-fluidic devices. *Structural and Multidisciplinary Optimization*, 42:495–516.

Lazarov, B.S. and Sigmund, O. (2011). Filters in topology optimization based on Helmholtz-type differential equations. *International Journal for Numerical Methods in Engineering*, 86(6):765–781.

Lin, C.Y., Kikuchi, N. and Hollister, S.J. (2004). A novel method for biomaterial scaffold internal architecture design to match bone elastic properties with desired porosity. *Journal of Biomechanics*, 37(5):623–636.

Liu, L., Yan, J. and Cheng, G. (2008). Optimum structure with homogeneous optimum truss-like material. *Computers & Structures*, 86(13-14):1417 – 1425.

Lévy, T. (1983). Fluid flow through an array of fixed particles. *International Journal of Engineering Science*, 21(1):11–23.

Michaleris, P., Tortorelli, D.A. and Vidal, C.A. (1994). Tangent operators and design sensitivity formulations for transient non-linear coupled problems with applications to elastoplasticity. *Int. J. Numer. Meth. Engng.*, 37(14):2471–2499.

Neves, M.M., Rodrigues, H. and Guedes, J.M. (1995). Generalized topology design of structures with a buckling load criterion. *Structural and Multidisciplinary Optimization*, 10(2):71–78.

Neves, M.M., Sigmund, O. and Bendsøe, M.P. (2002). Topology optimization of periodic microstructures with a penalization of highly localized buckling modes. *International Journal for Numerical Methods in Engineering*, 54(6):809–834.

Nui, B., Jun, Y. and Cheng, G. (2008). Optimum structure with homogeneous optimum cellular material for maximum fundamental frequency. *Structural and Multidisciplinary Optimization*, 39(2):115–132.

Okkels, F. and Bruus, H. (2007). Scaling behavior of optimally structured catalytic microfluidic reactors. *Physical Review E*, 75(1):016301.

Olesen, L.H., Okkels, F. and Bruus, H. (2006). A high-level programming-language implementation of topology optimization applied to steady-state Navier-Stokes flow. *International Journal for Numerical Methods in Engineering*, 65(7):975–1001.

Othmer, C. (2008). A continuous adjoint formulation for the computation of topological and surface sensitivities of ducted flows. *International Journal for Numerical Methods in Fluids*, 58(8):861–877.

Pedersen, P. and Pedersen, N.L. (2009). Analytical optimal designs for long and short statically determinate beam structures. *Structural and Multidisciplinary Optimization*, 39(4):343–357.

Pingen, G., Evgrafov, A. and Maute, K. (2007). Topology optimization of flow domains using the lattice Boltzmann method. *Structural and Multidisciplinary Optimization*, 34(6):507–524.

Rodrigues, H., Guedes, J. and Bendsøe, M. (2002). Hierarchical optimization of material and structure. *Structural and Multidisciplinary Optimization*, 24:1–10.

Sanchez-Palencia, E. (1980). *Non-homogeneous media and vibration theory*. Lecture Notes in Physics, 127. Berlin Heidelberg New York: Springer- Verlag.

Sigmund, O. (1997). On the design of compliant mechanisms using topology optimization. *Mechanics of Structures and Machines*, 25(4):493–524.

Sigmund, O. (1999). On the optimality of bone microstructure. In P. Pedersen and M. Bendsøe, editors, *Synthesis in Bio Solid Mechanics*, pages 221–234. IUTAM, Kluwer.

Sigmund, O. (2007). Morphology-based black and white filters for topology optimization. *Structural and Multidisciplinary Optimization*, 33(4-5):401–424.

Sigmund, O. and Clausen, P.M. (2007). Topology optimization using a mixed formulation: An alternative way to solve pressure load problems. *Computer Methods in Applied Mechanics and Engineering*, 196(13-16):1874–1889.

Sigmund, O. and Petersson, J. (1998). Numerical instabilities in topology optimization: A survey on procedures dealing with checkerboards, mesh-dependencies and local minima. *Structural and Multidisciplinary Optimization*, 16:68–75.

Sigmund, O. and Torquato, S. (1996). Composites with extremal thermal expansion coefficients. *Applied Physics Letters*, 69(21):3203–3205.

Sigmund, O. and Torquato, S. (1997). Design of materials with extreme thermal expansion using a three-phase topology optimization method. *Journal of the Mechanics and Physics of Solids*, 45(6):1037–1067.

Sigmund, O. (1994a). *Design of material structures using topology optimization*. Ph.D. thesis, Department of Solid Mechanics, Technical University of Denmark.

Sigmund, O. (1994b). Materials with prescribed constitutive parameters: An inverse homogenization problem. *International Journal of Solids and Structures*, 31(17):2313–2329.

Sigmund, O. (1995). Tailoring materials with prescribed elastic properties. *Mechanics of Materials*, 20(4):351–368.

Sigmund, O. (2000). A new class of extremal composites. *Journal of the Mechanics and Physics of Solids*, 48(2):397 – 428.

Stolpe, M. and Svanberg, K. (2001). An alternative interpolation scheme for minimum compliance topology optimization. *Structural and Multidisciplinary Optimization*, 22(2):116–124.

Stroock, A.D., Dertinger, S.K.W., Ajdari, A., Mezic, I., Stone, H.A. and Whitesides, G.M. (2002). Chaotic mixer for microchannels. *Science*, 295(5555):647–651.

Suzuki, K. and Kikuchi, N. (1991). A homogenization method for shape and topology optimization. *Computer Methods in Applied Mechanics and Engineering*, 93(3):291–318.

Svanberg, K. (1987). The method of moving asymptotes - a new method for structural optimization. *International Journal for Numerical Methods in Engineering*, 24(2):359–373.

Svanberg, K. (2001). A class of globally convergent optimization methods based on conservative convex separable approximations. *Siam Journal on Optimization*, 12(2):555–573.

Torquato, S. (2002). *Random Heterogeneous Materials*. Springer, 2nd edition.

Turteltaub, S. (2001). Optimal material properties for transient problems. *Structural and Multidisciplinary Optimization*, 22:157–166.

von Terzaghi, K. (1923). Die Berechnung der Durchlässigkeit des Tones aus dem Verlauf der hydromechanischen Spannungserscheinungen. *Sitzungsberichte der Akademie der Wissenschaften in Wien, Mathematisch-Naturwissenschaftliche Klasse*, 132(3-4):125–138.

Wang, H.F. (2000). *Theory of Linear Poroelasticity with Applications to Geomechanics and Hydrogeology*. Princeton University Press.

Wiker, N., Klarbring, A. and Borrvall, T. (2007). Topology optimization of regions of Darcy and Stokes flow. *International Journal for Numerical Methods in Engineering*, 69(7):1374–1404.

Wächter, A. and Biegler, L.T. (2006). On the implementation of an interior-point filter line-search algorithm for large-scale nonlinear programming. *Mathematical Programming*, 106:25–57.

Xu, S. and Cheng, G. (2010). Optimum material design of minimum structural compliance under seepage constraint. *Structural and Multidisciplinary Optimization*, 41(4):575–587.

Yang, J.T., Huang, K.J., Tung, K.Y., Hu, I.C. and Lyu, P.C. (2007). A chaotic micromixer modulated by constructive vortex agitation. *Journal of Micromechanics and Microengineering*, 17(10):2084.

Yoon, G.H. (2010). Topology optimization for stationary fluid-structure interaction problems using a new monolithic formulation. *International Journal for Numerical Methods in Engineering*, 82(5):591–616.

Zhou, M. and Rozvany, G. (1991). The COC algorithm, part II: Topological, geometrical and generalized shape optimization. *Computer Methods in Applied Mechanics and Engineering*, 89(1-3):309 – 336.

Appendix A
Two scale asymptotic expansion of the fluid-structure interaction problem

In this appendix, the homogenization procedure for the fluid-structure interaction problem is re-derived and commented to a larger detail than in the reference by Auriault et al. (2009). The equations considered are the Stokes equation and the steady-state Navier-Cauchy equations as stated in chapter 2, here rephrased

$$\nabla_X \cdot \boldsymbol{\sigma}_s = 0 \quad \Rightarrow \quad \nabla_X \cdot (\mathbf{c} : \boldsymbol{\varepsilon}_X(\mathbf{u})) = 0 \quad \text{in } \Omega_s \tag{A.1}$$

$$\nabla_X \cdot \boldsymbol{\sigma}_f = 0 \quad \Rightarrow \quad \nabla_X \cdot (2\mu\boldsymbol{\varepsilon}_X(\mathbf{v}) - p\mathbf{I}) = 0 \quad \text{in } \Omega_f \tag{A.2}$$

$$\nabla_X \cdot \mathbf{v} = 0 \quad \text{in } \Omega_f \tag{A.3}$$

$$(\boldsymbol{\sigma}_s - \boldsymbol{\sigma}_f)\mathbf{n} = 0 \quad \text{over } \Gamma \tag{A.4}$$

$$\dot{\mathbf{u}} - \mathbf{v} = 0 \quad \text{over } \Gamma \tag{A.5}$$

Multiple-scales procedure

The first step of the homogenization procedure is to expand the variables by an asymptotic expansion which yields

$$\mathbf{u}(\mathbf{x}, \mathbf{y}, t) = \mathbf{u}^{(0)}(\mathbf{x}, \mathbf{y}, t) + \epsilon\mathbf{u}^{(1)}(\mathbf{x}, \mathbf{y}, t) + \dots \tag{A.6}$$

$$\mathbf{v}(\mathbf{x}, \mathbf{y}, t) = \mathbf{v}^{(0)}(\mathbf{x}, \mathbf{y}, t) + \epsilon\mathbf{v}^{(1)}(\mathbf{x}, \mathbf{y}, t) + \dots \tag{A.7}$$

$$p(\mathbf{x}, \mathbf{y}, t) = p^{(0)}(\mathbf{x}, \mathbf{y}, t) + \epsilon p^{(1)}(\mathbf{x}, \mathbf{y}, t) + \dots \tag{A.8}$$

where $\mathbf{y} = \epsilon^{-1}\mathbf{x}$ and the expanded variables $\mathbf{u}^{(i)}$, $\mathbf{v}^{(i)}$ and $p^{(i)}$ are Ω-periodic in $\mathbf{y}$. Furthermore this expansion also influences the gradient $\nabla_X \to \nabla_x + \epsilon^{-1}\nabla_y$.

The homogenization procedure described in the following assumes that $\mathcal{Q} = \mathcal{O}(\epsilon^{-2})$ which implies that the viscosity should be multiplied by a factor ϵ^2 due to the appearance in $\mathcal{Q}$. Inserting into (A.2) which is now considered to contain non-dimensional variables yields

$$\epsilon^2\mu\nabla_X^2\mathbf{v} - \nabla_X p = \mathcal{O}(\epsilon) \tag{A.9}$$

$$\boldsymbol{\sigma}_f = 2\mu\epsilon^2\varepsilon_X(\mathbf{v}) - p\mathbf{I} \tag{A.10}$$

Expanding the fluid stress

$$\begin{aligned}\boldsymbol{\sigma}_f = &- \epsilon^0 p\mathbf{I} \\ &+ \epsilon^1 2\mu\varepsilon_y(\mathbf{v}^{(0)}) - \epsilon^1 p^{(0)}\mathbf{I} \\ &+ \dots\end{aligned} \tag{A.11}$$

Expanding the nondimensional Stokes equation (A.9) yields

$$\begin{aligned} &- \epsilon^{-1}\nabla_y p^{(0)} \\ &+ \mu\epsilon^0\nabla_y^2\mathbf{v}^{(0)} - \epsilon^0\nabla_x p^{(0)} - \epsilon^0\nabla_y p^{(1)} \\ &+ \epsilon^1\mu\nabla_y^2\mathbf{v}^{(1)} - \epsilon^1\nabla_x p^{(1)} + \ldots = 0 \end{aligned} \tag{A.12}$$

And the expanded continuity equation (A.3) yields

$$\begin{aligned} &\epsilon^{-1}\nabla_y \cdot \mathbf{v}^{(0)} \\ &+ \epsilon^0\nabla_x \cdot \mathbf{v}^{(0)} + \epsilon^0\nabla_y \cdot \mathbf{v}^{(1)} \\ &+ \epsilon^1\nabla_x \cdot \mathbf{v}^{(1)} + \ldots = 0 \end{aligned} \tag{A.13}$$

The expansion of the solid stress yields

$$\begin{aligned} \boldsymbol{\sigma}_s =& \epsilon^{-1}\mathbf{c} : \boldsymbol{\varepsilon}_y(\mathbf{u}^{(0)}) \\ &+ \epsilon^0(\mathbf{c} : \boldsymbol{\varepsilon}_y(\mathbf{u}^{(1)}) + \mathbf{c} : \boldsymbol{\varepsilon}_x(\mathbf{u}^{(0)})) \\ &+ \epsilon^1(\mathbf{c} : \boldsymbol{\varepsilon}_y(\mathbf{u}^{(2)}) + \mathbf{c} : \boldsymbol{\varepsilon}_x(\mathbf{u}^{(1)})) + \ldots \end{aligned} \tag{A.14}$$

which can be inserted into (A.1) yielding

$$\begin{aligned} &\nabla_x \cdot \boldsymbol{\sigma}_s + \epsilon^{-1}\nabla_y \cdot \boldsymbol{\sigma}_s \\ &= && \epsilon^{-2}\nabla_y \cdot (\mathbf{c} : \boldsymbol{\varepsilon}_y(\mathbf{u}^{(0)})) \\ &+ \epsilon^{-1}\nabla_x \cdot (\mathbf{c} : \boldsymbol{\varepsilon}_y(\mathbf{u}^{(0)}))+ && \epsilon^{-1}\nabla_y \cdot (\mathbf{c} : \boldsymbol{\varepsilon}_y(\mathbf{u}^{(1)}) + \mathbf{c} : \boldsymbol{\varepsilon}_x(\mathbf{u}^{(0)})) \\ &+ \epsilon^0\nabla_x \cdot (\mathbf{c} : \boldsymbol{\varepsilon}_y(\mathbf{u}^{(1)}) + \mathbf{c} : \boldsymbol{\varepsilon}_x(\mathbf{u}^{(0)}))+ && \epsilon^0\nabla_y \cdot (\mathbf{c} : \boldsymbol{\varepsilon}_y(\mathbf{u}^{(2)}) + \mathbf{c} : \boldsymbol{\varepsilon}_x(\mathbf{u}^{(1)})) \\ &+ \ldots \end{aligned} \tag{A.15}$$

Finally, the interface boundary conditions are expanded, first the continuous stress which yield

$$\begin{aligned} (\boldsymbol{\sigma}_s - \boldsymbol{\sigma}_f)\mathbf{n} = \\ &[\epsilon^{-1}\nabla_y \cdot (\mathbf{c} : \varepsilon_y(\mathbf{u}^{(0)})) \\ &+ \epsilon^0\nabla_y \cdot (\mathbf{c} : \varepsilon_y(\mathbf{u}^{(1)}) + \mathbf{c} : \varepsilon_x(\mathbf{u}^{(0)})) + \epsilon^0 p\mathbf{I} + \ldots]\mathbf{n} = 0 \end{aligned} \tag{A.16}$$

and the no-slip condition

$$\begin{aligned} &(\dot{\mathbf{u}}^{(0)} - \mathbf{v}^{(0)}) \\ &+ (\dot{\mathbf{u}}^{(1)} - \mathbf{v}^{(1)}) + \ldots = \mathbf{0} \end{aligned} \tag{A.17}$$

Having expanded the governing equations and the boundary conditions the orders should be separated and treated one at a time.

Lowest order solid

The equations in the solid domain is first considered. The lowest order expanded terms ϵ^{-2} for (A.15) and ϵ^{-1} for (A.16) yield a problem in $\mathbf{u}^{(0)}$:

$$\nabla_y \cdot (\mathbf{c} : \boldsymbol{\varepsilon}_y(\mathbf{u}^{(0)})) = 0 \qquad \text{in } \Omega_s \tag{A.18}$$

$$(\mathbf{c} : \boldsymbol{\varepsilon}_y(\mathbf{u}^{(0)}))\mathbf{n} = 0 \qquad \text{at } \Gamma \tag{A.19}$$

where $\mathbf{u}^{(0)}$ is Ω-periodic in $\mathbf{y}$. For the boundary condition it is seen that there is no corresponding fluid stress at this order. As there is no variation in $\mathbf{u}^{(0)}$ with respect to $\mathbf{y}$ the lowest order displacements only depend on $\mathbf{x}$ i.e. $\mathbf{u}^{(0)} = \mathbf{u}^{(0)}(\mathbf{x}, t)$

Next order solid

The terms of order ϵ^{-1} from (A.15) and the ϵ^0 expansion of the boundary condition (A.16) yield a problem in $\mathbf{u}^{(1)}$:

$$\nabla_y \cdot \left(\mathbf{c} : \boldsymbol{\varepsilon}_y(\mathbf{u}^{(1)}) + (\mathbf{c} : \boldsymbol{\varepsilon}_x(\mathbf{u}^{(0)})\right) = 0 \qquad \text{in } \Omega_s \tag{A.20}$$

$$\left(\mathbf{c} : \boldsymbol{\varepsilon}_y(\mathbf{u}^{(1)}) + (\mathbf{c} : \boldsymbol{\varepsilon}_x(\mathbf{u}^{(0)})\right)\mathbf{n} = -p^{(0)}\mathbf{n} \qquad \text{on } \Gamma \tag{A.21}$$

By applying Green's identity and the divergence theorem the weak form is obtained

$$\int_{\Omega_s} \varepsilon(\hat{\mathbf{u}})(\mathbf{c} : \varepsilon_y(\mathbf{u}^{(1)}) + (\mathbf{c} : \varepsilon_x(\mathbf{u}^{(0)}))\, \mathrm{d}\Omega = -\int_{\Gamma} \hat{\mathbf{u}} p^{(0)}\mathbf{n}\, \mathrm{d}\Gamma \tag{A.22}$$

It is seen that the microscale deformations $\mathbf{u}^{(1)}$ depend linearly on the macroscopic strain and the pressure. The microscale deformations can be expressed as

$$\mathbf{u}^{(1)} = \boldsymbol{\xi}^{lm}\varepsilon_{x\,lm}(\mathbf{u}^{(0)}) - \boldsymbol{\eta}p^{(0)} + \bar{\mathbf{u}}^{(1)}(\mathbf{x}) \tag{A.23}$$

where $\boldsymbol{\xi}$ is a third order tensor containing characteristic deformations related to prestress, $\boldsymbol{\eta}$ is a first order tensor containing the characteristic deformation related to a uniform pressure and $\bar{\mathbf{u}}^{(1)}$ is an arbitrary deformation (integration constant).

Lowest order fluid

For the lowest order ϵ^{-1} of (A.12) the problem yields

$$\nabla_y p^{(0)} = 0 \quad \text{in } \Omega_f \qquad \Rightarrow p^{(0)} = p^{(0)}(\mathbf{x}, t) \tag{A.24}$$

which shows that the lowest scale pressure only depend on the macroscopic scale.

Next order fluid

Collecting the next order fluid terms ϵ^0 from (A.12) and ϵ^{-1} from (A.13) yield a problem in $\mathbf{v}^{(0)}$ and $p^{(1)}$:

$$\mu\nabla_y^2\mathbf{v}^{(0)} - \nabla_y p^{(1)} = \nabla_x p^{(0)} \qquad \text{in } \Omega_f \tag{A.25}$$

$$\nabla_y \cdot \mathbf{v}^{(0)} = 0 \qquad \text{in } \Omega_f \tag{A.26}$$

In order to include the interface boundary condition (A.17) which ensures continuous velocity across the interface and thereby a no-slip condition on the fluid boundary the relative velocity $\mathbf{w} = \mathbf{v}^{(0)} - \dot{\mathbf{u}}^{(0)}$ is introduced and the problem yields

$$\mu\nabla_y^2\mathbf{w} - \nabla_y p^{(1)} = \nabla_x p^{(0)} \qquad \text{in}\Omega_f \tag{A.27}$$

$$\nabla_y \cdot \mathbf{w} = 0 \qquad \text{in}\Omega_f \tag{A.28}$$

$$\mathbf{w} = 0 \qquad \text{on } \Gamma \tag{A.29}$$

This is a Stokes flow problem with a volume force (gradient of macroscopic pressure), defined in the unit cell, where the velocities and pressure depend linearly on $p^{(0)}$ yielding

$$\mathbf{w} = -\frac{\mathbf{k}}{\mu}\nabla_x p^{(0)} \tag{A.30}$$

$$p^{(1)} = \mathbf{a} \cdot \nabla_x p^{(0)} + \bar{p}^{(1)}(\mathbf{x}) \tag{A.31}$$

where $\mathbf{k}$ is a 2nd order tensor defined in $\mathbf{y}$. $\mathbf{a}$ is a 1st order tensor with zero volume average. Taking the volumetric average over the unit-cell yields a Darcy's flow law

$$\langle\mathbf{w}\rangle = \left\langle\mathbf{v}^{(0)}\right\rangle - \phi\dot{\mathbf{u}}^{(0)} = -\frac{\boldsymbol{\kappa}}{\mu}\nabla_x p^{(0)} \tag{A.32}$$

where $< \circ >= \frac{1}{\Omega}\int_\Omega \circ \, \mathrm{d}\Omega$ is the volumetric average and $\boldsymbol{\kappa} = \langle\mathbf{k}\rangle$ is the permeability.

Compatibility I

Inspecting the next order of the expansion, a set of compatibility equations i.e. the macroscopic state equations can be obtained. The next order of fluid and solid equations ϵ^0 given in the domain and ϵ^1 at the interface yield

$$\nabla_y \cdot \boldsymbol{\sigma}_s^{(1)} + \nabla_x \cdot \boldsymbol{\sigma}_s^{(0)} = 0 \tag{A.33}$$

$$\nabla_y \cdot \boldsymbol{\sigma}_f^{(1)} - \nabla_x p^{(0)} = 0 \tag{A.34}$$

$$\left(\boldsymbol{\sigma}_s^{(1)} - \boldsymbol{\sigma}_f^{(1)}\right)\mathbf{n} = 0 \tag{A.35}$$

Integrating over the two partitions, solid and fluid, and using the divergence theorem on the first order stress terms yield

$$\int_{\Omega_s} \nabla_x \cdot \boldsymbol{\sigma}_s^{(0)} \, \mathrm{d}\Omega - \int_{\Omega_f} \nabla_x p^{(0)} \, \mathrm{d}\Omega = 0 \tag{A.36}$$

and using the identity $\nabla p = \nabla \cdot \mathbf{I}p$ it is seen that the stress, is divergence free

$$\nabla_x \cdot \left\langle \boldsymbol{\sigma}^0 \right\rangle = 0 \tag{A.37}$$

The macroscopic stress relation can be computed by inserting the first order displacements (A.23)

$$\begin{aligned}\left\langle \sigma_{ij}^0 \right\rangle &= \frac{1}{|\Omega|} \int_{\Omega_s} c_{ijkh} \left(\varepsilon_{y\,kh}(\boldsymbol{\xi}^{lm}) \varepsilon_{x\,lm}(\mathbf{u}^{(0)}) + \varepsilon_{x\,kh}(\mathbf{u}^{(0)}) - \varepsilon_{y\,kh}(\eta) p^{(0)} \right) \mathrm{d}\Omega \\ &\quad - \frac{1}{|\Omega|} \int_{\Omega_f} \delta_{ij} p^{(0)} \,\mathrm{d}\Omega \qquad \text{(A.38)} \\ &= c_{ijkh}^H \varepsilon_{x\,kh}(\mathbf{u}^{(0)}) - \alpha_{ij} p^{(0)} \qquad \text{(A.39)}\end{aligned}$$

Where the homogenized stiffness tensor is given by

$$c_{ijkh}^H = \frac{1}{|\Omega|} \int_{\Omega_s} c_{ijkh} + c_{ijlm} \varepsilon_{lm}(\boldsymbol{\xi}^{kh}) \,\mathrm{d}\Omega \tag{A.40}$$

and the pressure coupling tensor α also known as the *Biot-Willis* coefficient is given by

$$\alpha_{ij} = \phi \delta_{ij} - \frac{1}{|\Omega|} \int_{\Omega_s} \xi_{p,p}^{ij} \,\mathrm{d}\Omega \tag{A.41}$$

where ϕ is the porosity.

Compatibility II

A second compatibility equation is obtained if the fluid mass conservation (A.13) at order ϵ^0 is considered along with the interface condition (A.16) at order ϵ^1

$$\nabla_x \cdot \mathbf{v}^{(0)} + \nabla_y \cdot \mathbf{v}^{(1)} = 0 \tag{A.42}$$

$$\dot{\mathbf{u}}^{(1)} - \mathbf{v}^{(1)} = 0 \tag{A.43}$$

Averaging over the volume yields

$$\begin{aligned}\int_{\Omega_f} \nabla_x \cdot \mathbf{v}^{(0)} \,\mathrm{d}\Omega &= \int_{\Omega_s} \nabla_y \cdot \dot{\mathbf{u}}^{(1)} \,\mathrm{d}\Omega \\ &= \left\langle \xi_{i,i}^{lm} \right\rangle \varepsilon_{x\,lm}(\dot{\mathbf{u}}^{(0)}) - \left\langle \eta_{i,i} \right\rangle \dot{p}^{(0)} \qquad \text{(A.44)}\end{aligned}$$

which is obtained utilizing that the solution to $\mathbf{u}^{(1)}$ is known (A.23) and the divergence theorem can be applied to the first order velocity term $\mathbf{v}^{(1)}$ in combination with the boundary condition (A.16)

$$\begin{aligned}\int_{\Omega_f} \nabla_y \cdot \mathbf{v}^{(1)} \,\mathrm{d}\Omega &= -\int_{\Gamma} \mathbf{v}^{(1)} \mathbf{n} \,\mathrm{d}\Gamma \\ &= -\int_{\Gamma} \dot{\mathbf{u}}^{(1)} \mathbf{n} \,\mathrm{d}\Gamma \\ &= -\int_{\Omega_s} \nabla_y \cdot \dot{\mathbf{u}}^{(1)} \,\mathrm{d}\Omega \qquad \text{(A.45)}\end{aligned}$$

By considering the Darcy's law (A.32) the volume average (A.44) can be written as

$$\nabla_x \cdot \left(\frac{\mathbf{K}}{\mu} \nabla_x p^{(0)} \right) = \gamma_{lm} \varepsilon_{x\,lm}(\dot{\mathbf{u}}^{(0)}) + \bar{\beta} \dot{p}^{(0)} \tag{A.46}$$

which is the macroscopic equation governing the fluid flow where the tensor $\boldsymbol{\gamma}$ is given by

$$\gamma_{ij} = \phi \delta_{ij} + \frac{1}{|\Omega|} \int_{\Omega_s} c_{ijlm} \varepsilon_{lm}(\boldsymbol{\eta}) \, \mathrm{d}\Omega \tag{A.47}$$

and it can be shown that $\boldsymbol{\alpha} = \boldsymbol{\gamma}$ (Auriault et al., 2009). The final parameter $\bar{\beta}$ is the microstructure compressibility and is computed as

$$\bar{\beta} = \frac{1}{|\Omega|} \int_{\Omega_s} \eta_{p,p} \, \mathrm{d}\Omega \tag{A.48}$$

Defining the stiffness and pressure coupling in a monolithic formulation

The stress computed in (A.38) is based on a partitioned domain. However, in a topology optimization context the problem is recast in a monolithic formulation. One way of doing so is to use an indicator function $\mathcal{I}$ which indicates solid material.

$$\left\langle \sigma_{ij}^0 \right\rangle = \frac{1}{|\Omega|} \int_{\Omega} \Big[\mathcal{I} c_{ijkh} \left(\varepsilon_{y\,kh}(\boldsymbol{\xi}^{lm}) \varepsilon_{x\,lm}(\mathbf{u}^{(0)}) + \varepsilon_{x\,kh}(\mathbf{u}^{(0)}) - \varepsilon_{y\,kh}(\eta) p^{(0)} \right) - (1 - \mathcal{I}) \delta_{ij} p^{(0)} \Big] \, \mathrm{d}\Omega \tag{A.49}$$

Relaxing this representation of the partitioning of the domain such that it is not strictly solid or fluid, the indicator function might be changed into an interpolation function e.g. $\mathcal{I} = \rho^p$ as in SIMP. This influence the homogenization of the tensors and they are now computed

$$c_{ijkh}^H = \frac{1}{|\Omega|} \int_{\Omega} \mathcal{I} c_{ijkh} + \mathcal{I} c_{ijlm} \varepsilon_{lm}(\boldsymbol{\xi}^{kh}) \, \mathrm{d}\Omega \tag{A.50}$$

$$\alpha_{ij} = \frac{1}{|\Omega|} \int_{\Omega} (1 - \mathcal{I}) \delta_{ij} + \mathcal{I} c_{ijlm} \varepsilon_{lm}(\boldsymbol{\eta}) \, \mathrm{d}\Omega \tag{A.51}$$

Effective properties with dimensions

As the multiple-scale procedure is using nondimensionalized quantities the effective properties should regain the correct dimensions prior to insertion in the macroscopic equations. This can be stated as

$$C_{ijkh}^H = c_{ijkh}^H c^* \tag{A.52}$$

$$\beta = \bar{\beta} / K_b^* \tag{A.53}$$

where $c^* = C_{ijkh} / c_{ijkh}$ is the scalar used for nondimensionalizing the stiffness and K_b^* is the bulk modulus of the solid material.

Publication [P1]

Saturated poroelastic actuators generated by topology optimization

Struct Multidisc Optim (2011) 43:693–706
DOI 10.1007/s00158-010-0597-4

RESEARCH PAPER

Saturated poroelastic actuators generated by topology optimization

Casper Schousboe Andreasen · Ole Sigmund

Received: 1 July 2010 / Revised: 14 October 2010 / Accepted: 1 November 2010 / Published online: 24 December 2010

Abstract In this paper the fluid-structure interaction problem of a saturated porous media is considered. The pressure coupling properties of porous saturated materials change with the microstructure and this is utilized in the design of an actuator using a topology optimized porous material. By maximizing the coupling of internal fluid pressure and elastic shear stresses a slab of the optimized porous material deflects/deforms when a pressure is imposed and an actuator is created. Several phenomenologically based constraints are imposed in order to get a stable force transmitting actuator.

Keywords Topology optimization · FSI · Coupled problems · Homogenization · Multi-scale modeling

1 Introduction

Adaptive materials have proven to be successful in many applications, best known might be the piezoelectric materials used as small precise actuators in advanced products such as atomic force microscopes but also in everyday products such as the auto focus unit in a digital SLR camera. In this fashion we want to design a solid-fluid mechanical counterpart that does not rely on electric signals but on pressure in a fluid. Application of such actuators could be e.g. in modal control systems in wind turbine blades or in other non-electric environments.

C. S. Andreasen (✉) · O. Sigmund
Department of Mechanical Engineering, Solid Mechanics, Technical University of Denmark, 2800, Kgs. Lyngby, Denmark
e-mail: csan@mek.dtu.dk

O. Sigmund
e-mail: sigmund@mek.dtu.dk

Using a fluid saturated periodic porous material with an optimized microstructure such an actuator can be designed as exemplified in Fig. 1. The slab of porous saturated material shown is fixed and loaded by a pressure at the left face and all other faces are sealed. The left domain serves as a foundation and contains a porous isotropic media with relatively high stiffness and permeability whereas the right domain contains the optimized material that exhibits a large coupling between internal pressure and elastic stresses. The goal of this optimization is to either deform or distort the right face as much as possible under fixed loading conditions by applying topology optimization to the modeling of the material microstructure.

The interaction between solids and fluids in terms of consolidation of soil and water has been studied for a century. Fillunger (1913) and von Terzaghi (1923) developed some of the early theories on soil-liquid models. The poroelastic theory equivalent to the one used in this paper was described in Biot (1941, 1955) and extended to dynamic problems in Biot (1956). A review of the theories of deformable saturated porous materials was given by de Boer and Ehlers (1988) and a comparison between the two dominating descriptions was given in Schanz and Diebels (2003).

The Biot poroelastic theory can be shown to appear when solid-fluid interaction with certain assumptions are investigated using the homogenization method, i.e. expanding the problem using asymptotic expansions and handle the scales separately. This was done by Auriault and Sanchez-Palencia (1977) and Sanchez-Palencia (1980), and the theory was recently comprehensively described in Auriault et al. (2009).

Material optimization using the homogenization method and topology optimization has been studied for materials with prescribed elastic properties (Sigmund 1994, 2000) and for the permeability of microstructures by Guest and

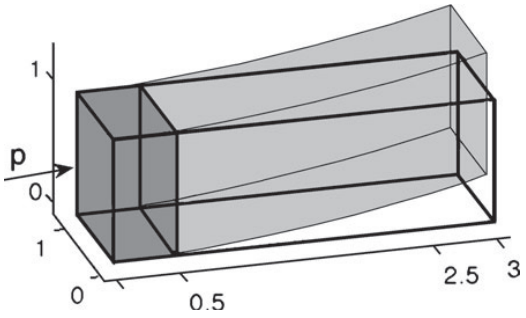

Fig. 1 Slab of porous material in a deformed state. In the *left dark gray domain* an isotropic material with relatively high stiffness and permeability is modeled. In the *right light gray domain* the optimized material is modeled. *Left face* is fixed and loaded by a fluid pressure p. All other faces are sealed

Prévost (2007). Stiffness and permeability were optimized simultaneously in Guest and Prévost (2006) and Xu and Cheng (2010) used the seapage equation as an alternative to a permeability constraint in a multiscale optimization problem.

The method has also been used for optimization of materials with extreme thermal expansion in Sigmund and Torquato (1996, 1997) and materials with prescribed piezoelectric properties in Sigmund et al. (1998). The combination of optimal strength and conductivity was investigated in Sigmund (1999) and Torquato et al. (2002).

Whereas the previous applications considered uncoupled fluid-structure problems this paper extends those works by taking the fluid structure interaction in the microstructure into account. The coupling of internal pressure and elastic stress is quantified by a 2nd order tensor $\boldsymbol{\alpha}$ which we optimize in order to get the largest possible deflection/distorsion of the right face of the macro structure (c.f. Fig. 1) under a number of constraints based on phenomenological observations.

Topology optimization of fluid-structure interaction problems in a more general context is a developing research area with only few reports. Aeroelastic structures were designed in Maute and Allen (2004) using a fixed interaction surface. A monolithic formulation allowing the interface to change has been presented by Yoon (2010) and Kreissl et al. (2010) applies topology optimization to flexible micro-fluidic devices exhibiting large elastic deformations.

The paper is organized as follows. In Section 2 the macro- and microscopic problems are defined along with the theory. Interpolation functions for the monolithic formulations as well as bounds on the coupling tensor are also presented. In Section 3 the microscopic modeling and optimization of the microstructure topology using several physics based constraints are shown. In Section 4 the macroscopic actuator problem is evaluated using the optimized materials and the characteristics are investigated. Finally the results are discussed and the paper is concluded in Section 5.

2 Theory

The fluid-structure interaction problem in saturated elastic porous media can, assuming a sufficiently large difference in length scales, be described using the homogenization method (Bensoussan et al. 1978; Sanchez-Palencia 1980). By expanding the governing equations using asymptotic expansions the scales can be separated such that two problems rise, namely a micro- and a macro problem which can be solved independently.

The poroelastic theory of Biot can be shown to appear when a two scale asymptotic expansion of Navier and Navier–Stokes equations is applied (Auriault et al. 2009). In Fig. 2 the periodic microstructure as well as the unit-cell are illustrated. The fluid Ω_f and solid Ω_s domains are colored white and black respectively and the interacting boundaries are labeled Γ and the periodic unit-cell boundaries are labeled Γ_p. The solid is governed by the Navier equation

$$\nabla \cdot \boldsymbol{\sigma}_s = \rho_s \frac{\partial^2 \mathbf{u}}{\partial t^2}, \quad \boldsymbol{\sigma}_s = \mathbf{E} : \boldsymbol{\varepsilon}(\mathbf{u}) \qquad \text{in } \Omega_s \qquad (1)$$

where $\boldsymbol{\sigma}_s$ is the solid stress tensor, $\boldsymbol{\varepsilon}(\mathbf{u}) = (u_{i,j} + u_{j,i})/2$ is the elastic strain tensor, $\mathbf{u}$ is the solid displacement vector, t is time, ρ_s the solid density and $\mathbf{E}$ the stiffness tensor. The fluid is governed by Navier–Stokes equation and the continuity condition

$$\nabla \cdot \boldsymbol{\sigma}_f = \rho_f \left(\frac{\partial \mathbf{v}}{\partial t} + \mathbf{v} \nabla \cdot \mathbf{v} \right),$$

$$\boldsymbol{\sigma}_f = 2\mu \mathbf{D}(\mathbf{v}) - p\mathbf{I} \qquad \text{in } \Omega_f \qquad (2)$$

$$\nabla \cdot \mathbf{v} = 0 \qquad \text{in } \Omega_f \qquad (3)$$

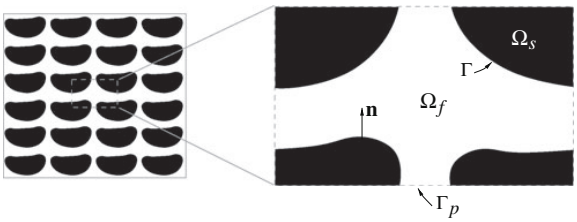

Fig. 2 2D illustration of the periodic repetitive unit cell. Labels indicate solid and fluid domain and interacting and periodic boundaries of the micro structural interaction problem

where $\mathbf{v}$ is fluid velocity, $\boldsymbol{\sigma}_f$ is the fluid stress tensor, ρ_f is the fluid density, p is fluid pressure and μ is viscosity. $\mathbf{D}(\mathbf{v}) = v_{ij} - \delta_{ij} v_{kk}/3$ is the strain rate tensor and $\mathbf{I}$ is the 2nd order identity tensor. At the interacting boundaries continuous stress and velocity conditions apply

$$(\boldsymbol{\sigma}_s - \boldsymbol{\sigma}_f)\mathbf{n} = 0 \qquad \text{at } \Gamma \tag{4}$$

$$\dot{\mathbf{u}} - \mathbf{v} = 0 \qquad \text{at } \Gamma \tag{5}$$

$$\mathbf{u}, \mathbf{v}, p \quad \text{periodic} \qquad \text{at } \Gamma_p \tag{6}$$

where $\mathbf{n}$ is the solid boundary outward pointing normal vector and $\dot{\mathbf{u}}$ is the time derivative of the solid displacements. Small strains are assumed and in order to obtain the equations of Biot the fluid velocity must be relatively high such that it does not intervene in the first order of the description but on the other hand small enough to neglect the inertial terms in Navier–Stokes equation. The formal and thorough derivation of the expansion is given in Auriault et al. (2009) and here we only show the resulting micro and macro problems that must be solved in order to achieve effective parameters and macroscopic behavior, respectively.

The macroscopic equations to be solved govern the elastic deformation and the fluid pressure in the structure.

Find $u_i \in \mathcal{V}$ and $p \in \mathcal{Q}$ for all $\hat{u}_i \in \mathcal{V}_0$ and $\hat{p} \in \mathcal{Q}$ such that

$$\int_\Omega E_{ijkl}\varepsilon_{ij}(\hat{\mathbf{u}})\varepsilon_{kl}(\mathbf{u})\mathrm{d}\Omega - \int_\Omega p\alpha_{ij}\varepsilon_{ij}(\hat{\mathbf{u}})\mathrm{d}\Omega = \int_\Omega \hat{u}_i f_i \mathrm{d}\Omega \tag{7}$$

$$\int_\Omega \alpha_{ij}\varepsilon_{ij}(\dot{\mathbf{u}})\hat{p}\mathrm{d}\Omega + \int_\Omega \beta\hat{p}\dot{p}\mathrm{d}\Omega - \int_\Omega \hat{p}_{,i}\frac{K_{ij}}{\mu}p_{,j}\mathrm{d}\Omega = 0 \tag{8}$$

The first equation is purely static and equilibrates the work done in the elastic structure with the work exerted by the fluid pore pressure and other loads. The second equation is a combination of the Darcy flow law and volume conservation for the fluid. Several coefficients are used of which the elastic stiffness tensor E_{ijkl} and the permeability K_{ij} are the most well known. Furthermore the equations contain a pressure-coupling tensor α_{ij} and a compressibility coefficient β which describe the coupling between the fluid pressure and the stresses acting on the structure and the compressibility of the elastic matrix, respectively.

In order to extract the effective parameters for a given material, a cell of the periodic microstructure c.f. Fig. 2 must be analyzed. By variational methods the effective parameters can be computed based on different loads applied to the periodic cell. The micro scale problems that must be solved are originally defined in separate domains, i.e. one set of equations for the solid domain and another for the fluid domain. In order to apply topology optimization we introduce a monolithic formulation with a relative material density field $\rho \in [0; 1]$ in order to interpolate between elastic material ($\rho = 1$) and fluid ($\rho = 0$), c.f. Guest and Prévost (2006). Based on the monolithic formulation we solve the following micro scale problems related to the solid material.

Find $u_i^{kh} \in \mathcal{V}$ and $\xi_i \in \mathcal{V}$ for all $\hat{u}_i \in \mathcal{V}_0$ such that

$$\int_\Omega E_{ijlm}(\rho)\varepsilon_{ij}(\hat{\mathbf{u}})\varepsilon_{lm}(\mathbf{u}^{kh})\mathrm{d}\Omega = \int_\Omega E_{ijkh}(\rho)\varepsilon_{ij}(\hat{\mathbf{u}})\mathrm{d}\Omega \tag{9}$$

$$\int_\Omega E_{ijlm}(\rho)\varepsilon_{ij}(\hat{\mathbf{u}})\varepsilon_{lm}(\boldsymbol{\xi})\mathrm{d}\Omega = \int_\Omega \delta_{ij}\varepsilon_{ij}(\hat{\mathbf{u}})\frac{E(\rho)}{E_0}\mathrm{d}\Omega \tag{10}$$

where E_0 is the Young's modulus of the elastic isotropic base material and $E(\rho)$ is the interpolated Young's modulus. The first equation is the standard homogenization problem in elasticity from which it is possible to extract the stiffness. The second makes it possible to determine the pressure coupling tensor and the compressibility. The $\frac{E(\rho)}{E_0}$ term on the right hand side of (10) makes the load unity in solid material and zero in void.

In order to find the permeability a Stokes flow problem must be solved but in order to model solid material with no flow the Brinkman equation which models the transitional flow between Stokes and porous flow is used. Instead of interpolating the stiffness tensor as for elastic problems the flow is penalized by the factor $\zeta(\rho)$ such that regions with $\rho = 0$ is Stokes flow and regions with solid material $\rho = 1$ have almost zero velocity. The model assumes negligible solid deformations. The micro structural flow problem yields.

Find $v_i \in \mathcal{V}$ and $p \in \mathcal{Q}$ for all $\hat{v} \in \mathcal{V}_0$ and $\hat{p} \in \mathcal{Q}$ such that

$$\int_\Omega \hat{v}_{i,j}v_{i,j}^k\mathrm{d}\Omega - \int_\Omega \hat{v}_i p_{,i}^k\mathrm{d}\Omega + \int_\Omega \zeta(\rho)v_i^k\hat{v}_i\mathrm{d}\Omega = \int_\Omega \hat{v}_i\delta_{ik}\mathrm{d}\Omega \tag{11}$$

$$\int_\Omega \hat{p}v_{i,i}^k\mathrm{d}\Omega = 0 \tag{12}$$

This yields three load cases (k) and from the corresponding velocity fields v_i^k the permeability tensor can be found.

Discrete optimization problems are difficult to solve and therefore optimization with continuous variables is preferred. The problem is relaxed such that intermediate densities are allowed during optimization. When the optimization is finished the variables should be binary and the relaxation should play no role. The interpolation used for the stiffness is the RAMP method (Stolpe and Svanberg 2001)

and for the fluid a similar interpolation scheme (Borrvall and Petersson 2003) is used. They yield

$$E(\rho) = \left(10^{-4} + \frac{\rho(1-10^{-4})}{1+p(1-\rho)}\right)E_0 \tag{13}$$

$$\zeta(\rho) = \zeta_{\max} + (\zeta_{\min} - \zeta_{\max})(1-\rho)\frac{1+q}{(1-\rho)+q} \tag{14}$$

where p and q are the penalization factors for the two schemes, here $p = 3$ and $q = 0.03$ have been used. The bounds of the inverse permeability ζ is set to $\{\zeta_{\min}, \zeta_{\max}\} = \{0, 10^6\}$ determined by a convergence analysis.

Having obtained the solution to the cell problems, the effective parameters can be computed by integrating over the domain

$$E^H_{ijkh} = < E_{ijkh}(\rho) + E_{ijlm}(\rho)\varepsilon_{lm}(\mathbf{u}^{kh}) > \tag{15}$$

$$\alpha_{ij} = < (1-\rho)\delta_{ij} + E_{ijlm}(\rho)\varepsilon_{lm}(\boldsymbol{\xi}) > \tag{16}$$

$$\beta = < \xi_{i,i}\frac{E(\rho)}{E_0} > \tag{17}$$

$$K_{ik} = < v^k_i > \tag{18}$$

where $< \bullet >= \frac{1}{|V|}\int \bullet \mathrm{d}\Omega$ is the volumetric mean of $\bullet$.

In the following sections the homogenized stiffness tensor is represented by a matrix using the following contraction of indices: $11 \rightarrow 1, 22 \rightarrow 2, 33 \rightarrow 3, (23, 32) \rightarrow 4, (13, 31) \rightarrow 5, (12, 21) \rightarrow 6$. This also applies to the stresses and strains but in order to deal with the multiplicity of the shear terms the shear-strains are defined as $\varepsilon_4 = 2\varepsilon_{23}, \varepsilon_5 = 2\varepsilon_{13}, \varepsilon_6 = 2\varepsilon_{12}$.

For all of the homogenized tensors certain bounds exist based on different criteria and microstructural symmetries. In this context it is appropriate to state the bounds and relations for the pressure coupling tensor as it is of major interest. For a cubic symmetric microstructure $\boldsymbol{\alpha}$ reduces to an isotropic coupling $\boldsymbol{\alpha} = \alpha\mathbf{I}$ and relates to the compressibility β by the porosity ϕ and the material bulk modulus K_s of the base material (c.f. Auriault and Sanchez-Palencia 1977) as

$$\beta = \frac{\alpha - \phi}{K_s} \tag{19}$$

For orthotropic materials α_{ij} stays diagonal as long as the material coordinates are aligned with the reference and for general anisotropic porous materials, Lydzba and Shao (2000) presented the following bounds on the pressure coupling tensor and the compressibility assuming an isotropic base material

$$\phi \leq \frac{1}{3}\alpha_{ij}\delta_{ij} \leq 1, \qquad 0 \leq \beta \leq \frac{1-\phi}{K_s} \tag{20}$$

which is an extension to the Hashin–Shtrickman bounds valid only for macro-isotropic materials.

3 Microscopic modeling and optimization

In this section the modeling and optimization of the microstructure is presented. The physics is modeled as presented in the previous section and an implementation of the microscopic model has been made in a framework of COMSOL 3.5 and Matlab 2008b where the elastic problem was solved using a CG (conjugate gradient) solver with incomplete Cholesky preconditioner and the flow problem was solved using the GMRES (GeneralizedMinimumRESidual) solver with a geometric multi-grid preconditioner. Trilinear elements were used for both type of problems and in order to avoid oscillations in the pressure field a GLS stabilization scheme (Hughes and Franca 1987) was imposed. This essentially means that a term is added to the continuity equation (12) such that it becomes

$$\int_\Omega \hat{p} v^k_{i,i}\mathrm{d}\Omega - \int_\Omega \tau_{GLS} p_{,i}\,\hat{p}_{,i}\mathrm{d}\Omega = 0 \tag{21}$$

which will penalize pressure oscillations. The stabilization parameter used was $\tau_{GLS} = h_e^2/6$ where h_e is a measure for the element size, here the edge length of the cubic element.

As mentioned in the introduction the maximization of the deflection of the actuator is linked to the pressure-stress coupling in the microstructure represented by the tensor α_{ij}. The diagonal entries represent a swelling of the structure whereas the off diagonal terms represent a distortion of the microstructure which will result in a deflection/deformation of the macrostructure. Therefore the optimization problem that we seek to solve is the maximization of the pressure-shear stress coupling terms for a general anisotropic porous media such that the actuator will deflect as sketched in Fig. 1. The optimization problem reads: Maximize the sum of the pressure-shear stress coupling terms such that the governing equation (10) is fulfilled along with a constraint on the solid volume fraction and a limit on the design variables ρ. Written in math style it reads

$$\begin{aligned}
\max_{\rho\in R^N} \quad & \Phi(\boldsymbol{\xi}, \rho) = \alpha_{12} + \alpha_{13} + \alpha_{23} \\
& = \frac{1}{2}\int_\Omega (1-\delta_{ij})E_{ijlm}(\rho)\varepsilon_{lm}(\boldsymbol{\xi})\mathrm{d}\Omega \\
\text{s.t.} \quad & \int_\Omega E_{ijkl}(\rho)\varepsilon_{ij}(\hat{\mathbf{u}})\varepsilon_{kl}(\boldsymbol{\xi})\mathrm{d}\Omega \\
& = \int_\Omega \varepsilon_{ij}(\hat{\mathbf{u}})\delta_{ij}\frac{E(\rho)}{E_0}\mathrm{d}\Omega \\
& \frac{1}{|V|}\int_\Omega \rho\mathrm{d}\Omega - \gamma \leq 0 \\
& 0 \leq \rho_i \leq 1 \qquad \text{for} \quad i = 1, ..., N
\end{aligned}$$

where γ is the allowed volume fraction of solid material and N is the number of elements.

The nested optimization problem is solved using the method of moving asymptotes (MMA) by Svanberg (1987). The sensitivities needed for the optimization are computed by the adjoint method where an extra problem similar to the state problem is solved for each design iteration. The problem is derived and presented in the appendix, and afterwards the sensitivity of each design element can be computed based on the two solutions.

In order to avoid checkerboard patterns in the optimized design a standard density filter (Bruns and Tortorelli 2001; Bourdin 2001) is applied. The used filter radius is very small only 1.4 times the element side length in order to minimize the amount of gray material. The convergence criterion used was $\max(|\Delta\rho|) < 10^{-3}$.

Two optimized designs can be seen in Fig. 3 allowing 30% solid and 50% solid, respectively and the corresponding effective pressure coupling tensors are

$$\boldsymbol{\alpha}_{0.3} = \begin{bmatrix} 0.8607 & 0.0494 & 0.0494 \\ & 0.8607 & 0.0494 \\ \text{sym} & & 0.8607 \end{bmatrix}$$

$$\boldsymbol{\alpha}_{0.5} = \begin{bmatrix} 0.7828 & 0.0870 & 0.0870 \\ & 0.7828 & 0.0870 \\ \text{sym} & & 0.7828 \end{bmatrix}$$

Comparing the normal with the shear components of $\boldsymbol{\alpha}$ it is seen that they are one order of magnitude larger for the two examples included. With increased volume fraction the shear components increase and the normal components decrease but pure shear is not possible.

The other effective parameters (for $\gamma = 0.5$) yield

$$\mathbf{E} = \begin{bmatrix} 0.2261 & 0.1072 & 0.1072 & 0.0056 & -0.1115 & -0.1115 \\ & 0.2261 & 0.1072 & -0.1115 & 0.0056 & -0.1115 \\ & & 0.2261 & -0.1115 & -0.1115 & 0.0056 \\ & & & 0.1152 & -0.0028 & -0.0028 \\ & & & & 0.1152 & -0.0028 \\ \text{sym} & & & & & 0.1152 \end{bmatrix} E_0$$

$$\beta = 0.8483/K_s$$

$$\mathbf{K} = \begin{bmatrix} 0.0010 & -0.0004 & -0.0004 \\ & 0.0010 & -0.0004 \\ \text{sym} & & 0.0010 \end{bmatrix} m^2$$

where $K_s = E_0/(3(1-2\nu))$ is the bulk modulus of the elastic material. The designs were obtained using $\nu = 0.3$.

The iteration history for the topology shown in Fig. 3b is shown in Fig. 4 along with some plots of intermediate designs. It is clearly seen that the changes in topology appear within the first 100 iterations after which the optimization is more shape/detail oriented.

All the effective material properties shown are sensitive to the choice of interpolation function including the choice of penalty parameters (p and q) and porosity limits (ζ) as the optimized design includes a small amount of gray elements. The computed permeability matrix $\mathbf{K}$ is for a unit-cell in consistent units, this means m^3 if SI units are used and the permeability must therefore be scaled in order to match the unit cell size. The permeability scales by the side length squared, i.e. if cell side length is 1 mm then a factor of 10^{-6} must be prefixed. The listed permeabilities are unscaled. No scalings apply for $\mathbf{E}$, $\boldsymbol{\alpha}$ and β. In order to get

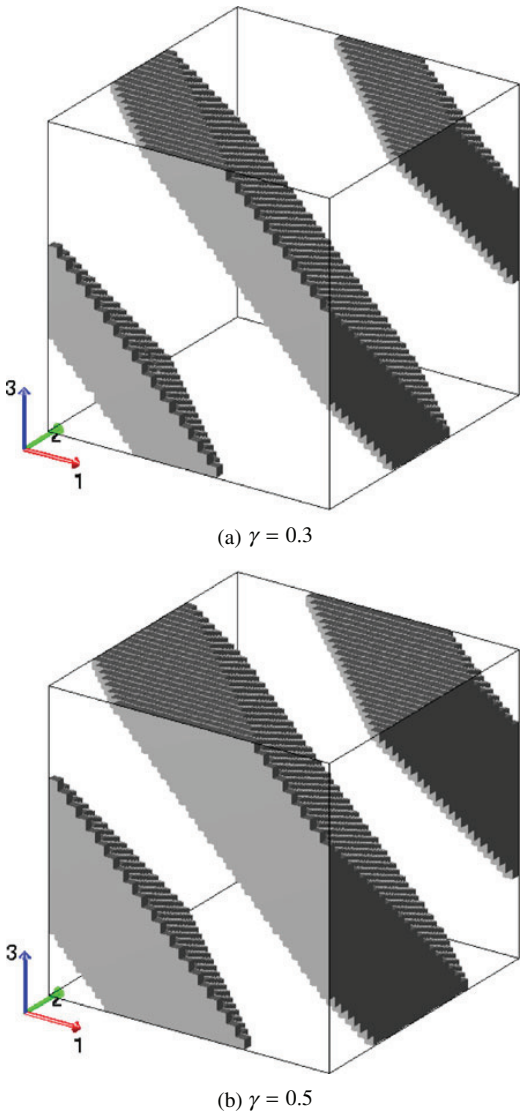

(a) $\gamma = 0.3$

(b) $\gamma = 0.5$

Fig. 3 Topologies obtained for maximum pressure-shear coupling performance. $\Phi_{0.3} = 0.1482$, $\Phi_{0.5} = 0.2610$. Density filter 1.4 element width. 27,000 elements. The design is thresholded ($\rho \geq 0.5$) for visualization purposes

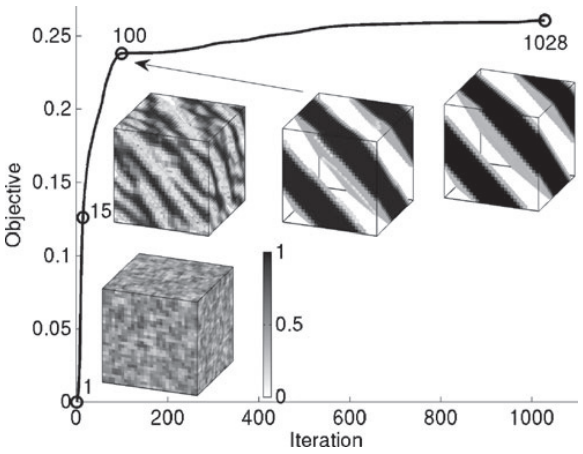

Fig. 4 Iteration history for the maximization of the shear coupling coefficients ($\gamma = 0.5$) using an initial random distribution

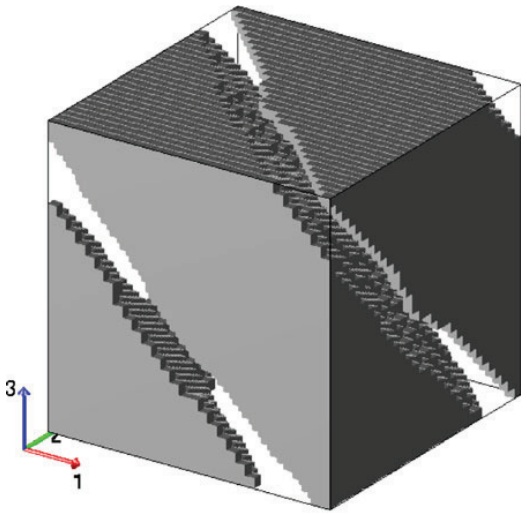

(a) $30 \times 30 \times 30$, $\Phi = 0.4158$

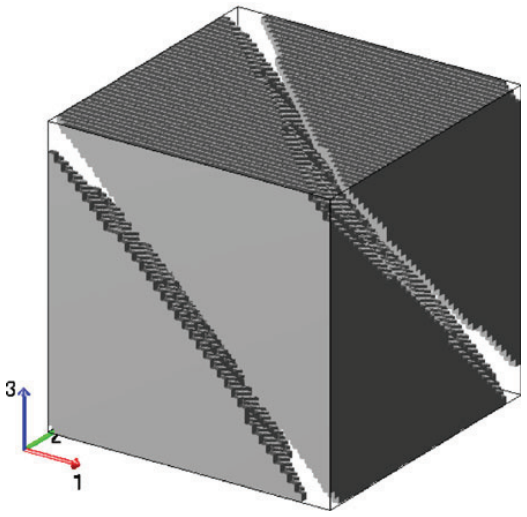

(b) $40 \times 40 \times 40$, $\Phi = 0.4557$

Fig. 5 Microstructure for maximized pressure shear coupling using $30 \times 30 \times 30$ and $40 \times 40 \times 40$ resolution

hold on the magnitude of the permeability one can compare it with the permeability of the three uniform distributions $\rho = \{0, 0.5, 1\}$ which yield the isotropic permeabilities $\mathbf{K} = \{\mathcal{O}(10^9), 0.35 \cdot 10^{-4}, 10^{-6}\}\mathbf{I}\,m^2$.

3.1 Optimal shear coupling microstructure

If the volume fraction of solid is not considered in the optimization one would expect that the microstructure that exhibits the largest possible coupling of pressure and shear stress will appear. This microstructure is shown in Fig. 5a and the pressure coupling coefficients yields

$$\boldsymbol{\alpha}^{30} = \begin{bmatrix} 0.6463 & 0.1386 & 0.1386 \\ & 0.6463 & 0.1386 \\ \text{sym} & & 0.6463 \end{bmatrix} \tag{22}$$

The optimized designs have very thin cavities/layers with no solid material where the fluid can reside and interact with inclined walls leading to the large shear coupling. As the layers are of a few element thicknesses it is essential to question if this is the optimal (or near optimal) solution or if the optimal solution consists of infinitely thin fluid layers which will maximize the fluid to inclined wall ratio. Even though the optimizer is allowed to make many layers of solid material such a configuration is not seen. This is due to the fact that the $\boldsymbol{\alpha}$ tensor is obtained by applying a triaxial load to the solid material and thereafter averaging the strains. As all the solid material has the same elastic modulus adding more solid material increases the coupling terms. The only necessity is that there is at least one void cavity as a uniform solid has no local strains and therefore zero coupling coefficient.

In order to study the mesh dependency the resolution is increased to $40 \times 40 \times 40$ elements and the result can be seen in Fig. 5b which confirms that the result is mesh dependent. This is seen in that the cavity is more narrow than previously and takes the width of a few elements. It should be recalled that a density filter with radius 1.4 element width is used

hence preventing features of 1 element widths. The resulting pressure coupling matrix is

$$\boldsymbol{\alpha}^{40} = \begin{bmatrix} 0.6381 & 0.1519 & 0.1519 \\ & 0.6381 & 0.1519 \\ \text{sym} & & 0.6381 \end{bmatrix} \tag{23}$$

This mesh dependency issue seems most important when the solid volume fraction is high which is indicated in Fig. 6 where the optimized performances for a sweep of allowed volume fraction γ is shown. The sweep was done using both 20^3 and 30^3 elements and only when the volume fraction is high the results deviate notably.

As seen from the figure the ratio between normal and shear coupling will not exceed ≈4.2 so the coupling from pressure to normal stress will always be more pronounced than the pressure shear coupling.

3.2 Constraining the permeability

The previously obtained microstructures all couple the pressure and shear stress optimally under the imposed constraints, however the layered design prohibits the saturating fluid to propagate through the structure which on the macroscopic level prevent the actuator in deflecting as much as intended. In order to let the fluid propagate through the structure a set of permeability constraints are formed.

The permeability of a microstructure ranges in theory from infinity when there is no solid material to zero when the microstructure is completely made of solid. This is relaxed in the modeling as the permeability is computed as

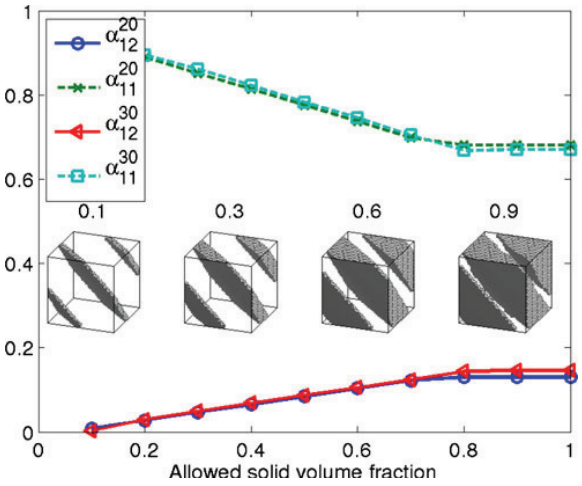

Fig. 6 Optimized performance ($\alpha_{12} + \alpha_{13} + \alpha_{23}$) for a sweep of allowed solid volume fraction. Two different meshes used with 20^3 and 30^3 elements

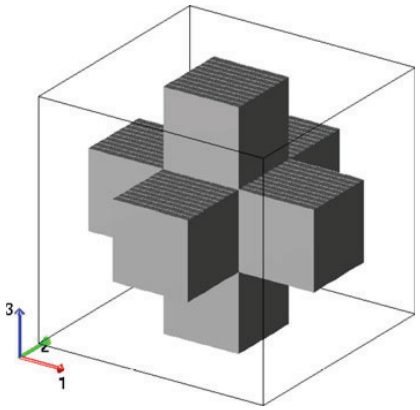

Fig. 7 Reference structure for the permeability constraint. A square-cross-sectioned cross with side length 0.3

the mean flow speed in the micro cell under a unit body force load in one direction. The monolithic formulation used in the modeling is also known as the Brinkman model which models the transition flow between Darcy flow in a porous media and Stokes flow. This is done by the introduction of a varying micro permeability which also determines the lowest possible effective permeability. The reference structure for the permeability constraint is a square-cross-sectioned cross with a side length of 0.3 (see Fig. 7) which yields an isotropic permeability $\mathbf{K} = \kappa_{\text{ref}}\mathbf{I}$ where $\kappa_{\text{ref}} = 0.0115$ m^2 (30^3 elements). The constraints added to the optimization problem yields

$$g_i = \frac{K_{ii}}{\kappa_{\text{ref}}} \leq 0 \quad \text{for } i = 1 \ldots 3 \tag{24}$$

which requires the microstructure flow problem (11) and (12) to be solved in every design iteration in order to evaluate the constraints and their sensitivities. Derivation of the sensitivities is in Appendix A.2 and can be computed from the state solution as

$$\frac{\mathrm{d}g_i}{\mathrm{d}\rho} = -\frac{1}{\kappa_{\text{ref}}}\frac{\mathrm{d}\zeta(\rho)}{\mathrm{d}\rho}(v_i^i)^2 \tag{25}$$

The optimized micro structure when allowing 50% solid material is shown in Fig. 8 and the pressure coupling tensor yields

$$\boldsymbol{\alpha} = \begin{bmatrix} 0.9421 & 0.0163 & 0.0163 \\ & 0.9421 & 0.0163 \\ \text{sym} & & 0.9421 \end{bmatrix} \tag{26}$$

Comparing the obtained topology with the ones shown in Fig. 5 it is seen that the inclined plane of solid material is

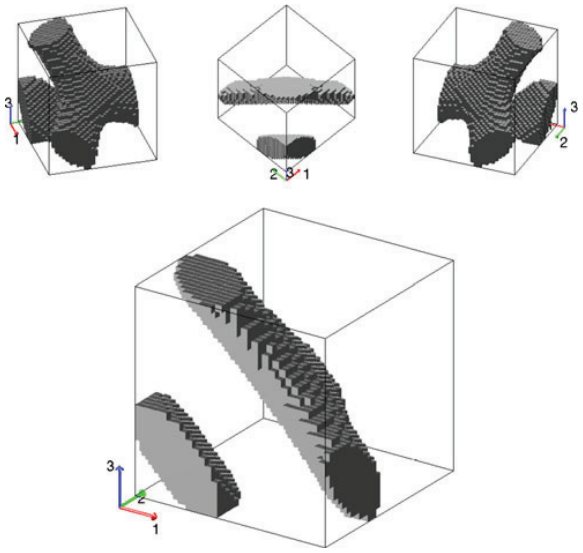

Fig. 8 Optimized topology using permeability constraints. Reference structure is a solid cross with cross section side length 0.3. $\Phi = 0.0489$

much thinner which indicates that not all allowed material is used. Furthermore parts of the plane is cut away allowing the fluid to propagate directly in the constraint directions.

The shear terms of the pressure coupling tensor $\boldsymbol{\alpha}$ shows a significantly lower coupling which is even less than the one obtained using 30% solid material ($\gamma = 0.3$). This is an effect of the choice of reference permeability structure which has a solid volume fraction of 0.252 and almost maximal permeability. This of course influenced the design and the volume constraint was not active.

Due to the very nonlinear behavior of the permeability the optimization results showed some dependency on the initial design variable distribution, several different distributions were tried; random, uniform, the reference solid cross and a small inclined disc. The results shown were obtained using the inclined disc initial design as it yielded a feasible starting design with a poor performance leaving as much design freedom to the optimizer as possible.

3.3 Constraining the stiffness

In the previous sections we have obtained designs that exhibits a high coupling and also permits the propagation of the fluid. It is however observed that the microstructure consist of unconnected layers of solid material which prohibits that forces can be transferred through the structure. From a macroscopic viewpoint the actuator will deflect during pressure loading but due to the lack of stiffness no forces can be transferred hence the actuator will not work as intended.

In order to ensure a certain degree of stiffness θ a set of constraints are added to the optimization problem. They take the form

$$g_i = -\frac{E_i^{dir}}{\theta E_0} - 1 \leq 0 \quad \text{for } i = 1 \ldots 3 \tag{27}$$

where E_i^{dir} is the directional stiffness in direction i and E_0 is the stiffness of the base material.

In order to impose such constraints the stiffness matrix $\mathbf{E}$ must be evaluated at every design iteration by solving (9) and evaluating (15) as the directional stiffness according to Jones (1999) is defined as

$$E_i^{dir} = \frac{1}{S_{ii}} \quad \text{for } i = 1 \ldots 3 \tag{28}$$

where $\mathbf{S} = \mathbf{E}^{-1}$ is the compliance matrix. The physical interpretation of the compliance matrix is that every column j holds the strains to a corresponding unit stress load in direction j. Having defined the constraint, the sensitivities are also needed. The sensitivities of the stiffness matrix is derived in Appendix A.1 and can be computed based on the state solution, they yield

$$\frac{\mathrm{d}E_{ij}}{\mathrm{d}\rho} = \sum_{l=1}^{6}\sum_{p=1}^{6}\int_\Omega \left[\frac{\mathrm{d}E_{ij}}{\mathrm{d}\rho} - \frac{\mathrm{d}E_{il}}{\mathrm{d}\rho}\varepsilon_l(\mathbf{u}^j) - \frac{\mathrm{d}E_{pj}}{\mathrm{d}\rho}\varepsilon_p(\mathbf{u}^i) + \varepsilon_p\frac{\mathrm{d}E_{pl}}{\mathrm{d}\rho}\varepsilon_l(\mathbf{u}^j)\right]\mathrm{d}\Omega \tag{29}$$

In order to find the sensitivities of the constraint each directional stress-strain relation is differentiated with respect to the design variables (the unit stress load is design independent)

$$\frac{\mathrm{d}\mathbf{E}}{\mathrm{d}\rho}\varepsilon^j + \mathbf{E}\frac{\mathrm{d}\varepsilon^j}{\mathrm{d}\rho} = 0 \Rightarrow \frac{\mathrm{d}\varepsilon^j}{\mathrm{d}\rho} = \mathbf{E}^{-1}\frac{\mathrm{d}\mathbf{E}}{\mathrm{d}\rho}\varepsilon^j \tag{30}$$

Since ε^j corresponds to column j of $\mathbf{S}$ the final sensitivities can be computed using the chain rule as

$$\frac{\mathrm{d}g_i}{\mathrm{d}\rho} = \frac{1}{\theta E_0 S_{ii}^2}\frac{\mathrm{d}\varepsilon_i^i}{\mathrm{d}\rho} = \frac{1}{\theta E_0 S_{ii}^2}\left(\mathbf{E}^{-1}\frac{\mathrm{d}\mathbf{E}}{\mathrm{d}\rho}\varepsilon^i\right)_i \quad \text{for } i = 1 \ldots 3. \tag{31}$$

When the stiffness constraints are imposed the structure changes such that the opposing sides are connected by solid material. This can be seen in Fig. 9 where a 10% stiffness constraint has been added in each direction. The pressure coupling tensor yields

$$\boldsymbol{\alpha} = \begin{bmatrix} 0.7580 & 0.0713 & 0.0713 \\ & 0.7580 & 0.0712 \\ \text{sym} & & 0.7580 \end{bmatrix} \tag{32}$$

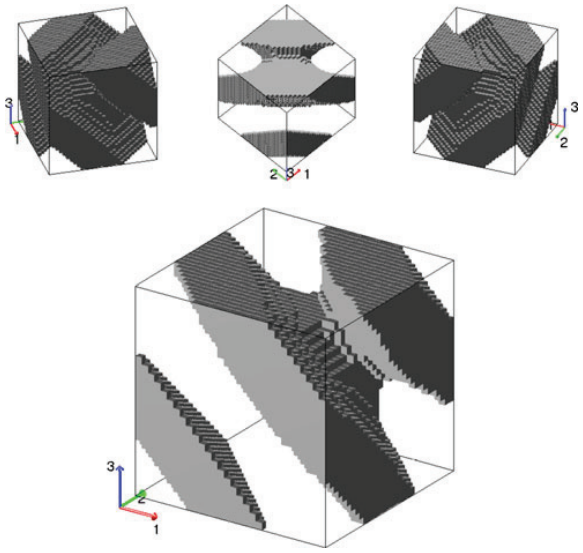

Fig. 9 Optimized microstructure with at least 10% stiffness ($\theta = 0.1$) in each coordinate direction and 50% solid volume fraction ($\gamma = 0.5$). $\Phi = 0.2138$

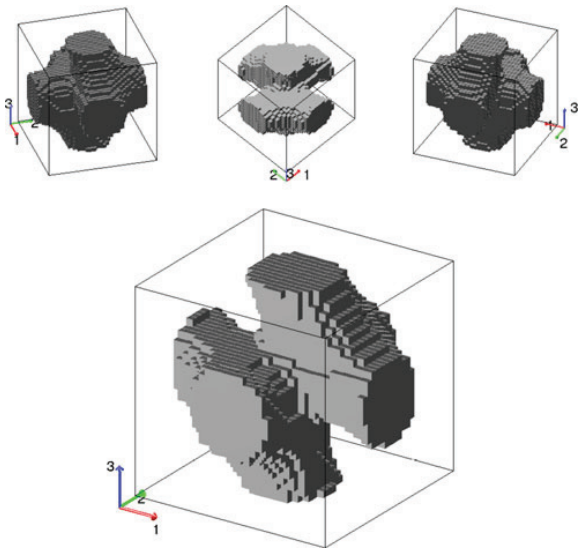

Fig. 10 Topology for optimized pressure shear coupling when imposing constraints both on the stiffness (10% of base material) and on the permeability (reference structure is a cross with side width 0.4 $\Rightarrow$ $\kappa_{\text{ref}} = 0.0056$). $\Phi = 0.0479$

and the shear coupling terms are slightly lower than without stiffness constraints as some material is used for connecting opposing sides.

3.4 Optimizing using both permeability and stiffness constraints

In order to ensure a certain degree of permeability and stiffness both types of constraints can be added. This, however, limits the design freedom. In Fig. 10 the optimized microstructure having at least the permeability of a square cross-sectioned microstructure with side length 0.4 is considered. Furthermore the stiffness needs to be at least 10% of the basis material. The effective parameters yield

$$\boldsymbol{\alpha} = \begin{bmatrix} 0.8979 & 0.0157 & 0.0157 \\ & 0.8974 & 0.0165 \\ \text{sym} & & 0.8974 \end{bmatrix}$$

$$\mathbf{E} = \begin{bmatrix} 0.1322 & 0.0240 & 0.0241 & -0.0003 & -0.0197 & -0.0197 \\ & 0.1325 & 0.0251 & -0.0206 & -0.0002 & -0.0193 \\ & & 0.1324 & -0.0205 & -0.0193 & -0.0002 \\ & & & 0.0271 & 0.0016 & 0.0016 \\ & & & & 0.0266 & 0.0017 \\ \text{sym} & & & & & 0.0266 \end{bmatrix} E_0$$

$$\beta = 0.6671/K_s$$

$$\mathbf{K} = \begin{bmatrix} 0.0056 & -0.0001 & -0.0001 \\ & 0.0056 & -0.0002 \\ \text{sym} & & 0.0056 \end{bmatrix} m^2$$

and it is seen that the pressure coupling is not even as strong as in the not so constrained design with 30% solid material shown in Fig. 3a, but the constraints ensure that the layers are connected and that the fluid can propagate in the material.

The microstructure looks almost like a cross but a cavity is present in the structure such that the inclined cavity walls can transfer the load from the fluid pressure to shear stress. A better impression of the resulting microstructure is obtained in Fig. 11 where a super-cell repeating $3 \times 3 \times 3$ unit-cells is shown.

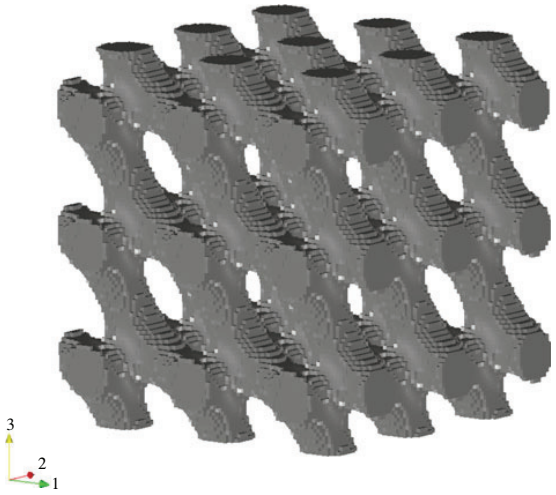

Fig. 11 Super-cell containing $3 \times 3 \times 3$ unit-cells of the optimized material. The connection among the cells is clear and the inclined planes for converting pressure to shear stress are also visible

3.5 Optimizing the pressure shear coupling in one direction

By optimizing the pressure-shear coupling in only one direction (α_{23}) it is possible to generate a microstructure that makes the slab cross section distort. As the microstructure should be stable in terms of not having unconnected layers a set of stiffness constraints are imposed ensuring 10% of the basis material stiffness. Furthermore a permeability constraint is imposed in the 1-direction in order to ensure sufficient flow. Leaving the permeability constraint out does not close the microstructure but stiffeners clearly limit the fluid flow.

The topology obtained without these constraints are an inclined plane with normal $n = (0\,1\,1)$. By imposing the constraints a connection is added between the inclined planes as seen in Fig. 12. This yields a design that has similarities with an inclined I-profile beam, but as the unit cell is repeated in order to get the resulting microstructure it looks totally different, a solid with oval fluid pipes which can be seen in the plot of the super-cell in Fig. 13. The resulting effective parameters are

$$\boldsymbol{\alpha} = \begin{bmatrix} 0.6983 & -0.0000 & 0.0000 \\ & 0.8076 & 0.0802 \\ \text{sym} & & 0.8076 \end{bmatrix}$$

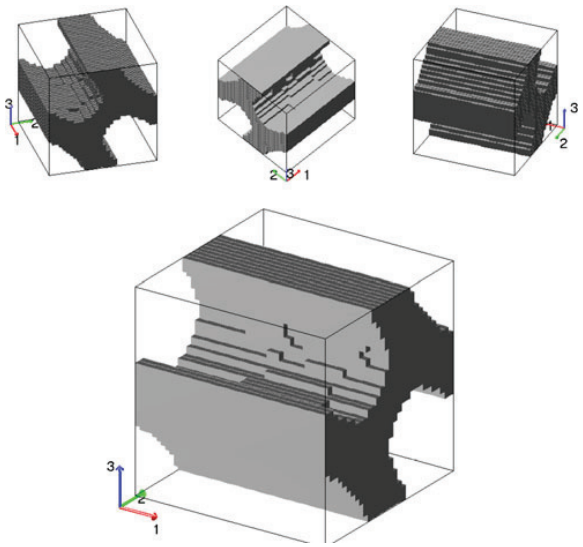

Fig. 12 Optimized topology for maximum coupling between pressure and shear stress in the 23-plane. Stiffness constraints ensuring at least 10% stiffness in the three reference directions are imposed. $\Phi = \max(\alpha_{23}) = 0.0802$, $\gamma = 0.5$

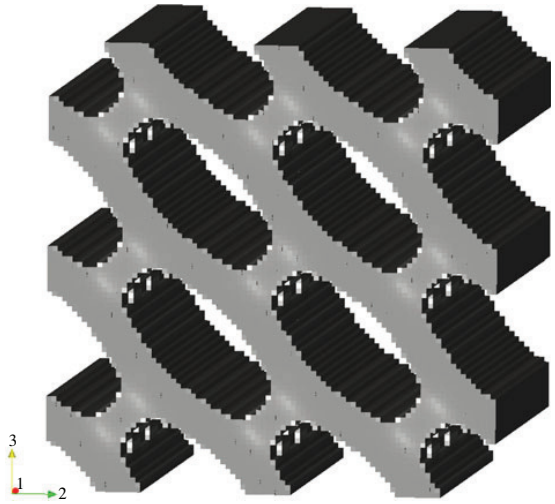

Fig. 13 Super-cell containing $3 \times 3 \times 3$ unit-cells of the optimized α_{23} material

$$E = \begin{bmatrix} 0.4805 & 0.0887 & 0.0887 & -0.0463 & 0.0000 & 0.0000 \\ & 0.1916 & 0.1043 & -0.0771 & 0.0000 & 0.0000 \\ & & 0.1916 & -0.0771 & -0.0000 & -0.0000 \\ & & & 0.0736 & -0.0000 & 0.0000 \\ & & & & 0.0990 & -0.0391 \\ \text{sym} & & & & & 0.0990 \end{bmatrix} E_0$$

$$\beta = 0.7128/K_s$$

$$K = \begin{bmatrix} 0.0056 & 0.0000 & 0.0000 \\ & 0.0004 & -0.0002 \\ \text{sym} & & 0.0004 \end{bmatrix} m^2$$

Comparing the α_{23} term with the previous designs even though they are obtained under other conditions, it is seen that the pressure-shear coupling is higher.

4 Macroscopic evaluation

In this section the optimized materials will be used in the modeling of an actuator based on the porous slab shown in Fig. 1. This is done using a steady-state model in the framework of COMSOL 3.5 and Matlab 2008b as only the final equilibrium state is investigated. The slab is discretized using trilinear hexahedral elements and the problem is solved using COMSOL's Pardiso implementation. The slab is constrained such that the boundaries of the small inlet domain to the left cannot move ($u_i = 0$) and is loaded by a fluid pressure $p = 1$ MPa on the left face. The unit cell size is set to 5 mm and the base material is isotropic with the elastic modulus $E_0 = 0.1$ GPa, Poisson's ratio $\nu = 0.3$ and fluid viscosity $\mu = 1$ Pa·s. The material in the left domain is isotropic with an elastic modulus of $0.2E_0$,

isotropic permeability $\kappa = 0.01$ and isotropic coupling tensor $\alpha = 1$. The resulting overall deformations using both the 3-direction (Fig. 10) and the single-direction pressure-shear coupling material (Fig. 12) can be seen in Fig. 14.

For the first material the pressure loading results in a deflection and an elongation of the slab. Furthermore the cross-section also distort slightly as it can be seen in Fig. 15a. This accommodates the idea of making an actuator for use in e.g. a linear motor. Such actuators must extend and deflect such that they can move the axle.

The second material behaves differently when subjected to the internal fluid pressure as it only couples to the transversal shear stresses. The shape of the slab is changed such that the cross section gets rhombic which can also be observed in Fig. 15b. In comparison to the previous example the actuation is a shape-change rather than a deflection.

In Table 1 the most important properties of the materials designed throughout the paper have been listed along with the resulting maximum cross-section deflection from

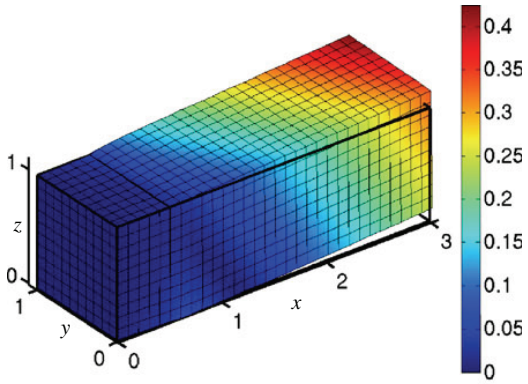

(a) Material: $max(\alpha_{12}+\alpha_{13}+\alpha_{23})$

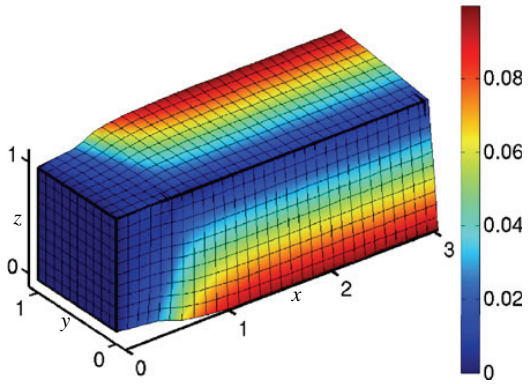

(b) Material: $max(\alpha_{23})$

Fig. 14 Deformed macro structure colored by cross section deformation ($\sqrt{u_2^2+u_3^2}$). The loading of the two columns are the same, but the microstructure differ. *Top* is the maximized shear $\boldsymbol{\alpha}$ microstructure and the *below* is the maximized α_{23} material

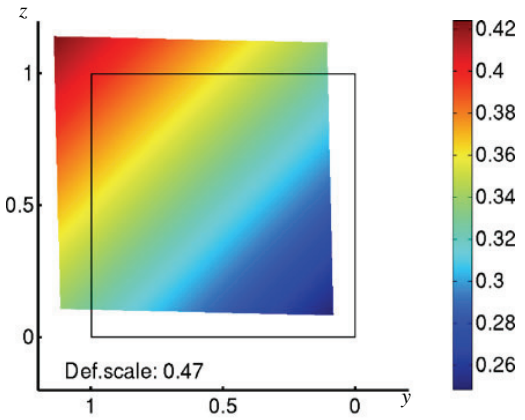

(a) $max(\alpha_{12}+\alpha_{13}+\alpha_{23})$

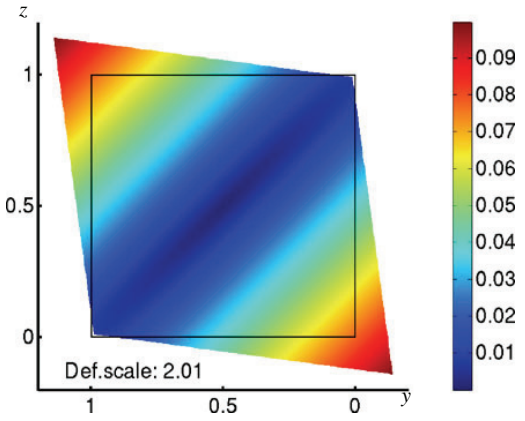

(b) $max(\alpha_{23})$

Fig. 15 The deformation of the rightmost face at $x = 2.5$ in Fig. 1 and colored by cross section deformation ($\sqrt{u_2^2+u_3^2}$). *Top* The maximized shear $\boldsymbol{\alpha}$ microstructure makes the slab end translate. *Bottom* The maximized α_{23} microstructure makes the slab end distort

the macroscopic model. It is seen that the deflections for the first designs without any stiffness constraints are large, especially for the case with the permeability constraint where the stiffness is low. With imposed stiffness constraints the deflection decreased but the micro-structure got connected which ensured stability due to structure and not modeling artifacts. From the table it can also be observed that as the design gets more constrained, the pressure coupling also gets lower which of course is inflicting the final deformation.

5 Discussion and conclusion

In this paper we show that it is possible to generate saturated poroelastic actuators by altering the internal microstructure

Table 1 Comparison of results including additional stiffness and permeability information for some cases

Figure	γ	vf	α_{11}	α_{23}	K_{11} (10^{-3} m^2)	K_{12} (10^{-3} m^2)	E_1^{dir}	E_2^{dir}	E_3^{dir}	$\max(\sqrt{u_2^2+u_3^2})$ (m)
3a	0.3	0.30	0.8607	0.0494	2.7226	−1.2089	0.001725	0.001725	0.001725	11.4
3b	0.5	0.50	0.7828	0.0870	0.9930	−0.4291	0.003607	0.003607	0.003607	6.28
5a	1.0	0.81	0.6463	0.1386	0.0435	−0.0105	0.020595	0.020595	0.020595	1.54
5b	1.0	0.86	0.6381	0.1519	0.0249	−0.0067	0.023184	0.023184	0.023183	1.38
8	0.5	0.19	0.9421	0.0163	11.515	−2.2108	0.000237	0.000237	0.000237	92.1
9	0.5	0.50	0.7580	0.0712	1.077	−0.4662	0.105785	0.105780	0.105802	0.489
10	0.5	0.32	0.8979	0.0165	5.5939	−0.1440	0.102063	0.102046	0.102058	0.424
12	0.5	0.47	0.6963	0.0802	5.5937	0	0.427325	0.103550	0.103568	0.0997

γ is the maximum solid volume fraction whereas vf denotes the obtained. The last column shows the largest cross-section deformation for the slab using the current material. The permeabilities are unscaled i.e. unit-cell size 1 m^3

using the topology optimization method. There are however some issues that needs some attention. One is the computation of effective parameters which is based on a periodic media assumption. The boundary of the structure is not fulfilling this condition so the representation of the physics at the boundary might be poor and would deviate from experimental observations. The influence from this is considered to be small as the dimensions of the structure is much larger than the unit cell size hence the error will be very local.

The obtained macroscopic deformations depend heavily on the constitutive parameters for the base material as the pressure induced deformations are more pronounced when the elastic material is weak.

The realization of the resulting porous structure might be difficult using traditional foam generating techniques where a chemical reaction generates the foam and thereby the microstructure. The popularity of additive manufacturing techniques is increasing and it might be a suitable process for the generation of these optimized materials.

This paper shows that by optimizing the microstructure of a periodic poroelastic material the macroscopic behavior can be changed such that adaptive structures can be generated, here exemplified by fluid pressure induced actuators.

Acknowledgments This research was conducted within the DCAMM Research School through a grant from the Danish Agency for Science, Technology and Innovation. The authors would like to thank the TopOpt research group (www.topopt.dtu.dk) for fruitful discussions.

Appendix A: Adjoint sensitivity analysis

The Lagrangian $\mathcal{L}$ is formed by adding the adjoint variable multiplied by the residual (= 0) to the objective function, Φ:

$$\mathcal{L} = \Phi(\mathbf{u}, \rho) + \boldsymbol{\lambda}^T R(\mathbf{u}, \rho) \tag{33}$$

The derivative of the Lagrangian is obtained using the chain rule

$$\begin{aligned}\frac{\mathrm{d}\mathcal{L}}{\mathrm{d}\rho} =& \frac{\partial \mathcal{L}}{\partial \rho} + \frac{\partial \mathcal{L}}{\partial \mathbf{u}}\frac{\mathrm{d}\mathbf{u}}{\mathrm{d}\rho} \\ =& \frac{\partial \Phi(\mathbf{u}, \rho)}{\partial \rho} + \frac{\partial \Phi(\mathbf{u}, \rho)}{\partial \mathbf{u}}\frac{\mathrm{d}\mathbf{u}}{\mathrm{d}\rho} \\ &+ \boldsymbol{\lambda}^T \frac{\partial R(\mathbf{u}, \rho)}{\partial \rho} + \boldsymbol{\lambda}^T \frac{\partial R(\mathbf{u}, \rho)}{\partial \mathbf{u}}\frac{\mathrm{d}\mathbf{u}}{\mathrm{d}\rho}\end{aligned} \tag{34}$$

rearranging and splitting yields: Find $\boldsymbol{\lambda}$ such that

$$\boldsymbol{\lambda}^T \frac{\partial R(\mathbf{u}, \rho)}{\partial \mathbf{u}}\frac{\mathrm{d}\mathbf{u}}{\mathrm{d}\rho} + \frac{\partial \Phi(\mathbf{u}, \rho)}{\partial \mathbf{u}}\frac{\mathrm{d}\mathbf{u}}{\mathrm{d}\rho} = 0 \tag{35}$$

and the sensitivities can be evaluated by computing

$$\frac{\mathrm{d}\mathcal{L}}{\mathrm{d}\rho} = \frac{\partial \Phi(\mathbf{u}, \rho)}{\partial \rho} + \boldsymbol{\lambda}^T \frac{\partial R(\mathbf{u}, \rho)}{\partial \rho} \tag{36}$$

This leads to the following adjoint problem for the objective function:

Find $\lambda_i \in \mathcal{V}$ for all $\hat{\lambda}_i \in \mathcal{V}_0$ such that

$$\int E_{ijlm}\varepsilon_{ij}(\boldsymbol{\lambda})\varepsilon_{lm}(\hat{\boldsymbol{\lambda}})\mathrm{d}\Omega = -\int \frac{1}{2}(1-\delta_{ij})E_{ijlm}\varepsilon_{lm}(\hat{\boldsymbol{\lambda}})\mathrm{d}\Omega \tag{37}$$

where the solution is used for the evaluation of the sensitivities

$$\begin{aligned}\frac{\mathrm{d}\Phi}{\mathrm{d}\rho} = \int \Bigg[&\frac{1}{2}(1-\delta_{ij})E'_{ijlm}\varepsilon_{lm}(\mathbf{u}) + \delta_{ij}\varepsilon_{ij}(\boldsymbol{\lambda})\frac{E'}{E_0} \\ &- \varepsilon_{ij}(\boldsymbol{\lambda})E_{ijlm}\varepsilon_{lm}(\mathbf{u})\Bigg]\mathrm{d}\Omega\end{aligned} \tag{38}$$

A.1 Stiffness constraints

The stiffness constraints are related to the problem above as the equation system is the same except for the loading that changes according to the direction considered. The stiffness tensor entries are computed as

$$E_{ijkh} = E_{ijkh} - E_{ijlm}\varepsilon_{lm}(\mathbf{u}^{kh}) \tag{39}$$

and the sensitivities of the entries can be derived using the adjoint method.

$$\begin{aligned}
R_{ijkh} &= \int_\Omega \varepsilon_{pq}(\boldsymbol{\lambda}^{ij}) E_{pqkh}\mathrm{d}\Omega \\
&\quad - \int_\Omega \varepsilon_{pq}(\boldsymbol{\lambda}^{ij}) E_{pqlm}\varepsilon_{lm}(\mathbf{u}^{kh})\mathrm{d}\Omega \\
\frac{\partial R_{ijkh}}{\partial \rho} &= \int_\Omega \varepsilon_{pq}(\boldsymbol{\lambda}^{ij}) E'_{pqkh}\mathrm{d}\Omega \\
&\quad - \int_\Omega \varepsilon_{pq}(\boldsymbol{\lambda}^{ij}) E'_{pqlm}\varepsilon_{lm}(\mathbf{u}^{kh})\mathrm{d}\Omega \\
\frac{\partial E_{ijkh}}{\partial \rho} &= \int_\Omega E'_{ijkh} - E'_{ijlm}\varepsilon_{lm}(\mathbf{u}^{kh})\mathrm{d}\Omega \\
\frac{\partial R_{ijkh}}{\partial \mathbf{u}}\frac{\mathrm{d}\mathbf{u}}{\mathrm{d}\rho} &= -\int_\Omega \varepsilon_{pq}(\boldsymbol{\lambda}^{ij}) E_{pqlm}\varepsilon'_{lm}(\mathbf{u}^{kh})\mathrm{d}\Omega \\
\frac{\partial E_{ijkh}}{\partial \mathbf{u}}\frac{\mathrm{d}\mathbf{u}}{\mathrm{d}\rho} &= -\int_\Omega E_{ijlm}\varepsilon'_{lm}(\mathbf{u}^{kh})\mathrm{d}\Omega
\end{aligned}$$

which yields the following adjoint problem

$$-\int_\Omega \varepsilon_{pq}(\boldsymbol{\lambda}^{ij}) E_{pqlm}\varepsilon'_{lm}(\mathbf{u}^{kh})\mathrm{d}\Omega - \int_\Omega E_{ijlm}\varepsilon'_{lm}(\mathbf{u}^{kh})\mathrm{d}\Omega = 0 \tag{40}$$

$$\Rightarrow \int_\Omega \varepsilon_{pq}(\boldsymbol{\lambda}^{ij}) E_{pqlm}\varepsilon_{lm}(\hat{\boldsymbol{\lambda}})\mathrm{d}\Omega = -\int_\Omega E_{ijlm}\varepsilon_{lm}(\hat{\boldsymbol{\lambda}})\mathrm{d}\Omega \tag{41}$$

which due to the symmetry of $\mathbf{E}$ is equivalent to the original problem but with opposing sign and hence the sensitivities can be computed from the original solution as

$$\begin{aligned}
\frac{\mathrm{d}E_{ijkh}}{\mathrm{d}\rho} = \int_\Omega \Big[& E'_{ijkh} - E'_{ijlm}\varepsilon_{lm}(\mathbf{u}^{kh}) \\
& + \varepsilon_{pq}(\mathbf{u}^{ij}) E'_{pqlm}\varepsilon_{lm}(\mathbf{u}^{kh}) \\
& - E'_{pqkh}\varepsilon_{pq}(\mathbf{u}^{ij}) \Big]\mathrm{d}\Omega
\end{aligned} \tag{42}$$

A.2 Permeability constraints

For each constraint based on the normal permeability ($i = k$),

$$K_{ik} = \frac{1}{|\Omega|}\int_\Omega v_i^k \mathrm{d}\Omega \tag{43}$$

the sensitivity needs to be computed. The derivation is as follows. Forming the residual

$$\begin{aligned}
R(\hat{\mathbf{v}}, \mathbf{v}^k, \rho) = & -\int_\Omega \hat{v}_{i,j} v^k_{i,j}\mathrm{d}\Omega - \int_\Omega \zeta(\rho) v_i^k \hat{v}_i \mathrm{d}\Omega \\
& + \int_\Omega \hat{v}_{i,i}\, p\mathrm{d}\Omega + \int_\Omega \hat{v}_i \delta_{ik}\mathrm{d}\Omega - \int_\Omega \hat{p} v^k_{i,i}\mathrm{d}\Omega
\end{aligned} \tag{44}$$

Then forming the derivative of the Lagrangian

$$\begin{aligned}
\frac{\mathrm{d}\mathcal{L}}{\mathrm{d}\rho} = & \frac{\partial K(\mathbf{v})}{\partial \mathbf{v}}\frac{\mathrm{d}\mathbf{v}}{\mathrm{d}\rho} + \frac{\partial R(\boldsymbol{\lambda}, \mathbf{v}, \rho)}{\partial \rho} \\
& + \frac{\partial R(\boldsymbol{\lambda}, \mathbf{v}, \rho)}{\partial \mathbf{v}}\frac{\mathrm{d}\mathbf{v}}{\mathrm{d}\rho} + \frac{\partial R(\boldsymbol{\lambda}, \mathbf{v}, \rho)}{\partial p}\frac{\mathrm{d}p}{\mathrm{d}\rho}
\end{aligned} \tag{45}$$

which leads to the following adjoint problem

Find $\lambda_i^k \in \mathcal{V}$ and $p^k \in \mathcal{Q}$ such that $\hat{\lambda} \in \mathcal{V}_0$ and $\hat{p} \in \mathcal{Q}$

$$\begin{aligned}
& -\int_\Omega \lambda^k_{i,j}\hat{\lambda}_{i,j}\mathrm{d}\Omega - \int_\Omega \zeta(\rho)\hat{\lambda}_i\lambda_i^k\mathrm{d}\Omega - \int_\Omega \lambda^k_{i,i}\, p\mathrm{d}\Omega \\
& \qquad + \int_\Omega \lambda_i^k \mathrm{d}\Omega + \int_\Omega p\hat{\lambda}_{i,i}\mathrm{d}\Omega = 0
\end{aligned} \tag{46}$$

which is seen to be equivalent to the state problem when $i = k$ and $\lambda_i = v_i$. Hence the sensitivities can be computed by evaluating

$$\frac{\mathrm{d}K_{ik}(\mathbf{v})}{\mathrm{d}\rho} = -\frac{\mathrm{d}\zeta(\rho)}{\mathrm{d}\rho} v_i^k v_i^k \tag{47}$$

but only for $i = k$.

References

Auriault JL, Boutin C, Geindreau C (2009) Homogenization of coupled phenomena in heterogeneous media. ISTE Ltd and Wiley

Auriault JL, Sanchez-Palencia E (1977) Study of macroscopic behavior of a deformable saturated porous-medium. J Méc 16(4):575–603

Bensoussan A, Lions J, Papanicolaou G (1978) Asymptotic analysis for periodic structures. North-Holland, Amsterdam

Biot MA (1941) General theory of three-dimensional consolidation. J Appl Phys 12(2):155–164

Biot MA (1955) Theory of elasticity and consolidation for a porous anisotropic solid. J Appl Phys 26(2):182–185

Biot MA (1956) Theory of propagation of elastic waves in a fluid-saturated porous solid. I. Low-frequency range. J Acoust Soc Am 28(2):168–178

Borrvall T, Petersson J (2003) Topology optimization of fluids in Stokes flow. Int J Numer Methods Fluids 41(1):77–107

Bourdin B (2001) Filters in topology optimization. Int J Numer Methods Eng 50:2143–2158

Bruns T, Tortorelli D (2001) Topology optimization of non-linear elastic structures and compliant mechanisms. Comput Methods Appl Mech Eng 190:3443–3459

de Boer R, Ehlers W (1988) A historical review of the formulation of porous media theories. Acta Mech 74(1):1–8

Fillunger P (1913) Der auftrieb in talsperren. Österr. Wochenzeitschrift für den öffentl. Baudienst., vols I, II, III, pp 532–552, 522–556, 567–570

Guest JK, Prévost JH (2006) Optimizing multifunctional materials: design of microstructures for maximized stiffness and fluid permeability. Int J Solids Struct 43(22–23):7028–7047

Guest JK, Prévost JH (2007) Design of maximum permeability material structures. Comput Methods Appl Mech Eng 196(4–6):1006–1017

Hughes TJR, Franca LP (1987) A new finite element formulation for computational fluid dynamics: VII. The Stokes problem with various well-posed boundary conditions: symmetric formulations that converge for all velocity/pressure spaces. Comput Methods Appl Mech Eng 65(1):85–96

Jones R (1999) Mechanics of composite materials, 2nd edn. Taylor & Francis, New York

Kreissl S, Pingen G, Evgrafov A, Maute K (2010) Topology optimization of flexible micro-fluidic devices. Struct Multidiscipl Optim 42:495–516. doi:10.1007/s00158-010-0526-6

Lydzba D, Shao JF (2000) Study of poroelasticity material coefficients as response of microstructure. Mech Cohes-Frict Mater 5(2):149–171

Maute K, Allen M (2004) Conceptual design of aeroelastic structures by topology optimization. Struct Multidiscipl Optim 27:27–42. doi:10.1007/s00158-003-0362-z

Sanchez-Palencia E (1980) Non-homogeneous media and vibration theory. In: Lecture notes in physics, vol 127. Springer, Berlin

Schanz M, Diebels S (2003) A comparative study of Biot's theory and the linear theory of porous media for wave propagation problems. Acta Mech 161(3):213–235

Sigmund O (1994) Materials with prescribed constitutive parameters: an inverse homogenization problem. Int J Solids Struct 31(17):2313–2329

Sigmund O (1999) On the optimality of bone microstructure. In: Pedersen P, Bendsøe M (eds) Synthesis in bio solid mechanics. Kluwer, IUTAM, pp 221–234

Sigmund O (2000) A new class of extremal composites. J Mech Phys Solids 48(2):397–428

Sigmund O, Torquato S (1996) Composites with extremal thermal expansion coefficients. Appl Phys Lett 69(21):3203–3205

Sigmund O, Torquato S (1997) Design of materials with extreme thermal expansion using a three-phase topology optimization method. J Mech Phys Solids 45(6):1037–1067

Sigmund O, Torquato S, Aksay IA (1998) On the design of 1–3 piezocomposites using topology optimization. J Mater Res 13(4):1038–1048

Stolpe M, Svanberg K (2001) An alternative interpolation scheme for minimum compliance topology optimization. Struct Multidisc Optim 22(2):116–124

Svanberg K (1987) The method of moving asymptotes—a new method for structural optimization. Int J Numer Methods Eng 24(2):359–373

Torquato S, Hyun S, Donev A (2002) Multifunctional composites: optimizing microstructures for simultaneous transport of heat and electricity. Phys Rev Lett 89(26):266601

von Terzaghi K (1923) Die Berechnung der Durchlässigkeit des Tones aus dem Verlauf der hydromechanischen Spannungserscheinungen. Sitzungsber Akad Wiss Wien, Math-Naturwiss Kl 132(3–4):125–138

Xu S, Cheng G (2010) Optimum material design of minimum structural compliance under seepage constraint. Struct Multidisc Optim 41(4):575–587

Yoon GH (2010) Topology optimization for stationary fluid-structure interaction problems using a new monolithic formulation. Int J Numer Methods Eng 82(5):591–616

Publication [P2]

Multiscale optimization of poroelastic actuators

Multiscale optimization of poroelastic actuators

C.S. Andreasen, O. Sigmund

Department for Mechanical Engineering, Solid Mechanics, Technical University of Denmark, Building 404, 2800 Kgs. Lyngby, Denmark

E-mail: csan@mek.dtu.dk

Abstract. This paper presents a method to design optimized poroelastic materials which under internal pressurization turn into actuators for application in e.g. linear motors. It elaborates on the two scale asymptotic expansion of the fluid-structure interaction problem. The actuator is modeled in a two scale approach where the material microstructure is optimized using topology optimization in order to achieve a better macroscopic performance quantified by the transversal deflection. Constraints are introduced to ensure a certain deflection / extension ratio of the actuator.

1. Introduction

Poroelasticity mostly applied in the field of earth mechanics might also be used in the modeling and design of smart saturated porous structures. This could for instance be a pressure driven linear motor in which the actuators are composed of sealed saturated poroelastic materials. Ordinary random structured poroelasic materials such as foams usually swell equally in all directions when pressurized. By designing the microstructure it is possible to make the structure deflect in a prescribed manner like e.g. bending or twisting. This could be of use in e.g. a linear motor. Usually linear motors for use in e.g. atomic force microscopes use piezo eletric actuators, however in a non-electronics environment the use of poroelastic actuators driven by a pressure change might be an alternative.

An illustration of the working principle in a linear motor is shown in figure 1. The linear motor is based on a bi-morph actuator and works in a sequence of four steps. At first the actuator is at rest. Then one of the materials elongate which makes it bend and grip the rod. The other material starts to elongate while the first starts to retract, this moves the rod sideways. Finally the second material is elongated and the rod has been moved.

In Andreasen & Sigmund (2011) the microstructure of saturated poroelastic materials were optimized with respect to the pressure coupling. The obtained material designs made an actuator deflect when pressurized but no direct aims were taken towards maximizing the macroscopic deflection. However to maximize the macroscopic deflection a multiscale approach should be applied as the deflection will not depend on the pressure

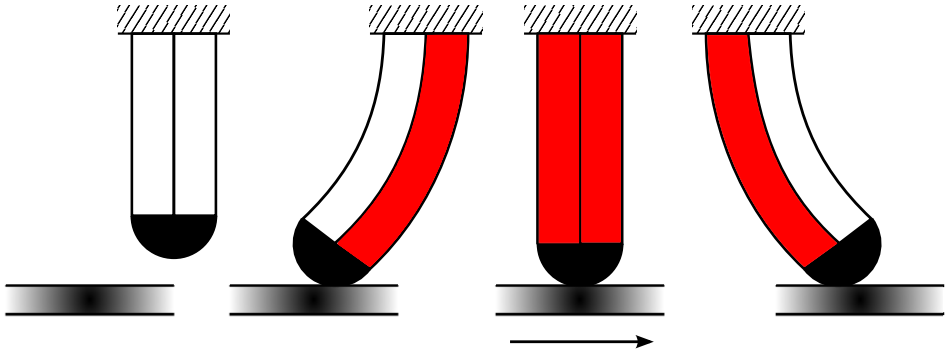

Figure 1. Working principle of a linear motor based on a bi-morph actuator. Step 1: Actuator is unloaded. Step 2: The right material elongates and *grips* the rod. Step 3: The left material elongates increasingly while the right material retracts which makes the rod move. Step 4: The left material is now elongated alone.

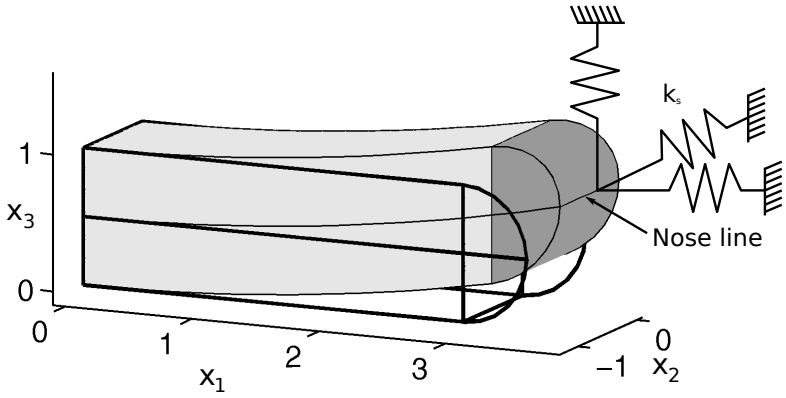

Figure 2. Actuator problem; two individually sealed porous slabs (light grey) assembled with a half cylinder of a stiffer elastic material (dark). Initial and deformed geometry shown. Line springs are attached to the nose line of the actuator.

coupling alone. The stiffness of the structure and the material layup will have a large influence on the performance of the poroelastic actuator as well. This paper therefore presents the theory and application for multiscale modeling of poroelastic actuators along with the optimization of periodic poroelastic materials.

A simple sketch of the problem is shown in figure 2. The actuator consists of two aligned and individually sealed slabs of porous material which are assembled with a stiff half cylinder of elastic material at the right face and fixed at the left. The individual sealing of the two porous materials allow each of them to be individually pressurized. Using an isotropic poroelastic material the actuator is actually working, however the performance can be significantly improved by altering the material microstructure.

Multi-scale modeling is a common technique within the field of computational mechanics. By assuming that a representative volume element (RVE) can be defined, small material scale details can be included in the computation which would otherwise be impossible to resolve.

The methods can be applied to both elastic and inelastic problems and there

are several approaches to multiscala modeling. This work has its basis in the asymptotic expansion of the fluid-structure interaction problem (Auriault & Sanchez-Palencia 1977, Sanchez-Palencia 1980, Auriault et al. 2009). Aspects of the numerical implementation of the homogenization for porous elastic and internally pressurized composites were described in Guedes & Kikuchi (1990). Terada et al. (1998) gives insight in both the asymptotic expansion of the solid-fluid mixture problem as well as the implementation. Both a diphasic macroscopic model (poro-elasticity, Biot type) and a monophasic viscoelastic model is treated therein.

Multi-scale topology optimization is an evolving area in which not only a material distribution problem is optimized but also the material design. This is also the concept in the seminal paper on topology optimization (Bendsøe & Kikuchi 1988) where the homogenization approach to topology optimization is presented. By varying the size of the members in a fixed topology microstructure, interpolation functions were obtained for use in the macroscopic distribution problem. This is in contrast to most applications of topology optimization where an interpolation scheme (Bendsøe 1989) is imposed to avoid microstructural considerations.

Elaborating further on this homogenization approach to topology optimization a natural extension is the hierahical optimization of heterogenous porous materials meaning a simultaneous optimization of material distribution and material design. Rodrigues et al. (2002) introduces a framework in which the multiple scale designs can be handled. One macroscale and multiple microscale problems are solved iteratively. The methodology was applied to bone remodelling in Coelho et al. (2008) and Coelho et al. (2009). A slightly different approach using interpolation schemes at both the macro and the micro scale were introduced in Liu et al. (2008) for compliance optimization and Nui et al. (2008) for frequency optimization. A two scale method for optimizing the structural compliance by material design and subjected to a seepage constraint was presented by Xu & Cheng (2010).

Free material optimization (FMO) introduced in Bendsøe et al. (1994) is another approach to multiscale optimization as it is distribution of material parameters rather than densities allowing for anisotropic materials. However the method itself does not consider the material designs or composite layups that are needed.

In fluid mechanics topology optimization was applied to Stokes flow problems in Borrvall & Petersson (2003) and extended to Navier-Stokes flow in Gersborg-Hansen et al. (2005) using a Brinkman term which introduce an infinitely stiff solid material. The application of topology optimization to fluid structure interaction problems has only recently been approached. Yoon (2010) presents a method for converting the interface stresses to a volume integral which is suited for a monolithic formulation. Kreissl et al. (2010) presents a one way coupling used for the design of flexible micro-fluidic devices.

The fluid-structure interaction is in the present method handled by the homogenization of the Stokes flow in the microstructure which results in a pressure coupling at the macro scale. The multiscale approach taken in this paper deals alone with the material optimization in two predefined subdomains using a macroscopic

objective function.

The paper is organized such that first an introduction to the model and optimization method is given in section 2. The theory on the two scale expansion of the fluid-structure interaction problem is explained in section 3 presenting the state equations. In section 4 the optimization problem is introduced along with the interpolation functions needed for applying topology optimization to the microstructure design. Section 5 presents the numerical implementation and the results are presented in section 6. Finally the findings are concluded in section 7.

2. Mechanical model and optimization problem

The approach taken in this paper towards the optimization of a bi-morph pressure driven actuator restricts itself to the design of two porous materials used in the two slabs as illustrated in figure 2.

The operation of the actuator is of course transient, however to simplify the optimization procedure we shall limit the optimization to consider two load cases and assume that the transient response due to e.g. internal flow is negligible such that the general motion can be represented by a superposition of the two load cases.

This means that we will consider the quasi-static equations of motion meaning that any inertia and any convection in the fluid will be neglected. Furthermore the pressure will be prescribed in the domains mimicking a steady state solution. By this all description of fluid motion can be neglected and only the formulation regarding the solid deformation needs to be considered.

The objective for this optimization is to maximize the deflection of the actuator subject to the two loads. When optimizing an actuator it is important to ensure that it actually applies a force at the contact point. This can be ensured by attaching a set of springs at the end of the actuator also shown in the illustration. The spring stiffness usually influence the stiffness of the obtained design (Sigmund 1997).

The actuator is optimized by altering the microstructure of the two porous materials by applying topology optimization. In order to do so the microstructure equations are cast in a monolithic form such that a density is associated to each finite element in the microstructure model representing either solid or void. However as discrete optimization problems are difficult the problem is relaxed by the introduction of a continuous density interpolation and solved by a gradient based optimization method.

3. Theory

The physical setting is the solid-fluid interaction at the microscale of a saturated periodic porous elastic material. A simplified illustration is shown in figure 3 and the interaction problem can be described as follows.

In the solid elastic material the stress is given by the Cauchy stress tensor $\sigma_s = \mathbf{E} : \varepsilon(\mathbf{u})$ where $\varepsilon(\mathbf{u})$ is the infinitesimal strain tensor and $\mathbf{u}$ is the displacement

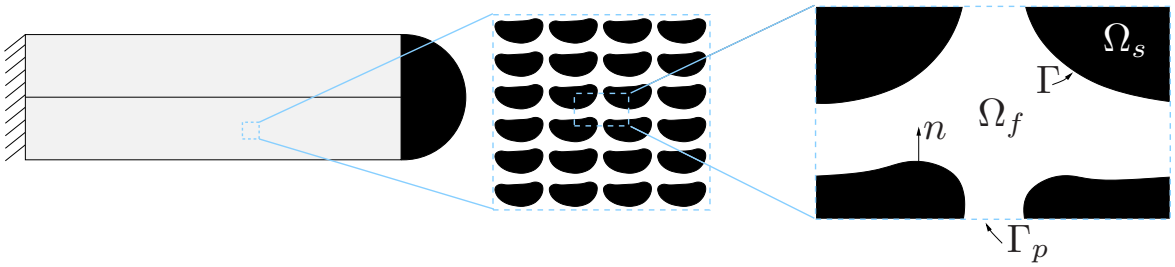

Figure 3. Schematic showing a 2D schematic of the multiscale problem. The macro problem, the actuator, shown left. The periodic porous material in the center and the unit-cell (RVE) to the right. Solid and fluid domains indicated by black and white, interfacing boundaries by Γ and periodic boundaries by Γ_p. $\mathbf{n}$ denotes the unit normal vector to the interface

vector. The fluid is assumed to be Newtonian and incompressible and the stress is given by $\boldsymbol{\sigma}_f = 2\mu D(\mathbf{v}) - p\mathbf{I}$ where $D(\mathbf{v}) = v_{ij} - \delta_{ij}v_{kk}/3$ is the strain rate tensor, p the pressure, $\mathbf{I}$ the 2nd order identity tensor and $\mathbf{v}$ the velocity. Omitting inertial effects, convection and body forces yields the following conservation equations

$$\nabla \cdot \boldsymbol{\sigma}_s = \mathbf{0} \qquad \text{in } \Omega_s \tag{1}$$

$$\nabla \cdot \boldsymbol{\sigma}_f = \mathbf{0} \qquad \text{in } \Omega_f \tag{2}$$

$$\nabla \cdot \mathbf{v} = 0 \qquad \text{in } \Omega_f \tag{3}$$

The boundary conditions between the solid and the fluid requires continuity in the stress over the boundary and the fluid has a no-slip condition along the interfacing boundaries. Furthermore periodicity of displacements, velocities and pressure is required.

$$(\boldsymbol{\sigma}_s - \boldsymbol{\sigma}_f) \cdot \mathbf{n} = \mathbf{0} \qquad \text{at } \Gamma \tag{4}$$

$$\mathbf{v} - \dot{\mathbf{u}} = \mathbf{0} \qquad \text{at } \Gamma \tag{5}$$

$$\mathbf{u}, \mathbf{v}, p \qquad \text{periodic} \qquad \text{at } \Gamma_p \tag{6}$$

where $\mathbf{n}$ is the normal vector to the boundary Γ.

By two scale asymptotic expansion and assuming that the scales are seprable this yields a mixed stiffness formulation (Wang 2000) which is derived thoroughly in e.g. Auriault et al. (2009). Finally this leaves us with two sets of equations that can be solved independently, one describing the macroscopic behaviour and another describing the microscopic. As mentioned previously only the steady state will be considered and therefore the macro equation yields

Find $\mathbf{u} \in \mathcal{V}^3$ for all $\widehat{\mathbf{u}} \in \mathcal{V}_0^3$ such that

$$\int_V \varepsilon_{ij}(\widehat{\mathbf{u}}) E^H_{ijlm} \varepsilon_{lm}(\mathbf{u}) \, \mathrm{d}V - \int_L \widehat{u}_i u_i k_s \, \mathrm{d}L = \int_V \alpha_{ij} \varepsilon_{ij}(\widehat{\mathbf{u}}) p \, \mathrm{d}V \tag{7}$$

where $\mathbf{u}$ is displacement, p is pressure and k_s is the spring stiffness of the attached springs. These are attached to the tip-edge L (line perpendicular to 1-3 plane). E^H_{ijlm}

and α_{ij} are the homogenized stiffness and pressure coupling tensors obtained from the micro model analysis, respectively. The pressure term is located at the right hand side as the pressure distribution is assumed to be known a priori in the simulations.

3.1. Micromodel

The homogenized coefficients that are needed in the poroelastic model are computed by use of homogenization. The deformations of a representative unit cell from the periodic microstructure are obtained using 7 different loads. Afterwards the homogenized coefficients can be computed based on volume averages of the obtained deformations. There are 6 loads associated to the homogenization of the stiffness tensor $\mathbf{E}^H$ and 1 load to the homogenization of the pressure coupling tensor $\boldsymbol{\alpha}$. The analyzed unit cell has periodic boundary conditions. The homogenized stiffness tensor can be computed by solving the following problem

Find $\boldsymbol{\xi}^{kh} \in \mathcal{V}^3$ for all $\widehat{\mathbf{u}} \in \mathcal{V}_0^3$ such that

$$\int_\Omega \varepsilon_{ij}(\widehat{\mathbf{u}}) E_{ijlm}(\rho) \varepsilon_{lm}(\boldsymbol{\xi}^{kh}) \,\mathrm{d}V = \int_\Omega E_{ijlm}(\rho) \varepsilon_{lm}^{0,kh} \varepsilon_{ij}(\widehat{\mathbf{u}}) \,\mathrm{d}V \tag{8}$$

$$E_{ijkh}^H = \frac{1}{|\Omega|} \int_\Omega \left(\varepsilon_{lm}^{0,ij} - \varepsilon_{lm}(\boldsymbol{\xi}^{ij})\right) E_{lmpq}(\rho) \left(\varepsilon_{pq}^{0,kh} - \varepsilon_{pq}(\boldsymbol{\xi}^{kh})\right) \,\mathrm{d}\Omega \tag{9}$$

where $\varepsilon^{0,kh}$ is a second order tensor with only a single entry $\varepsilon_{kh}^{0,kh} = 1$. The stiffness tensor depends on the design denoted by ρ which will be discussed later. In equation (9) the mutual energies are used to compute the homogenized stiffness tensor.

There are two methods for computing the pressure coupling tensor, one is to use the solution $\boldsymbol{\xi}^{kh}$ of the previous problems which is attractive when $\mathbf{E}^H$ is also needed this yields

$$\alpha_{kh} = \int_\Omega \left[(1 - \zeta(\rho))\delta_{kh} + \varepsilon_{ij}(\boldsymbol{\xi}^{kh})\delta_{ij}\zeta(\rho)\right] \,\mathrm{d}\Omega \tag{10}$$

where δ_{kh} is the Kronecker delta and $\zeta(\rho)$ is a design dependent function which will be introduced later. Another method is to apply a slightly different load to the same equation as above, which is interesting for the case where only $\boldsymbol{\alpha}$ is of interest, yielding

Find $\boldsymbol{\eta} \in \mathcal{V}^3$ for all $\widehat{\mathbf{u}} \in \mathcal{V}_0^3$ such that

$$\int_\Omega \varepsilon_{ij}(\widehat{\mathbf{u}}) E_{ijlm}(\rho) \varepsilon_{lm}(\boldsymbol{\eta}) \,\mathrm{d}V = \int_\Omega \zeta(\rho)\delta_{ij}\varepsilon_{ij}(\widehat{\mathbf{u}}) \,\mathrm{d}V \tag{11}$$

$$\alpha_{ij} = \frac{1}{|\Omega|} \int_\Omega \left[(1 - \zeta(\rho))\delta_{ij} + E_{ijlm}(\rho)\varepsilon_{lm}(\boldsymbol{\eta})\right] \,\mathrm{d}\Omega \tag{12}$$

There is a slight difference in first term in the interpolation formula (12) compared to the one used in Andreasen & Sigmund (2011). Here the density ρ were used instead of the interpolation function $\zeta(\rho)$. Revisiting the derivation of the homogenization formula it is seen that the interpolation function is a more consistent choice.

However the solution of (11) and the following integration (12), alternatively the integration of (10), can be avoided following Mei & Vernescu (2010) as the pressure coupling tensor $\boldsymbol{\alpha}$ for a micro structure which is made from a homogeneous microscopically isotropic elastic solid can be computed from the homogenized stiffness as

$$\alpha_{ij} = \delta_{ij} - \frac{E^H_{pqij}\delta_{pg}}{3\lambda + 2G} \tag{13}$$

where $\lambda = E\nu/[(1+\nu)(1-2\nu)]$ and $G = E/[2(1+\nu)]$ are the Lamé coefficents. For macroscopically isotropic materials the fraction reduce to the ratio between the bulk modulus of the composite and the basis material. This means that the pressure coupling approaches unity if an incompressible basis material is used.

3.2. FEM

The partial differential equations can be solved using the finite element method and for the macroscale equation (7) this yields the following equation system

$$\mathbf{Ku} = \mathbf{Qp}$$

where $\mathbf{K}$ is the stiffness matrix and $\mathbf{Q}$ is the pressure coupling matrix defined as

$$\mathbf{K} = \int_V \mathbf{B}^T\mathbf{D}^H\mathbf{B}\,\mathrm{d}V + \int_L k_s\mathbf{N}^T\mathbf{N}\,\mathrm{d}L, \qquad \mathbf{Q} = \int_V \mathbf{B}^T\bar{\boldsymbol{\alpha}}\mathbf{N}_p\,\mathrm{d}V$$

where $\mathbf{N}$ and $\mathbf{N}_p$ are the shape functions for displacements and pressure, respectively. $\mathbf{B}$ is the strain displacement matrix, $\mathbf{D}^H$ is the matrix form of the homogenized stiffness tensor and $\bar{\boldsymbol{\alpha}}$ is the vector form of the pressure coupling tensor. The stiffness matrix contains contributions from both the element and the spring stiffnesses. The displacements can easily be found by solving this equation system as the pressure field is assumed to be uniform and given a priori.

For the micro scale problems the discretization yields the equation systems

$$\breve{\mathbf{K}}\boldsymbol{\xi}^i = \breve{\mathbf{f}}^i, \qquad \breve{\mathbf{K}}\boldsymbol{\eta} = \breve{\mathbf{g}}$$

for $i = 1, 6$ where $\boldsymbol{\xi}$ and $\boldsymbol{\eta}$ are periodic. The stiffness matrix and load vectors are given by

$$\breve{\mathbf{K}} = \int_\Omega \mathbf{B}^T\mathbf{D}\mathbf{B}\,\mathrm{d}\Omega,$$
$$\breve{\mathbf{f}}^i = \int_\Omega \mathbf{B}^T\mathbf{D}\mathbf{b}^i\,\mathrm{d}\Omega, \qquad \breve{\mathbf{g}} = \int_\Omega \mathbf{B}^T\mathbf{m}\zeta(\rho)\,\mathrm{d}\Omega$$

where $\mathbf{b}^i$ is the i'th column of the 6×6 identity matrix and $\mathbf{m} = \{1\,1\,1\,0\,0\,0\}^T$.

This formulation resembles (8) and (11). Casting the weak form in matrix notation simplifies the sensitivity derivation for use in the optimization procedure.

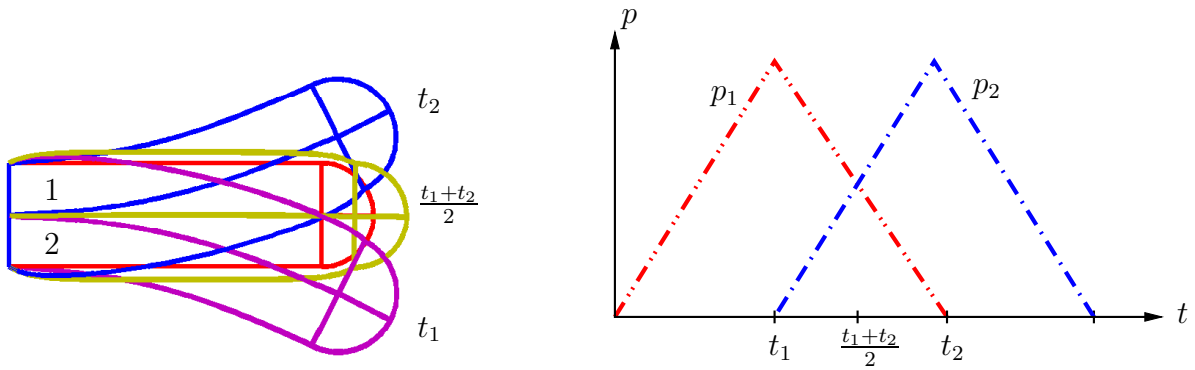

Figure 4. Left: Sketch of actuator motion path. Right: Pressure-time relation for the domains. First the upper domain(1) is loaded by a pressure, which then decays linearly while the lower domain(2) is loaded by a linearly increasing pressure. Finally this pressure is also decreased and the actuator returns to its initial state.

4. Optimization

The goal for the optimization of the poroelastic actuator is to maximize its transversal deflection such that the performance of a poroelastic linear motor can be increased. This is done by optimizing the macroscopic properties i.e. deflection with respect to the material microstructure. Topology optimization is imposed in the material design process in which the strict distinction between solid and void is relaxed by the introduction of a design interpolation function. At design convergence the densities are supposed to be either 0 or 1 due to the imposed penalization of intermediate densities.

Considering the actuator displayed in figure 2 having a movement as illustrated in figure 4 the performance is quantified by the transversal deflection u_3 integrated along the nose line. Assuming a nearly linear response to the pressurization of either domain, the optimization is based on the two solutions corresponding to pressurization of each domain. These two load cases are referred to using a superscript parenthesized number.

In order to apply topology optimization to the unit cell design, each element in the FEM discretization is given a density $\rho \in [0;1]$ such that it can represent either void or solid. During the topology optimization intermediate densities are allowed and the stiffness is interpolated using RAMP (Stolpe & Svanberg 2001)

$$\zeta(\rho) = \left(10^{-4} + \frac{\rho(1-10^{-4})}{1+p(1-\rho)}\right) \tag{14}$$

where p is a penalization factor, here $p = 3$. For the stiffness this yields $\mathbf{E}(\rho) = \zeta(\rho)\mathbf{E}_0$ where $\mathbf{E}_0$ is the stiffness tensor of the isotropic basis material. This scheme imposes a lower bound on the stiffness which avoids the equation system being singular. This design dependence of the stiffness applies to the micro problems (8),(11) and the volume averaging (9),(12) and (10).

The optimization problem can be formulated as a min-max optimization problem:

$$\left.\begin{array}{rll} \min\limits_{\boldsymbol{\rho}\in\mathbb{R}^N} & \max\left\{u_3^{(1)}, -u_3^{(2)}\right\} & \\ \text{s.t.} & \text{Macro equation} & \\ & \text{Micro equations} & \\ & \sum\limits_{e=1}^{N_1} v_e\rho_e - \gamma_1 V_0 \leq 0, & \\ & \sum\limits_{e=N_1+1}^{N_2} v_e\rho_e - \gamma_2 V_0 \leq 0, & \\ & g_i \leq 0 & \\ & 0 \leq \rho_e \leq 1, & \text{for } e = 1, ..., N \end{array}\right\} \tag{15}$$

where u_3 denotes the deflection in the 3rd direction integrated along the nose line. $N = N_1+N_2$ is the number of elements (total and in each material), γ is the allowed solid volume fraction for each material, v_e is the element volume and V_0 is the total volume of the unit-cell. g_i denotes a set of inequality constraints which will be introduced later.

To ensure that the optimized actuator is providing a force at the contact point a set of springs are attached to the nose line of the actuator. It has previously been shown in actuator design (Sigmund 2001) that an increase in the spring stiffness will influence the general stiffness of the structure in order to provide a better support.

4.1. Sensitivity analysis

The stiffness matrix $\mathbf{K}$ of the macro problem depends on the homogenized stiffness tensor that again depends on the design variables. This also holds for the pressure coupling matrix $\mathbf{Q}$ that depends on the homogenized pressure coupling tensor. Therefore the sensitivity of the objective must be computed by the chain rule as

$$\frac{\mathrm{d}\Phi}{\mathrm{d}\boldsymbol{\rho}} = \frac{\partial\Phi}{\partial\widetilde{\mathbf{E}}}\frac{\mathrm{d}\widetilde{\mathbf{E}}}{\mathrm{d}\boldsymbol{\rho}} + \frac{\partial\Phi}{\partial\widetilde{\boldsymbol{\alpha}}}\frac{\mathrm{d}\widetilde{\boldsymbol{\alpha}}}{\mathrm{d}\boldsymbol{\rho}} \tag{16}$$

where $\widetilde{\mathbf{E}}$ and $\widetilde{\boldsymbol{\alpha}}$ are vector forms of the stiffness and pressure coupling; $\mathbf{E}$ and $\boldsymbol{\alpha}$, respectively.

In order to compute the first factor of both terms an adjoint sensitivity analysis (Michaleris et al. 1994) of the macroscopic equations can be made. First the augmented Lagrangian $\mathcal{L}$ is defined by the objective function, the adjoint variable and the residual as

$$\mathcal{L} = \Phi + \boldsymbol{\lambda}^T(-\mathbf{K}\mathbf{u} + \mathbf{Q}\mathbf{p}) \tag{17}$$

Then the sensitivities with respect to the stiffness are computed by differentiating the

Lagrangian by the stiffness

$$\frac{\mathrm{d}\mathcal{L}}{\mathrm{d}\widetilde{\mathbf{E}}} = \frac{\partial\Phi}{\partial\widetilde{\mathbf{E}}} + \boldsymbol{\lambda}^T\frac{\partial(-\mathbf{K}\mathbf{u}+\mathbf{Q}\mathbf{p})}{\partial\widetilde{\mathbf{E}}} + \underbrace{\left(\frac{\partial\Phi}{\partial\mathbf{u}} + \boldsymbol{\lambda}^T\frac{\partial(-\mathbf{K}\mathbf{u}+\mathbf{Q}\mathbf{p})}{\partial\mathbf{u}}\right)}_{X}\frac{\mathrm{d}\mathbf{u}}{\mathrm{d}\widetilde{\mathbf{E}}} \tag{18}$$

Letting the X-marked terms be zero the computation of the state field sensitivity can be avoided and an adjoint problem is obtained

$$\mathbf{K}^T\boldsymbol{\lambda} = \frac{\partial\Phi}{\partial\mathbf{u}} \tag{19}$$

Having solved this problem for $\boldsymbol{\lambda}$ it is possible to compute the sensitivities by inserting into the reminding terms of (18)

$$\frac{\mathrm{d}\mathcal{L}}{\mathrm{d}\widetilde{\mathbf{E}}} = \frac{\partial\Phi}{\partial\widetilde{\mathbf{E}}} - \boldsymbol{\lambda}^T\frac{\partial\mathbf{K}}{\partial\widetilde{\mathbf{E}}}\mathbf{u} \tag{20}$$

Analogously the sensitivity with respect to the pressure coupling tensor can be obtained:

$$\frac{\mathrm{d}\mathcal{L}}{\mathrm{d}\widetilde{\boldsymbol{\alpha}}} = \frac{\partial\Phi}{\partial\widetilde{\boldsymbol{\alpha}}} + \boldsymbol{\lambda}^T\frac{\partial\mathbf{Q}}{\partial\widetilde{\boldsymbol{\alpha}}}\mathbf{p} \tag{21}$$

using the same adjoint solution as obtained previously.

4.2. Micro model sensitivities

The derivation of the micromodel sensitivities is found in the appendix. The sensitivities of stiffness tensor $\mathbf{E}^H$ and the pressure coupling tensor $\boldsymbol{\alpha}$ with respect to the design variable ρ yields

$$\frac{\mathrm{d}E^H_{ijkh}}{\mathrm{d}\rho_e} = \frac{1}{|\Omega|}\int_{\Omega_e}\left(\varepsilon^{0,ij}_{lm} - \varepsilon_{lm}\left(\boldsymbol{\xi}^{ij}\right)\right)E'_{lmpq}(\rho_e)\left(\varepsilon^{0,kh}_{pq} - \varepsilon_{pq}\left(\boldsymbol{\xi}^{kh}\right)\right)\,\mathrm{d}\Omega \tag{22}$$

where $()'$ denotes the partial derivative with respect to the design variables and

$$\frac{\mathrm{d}\alpha_{kh}}{\mathrm{d}\rho_e} = \frac{1}{|\Omega|}\int_{\Omega_e}\big[-\zeta'(\rho_e)\delta_{kh} + \varepsilon_{ij}(\boldsymbol{\xi}^{kh})\delta_{ij}\zeta'(\rho_e) + \varepsilon_{ij}(\boldsymbol{\eta})E'_{ijkh}(\rho_e) - \varepsilon_{ij}(\boldsymbol{\eta})E'_{ijlm}(\rho_e)\varepsilon_{lm}(\boldsymbol{\xi}^{kh})\big]\,\mathrm{d}\Omega \tag{23}$$

where $\boldsymbol{\xi}^{kh}$ and $\boldsymbol{\eta}$ are the solutions obtained during the micro analysis, see equation (8) and (11). However the sensitivities of $\boldsymbol{\alpha}$ can also be computed, by differentiating (13), as

$$\frac{\mathrm{d}\alpha_{kh}}{\mathrm{d}\boldsymbol{\rho}} = -\frac{\mathrm{d}E^H_{ijkh}}{\mathrm{d}\boldsymbol{\rho}}\frac{\delta_{ij}}{3\lambda+2G} \tag{24}$$

which is computationally more attractive since there the solution for $\boldsymbol{\eta}$ can be avoided.

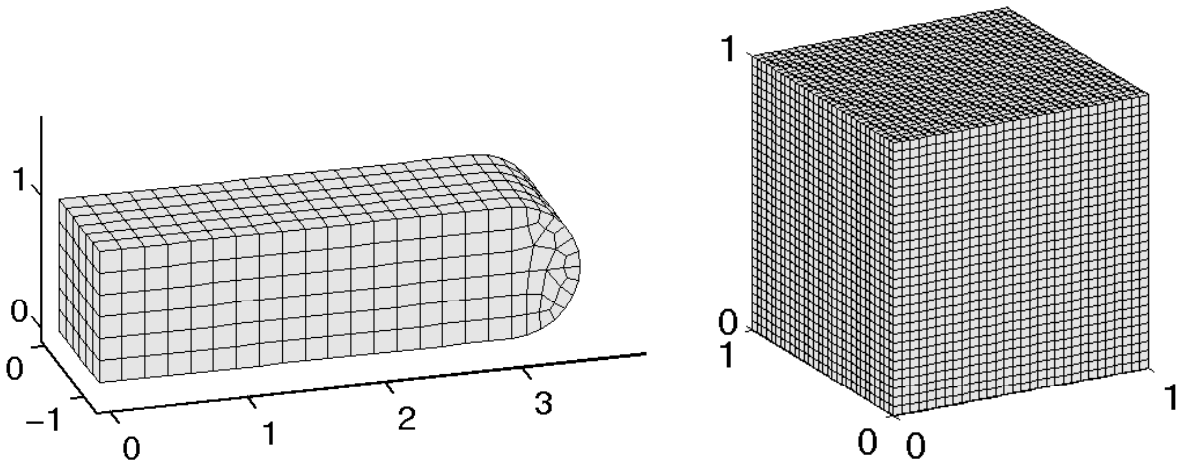

Figure 5. The meshes used in the analysis: a) Macro mesh, 810 hexahedral elements. b) Micro mesh with 30^3 brick elements.

5. Numerical implementation

An optimization software has been written in the framework of Comsol Multiphysics 3.5a and Matlab 2008b. The macroscopic modeling of the actuator is done using the FEM functionality within Comsol using 2nd order hexahedral elements. The mesh used for the macroscopic model is shown in figure 5(a). The solution is obtained using the built-in geometric multi grid (GMG) preconditioned conjugate gradient (PCG) method.

The homogenization procedure has been written solely in Matlab using 1st order regular hexahedral elements in order to get the highest possible resolution. The mesh is shown in figure 5(b). All faces have periodic boundary conditions and they are enforced using the same node numbers on the opposing sides of the unit-cell. In order to prevent rigid body motion a single node has been fully constrained. The solution is obtained using an incomplete Choleskey PCG method.

The optimization problem is solved using the method of moving asymptotes (MMA) by Svanberg (1987) and the convergence criteria used is $\|\boldsymbol{\rho}^i - \boldsymbol{\rho}^{i-1}\|_\infty < 0.001$. The non-smooth min-max problem formulation is converted into a smooth problem by adding an additional variable which is minimized for. The original objective function are converted into inequality constraints using this additional variable.

Furthermore a standard density filter (Bruns & Tortorelli 2001, Bourdin 2001) has been used in order to avoid checkerboard patterns. The filter radius R is chosen such that its final value is 1.4 times the element side length and a linear weighting is used. Neighboring elements at the opposite side of the unit-cell are also included in the filter as the design is of a periodic material. The optimization problems solved are prone to find local minima. In order to diminish a continuation has been applied on the filter size such that it decreases in steps when the design converges.

The optimization procedure can be summarized as follows

(i) Initialize
(ii) While $\|\boldsymbol{\rho}^i - \boldsymbol{\rho}^{i-1}\|_\infty < 0.001$ and $R_{min} \leq R$
  (a) Solve micro problems, compute $\mathbf{E}$,$\boldsymbol{\alpha}$, $\frac{\mathrm{d}\widetilde{\mathbf{E}}}{\mathrm{d}\boldsymbol{\rho}}$,$\frac{\mathrm{d}\widetilde{\boldsymbol{\alpha}}}{\mathrm{d}\boldsymbol{\rho}}$, Eq. (8),(9),(13),(22),(24)
  (b) Solve macro problem, compute Φ, Eq. (7)
  (c) Solve adjoint macro problem, compute $\frac{\partial\Phi}{\partial\widetilde{\mathbf{E}}}$, $\frac{\partial\Phi}{\partial\widetilde{\boldsymbol{\alpha}}}$, Eq. (19),(20),(21)
  (d) Find sensitivities using chain rule, $\frac{\mathrm{d}\Phi}{\mathrm{d}\boldsymbol{\rho}} = \frac{\partial\Phi}{\partial\widetilde{\mathbf{E}}}\frac{\mathrm{d}\widetilde{\mathbf{E}}}{\mathrm{d}\boldsymbol{\rho}} + \frac{\partial\Phi}{\partial\widetilde{\boldsymbol{\alpha}}}\frac{\mathrm{d}\widetilde{\boldsymbol{\alpha}}}{\mathrm{d}\boldsymbol{\rho}}$, Eq. (16)
  (e) Update $\boldsymbol{\rho}$ using MMA
  (f) Decrease R if $\|\boldsymbol{\rho}^i - \boldsymbol{\rho}^{i-1}\|_\infty < 0.001$
(iii) Post process

6. Results

In this section results from the optimization of the materials used in the actuator shown in figure 2 will be presented. First a comparison with the method from Andreasen & Sigmund (2011) will be given for the optimization of a single material actuator. Then a two material design will be presented and finally a two material design with constraints on the deflection-extension ratio will be shown. All optimization problems are subject to a 30% volume constraint ($\gamma = 0.3$) and the elastic basis material has the properties $E = 1$ and $\nu = 0.3$.

6.1. One material design

In the paper by Andreasen & Sigmund (2011) a method for optimization of a single material actuator was presented. This was done under the assumption that the lateral deflection could be maximized by increasing the magnitude of the corresponding entry in the pressure coupling tensor, e.g. increasing deflection in the direction 3 by maximizing the magnitude of α_{13}. Using the same code and formulation as in the reference, a material is generated for which the α_{13} is minimized. The result is shown to in figure 6(a).

The material plotted in figure 6(b) is obtained using the macro problem as it is presented in figure 2 with springs attached to the tip line having the stiffness $k_s = 10^{-3}$. The optimized material design does not completely resemble that of the minimized α_{13} entry. The fact that the material is also extending due to the internal pressure makes it impossible to rely on the shear effects alone. The inclined planes are still present but a very thick layer of material ensures stiffness in the 1-direction such that the pressure is not *wasted* on deforming the extension spring, when it is the lateral deflection that matters.

By detaching the springs from the right edge the design changes and this is shown in figure 6(c). Not having any springs means that no force should be transmitted and thereby no or only small stiffness is required. It is clearly seen from the material design

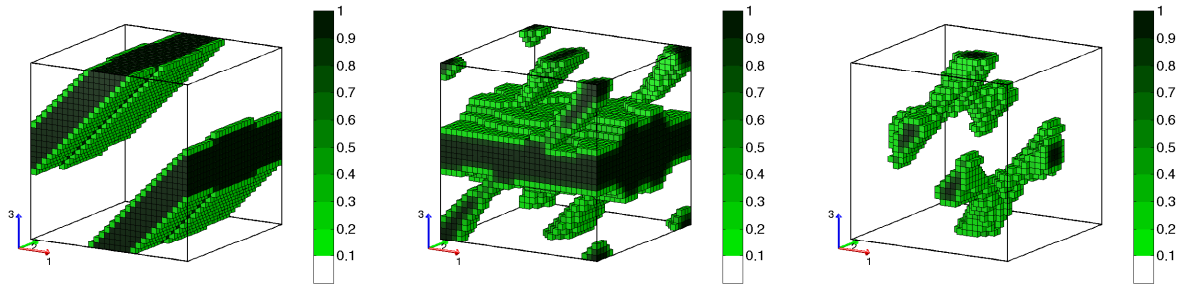

(a) (b) (c)

Figure 6. (a) Material with minimized α_{13} component. (b) Resulting material from maximizing the vertical displacement of a single material actuator with springs with stiffness $k_s = 10^{-3}$ attached. (c) As (b) but with no springs attached.

Figure	α_{13}	u_3, $(k_s = 10^{-3})$	u_3, $(k_s = 0)$
6(a)	**−0.0602**	−10.36	−77.56
6(b)	−0.0027	**−646.24**	−6858.45
6(c)	−0.0002	−10.42	**−16166.65**

Table 1. Cross check for optimized single material actuators shown in figure 6. The post evaluation was subjected to a pressure of $p = 1$. The minimum value for each column is emphasized.

that not all material is utilized which of course also is evident when evaluating the stiffness and pressure coupling. A comparison of the performance of the three designs is listed in table 1. It is seen that they individually perform best for the problem formulation for which it was obtained.

6.2. Two material design

In this section the design of a bi-morph poroelastic actuator will be considered. The objective is to make the actuator move as illustrated in figure 4, namely extension and downwards deflection followed by an upwards deflection. The figure also presents a pressure-time relation which indicates the sequence in which the domains are pressurized. First the upper domain is pressurized. This is followed by a linear pressure decrease in the upper domain and an increase in lower domain until the lower domain is fully pressurized. Removing the pressure the actuator moves back to its initial configuration.

As described in section 4 the optimization will only consider two static load cases. One for the pressurization of each domain. Figure 7 shows the designs obtained using the formulation in equation (15). The initial design was a solid cross and the final result has been obtained using a continuation approach on the used filter radius (R={2, 1.4} elements side length). From 7(a) and 7(c) it is seen that the material unit cell has a

main beam in the 1st direction (along the actuator) while the connections in the 2nd and 3rd direction is rather thin. This results in a low transversal stiffness of the material. The stiffness and pressure coupling matrices of the two materials are:

$$\mathbf{E}_1 = \begin{bmatrix} 25.527 & 0.153 & 0.175 & -0.000 & -0.262 & -0.000 \\ & 0.128 & 0.102 & -0.000 & -0.150 & -0.000 \\ & & 0.148 & 0.000 & -0.182 & -0.000 \\ & & & 0.055 & 0.000 & -0.061 \\ & & & & 0.296 & 0.000 \\ \text{sym} & & & & & 0.097 \end{bmatrix} \cdot 10^{-2}, \tag{25}$$

$$\boldsymbol{\alpha}_1 = \begin{bmatrix} 0.897 & -0.000 & 0.002 \\ & 0.998 & -0.000 \\ \text{sym} & & 0.998 \end{bmatrix} \tag{26}$$

$$\mathbf{E}_2 = \begin{bmatrix} 25.527 & 0.153 & 0.175 & -0.000 & 0.262 & 0.000 \\ & 0.128 & 0.102 & 0.000 & 0.150 & -0.000 \\ & & 0.148 & -0.000 & 0.182 & 0.000 \\ & & & 0.055 & 0.000 & 0.061 \\ & & & & 0.296 & 0.000 \\ \text{sym} & & & & & 0.097 \end{bmatrix} \cdot 10^{-2}, \tag{27}$$

$$\boldsymbol{\alpha}_2 = \begin{bmatrix} 0.897 & -0.000 & -0.002 \\ & 0.998 & -0.000 \\ \text{sym} & & 0.998 \end{bmatrix} \tag{28}$$

from which it is seen that the material properties are symmetric. No explicit symmetry constraint is enforced but starting with a symmetric initial design and optimizing using a symmetric objective function does not leave any motivation to the optimizer to make two different designs.

From figure 7(b) and 7(d) the deformed actuator can be observed. The in-and-out of plane deformations are minimal as they do not directly enter the objective. It is seen that the deflection is dominating the deformation. The upper and lower boundaries are nearly straight which might indicate that the shear strain is important. This might be linked to the low transversal stiffness of the materials together with the pressure coupling which will make the actuator deflect. In order to explore the nature of the deformation the stress state can be analyzed.

The total stress $\boldsymbol{\sigma} = \mathbf{E}\boldsymbol{\varepsilon}(\mathbf{u}) - \boldsymbol{\alpha}p$ in point $\mathbf{x}_{low} = (1.5, -0.5, 0.25)$ and $\mathbf{x}_{up} = (1.5, -0.5, 0.75)$ while pressurizing the lower domain are

$$\boldsymbol{\sigma}_{\mathbf{x}_{low}} = \begin{Bmatrix} -1.548 \\ 1.001 \\ 0.987 \\ -0.001 \\ -2.283 \\ 0.001 \end{Bmatrix} \cdot 10^{-3} - \begin{Bmatrix} 0.897 \\ 0.998 \\ 0.998 \\ -0.000 \\ 0.002 \\ -0.000 \end{Bmatrix} \cdot 10^{-3} = \begin{Bmatrix} -2.444 \\ 0.003 \\ -0.011 \\ -0.001 \\ -2.286 \\ 0.001 \end{Bmatrix} \cdot 10^{-3}, \quad \boldsymbol{\sigma}_{\mathbf{x}_{up}} = \begin{Bmatrix} 2.714 \\ 0.097 \\ 0.016 \\ -0.000 \\ 0.455 \\ -0.000 \end{Bmatrix} \cdot 10^{-3} \tag{29}$$

and it is seen that σ_1 and σ_5 in the lower domain are nearly equal. As seen in figure 8

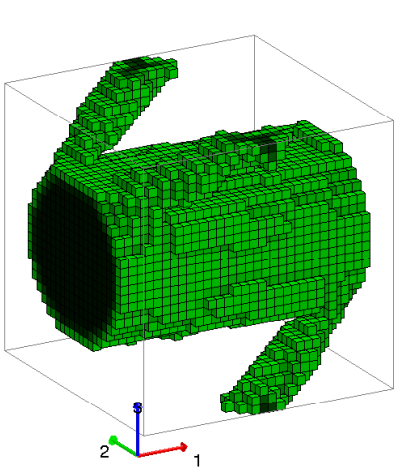

(a) Material 1

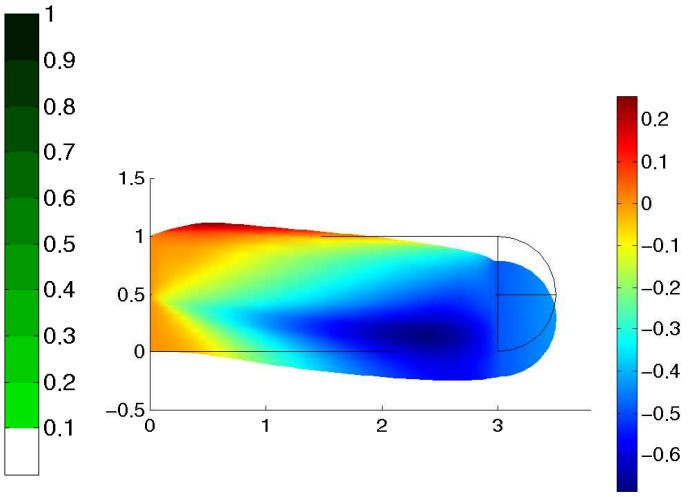

(b) Deformation load case 1. Color: u_3

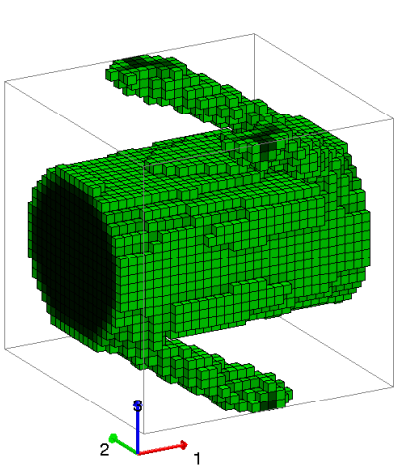

(c) Material 2

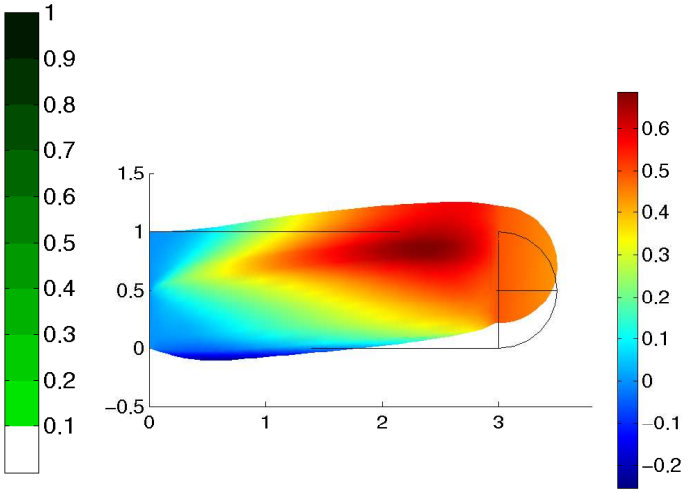

(d) Deformation load case 2. Color: u_3

Figure 7. Optimized material configuration and deflections for each of the two load cases. Optimized with spring stiffness $k = 10^{-3}$. Same deformation scaling apply to both plots. $\Phi_{final} = max\{-u_3^{(1)}, u_3^{(2)}\} = 0.424$, $p = 10^{-3}$

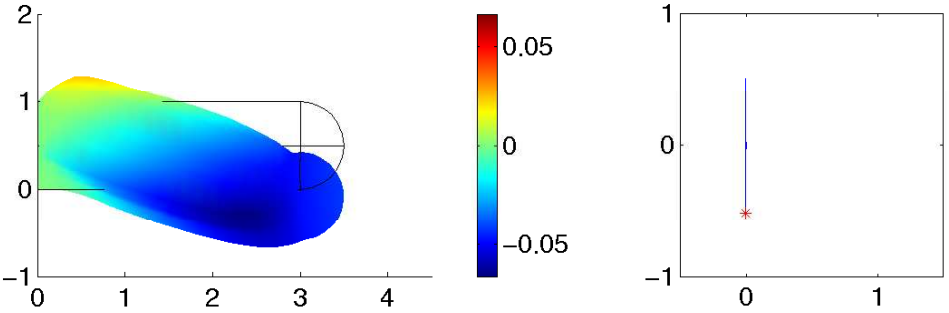

Figure 8. Left: Deformed actuator with pressurized upper domain. Right: Motion path with indication of current state. Deformations are exaggerated.

the actuator only moves transversally while pressurized. This kind of actuator that only provides a transversal actuation may be applicable in some cases, but for the design of a linear motor the actuator needs to be able to provide both an extension as well as a deflection. This might be introduced in the optimization procedure by employing a set of constraints on the deformation.

6.2.1. Localization Having computed the macroscopic response the corresponding deformation of the unit cell can be investigated. In general (Auriault et al. 2009) the micro deformation is given by

$$u_i^{(1)} = \xi_i^{lm}\varepsilon_{lm}(\mathbf{u}^{(0)}) - \eta_i p^{(0)} + \bar{u}_i^{(1)}(\mathbf{x}) \tag{30}$$

where the first two terms are linear combinations of the homogenization equation solutions and the macroscopic strain and pressure, respectively. The final term is a rigid body movement of the unit-cell. However as the macro and the micro structure have a finite scale ratio a uniform straining of the unit cell also needs to be superposed to the local deformations. This uniform straining corresponds to the macroscopic strain field applied to the unit cell

$$u_i^{def}(\mathbf{y}, \mathbf{x}) = \varepsilon_{ij}(\mathbf{u}^{(0)})y_j \tag{31}$$

where $\mathbf{y}$ the nondimensional local coordinate. This deformation field is superposed that of equation (30). The unit cell deformations corresponding to the design and loads shown in figure 7 are shown in figure 9. It is seen that as the material is pressurized the center solid body is compressed.

6.3. Deflection/extension constraints

The previous actuator shown in figure 7 performs very well with respect to transversal deflection for which the design was optimized. However in order to use the actuator in e.g. a linear motor an extension is required. This can be ensured by adding a set of constraints that restricts the ratio of the extension and the deflection to be approximately one. The constraints are given by

$$g_1 = (-u_3^{(1)}/u_1^{(1)} - 1)^2 - \epsilon \leq 0 \tag{32}$$

$$g_2 = (u_3^{(2)}/u_1^{(2)} - 1)^2 - \epsilon \leq 0 \tag{33}$$

where ϵ is a small number (here $\epsilon = 0.01$).

Taking these constraints into consideration the material design changes and the resulting materials are shown in figure 10. Again (a) and (c) shows the material microstructures and (b) and (d) display the deformations. It is clearly seen that the actuator now also extends. In comparison to the deformations of the previous actuator it seems to bend more than it shears.

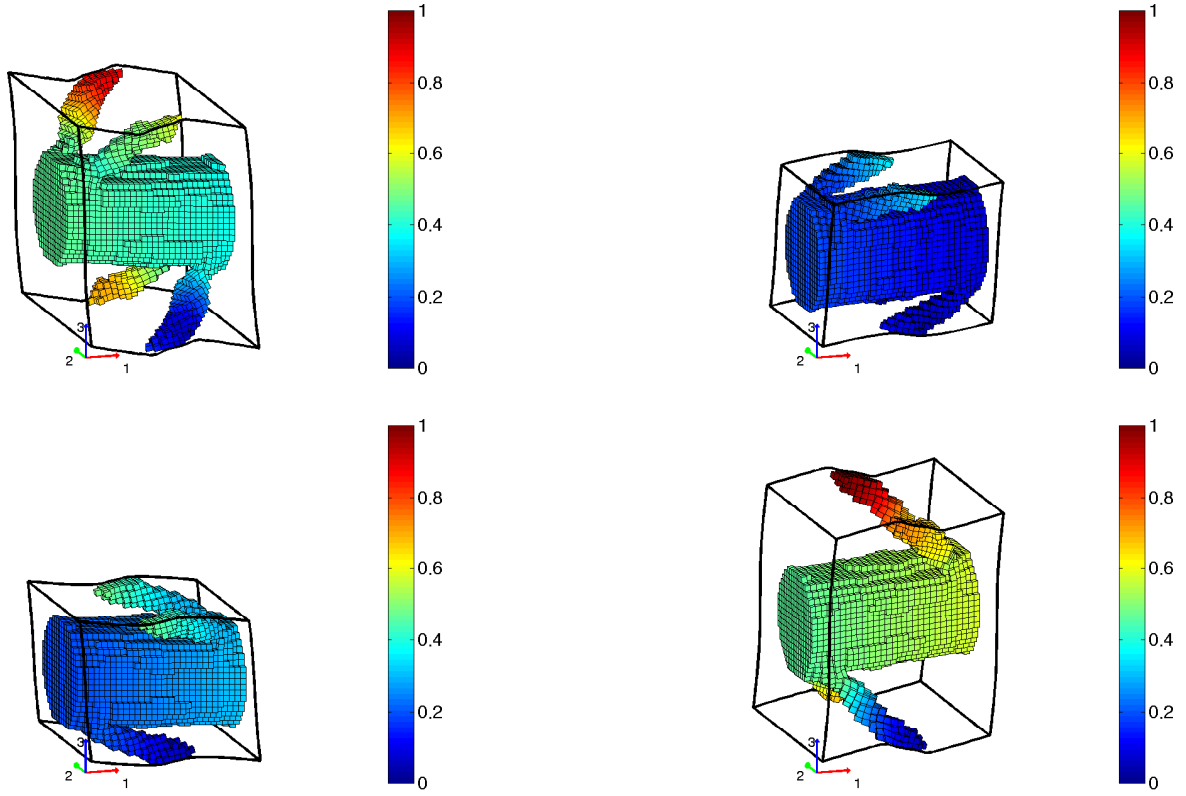

Figure 9. Deformed unit cells for the two materials (top and bottom) and for each load case (left/right). Color shows the deformation vector sum ($\sqrt{u_1^2+u_2^2+u_3^2}$). The unit cell has a side length of 0.01 and the deformations are scaled by a factor 0.5. The unit-cells are located in the same points as used for the stress evaluation; $\mathbf{x}_{low} = (1.5, -0.5, 0.25)$ and $\mathbf{x}_{up} = (1.5, -0.5, 0.75)$

The material parameters yield:

$$\mathbf{E}_1 = \begin{bmatrix} 2.811 & -0.186 & -0.266 & -0.000 & 0.280 & 0.000 \\ & 0.113 & 0.049 & 0.000 & -0.041 & -0.000 \\ & & 0.088 & 0.000 & -0.056 & -0.000 \\ & & & 0.071 & -0.000 & -0.051 \\ & & & & 0.064 & 0.000 \\ \text{sym} & & & & & 0.063 \end{bmatrix} \cdot 10^{-2} \tag{34}$$

$$\boldsymbol{\alpha}_1 = \begin{bmatrix} 0.991 & -0.000 & -0.001 \\ & 1.000 & 0.000 \\ \text{sym} & & 1.001 \end{bmatrix} \tag{35}$$

$$\mathbf{E}_2 = \begin{bmatrix} 2.811 & -0.186 & -0.266 & 0.000 & -0.280 & 0.000 \\ & 0.113 & 0.049 & -0.000 & 0.041 & -0.000 \\ & & 0.088 & -0.000 & 0.056 & -0.000 \\ & & & 0.071 & -0.000 & 0.051 \\ & & & & 0.064 & -0.000 \\ \text{sym} & & & & & 0.063 \end{bmatrix} \cdot 10^{-2} \tag{36}$$

$$\boldsymbol{\alpha}_2 = \begin{bmatrix} 0.991 & -0.000 & 0.001 \\ & 1.000 & -0.000 \\ \text{sym} & & 1.001 \end{bmatrix} \tag{37}$$

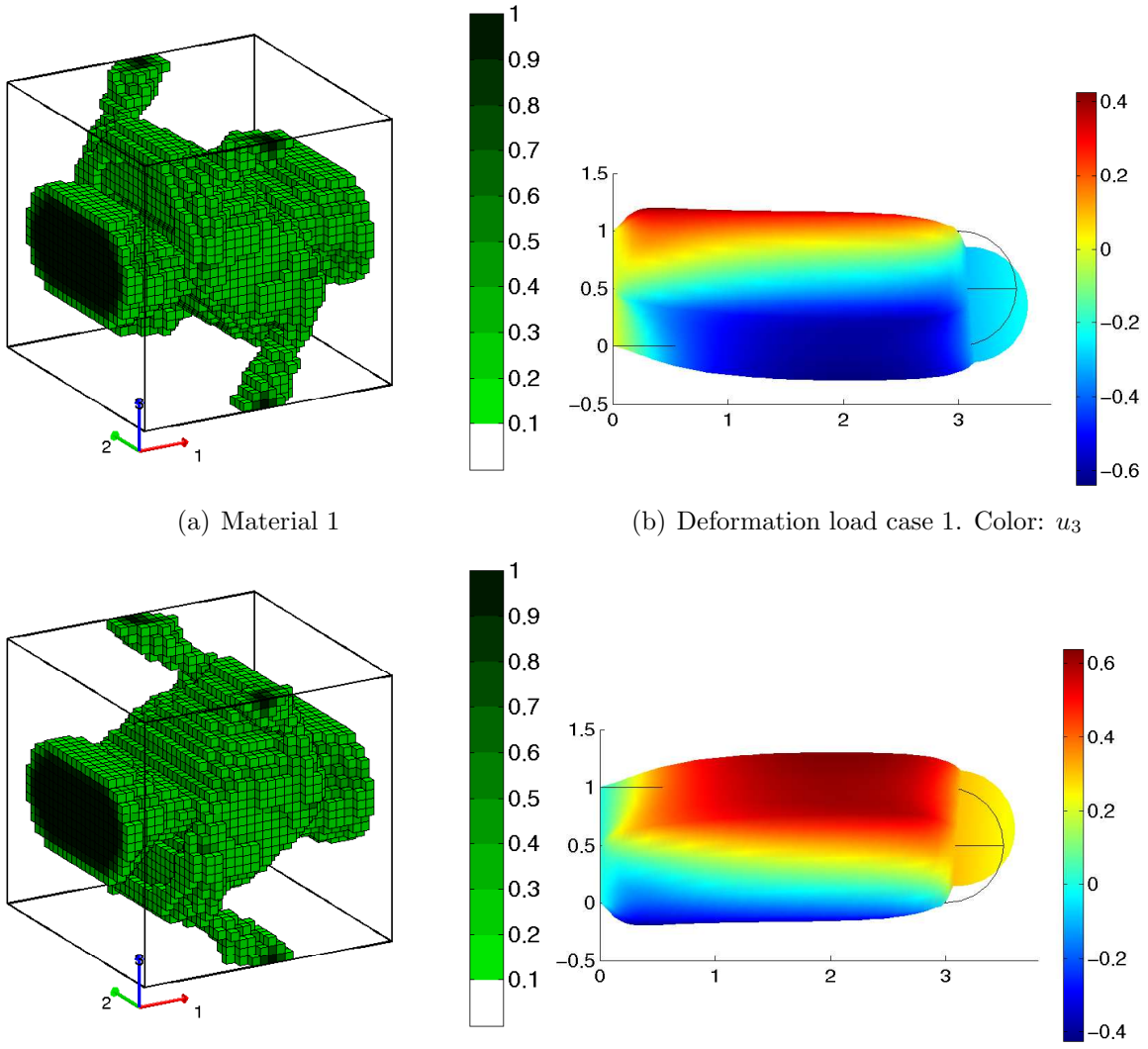

(a) Material 1

(b) Deformation load case 1. Color: u_3

(c) Material 2

(d) Deformation load case 2. Color: u_3

Figure 10. Optimized material configuration and deflections for each of the two load cases. A set of constraints ensure that the extension-deflection ratio is approximately one. Optimized with spring stiffness $k = 10^{-3}$. Same deformation scaling apply to both plots. $\Phi_{final} = max\{-u_3^{(1)}, u_3^{(2)}\} = 0.226$, $p = 10^{-3}$

This is also revealed if the stress state is investigated:

$$\boldsymbol{\sigma}_{\mathbf{x}_{low}} = \begin{Bmatrix} -1.534 \\ 0.978 \\ 0.969 \\ 0.001 \\ -0.920 \\ -0.000 \end{Bmatrix} \cdot 10^{-3} - \begin{Bmatrix} 0.991 \\ 1.000 \\ 1.001 \\ 0.000 \\ -0.001 \\ -0.000 \end{Bmatrix} \cdot 10^{-3} = \begin{Bmatrix} -2.524 \\ -0.022 \\ -0.032 \\ 0.001 \\ -0.919 \\ -0.000 \end{Bmatrix} \cdot 10^{-3}, \quad \boldsymbol{\sigma}_{\mathbf{x}_{up}} = \begin{Bmatrix} 1.468 \\ 0.071 \\ 0.018 \\ 0.001 \\ -0.102 \\ 0.001 \end{Bmatrix} \cdot 10^{-3} \tag{38}$$

If the pressure is varied linearly as shown in figure 4 then the actuator moves

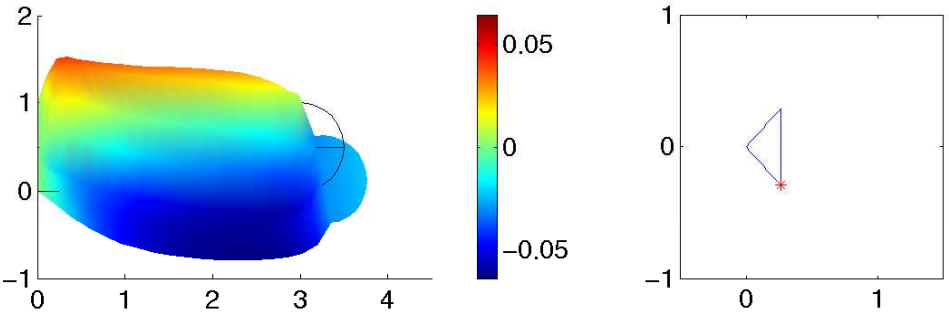

Figure 11. Left: Deformed actuator with pressurized upper domain. Right: Motion path with indication of current state. Deformations are exaggerated.

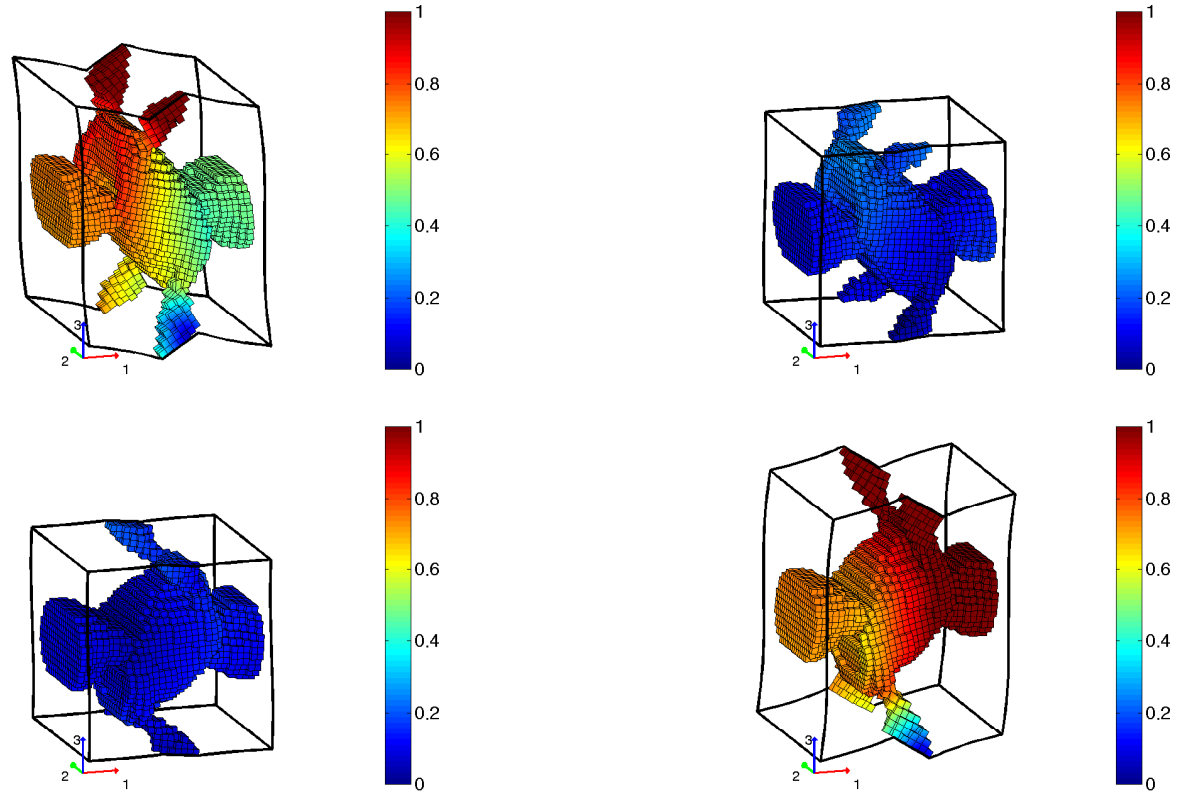

Figure 12. Deformed unit cells for the two materials (top and bottom) and for each load case (left/right). Color shows the deformation vector sum $\sqrt{u_1^2 + u_2^2 + u_3^2}$. Deformations are scaled by a factor 0.25. The unit-cells are located in the same points as the stresses are evaluated; $\mathbf{x}_{low} = (1.5, -0.5, 0.25)$ and $\mathbf{x}_{up} = (1.5, -0.5, 0.75)$

as shown in figure 11. The actuator is shown in a state where the upper domain is pressurized and the computed motion path is shown in the right figure.

7. Conclusion

This paper presents a method for multiscale optimization of poroelastic materials which might naturally be extended to dynamic or quasi-static problems using the full Biot

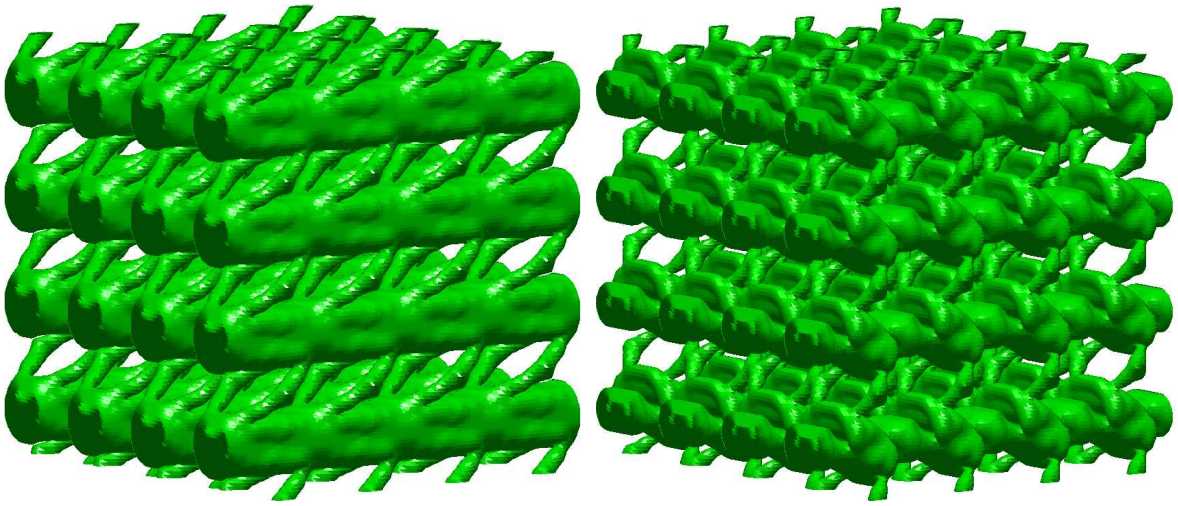

Figure 13. Smoothed and repeated unit cells for the optimized material 1 shown in figure 7 and 10

equations. The optimization of a single material actuator was compared with the results obtained optimizing the pressure coupling of the microstructure. A bimorph poroelastic actuator was optimized subject to a volume constraint and a set of additional constraints was imposed in order to ensure both extension and deflection of the actuator.

A future extension include the possibility of making hirahical optimization in which either each element or regions of elements have individual material configuration in the same fashion as shown by Coelho et al. (2008). By employing the poroelastic model in a bone remodelling process it would be possible to study the impact of internal fluid flow on the design of the scaffolds.

Acknowledgments

This research was conducted within the DCAMM Research School through a grant from the Danish Agency for Science, Technology and Innovation. The authors would like to thank the members of the TopOpt research group (www.topopt.dtu.dk) for fruitful discussions.

References

Andreasen C S & Sigmund O 2011 *Structural and Multidisciplinary Optimization* **43**, 693–706.

Auriault J L, Boutin C & Geindreau C 2009 *Homogenization of Coupled Phenomena in Heterogeneous Media* ISTE Ltd and John Wiley & Sons Inc.

Auriault J L & Sanchez-Palencia E 1977 *Journal De Mecanique* **16**(4), 575–603.

Bendsøe M P 1989 *Structural and Multidisciplinary Optimization* **1**, 193–202. 10.1007/BF01650949.

Bendsøe M P, Guedes J M, Haber R B, Pedersen P & Taylor J E 1994 *Journal of Applied Mechanics* **61**(4), 930–937.

Bendsøe M P & Kikuchi N 1988 *Computer Methods in Applied Mechanics and Engineering* **71**(2), 197–224.

Borrvall T & Petersson J 2003 *International Journal For Numerical Methods In Fluids* **41**(1), 77–107.

Bourdin B 2001 *International Journal For Numerical Methods In Engineering* **50**, 2143–2158.

Bruns T & Tortorelli D 2001 *Computer Methods in Applied Mechanics and Engineering* **190**, 3443–3459.

Coelho P G, Fernandes P R, Guedes J M & Rodrigues H C 2008 *Structural and Multidisciplinary Optimization* **35**(2), 107–115.

Coelho P G, Fernandes P R, Rodrigues H C, Cardoso J B & Guedes J M 2009 *Journal of Biomechanics* **42**(7), 830–837.

Gersborg-Hansen A, Sigmund O & Haber R 2005 *Structural and Multidisciplinary Optimization* **30**, 181–192. 10.1007/s00158-004-0508-7.

Guedes J & Kikuchi N 1990 *Computer Methods in Applied Mechanics and Engineering* **83**(2), 143–198.

Kreissl S, Pingen G, Evgrafov A & Maute K 2010 *Structural and Multidisciplinary Optimization* **42**, 495–516. 10.1007/s00158-010-0526-6.

Liu L, Yan J & Cheng G 2008 *Computers & Structures* **86**(13-14), 1417 – 1425.

Mei C C & Vernescu B 2010 *Homogenization methods for multiscale mechanics* World Scientific Singapore; Hackensack, NJ.

Michaleris P, Tortorelli D A & Vidal C A 1994 *Int. J. Numer. Meth. Engng.* **37**(14), 2471–2499.

Nui B, Jun Y & Cheng G 2008 *Structural And Multidisciplinary Optimization* **39**(2), 115–132.

Rodrigues H, Guedes J & Bendsøe M 2002 *Structural and Multidisciplinary Optimization* **24**, 1–10. 10.1007/s00158-002-0209-z.

Sanchez-Palencia E 1980 *Non-homogeneous media and vibration theory* Lecture Notes in Physics, 127. Berlin Heidelberg New York: Springer- Verlag.

Sigmund O 1997 *Mechanics of Structures and Machines* **25**(4), 493–524.

Sigmund O 2001 *Computer Methods in Applied Mechanics and Engineering* **190**(49-50), 6577–6604.

Stolpe M & Svanberg K 2001 *Structural and Multidisciplinary Optimization* **22**(2), 116–124.

Svanberg K 1987 *International Journal for Numerical Methods in Engineering* **24**(2), 359–373.

Terada K, Ito T & Kikuchi N 1998 *Computer Methods in Applied Mechanics and Engineering* **153**, 223–257.

Wang H F 2000 *Theory of Linear Poroelasticity with Applications to Geomechanics and Hydrogeology* Princeton University Press.

Xu S & Cheng G 2010 *Structural and Multidisciplinary Optimization* **41**(4), 575–587.

Yoon G H 2010 *International Journal for Numerical Methods in Engineering* **82**(5), 591–616.

Appendix A. Sensitivity calculation

The sensitivities can all be obtained without having to solve any adjoint problems.

Appendix A.1. Pressure coupling coefficient

$$\int_\Omega \varepsilon_{ij}(\mathbf{v}) E_{ijlm}(\rho) \varepsilon_{lm}(\boldsymbol{\xi}^{kh}) \,\mathrm{d}\Omega = \int_\Omega \varepsilon_{ij}(\mathbf{v}) E_{ijkh}(\rho) \,\mathrm{d}\Omega \tag{A.1}$$

$$\alpha_{kh} = \frac{1}{|\Omega|} \int_\Omega \left[(1 - \zeta(\rho)) \delta_{kh} + \varepsilon_{ij}(\boldsymbol{\xi}^{kh}) \delta_{ij} \zeta(\rho) \right] \,\mathrm{d}\Omega \tag{A.2}$$

By defining the augmented Lagrangian ($\mathcal{L}$) from the objective and the residual multiplied by the adjoint variable the sensitivities can be found by differentiating $\mathcal{L}$

$$\begin{aligned} \frac{\partial \mathcal{L}_{kh}}{\partial \rho} = & \frac{1}{|\Omega|} \int_\Omega \left[-\zeta'(\rho) \delta_{kh} + \varepsilon_{ij}(\boldsymbol{\xi}^{kh}) \delta_{ij} \zeta'(\rho) \right] \,\mathrm{d}\Omega \\ & + \frac{1}{|\Omega|} \int_\Omega \varepsilon_{ij}(\boldsymbol{\lambda}^{kh}) E'_{ijkh}(\rho) \,\mathrm{d}\Omega - \frac{1}{|\Omega|} \int_\Omega \varepsilon_{ij}(\boldsymbol{\lambda}^{kh}) E'_{ijlm}(\rho) \varepsilon_{lm}(\boldsymbol{\xi}^{kh}) \,\mathrm{d}\Omega \end{aligned} \tag{A.3}$$

$$\frac{\partial \mathcal{L}_{kh}}{\partial \mathbf{u}} \frac{\mathrm{d}\mathbf{u}}{\mathrm{d}\rho} = \frac{1}{|\Omega|} \int_\Omega \varepsilon_{ij}(\boldsymbol{\xi}'^{kh}) \delta_{ij} \zeta(\rho) \,\mathrm{d}\Omega - \frac{1}{|\Omega|} \int_\Omega \varepsilon_{ij}(\boldsymbol{\lambda}^{kh}) E_{ijlm} \varepsilon_{lm}(\boldsymbol{\xi}'^{kh}) \,\mathrm{d}\Omega \tag{A.4}$$

Letting all terms that are multiplied by the state sensitivity $\frac{\mathrm{d}\mathbf{u}}{\mathrm{d}\rho}$ be zero the adjoint problem is obtained

Find $\boldsymbol{\lambda} \in \mathcal{V}^3$ for all $\hat{\boldsymbol{\lambda}} \in \mathcal{V}_0^3$ such that

$$\int_\Omega \varepsilon_{ij}(\boldsymbol{\lambda}^{kh}) E_{ijlm} \varepsilon_{lm}(\hat{\boldsymbol{\lambda}}^{kh}) \,\mathrm{d}\Omega = \int_\Omega \varepsilon_{ij}(\hat{\boldsymbol{\lambda}}^{kh}) \delta_{ij} \zeta(\rho) \,\mathrm{d}\Omega \tag{A.5}$$

which does not change for kh and is equivalent to the triaxial loading problem (11). This yields the final sensitivity expression

$$\begin{aligned} \frac{\mathrm{d}\alpha_{kh}}{\mathrm{d}\rho} = & \frac{1}{|\Omega|} \int_\Omega \left[-\zeta(\rho) \delta_{kh} + \varepsilon_{ij}(\boldsymbol{\xi}^{kh}) \delta_{ij} \zeta'(\rho) \right] \,\mathrm{d}\Omega \\ & + \frac{1}{|\Omega|} \int_\Omega \varepsilon_{ij}(\boldsymbol{\eta}) E'_{ijkh}(\rho) \,\mathrm{d}\Omega - \frac{1}{|\Omega|} \int_\Omega \varepsilon_{ij}(\boldsymbol{\eta}) E'_{ijlm}(\rho) \varepsilon_{lm}(\boldsymbol{\xi}^{kh}) \,\mathrm{d}\Omega \end{aligned} \tag{A.6}$$

Appendix A.2. Stiffness

The sensitivities of the homogenized stiffness tensor with respect to the design variables can be computed by direct differentiation of the averaging expression

$$E^H_{ijkl} = \frac{1}{|\Omega|} \int_\Omega \left(\varepsilon^{(0)kl}_{pq} - \varepsilon^{kl}_{pq} \right) E_{pqrs} \left(\varepsilon^{(0)ij}_{rs} - \varepsilon^{ij}_{rs} \right) \,\mathrm{d}V \tag{A.7}$$

Taking the derivative yields

$$\begin{aligned}\frac{\mathrm{d}E^H_{ijkl}}{\mathrm{d}\rho} =& -\frac{1}{|\Omega|}\int_\Omega \frac{\partial \varepsilon^{kl}_{pq}}{\partial \rho} E_{pqrs}\left(\varepsilon^{(0)ij}_{rs} - \varepsilon^{ij}_{rs}\right)\,\mathrm{d}V \\ &+\frac{1}{|\Omega|}\int_\Omega \left(\varepsilon^{(0)kl}_{pq} - \varepsilon^{kl}_{pq}\right)\frac{\partial E_{pqrs}}{\partial \rho}\left(\varepsilon^{(0)ij}_{rs} - \varepsilon^{ij}_{rs}\right)\,\mathrm{d}V \\ &-\frac{1}{|\Omega|}\int_\Omega \left(\varepsilon^{(0)kl}_{pq} - \varepsilon^{kl}_{pq}\right) E_{pqrs}\frac{\partial \varepsilon^{ij}_{rs}}{\partial \rho}\,\mathrm{d}V \end{aligned} \tag{A.8}$$

Differentiating equation (8) yields

$$\int_\Omega \frac{\partial E_{ijpq}}{\partial \rho}\left(\varepsilon^{(0)kl}_{pq} - \varepsilon^{kl}_{pq}\right)\widehat{\varepsilon}_{ij}\,\mathrm{d}V = \int_\Omega E_{ijpq}\frac{\partial \varepsilon^{kl}_{pq}}{\partial \rho}\widehat{\varepsilon}_{ij}\,\mathrm{d}V \tag{A.9}$$

As $\widehat{\varepsilon}_{ij}$ is any admissible strain field it can be inserted in equation (A.8) which then reduce to

$$\frac{\mathrm{d}E^H_{ijkl}}{\mathrm{d}\rho} = -\frac{1}{|\Omega|}\int_\Omega \left(\varepsilon^{(0)kl}_{pq} - \varepsilon^{kl}_{pq}\right)\frac{\partial E_{pqrs}}{\partial \rho}\left(\varepsilon^{(0)ij}_{rs} - \varepsilon^{ij}_{rs}\right)\,\mathrm{d}V \tag{A.10}$$

Publication [P3]

Topology optimization of fluid-structure-interaction problems using the Biot consolidation equations

Topology optimization of fluid-structure-interaction problems using the Biot consolidation equations

Casper Schousboe Andreasen*[,1], Ole Sigmund[1]

Department of Mechanical Engineering, Solid Mechanics, Technical University of Denmark, Nils Koppels Alle, Building 404, DK-2800 Kgs. Lyngby, Denmark

Abstract

This paper presents a method for applying topology optimization to fluid-structure interaction problems in a saturated poroelastic media. The method relies on the multiple-scales method applied to a periodic media. The resulting model couples the Stokes flow in the pores of the structure with the deformation of the elastic skeleton through a macroscopic Darcy-type flow law. The method allows to impose pressure loads for static problems through a one way coupling, while transient problems are fully coupled.

Key words: Topology optimization, Finite elements, poroelasticity, coupled problem

1. Introduction

Fluid structure interaction (FSI) problems appear in many engineering problems in e.g. the aircraft and automotive industry as well as in porous flow problems. Tools for simulating the interaction between a flow and a structure are widely available. Performance optimization plays a major role in the industry and tools for optimizing the shape of a design are available; however, these optimization tools rely on a priori design consideration where the boundaries are given explicitly. An alternative approach where the initial design is unimportant is topology optimization in which material is distributed within a design domain and thereby omits the need for any explicitly defined internal boundaries.

Topology optimization has been applied to a variety of different physics problems and has been shown to be a remarkably efficient tool when a new design or material layout is sought for [5]. The method presented in this paper relies on the same principles used in the seminal paper by Bendsøe and Kikuchi[7]. This method is often referred to as the homogenization approach to topology optimization as the effective parameters for a unit cell with fixed topology but varying density are computed. The homogenized properties link the design interpolation to a known microstructure. This as opposed to the more popular SIMP method [6] in which the microstructures are of less interest as the desired final design is supposed to be binary, solid-void with a fixed length-scale.

The topology optimization method has successfully been applied to fluid mechanical design problems. Borrvall and Petersson[9] optimized Stokes flow problems using the Brinkman equation. This was further extended to low to moderate Reynolds number flows in [15]. However, this approach represents the non-fluid regions as infinitely stiff, a penalty to the flow, such that no interaction is modeled. The application of topology optimization to FSI-problems has only recently been approached as the development of a monolithic formulation that describes both the fluid motion and the solid deformation is difficult. Yoon[40] presents a method for solving static FSI-problems by converting the stresses at the fluid-solid interfaces into a volume integral representation. In [20] flexible micro-fluidic devices are optimized using a one way coupling. Acoustic-structure interaction problems were optimized in [41] using a mixed formulation and in [21, 22] using Biot theory.

The approach taken in this paper differs from the former as it is based on the homogenization theory of deformable saturated porous media [4, 25, 3]. The resulting macroscopic equations are similar to those of Biot[8] which were derived using a phenomenological approach without microstructure considerations. The two scale model assumes Stokes flow through the microstructure, which at the macroscopic scale results in a Darcy flow model, which might seem odd as this models a potential flow. However, the friction is handled in the microstructure and hence included through the permeability. At the macroscale effective material can be distributed and due to the homogenization all densities represent a specific microstructure.

Previously, the homogenization theory and topology optimization has been combined in the design of new and better materials. This includes materials with prescribed elastic properties [26, 27], maximum bulk modulus[28, 29], extreme thermal expansion coefficients [31, 32], piezoelectric properties[33], permeability [17, 18], maximum pressure coupling [1] etc.

The optimization of the material microstructure has also been coupled to the macrostructure performance. Minimum compliance designs under a seepage constraint are considered in [39] while a two scale model was used to optimize the material design based on the performance of a poroelastic actuator in [2]. The multiscale idea was taken even further for hierachial de-

*Corresponding author. Ph.: +45 4525 4262, Fax: +45 4525 1475

Email addresses: csan@mek.dtu.dk (Casper Schousboe Andreasen), sigmund@mek.dtu.dk (Ole Sigmund)

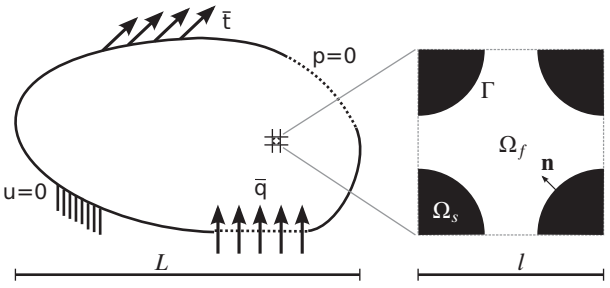

Figure 1: Illustration of macro problem with boundary conditions and the periodic microstructure along with their length scales.

signs of elastic structures in [24, 14] and in [37] for thermal structures.

In this paper the microstructure topology is not optimized; however, the interpolation schemes are obtained by the homogenization approach in order to provide a physical interpretation of the design variables. The optimization concerns the macroscopic material distribution in a saturated porous media. Due to the flow coupling the governing equations are transient even though the original problem is assumed quasi-static i.e. inertia terms are negligible.

Section 2 is an introduction to multiple-scales expansion and the resulting scale related equations. In section 3 the finite element discretization is presented while the material interpolation schemes are obtained using interpolation of the homogenization results in section 4. In section 5 the optimization problem is presented and the optimization results are shown in section 6. Finally, conclusions are drawn in section 7.

2. Physical Model

In this work a structure consisting of a saturated porous elastic material is considered. This is shown in figure 1 where both the macroscale problem and the locally periodic microstructure are illustrated. Considering the periodic microstructure which consists of a solid domain Ω_s (governed by the Navier-Cauchy equation) and a fluid domain Ω_f (governed by the incompressible Navier-Stokes equation) along with the interface boundary conditions on Γ, the fundamental behavior is described by

$$\nabla_X \cdot \boldsymbol{\sigma}_s = \rho_s \frac{\partial^2 \mathbf{u}}{\partial t^2} \qquad \text{in } \Omega_s \qquad (1)$$

$$\text{where} \quad \boldsymbol{\sigma}_s = \mathbf{C} : \boldsymbol{\varepsilon}_X(\mathbf{u})$$

$$\nabla_X \cdot \boldsymbol{\sigma}_f = \rho_f \left(\frac{\partial \mathbf{v}}{\partial t} + \mathbf{v} \nabla \cdot \mathbf{v} \right) \qquad \text{in } \Omega_f \qquad (2)$$

$$\text{where} \quad \boldsymbol{\sigma}_f = 2\mu \mathbf{D}(\mathbf{v}) - p\mathbf{I}$$

$$\nabla_X \cdot \mathbf{v} = 0 \qquad \text{in } \Omega_f \qquad (3)$$

$$(\boldsymbol{\sigma}_s - \boldsymbol{\sigma}_f)\mathbf{n} = 0 \qquad \text{on } \Gamma \qquad (4)$$

$$\dot{\mathbf{u}} - \mathbf{v} = 0 \qquad \text{on } \Gamma \qquad (5)$$

where $\mathbf{u}$ is the solid deformation, $\mathbf{C}$ is the elastic stiffness tensor, $\boldsymbol{\varepsilon}_X(\mathbf{u})$ is the linear strain, $\dot{\mathbf{u}}$, $\mathbf{v}$ the solid and fluid velocity respectively, $\mathbf{n}$ the unit normal to Γ and $\mathbf{D}(\mathbf{v})$ is the strain rate tensor.

By assuming a periodic medium and applying a two scale expansion of the above system several different models can appear depending on the influence from viscosity[3]. This ranges from a relatively slow moving fluid with low viscosity which results in a diphasic macroscopic formulation, meaning that both solid and fluid movement is solved at the macroscopic scale, to a monophasic viscoelastic description where the fluid has a high viscosity and moves so slow relative to the solid that it is better described using displacements than velocity.

In this study the fluid is moving slowly relative to the solid which justifies that the convective term in the Navier-Stokes equation is neglected. Furthermore the inertia terms are assumed small and therefore also neglected. Following the two-scale asymptotic expansion and separation of scales as presented in [25, 3] two sets of equations are obtained, namely: one set describing the microscopic behavior and another describing the macroscopic which is similar to those of Biot [8].

In this study the microstructure equations are used to obtain the design interpolation functions for a fixed microstructure topology. The elastic micro-scale equations yield

Find $\boldsymbol{\xi}^{kh} \in \mathcal{V}^3$ and $\boldsymbol{\eta} \in \mathcal{V}^3$ such that

$$\int_\Omega c_{ijlm}\varepsilon_{ij}(\hat{\mathbf{u}})\varepsilon_{lm}(\boldsymbol{\xi}^{kh})\mathrm{d}\Omega = \int_\Omega c_{ijkh}\varepsilon_{ij}(\hat{\mathbf{u}})\mathrm{d}\Omega \quad \forall \hat{\mathbf{u}} \in \mathcal{V}_0^3 \qquad (6)$$

$$\int_\Omega c_{ijlm}\varepsilon_{ij}(\hat{\mathbf{u}})\varepsilon_{lm}(\boldsymbol{\eta})\mathrm{d}\Omega = \int_\Omega \varepsilon_{ij}(\hat{\mathbf{u}})\delta_{ij}\mathrm{d}\Omega \quad \forall \hat{\mathbf{u}} \in \mathcal{V}_0^3 \qquad (7)$$

where $c_{ijlm} = C_{ijlm}/c^*$ is the nondimensionalized stiffness tensor of the basis material. From these, the homogenized properties can be extracted using the volumetric averages:

$$C^H_{ijkh} = \frac{c^*}{|\Omega|}\int_\Omega \left(c_{ijkh} - c_{ijlm}\varepsilon_{lm}(\boldsymbol{\xi}^{kh}) \right) \mathrm{d}\Omega \qquad (8)$$

$$\alpha_{ij} = \frac{1}{|\Omega|}\int_\Omega \left(\phi\delta_{ij} + c_{ijlm}\varepsilon_{lm}(\boldsymbol{\eta}) \right) \mathrm{d}\Omega \qquad (9)$$

$$\beta = \frac{1}{|\Omega|K_b^*}\int_\Omega \varepsilon_{ii}(\boldsymbol{\eta})\mathrm{d}\Omega \qquad (10)$$

where K_b^* is the bulk modulus of the basis material. However, using an isotropic basis material for the microstructure, the $\boldsymbol{\alpha}$ and β parameters can be computed as a function of the homogenized stiffness tensor and hence there is no need for solving equation (7) and computing (9) and (10) c.f. [23]. They yield

$$\alpha_{ij} = \delta_{ij} - \frac{C^H_{pqij}\delta_{pq}}{3\lambda + 2G} \qquad (11)$$

$$\beta = \frac{1}{3\lambda + 2G}\left(3(1-\phi) - \frac{C^H_{ppjj}}{3\lambda + 2G} \right) \qquad (12)$$

where $\lambda = E\nu/[(1+\nu)(1-2\nu)]$ and $G = E/[2(1+\nu)]$ are the Lamé coefficients of the basis material with Youngs modulus E and Poisson's ration ν.

The fluid flow through the microstructure is governed by the Stokes equations. The microscale flow equations yield

Find $\mathbf{v} \in \mathcal{W}^3$ and $p \in \mathcal{P}$ such that

$$\int_\Omega \hat{v}_{i,j} v^k_{i,j} \mathrm{d}\Omega - \int_\Omega p^k \hat{v}_{i,i} \mathrm{d}\Omega = \int_\Omega \hat{v}_i \delta_{ik} \mathrm{d}\Omega \quad \forall \hat{\mathbf{v}} \in \mathcal{W}^3_0 \tag{13}$$

$$\int_\Omega \hat{p} v^k_{i,i} \mathrm{d}\Omega = 0 \quad \forall \hat{p} \in \mathcal{P}_0 \tag{14}$$

from which the permeability can be computed as

$$K_{ik} = \frac{l^2}{|\Omega|} \int_\Omega v^k_i \mathrm{d}\Omega \tag{15}$$

where l is the characteristic length of the unit cell c.f. figure 1.

2.1. Macro equations

Having obtained the homogenized properties of the porous material these can be used in the macroscopic equations to compute the response to the loading. The equations yield

Find $\mathbf{u} \in \mathcal{V}^3$ and $p \in \mathcal{P}$ for all $\hat{\mathbf{u}} \in \mathcal{V}^3_0$ and $\hat{p} \in \mathcal{P}_0$ such that

$$\int_\Omega C^H_{ijkl} \varepsilon_{ij}(\hat{\mathbf{u}}) \varepsilon_{kl}(\mathbf{u}) \mathrm{d}\Omega - \int_\Omega p \alpha_{ij} \varepsilon_{ij}(\hat{\mathbf{u}}) \mathrm{d}\Omega = \int_{\Gamma_t} \hat{u}_i \bar{t}_i \mathrm{d}\Gamma \tag{16}$$

$$\int_\Omega \alpha_{ij} \varepsilon_{ij}(\dot{\mathbf{u}}) \hat{p} \mathrm{d}\Omega + \int_\Omega \beta \hat{p} \dot{p} \mathrm{d}\Omega + \int_\Omega \hat{p}_{,i} \frac{K_{ij}}{\mu} p_{,j} \mathrm{d}\Omega = -\int_{\Gamma_v} \bar{q} \hat{p} \mathrm{d}\Gamma \tag{17}$$

where C^H_{ijkl}, K_{ij}, α_{ij} and β are found using the interpolation functions. $\bar{t}_i$ denotes the traction applied at Γ_t and $\bar{q}$ denotes the flow flux at boundary Γ_v.

3. FEM discretization

Having the equation system given as in the equations (16) and (17) the system is discretized using finite elements resulting in the following equation system.

$$\begin{bmatrix} \mathbf{0} & \mathbf{0} \\ \mathbf{Q} & \mathbf{S} \end{bmatrix} \begin{Bmatrix} \dot{\mathbf{u}} \\ \dot{\mathbf{p}} \end{Bmatrix} + \begin{bmatrix} \mathbf{K}_s & -\mathbf{Q}^T \\ \mathbf{0} & \mathbf{H} \end{bmatrix} \begin{Bmatrix} \mathbf{u} \\ \mathbf{p} \end{Bmatrix} = \begin{Bmatrix} \mathbf{f} \\ \mathbf{g} \end{Bmatrix} \tag{18}$$

where the matrices are given by the following finite element assemblies

$$\mathbf{K}_s = \int_V \mathbf{B}^T \mathbf{C} \mathbf{B} \mathrm{d}\Omega, \qquad \mathbf{Q} = \int_V \mathbf{N}_p^T \boldsymbol{\alpha} \mathbf{B} \mathrm{d}\Omega \tag{19}$$

$$\mathbf{S} = \int_V \mathbf{N}_p^T \beta \mathbf{N}_p \mathrm{d}\Omega, \qquad \mathbf{H} = \int_V \mathbf{B}_p^T \mathbf{K} \mathbf{B}_p \mathrm{d}\Omega \tag{20}$$

$$\mathbf{f} = \int_{\Gamma_t} \mathbf{N}^T \bar{\mathbf{t}} \mathrm{d}\Gamma, \qquad \mathbf{g} = -\int_{\Gamma_v} \mathbf{N}_p^T \bar{\mathbf{q}} \mathrm{d}\Gamma \tag{21}$$

where $\mathbf{N}$ is the displacement shape function, $\mathbf{B}$ the strain displacement matrix, $\mathbf{N}_p$ the pressure shape function, $\mathbf{B}_p$ the pressure derivative and $\mathbf{C}$ the material stiffness matrix. The pressure coupling $\boldsymbol{\alpha}$ and the permeability $\mathbf{K}$ are given on vector form.

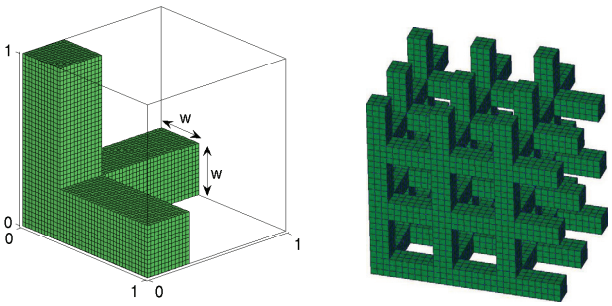

Figure 2: *Left:* Submersed cross microstructure topology studied in order to obtain the material interpolation scheme. Discretized by $40 \times 40 \times 40$ FEM mesh using first order elements for the homogenization of the permeability and stiffness. Periodic boundary conditions and corner node (0,0,0) fixed in order to prevent rigid body motion. Here shown for $w = 0.3$ *Right:* $3 \times 3 \times 3$ unit-cell ensemble.

4. Material interpolation

In order to obtain a material interpolation scheme a single microstructure topology is studied, in this case a submersed cross which is shown in figure 2. By varying the width of the cross section w the topology stays the same, but the relative density ($\rho = 3w^2 - 2w^3$) changes and by solving (13) and (6) and inserting in (15), (8), (11) and (12) the interpolation schemes in figure 3-5 are obtained.

The homogenization procedure is implemented using a fixed grid approach used in [1] which share similarities with that of Guedes and Kikuchi [16]. This means that the microscale equations are cast in a monolithic form where the stiffness is interpolated such that void has a very small stiffness to avoid a singular system. For the permeability computation this means that a Brinkman term [11] is added to the Stokes equation in order to penalize fluid flow in solid regions as in [9].

4.1. Interpolating the elastic parameters

The homogenized elastic properties have been plotted in figure 3 and denoted by their indices in the material stiffness matrix. As the material is orthotropic with cubic symmetry it is characterized by 3 unique material parameters, in this case represented by 3 entries from the stiffness matrix. For the curve fitting these properties may be interpolated using different schemes for the normal and shear stiffnesses. For the normal direction represented by $\tilde{C}_{1111} = C^H_{1111}/C_{1111}$ the RAMP interpolation scheme [34]

$$C^H_{1111}(\rho) = \left(C_{min} + \frac{\rho(1 - C_{min})}{1 + q(1 - \rho)} \right) C_{1111} \tag{22}$$

seems to fit well using the penalty factor $q = 2$ and a lower bound $C_{min} = 10^{-4}$ for the stiffness. The remaining two quantities are well interpolated by a power function also used for the SIMP approach [6]

$$C^H_x(\rho) = \rho^p C_x \tag{23}$$

using $p = 2.7$ and $p = 3.5$ for $\tilde{C}_{1122} = C^H_{1122}/C_{1122}$ and $\tilde{C}_{1212} = C^H_{1212}/C_{1212}$, respectively.

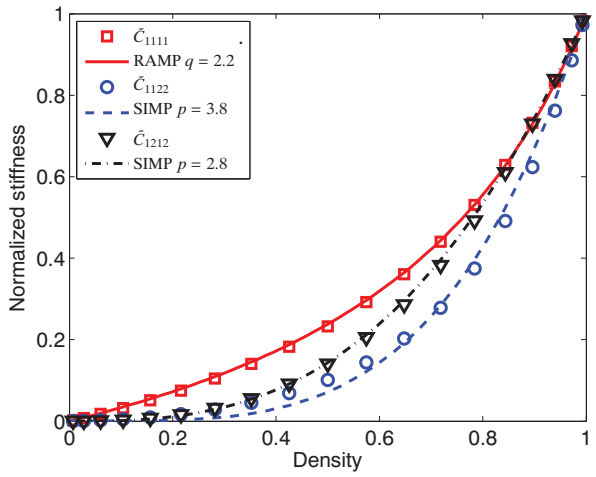

Figure 3: Homogenization results for the effective elastic tensor and the interpolation functions based on RAMP (22) and SIMP (23).

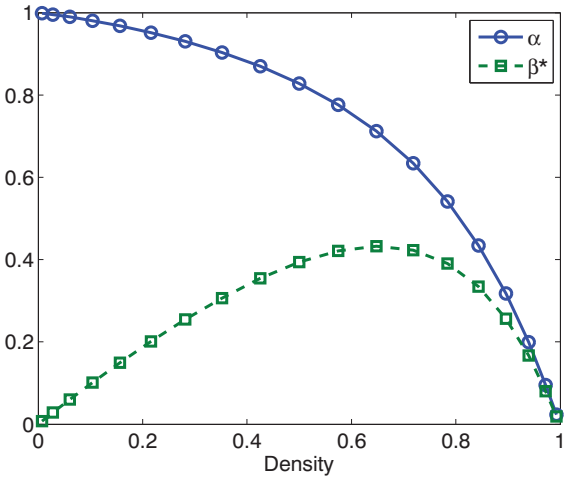

Figure 4: Homogenization results for the pressure coupling α and the compressibility β along with the interpolation curves computed by (11) and (12).

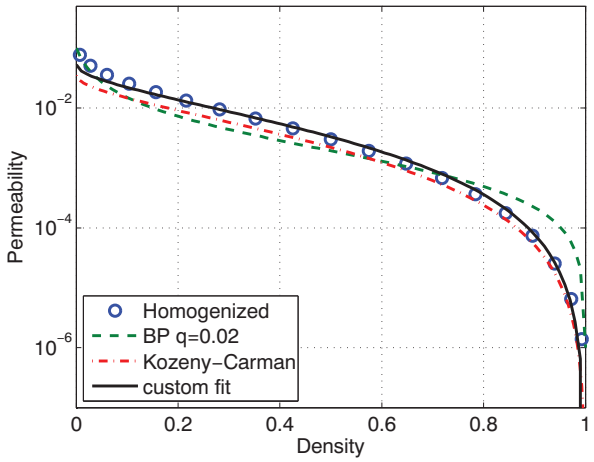

Figure 5: Homogenization results for the permeability and 3 interpolations. *BP* refers to equation (24), *KC* to equation (25) and *modified KC* to (26)

The coupling coefficient α is shown in figure 4 and yields a high interaction at low solid densities and decreases towards zero when the solid density is increased. The compressibility of the elastic skeleton, or the constrained specific storage[38], is described by the β parameter, which is also shown in the figure. These are, as mentioned previously, obtained directly from the effective stiffness and hence no interpolation is needed.

4.2. Interpolating the permeability

The homogenized permeability is shown in figure 5 and is compared to two different permeability interpolations. When the density gets very low it is seen that the permeability is increasing. This is of course due to the limiting case of free flow which however, is not covered by the model. At very high densities the microstructure is almost impermeable as the pores get very small. Even though the flow is computed three dimensionally the topology of the micro-structure makes the permeability tensor isotropic such that the permeability can be represented by a scalar. The permeability can then be computed as $K_{ij} = k\delta_{ij}$. The first interpolation function plotted is used in [9] and yields

$$k = \bar{k} + (\underline{k} - \bar{k})\rho\frac{1+r}{\rho+r} \tag{24}$$

here with $r = 0.03$, $\underline{k} = 10^{-6}$ and $\bar{k} = 0.1$. It is seen that this interpolation scheme does not interpolate the intermediate and high-density values very well, therefore a second interpolation scheme is proposed. This is the Kozeny-Carman (KC) relation [13], an empirical relation that relies on the topology of the microstructure and assumes a unidirectional flow. The permeability can be computed by

$$k = \frac{\phi^3}{cs^2} \tag{25}$$

where c is a geometric cross-section property ($c = 1.78$ for square pipes), ϕ is the porosity and s is the specific surface per

unit volume which for a square pipe yield $s = 4\phi/w_f$, where w_f is the pipe width. The submersed cross microstructure that is considered here is essentially a square pipe where a part of the boundary is fluid instead of solid. However as the other channels are orthogonal, the influence must be considered low. The KC relation is therefore plotted for an equivalent pipe i.e. with the same cross section size.

It is seen that the relation under predicts the permeability slightly, which could be due to a part of the boundary being fluid. A modification of the KC relation is proposed as an interpolation expression

$$k = 1.5\frac{\phi^3}{cs^2} \tag{26}$$

5. Topology Optimization

The optimization problems presented in this paper can all be cast into the general formulation of a non linear program

$$\min_{\boldsymbol{\rho}\in\mathbb{R}^N} \quad f_0(\boldsymbol{\rho}, \mathbf{u}, \mathbf{p}) \tag{27}$$

$$\text{s.t.} \quad \mathbf{r}(\boldsymbol{\rho}, \mathbf{u}(t), \mathbf{p}(t), \dot{\mathbf{u}}(t), \dot{\mathbf{p}}(t)) = 0 \tag{28}$$

$$\frac{1}{V_0}\sum_{e=1}^{N}\rho_e v_e - \gamma \leq 0 \tag{29}$$

$$\underline{\rho} \leq \rho_e \leq \bar{\rho} \qquad \text{for } e = 1, N \tag{30}$$

where $\mathbf{r}$ is the residual of the state equations, γ is the allowed solid volume fraction, N is the number of design variables and $(\underline{\rho}, \bar{\rho}) = (0.01, 0.99)$ are the limits for the design variables. These values are chosen such that the material will never be either solid or fluid as the interpolation of the permeability in the pure fluid limit is problematic. From a physical point of view the permeability in the pure fluid case is infinite and this is not covered by the model. Opposed to most topology optimization problems the scope of this study is not necessarily to end up in a black-white design as the intermediate design values have a clear interpretation.

The optimization problem is solved by the Method of Moving Asymptotes (MMA) by Svanberg[35] which requires the computation of the sensitivities of both objective function and constraints. Some of the objective functions used, vary in time, which is computationally demanding as opposed to the volume constraint for which the sensitivities are easily computed.

5.1. Sensitivity analysis

The discretized equation system in equation (18) can be generalized as

$$\mathbf{A}\dot{\mathbf{z}} + \mathbf{B}\mathbf{z} = \mathbf{f} \tag{31}$$

where neither the $\mathbf{A}$ nor the $\mathbf{B}$ matrix are symmetric. An objective function is introduced that may depend on design, time, deflection and velocity

$$g = \int_0^T h(\mathbf{z}, \dot{\mathbf{z}}, \boldsymbol{\rho}, t)\mathrm{d}t \tag{32}$$

The sensitivity of the general function g can be computed using the adjoint variable method [36, 19]. First the augmented Lagrangian is constructed which yields

$$L = \int_0^T h(\mathbf{z}, \dot{\mathbf{z}}, \boldsymbol{\rho}, t)\mathrm{d}t + \int_0^T \boldsymbol{\lambda}^T\left(\mathbf{A}\dot{\mathbf{z}} + \mathbf{B}\mathbf{z} - \mathbf{f}\right)\mathrm{d}t \tag{33}$$

where $\boldsymbol{\lambda}$ is the adjoint variable. In order to obtain the sensitivities of the Lagrangian it is differentiated with respect to the design variables $\boldsymbol{\rho}$

$$\frac{\mathrm{d}L}{\mathrm{d}\boldsymbol{\rho}} = \int_0^T \frac{\partial h}{\partial \boldsymbol{\rho}}\mathrm{d}t + \int_0^T \boldsymbol{\lambda}^T\left(\frac{\partial \mathbf{A}}{\partial \boldsymbol{\rho}}\dot{\mathbf{z}} + \frac{\partial \mathbf{B}}{\partial \boldsymbol{\rho}}\mathbf{z} - \frac{\partial \mathbf{f}}{\partial \boldsymbol{\rho}}\right)\mathrm{d}t \tag{34}$$

$$+ \underbrace{\int_0^T\left(\frac{\partial h}{\partial \mathbf{z}}\frac{\partial \mathbf{z}}{\partial \boldsymbol{\rho}} + \frac{\partial h}{\partial \dot{\mathbf{z}}}\frac{\partial \dot{\mathbf{z}}}{\partial \boldsymbol{\rho}}\right)\mathrm{d}t + \int_0^T \boldsymbol{\lambda}^T\left(\mathbf{A}\frac{\partial \dot{\mathbf{z}}}{\partial \boldsymbol{\rho}} + \mathbf{B}\frac{\partial \mathbf{z}}{\partial \boldsymbol{\rho}}\right)\mathrm{d}t}_{*} \tag{35}$$

By letting the $*$-marked terms equate zero, the computation of the derivative of the state variables with respect to the design can be omitted. The adjoint problem is hidden within these terms and by applying partial integration the sensitivity of the velocity can be eliminated. Furthermore assuming that $\mathbf{z}(0) = \mathbf{0}$ the adjoint system and its terminal condition yield

$$-\mathbf{A}^T\dot{\boldsymbol{\lambda}} + \mathbf{B}^T\boldsymbol{\lambda} = \left(-\frac{\partial h}{\partial \mathbf{z}} + \frac{\mathrm{d}}{\mathrm{d}t}\frac{\partial h}{\partial \dot{\mathbf{z}}}\right)^T \tag{36}$$

$$\frac{\partial h}{\partial \dot{\mathbf{z}}}(T) + \boldsymbol{\lambda}^T(T)\mathbf{A} = 0 \tag{37}$$

The sensitivities can now be evaluated using the remaining part of equation (35) as

$$\frac{\mathrm{d}g}{\mathrm{d}\boldsymbol{\rho}} = \frac{\mathrm{d}L}{\mathrm{d}\boldsymbol{\rho}} = \int_0^T \frac{\partial h}{\partial \boldsymbol{\rho}}\mathrm{d}t + \int_0^T \boldsymbol{\lambda}^T\left(\frac{\partial \mathbf{A}}{\partial \boldsymbol{\rho}}\dot{\mathbf{z}} + \frac{\partial \mathbf{B}}{\partial \boldsymbol{\rho}}\mathbf{z} - \frac{\partial \mathbf{f}}{\partial \boldsymbol{\rho}}\right)\mathrm{d}t \tag{38}$$

5.2. Density filtering

A standard density filter [12, 10] is imposed in order to ensure a smooth transition from dense to porous structure and to avoid too many local variations. The filter is defined by letting N_e be a list with the neighbors within the radius R to element e with corresponding coordinate $\mathbf{x}_e$. The filtered, *physical*, densities $\tilde{\rho}$ are then computed as

$$\tilde{\rho}_e = \frac{\sum_{i\in N_e} w(\mathbf{x}_i, \mathbf{x}_e)v_i\rho_i}{\sum_{i\in N_e} w(\mathbf{x}_i, \mathbf{x}_e)v_i} \tag{39}$$

where $w(\mathbf{x}_i, \mathbf{x}_e) = R - \|\mathbf{x}_i - \mathbf{x}_e\|$ is the weighting function and v_i the element volume. The chain-rule which is used to update the sensitivities is given as

$$\frac{\mathrm{d}f_0}{\mathrm{d}\rho_e} = \sum_{i\in N_e}\frac{\mathrm{d}f_0}{\mathrm{d}\tilde{\rho}_i}\frac{w(\mathbf{x}_e, \mathbf{x}_i)v_e}{\sum_{j\in N_i} w(\mathbf{x}_j, \mathbf{x}_i)v_j} \tag{40}$$

The filter is imposed for the FEM analysis as well as for the volume constraint.

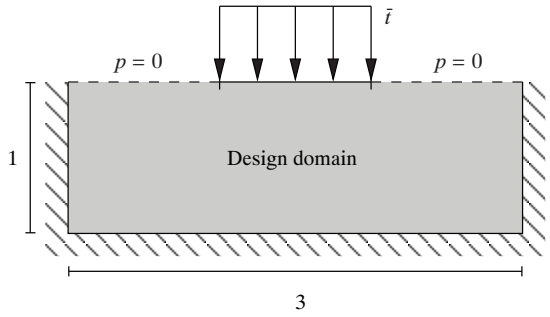

Figure 6: Computational domain and boundary conditions for the optimization of a deflection curve. The top boundary is divided into a loaded impermeable center part and two permeable (p=0) parts. The remaining boundaries are impermeable and displacements are fixed. Mesh 90×30 square u_2p_1 elements.

6. Results

Several examples are presented in order to demonstrate and discuss the advantages and limitations of the method. Transient topology optimization is very time and memory consuming and the problems call for a parallel approach; however, the modeling in this paper is based on a framework of Comsol Multiphysics and Matlab and therefore only 2D plane strain models will be presented.

6.1. Attaining a prescribed time-deflection curve

A potential application could be in the design of energy absorbers where the energy dissipation is due to the flow resistance. For such an application the deformation path is of interest. Here the rectangular semi-sealed bed shown in figure 6 is considered. The left, right and bottom boundaries are fixed. The top boundary is divided into an impermeable loaded center part ($\bar{t} = 0.01C_{1111}$) and two outer permeable parts ($p = 0$). The objective is to minimize the difference between a prescribed deflection and the actual deflection

$$f_0 = \int_0^T \int_{\Gamma_t} (u_2^* - u_2)^2 \mathrm{d}\Gamma \mathrm{d}t \tag{41}$$

The choice of micro structure size is influencing the permeability c.f. (15). The interplay between stiffness, loading and permeability determines the consolidation time which influences the optimized designs. If the microstructure size is very small the permeability is small and the structure will therefore not consolidate within the simulation time. Increasing the unit-cell size will introduce more entangled designs as the fluid needs to travel for a longer time in order to fit to the prescribed curve and consolidate around $t = 100s$. Figure 7 shows the optimized distribution for $E = 1MPa$, $\nu = 0.3$, $l = 10^{-3}m$, $\mu = 0.1Pa \cdot s$ using a simulation time of $100s$ and the prescribed deflection curve $u_2^* = 10^{-3}(t^2 - 200t)$. It should be noted that the loading is ramped such that the structure is only fully loaded after $5s$ using a smoothed Heaviside approximation function defined as

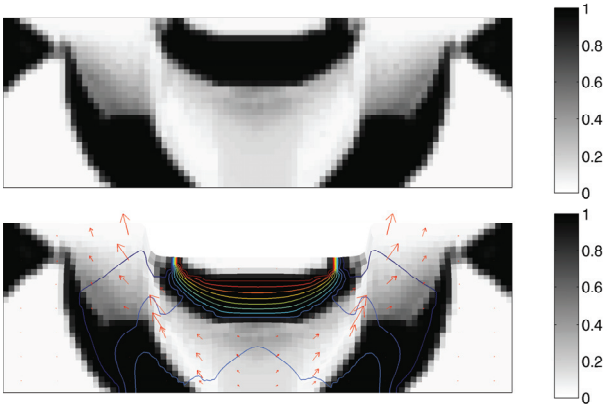

Figure 7: Optimized material distribution for the absorber problem using a simulation time of $100s$ and the predefined curve $u_2^* = 10^{-3}(t^2 - 200t)$. The lower figure shows the deformed state and the pressure contours along with indicators of flow direction.

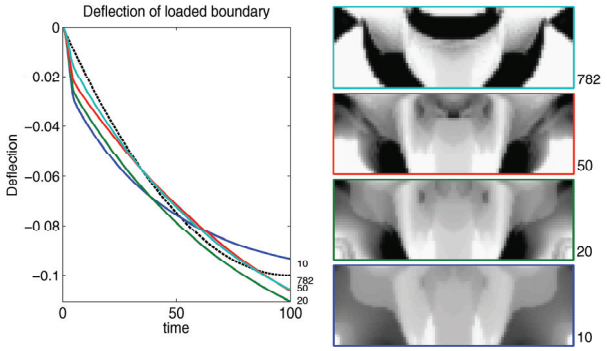

Figure 8: Optimization history for the optimization of the absorber problem. Deflection of the loaded boundary and the corresponding four designs are shown along with the predefined curve $u_2^* = 10^{-3}(t^2 - 200t)$

a piecewise smooth 3rd degree polynomial

$$H(t,a) = \begin{cases} 0 & ,t < -a \\ \frac{1}{2} + \frac{t}{a}(\frac{3}{4} - \frac{1}{4}\frac{t^2}{a^2}) & ,-a < t < a \\ 1 & ,t > a \end{cases} \tag{42}$$

where t is the time and $2a$ is the time for transition from 0 to 1.

The initial material distribution was uniform with density $\rho = 0.5$ and no constraint was imposed on the solid volume fraction during optimization. In order to give an impression of the evolution of the design, four design snapshots along with their respective deflection curves are shown in figure 8. It is seen that even though the curve approaches the predefined it is not possible to match the two exactly. It is furthermore evident that not much improvement is achieved from iteration 50 to 782 where the optimization process was considered converged. The final objective was $f_0 = 9.1 \cdot 10^{-4}$.

6.2. Internally pressurized lid

Another example, in which the loading is induced by a pressure, is that of an internally pressurized lid, see figure 9. A sim-

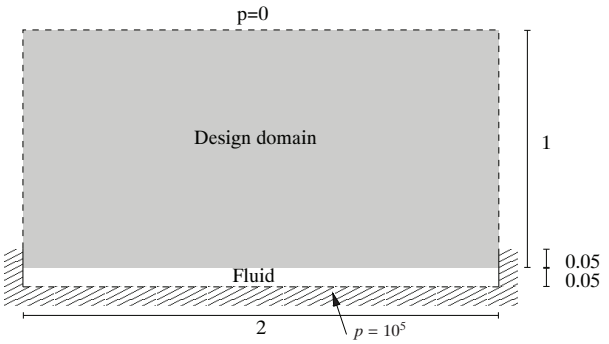

Figure 9: The design domain is fixed at the lower part of the vertical boundaries and loaded by the fluid at the lower boundary. The remaining boundary is free and permeable (p=0). The bottom part of the domain is fixed fluid domain.

ilar problem was presented in Sigmund and Clausen [30] which motivated the use of the mixed formulation for solving pressure loading problems. The design domain is loaded by a fluid which is present in a small domain below the design domain. The lower part of the vertical sides are fixed and the remaining boundary is free to move and is permeable (p=0).

The objective is the compliance function

$$f_0 = \int_0^T \int_\Omega \varepsilon_{ij} C_{ijkl} \varepsilon_{kl} \, \mathrm{d}\Omega \, \mathrm{d}t \tag{43}$$

and the solid volume fraction is limited to 50%.

The resulting topology from an optimization using steady-state modeling is shown in figure 10(a). It is seen that the structure is an arch just as obtained in Sigmund and Clausen [30] however, the final material distribution is not completely black-white. Some low-density material is present underneath the arch. Low density material is also deformed by the fluid and hence these intermediate densities lowers the compliance.

The steady-state design is compared to two transient optimization results with the same or smaller microstructure size shown in figure 10(b) and 10(c). The microstructure size used in figure 10(a) and figure 10(b) is the same and it is so large that the structure in the transient case consolidates within the simulation time. This, of course, is also reflected in the designs which are similar. When the microstructure is decreased, the permeability is also decreased and the simulation time is not long enough to make the structure consolidate. This is reflected in the design, figure 10(c), that does not have intermediate density material underneath the arch. This is due to the undeveloped fluid flow which induce less interaction with the low density material. The streamlines of the flow are also shown in the figures and it is seen that the fluid penetrates the *solid* material as it has a finite permeability.

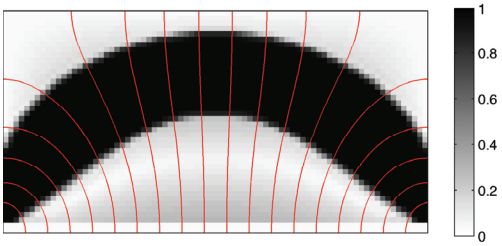

(a) Steady-state, $l = 10^{-3}$

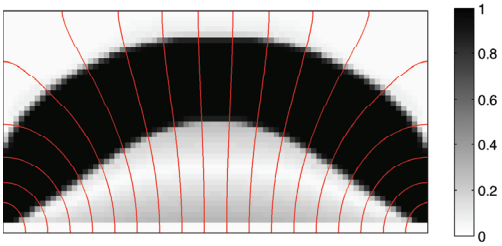

(b) Transient, $l = 10^{-3}$

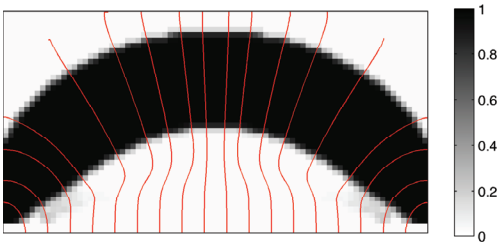

(c) Transient, $l = 10^{-3.5}$

Figure 10: Optimized topology obtained for minimum compliance design using a $p = 10^5$ with basis material parameters: $E = 10^6 Pa$, $\nu = 0.3$, $\mu = 1 Pa \cdot s$. Mesh 80×40 square $\mathrm{u_2p_1}$ elements. Streamlines are also plotted.

7. Conclusions

This paper presents a new method to optimize fluid-structure-interaction problems is porous elastic media.

References

[1] Andreasen, C. S. and Sigmund, O. (2011). Saturated poroelastic actuators generated by topology optimization. *Structural and Multidisciplinary Optimization*, 43:693–706.

[2] Andreasen, C. S. and Sigmund, O. (to be submitted). Multiscale optimization of poroelastic actuators. *Smart Materials & Structures*.

[3] Auriault, J. L., Boutin, C., and Geindreau, C. (2009). *Homogenization of Coupled Phenomena in Heterogeneous Media*. ISTE Ltd and John Wiley & Sons Inc.

[4] Auriault, J. L. and Sanchez-Palencia, E. (1977). Study of macroscopic behavior of a deformable saturated porous-medium. *Journal De Mecanique*, 16(4):575–603.

[5] Bendsøe, M. and Sigmund, O. (2003). *Topology Optimization - Theory, Methods and Applications*. Springer Verlag, 2nd edition.

[6] Bendsøe, M. P. (1989). Optimal shape design as a material distribution problem. *Structural and Multidisciplinary Optimization*, 1:193–202. 10.1007/BF01650949.

[7] Bendsøe, M. P. and Kikuchi, N. (1988). Generating optimal topologies in structural design using a homogenization method. *Computer Methods in Applied Mechanics and Engineering*, 71(2):197–224.

[8] Biot, M. A. (1941). General theory of three-dimensional consolidation. *Journal of Applied Physics*, 12(2):155–164.

[9] Borrvall, T. and Petersson, J. (2003). Topology optimization of fluids in Stokes flow. *International Journal for Numerical Methods in Fluids*, 41(1):77–107.

[10] Bourdin, B. (2001). Filters in topology optimization. *International Journal for Numerical Methods in Engineering*, 50:2143–2158.

[11] Brinkman, H. C. (1947). A calculation of the viscous force exerted by a flowing fluid on a dense swarm of particles. *Applied Scientific Research Section A-mechanics Heat Chemical Engineering Mathematical Methods*, 1(1):27–34.

[12] Bruns, T. and Tortorelli, D. (2001). Topology optimization of non-linear elastic structures and compliant mechanisms. *Computer Methods in Applied Mechanics and Engineering*, 190:3443–3459.

[13] Carman, P. (1937). Fluid flow through granular beds. *Transactions, Institution of Chemical Engineers, London*, 15:150–166.

[14] Coelho, P. G., Fernandes, P. R., Guedes, J. M., and Rodrigues, H. C. (2008). A hierarchical model for concurrent material and topology optimisation of three-dimensional structures. *Structural and Multidisciplinary Optimization*, 35(2):107–115.

[15] Gersborg-Hansen, A., Sigmund, O., and Haber, R. (2005). Topology optimization of channel flow problems. *Structural and Multidisciplinary Optimization*, 30:181–192. 10.1007/s00158-004-0508-7.

[16] Guedes, J. and Kikuchi, N. (1990). Preprocessing and postprocessing for materials based on the homogenization method with adaptive finite element methods. *Computer Methods in Applied Mechanics and Engineering*, 83(2):143–198.

[17] Guest, J. K. and Prévost, J. H. (2006). Optimizing multifunctional materials: Design of microstructures for maximized stiffness and fluid permeability. *International Journal of Solids and Structures*, 43(22-23):7028–7047.

[18] Guest, J. K. and Prévost, J. H. (2007). Design of maximum permeability material structures. *Computer Methods in Applied Mechanics and Engineering*, 196(4-6):1006–1017.

[19] Kang, B. S., Park, G. J., and Arora, J. S. (2006). A review of optimization of structures subjected to transient loads. *Structural and Multidisciplinary Optimization*, 31(2):81–95.

[20] Kreissl, S., Pingen, G., Evgrafov, A., and Maute, K. (2010). Topology optimization of flexible micro-fluidic devices. *Structural and Multidisciplinary Optimization*, 42:495–516. 10.1007/s00158-010-0526-6.

[21] Lee, J. S., Kim, E., Kim, Y. Y., Kim, J. S., and Kang, Y. J. (2007). Optimal poroelastic layer sequencing for sound transmission loss maximization by topology optimization method. *Journal of the Acoustical Society of America*, 122(4):2097–2106.

[22] Lee, J. S., Kim, Y. Y., Kim, J. S., and Kang, Y. J. (2008). Two-dimensional poroelastic acoustical foam shape design for absorption coefficient maximization by topology optimization method. *Journal of the Acoustical Society of America*, 123(4):2094–2106.

[23] Mei, C. C. and Vernescu, B. (2010). *Homogenization methods for multiscale mechanics*. World Scientific, Singapore; Hackensack, NJ.

[24] Rodrigues, H., Guedes, J., and Bendsøe, M. (2002). Hierarchical optimization of material and structure. *Structural and Multidisciplinary Optimization*, 24:1–10. 10.1007/s00158-002-0209-z.

[25] Sanchez-Palencia, E. (1980). *Non-homogeneous media and vibration theory*. Lecture Notes in Physics, 127. Berlin Heidelberg New York: Springer-Verlag.

[26] Sigmund, O. (1994). Materials with prescribed constitutive parameters: An inverse homogenization problem. *International Journal of Solids and Structures*, 31(17):2313–2329.

[27] Sigmund, O. (1995). Tailoring materials with prescribed elastic properties. *Mechanics of Materials*, 20(4):351–368.

[28] Sigmund, O. (1999). On the optimality of bone microstructure. In Pedersen, P. and Bendsøe, M., editors, *Synthesis in Bio Solid Mechanics*, pages 221–234. IUTAM, Kluwer.

[29] Sigmund, O. (2000). A new class of extremal composites. *Journal of the Mechanics and Physics of Solids*, 48(2):397 – 428.

[30] Sigmund, O. and Clausen, P. M. (2007). Topology optimization using a mixed formulation: An alternative way to solve pressure load problems. *Computer Methods in Applied Mechanics and Engineering*, 196(13-16):1874–1889.

[31] Sigmund, O. and Torquato, S. (1996). Composites with extremal thermal expansion coefficients. *Applied Physics Letters*, 69(21):3203–3205.

[32] Sigmund, O. and Torquato, S. (1997). Design of materials with extreme thermal expansion using a three-phase topology optimization method. *Journal of the Mechanics and Physics of Solids*, 45(6):1037–1067.

[33] Sigmund, O., Torquato, S., and Aksay, I. A. (1998). On the design of 1-3 piezocomposites using topology optimization. *Journal Of Materials Research*, 13(4):1038–1048.

[34] Stolpe, M. and Svanberg, K. (2001). An alternative interpolation scheme for minimum compliance topology optimization. *Structural and Multidisciplinary Optimization*, 22(2):116–124.

[35] Svanberg, K. (1987). The method of moving asymptotes - a new method for structural optimization. *International Journal for Numerical Methods in Engineering*, 24(2):359–373.

[36] Tortorelli, D. A., Lu, S. C. Y., and Haber, R. B. (1990). Design sensitivity analysis for elastodynamic systems. *Mechanics of Structures and Machines*, 18(1):77–106.

[37] Turteltaub, S. (2001). Optimal material properties for transient problems. *Structural and Multidisciplinary Optimization*, 22:157–166. 10.1007/s001580100133.

[38] Wang, H. F. (2000). *Theory of Linear Poroelasticity with Applications to Geomechanics and Hydrogeology*. Princeton University Press.

[39] Xu, S. and Cheng, G. (2010). Optimum material design of minimum structural compliance under seepage constraint. *Structural and Multidisciplinary Optimization*, 41(4):575–587.

[40] Yoon, G. H. (2010). Topology optimization for stationary fluid-structure interaction problems using a new monolithic formulation. *International Journal for Numerical Methods in Engineering*, 82(5):591–616.

[41] Yoon, G. H., Jensen, J. S., and Sigmund, O. (2007). Topology optimization of acoustic-structure interaction problems using a mixed finite element formulation. *International Journal For Numerical Methods In Engineering*, 70(9):1049–1075.

Publication [P4]

Topology optimization of microfluidic mixers

INTERNATIONAL JOURNAL FOR NUMERICAL METHODS IN FLUIDS
Int. J. Numer. Meth. Fluids 2009; **61**:498–513
Published online 26 November 2008 in Wiley InterScience (www.interscience.wiley.com). DOI: 10.1002/fld.1964

Topology optimization of microfluidic mixers

Casper Schousboe Andreasen*, †, Allan Roulund Gersborg and Ole Sigmund

Department of Mechanical Engineering, Solid Mechanics, Nils Koppels Allé, Technical University of Denmark, 2800 Kgs. Lyngby, Denmark

SUMMARY

This paper demonstrates the application of the topology optimization method as a general and systematic approach for microfluidic mixer design. The mixing process is modeled as convection dominated transport in low Reynolds number incompressible flow. The mixer performance is maximized by altering the layout of flow/non-flow regions subject to a constraint on the pressure drop between inlet and outlet. For a square cross-sectioned pipe the mixing is increased by 70% compared with a straight pipe at the cost of a 2.5 fold increase in pressure drop. Another example where only the bottom profile of the channel is a design domain results in intricate herring bone patterns that confirm findings from the literature. Copyright © 2008 John Wiley & Sons, Ltd.

Received 27 June 2008; Revised 6 October 2008; Accepted 6 October 2008

KEY WORDS: topology optimization; microfluidic mixing; stabilized FEM; convection dominated transport; sensitivity analysis; finite element methods; porous media; optimization; incompressible flow; Navier–Stokes; transport; micro-fluids; laminar flow

1. INTRODUCTION

Static microfluidic mixers appear in an abundance of different configurations, having all kinds of mixing improvers such as slanted grooves, herring bones, zig-zag walls, etc. The great variety of microfluidic mixers originate from the fact that the flow is laminar with a small Reynolds number. Therefore the mixing process relies mainly on the diffusive properties of the transported matter (see e.g. [1] for an introduction to mixing in microfluidics). To mix solutes with poor

*Correspondence to: Casper Schousboe Andreasen, Department of Mechanical Engineering, Solid Mechanics, Nils Koppels Allé, Technical University of Denmark, 2800 Kgs. Lyngby, Denmark.
†E-mail: csan@mek.dtu.dk

Contract/grant sponsor: DCAMM Research School through a grant from the Danish Agency for Science, Technology and Innovation
Contract/grant sponsor: Eurohorcs/ESF European Young Investigator Award (EURYI): 'Synthesis and topology optimization of optomechanical systems'
Contract/grant sponsor: Danish Center for Scientific Computing (DCSC)

diffusive properties, one can alter the geometry such that the flow distributes the matter more evenly in the solvent. By doing so, convection of matter is used as a mechanism to enhance mixing which; however, comes at the cost of an increased pressure drop between inlet and outlet. Stroock *et al*. [2] presented a mixer that induces chaotic advection by sequencing asymmetric microchannel sections containing staggered herringbones. For the systematic design of such microchannel mixers, topology optimization could be useful since no prerequisites are taken with respect to the geometry, only a design domain and boundary conditions need to be specified *a priori*.

The material distribution method for topology optimization was first presented by Bendsøe and Kikuchi [3] for solid mechanics problems. Since then, topology optimization has been introduced in several other branches of physics such as optics, acoustics and flows (see e.g. Bendsøe and Sigmund [4] for an overview of the subject).

Optimal design in fluid mechanics has been studied long before topology optimization was invented and optimal shapes minimizing the dissipated power for different profiles subjected to Stokes flow were already determined analytically in the 1970s by Pironneau [5] using shape optimization. As opposed to shape optimization, however, topology optimization allows introduction of new boundaries as the optimization progresses. This allows the topology to change several times during the optimization, which is impossible in shape optimization where the topology (i.e. the number of boundaries and connectivity) is predetermined.

In topology optimization the geometry is represented as a gray-scale image. The color in each pixel (finite element) represents a value of a physical parameter, e.g. permeability, such that black pixels represent small permeability (no-flow regions with 'solid-like' material) and white pixels represent large permeability (fluid regions). Computationally, the gray-scale in each element is a design variable. Based on repeated finite element analyses the design variables are updated using gradient driven math programming tools as described in e.g. [4].

Topology optimization in fluid mechanics was introduced by Borrvall and Petersson [6] modeling 2D flow in a Brinkman medium minimizing the dissipated power. The flow modeling was restricted to incompressible Stokes flow, neglecting the influence of inertia. In order to relax the optimization problem from an integer (black–white) problem where either fluid or solid property is allowed in an element, a porous flow model was introduced with a continuous (gray) permeability variable for each element. This leads to a design problem where flow and (all-most) non-flow regions develop by allowing interpolation between the lower and upper value of the permeability. The mathematical foundation was further investigated by Evgrafov [7] and the limiting cases of pure fluid and solid were included. A variation of the approach is presented in Guest and Prévost [8] where the Stokes and Darcy equations exist as two different models that are combined and scaled according to the permeability of each element. Furthermore, stabilized finite elements were used in order to use equal order velocity and pressure interpolation, as well as for avoiding a singular perturbation problem due to the coupled Stokes–Darcy problem. Wiker *et al*. [9] also considered topology optimization of Darcy–Stokes problems with focus on area-to-point flow problems.

The method has been extended to cover low to moderate Reynolds number flows in 2D, though still in the laminar regime, by Gersborg-Hansen *et al*. [10] and Olesen *et al*. [11]. The well posedness of the extension to the incompressible Navier–Stokes equations was discussed in detail by Evgrafov [12]. With respect to topology optimization of fluid transport problems, Thellner [13] provided examples with heat-transfer in 2D Stokes flow, Gersborg-Hansen [14] considered a convection dominated transport problem in a 2D rectangular microchannel and Okkels and Bruus [15] have investigated 2D catalytic microfluidic reactors. Recently, other approaches such as the

DOI: 10.1002/fld

lattice Boltzmann method by Pingen *et al*. [16] and kinetic gas theory by Evgrafov *et al*. [17] have been presented as alternative simulation methods.

Little work has been presented using 3D simulation methods, mainly due to the many design iterations, which limit the problem sizes in order to achieve an acceptable execution time. Recently, Pingen *et al*. [16] showed 3D nozzle design and Aage *et al*. [18] presented 3D Stokes flow problems and minimized the dissipative energy of some academic 3D problems which can be compared with the analytical results by Pironneau [5]. Three-dimensional Darcy–Stokes flow was also considered by Guest and Prévost [19] in order to optimize the permeability of material microstructures by a homogenization approach. Othmer [20] presents a method for implementing topology optimization of ducted flows with commercial CFD codes.

This work extends topology optimization of convection dominated transport problems to 3D. In this context, a standard streamline-upwind/Petrov–Galerkin (SUPG) stabilization scheme by Brooks and Hughes [21] is applied to stabilize the transport problem and the underlying flow problem is stabilized by the classical Galerkin-least-square (GLS) scheme by Hughes and Franca [22]. The former stabilization technique avoids numerical instabilities in transport problems due to a small coefficient of diffusion. The latter stabilization circumvents the Ladyzhenskaya–Babuška–Brezzi (LBB) condition, such that equal order velocity and pressure elements can be used to reduce the computational cost. The LBB condition is a compatibility condition that ensures convergence for the finite element problem, which in practice means that the polynomial order of the velocity interpolation should be one degree higher than the pressure interpolation.

The paper is organized as follows: Section 2 describes the continuous problem, Section 3 presents the stabilized finite element formulation, Section 4 introduces the topology optimization problem and associated sensitivity analysis and Section 5 covers further implementation aspects. Section 6 presents design examples and Section 7 contains a discussion and conclusions.

2. GOVERNING EQUATIONS

The flows considered in this paper are assumed to be microscale and therefore laminar. Furthermore, the flow speed is small compared with the speed of sound, which motivates a negligible compressibility; therefore the flow is modeled as incompressible. A porosity field is introduced in order to control the fluid paths through the domain. Regions with very high permeability can be considered pure fluid, whereas nearly no fluid can penetrate porous regions with low permeability. These low permeability regions are interpreted as solid regions.

For a domain Ω with partitioned boundary $\Gamma=\overline{\Gamma_{\text{in}}\cup\Gamma_{\text{wall}}\cup\Gamma_{\text{out}}}$, $\emptyset=\Gamma_{\text{in}}\cap\Gamma_{\text{wall}}\cap\Gamma_{\text{out}}$ cf. Figure 1, the porosity field is introduced in the steady-state Navier–Stokes equation as a source term $\alpha(\xi)\mathbf{u}$ yielding a Brinkman model with a convection term:

$$-\nabla\cdot(\mu(\nabla\mathbf{u}+(\nabla\mathbf{u})^{\mathrm{T}})-\mathbf{I}p)+\mathbf{u}\cdot\rho\nabla\mathbf{u}+\alpha(\xi)\mathbf{u}=\mathbf{0}\quad\text{in }\Omega \tag{1}$$

where α is the porosity field, ξ is the spatially varying design variable field, $\mathbf{u}$ is the velocity field, p is the pressure and $\mathbf{I}$ the identity tensor. The ξ field is fixed in the flow problem and determined by the optimization algorithm described in Section 4. μ is the viscosity and ρ is the mass density which are both constant throughout the domain. In this work the low Reynolds number limit is considered $Re=\rho U d_{\text{h}}/\mu<1$, where U is a reference velocity (here mean velocity) and d_{h} a length scale (here the hydraulic diameter). The hydraulic diameter is given by $d_{\text{h}}=4\mathscr{A}/\mathscr{C}$, where $\mathscr{A}$ is a cross-sectional area and $\mathscr{C}$ its circumference. The hydraulic diameter is a unification of the

DOI: 10.1002/fld

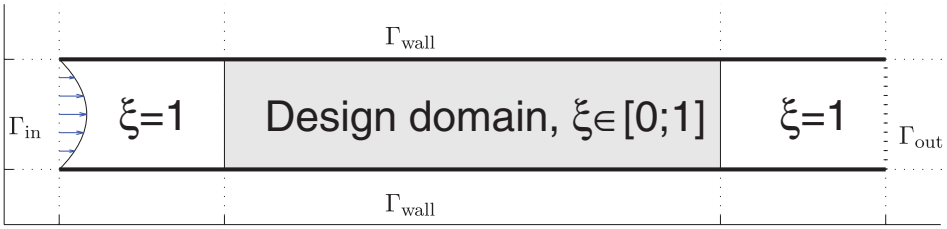

Figure 1. Principle sketch of the domain Ω. The design variable field ξ interpolates between a laminar flow model ($\xi=1$) and a model for porous flow ($\xi=0$). The boundary Γ consists of an inlet, a wall and an outlet part.

characteristic length for pipes with arbitrary cross-section, such that flow conditions for e.g. square and circular cross-sectioned pipes can be compared. In order to perform topology optimization, the α term in an element may take a finite value in the interval $0 \leqslant \alpha < +\infty$.

The incompressibility imposed on the conservation of mass yields the continuity equation:

$$-\nabla \cdot \mathbf{u} = 0 \quad \text{in } \Omega \tag{2}$$

Transport of matter with the flow is modeled by a convection–diffusion equation:

$$\mathbf{u} \cdot \nabla \phi - \frac{1}{Pe} \nabla^2 \phi = 0 \quad \text{in } \Omega \tag{3}$$

where ϕ measures the concentration of the matter, $Pe = U d_h / D$ is the Péclet number with U being a reference velocity (here mean velocity), D is the diffusivity and d_h the hydraulic diameter. In order to consider convection dominated transport, the $Pe \gg 1$ limit is considered and furthermore Pe is constant throughout the domain. Finally, a one-way coupling is assumed such that the flow Equations (1)–(2) are independent of the concentration ϕ governed by Equation (3).

The boundary conditions for the mixing problem take the following form: At Γ_{in} the velocity profile and a Heaviside concentration profile are prescribed (Dirichlet boundary conditions), at Γ_{wall} the velocity and the concentration flux are zero (Dirichlet and Neumann boundary conditions, respectively) and Γ_{out} is a free boundary where the pressure and normal stress are prescribed to zero and the concentration flux is zero (Neumann boundary conditions). In mathematical terms this becomes

$$\mathbf{u} = \mathbf{u}^*(s_1, s_2) \quad \text{and} \quad \phi(s_1) = \begin{cases} 0, & s_1 < 0.5 \\ 1, & s_1 = 0.5 \\ 2 & \text{otherwise} \end{cases} \quad \text{on } \Gamma_{in} \tag{4}$$

$$\mathbf{u} = \mathbf{0} \quad \text{and} \quad \nabla \phi \cdot \mathbf{n} = 0 \quad \text{on } \Gamma_{wall} \tag{5}$$

$$p = 0, \ (\mu(\nabla \mathbf{u} + (\nabla \mathbf{u})^T) - p\mathbf{I}) \cdot \mathbf{n} = \mathbf{0} \quad \text{and} \quad \nabla \phi \cdot \mathbf{n} = 0 \quad \text{on } \Gamma_{out} \tag{6}$$

where $\mathbf{I}$ is the identity tensor, $\mathbf{n}$ is the outward unit normal vector and (s_1, s_2) parameterize the boundaries Γ_{in} and Γ_{out} with $(s_1, s_2) \in [0; 1]^2$.

DOI: 10.1002/fld

3. FINITE ELEMENT FORMULATION

The finite element trial and test function spaces $\mathscr{J}_{\mathbf{u}}^{\mathrm{h}}$ and $\mathscr{V}_{\mathbf{u}}^{\mathrm{h}}$ for velocity, $\mathscr{J}_{p}^{\mathrm{h}}=\mathscr{V}_{p}^{\mathrm{h}}$ for pressure and $\mathscr{J}_{\phi}^{\mathrm{h}}$, $\mathscr{V}_{\phi}^{\mathrm{h}}$ for concentration are defined on Ω by use of tri-linear polynomials. For the design variable field ξ, the finite element trial and test function spaces $\mathscr{J}_{\xi}^{\mathrm{h}}=\mathscr{V}_{\xi}^{\mathrm{h}}$ are defined on Ω by use of piecewise constant polynomials. For the flow problem, this equal order interpolation of the velocity and the pressure fields does not fulfill the LBB condition [23], which is revealed numerically by pressure oscillations, if none or insufficient stabilization is introduced. The standard procedure to circumvent this is to use a GLS stabilized weak form [22], which penalizes large pressure gradients. With GLS stabilization the weak form of the flow Equations (1)–(2) is given as

Find $\mathbf{u}^{\mathrm{h}}\in\mathscr{J}_{\mathbf{u}}^{\mathrm{h}}$ and $p^{\mathrm{h}}\in\mathscr{J}_{p}^{\mathrm{h}}$ such that $\forall\hat{\mathbf{u}}^{\mathrm{h}}\in\mathscr{V}_{\mathbf{u}}^{\mathrm{h}}$ and $\forall\hat{p}^{\mathrm{h}}\in\mathscr{V}_{p}^{\mathrm{h}}$

$$\begin{aligned}&\mu\int_{\Omega}\nabla\hat{\mathbf{u}}^{\mathrm{h}}\cdot(\nabla\mathbf{u}^{\mathrm{h}}+(\nabla\mathbf{u}^{\mathrm{h}})^{\mathrm{T}})\,\mathrm{d}\Omega+\int_{\Omega}\hat{\mathbf{u}}^{\mathrm{h}}\cdot(\mathbf{u}^{\mathrm{h}}\cdot\rho\nabla\mathbf{u}^{\mathrm{h}})\,\mathrm{d}\Omega+\int_{\Omega}\hat{\mathbf{u}}^{\mathrm{h}}\cdot\alpha\mathbf{u}^{\mathrm{h}}\,\mathrm{d}\Omega\\&-\int_{\Gamma_{\mathrm{out}}}\hat{\mathbf{u}}^{\mathrm{h}}\cdot(\mu(\nabla\mathbf{u}^{\mathrm{h}}+(\nabla\mathbf{u}^{\mathrm{h}})^{\mathrm{T}})-\mathbf{I}p^{\mathrm{h}})\cdot\mathbf{n}\,\mathrm{d}\Gamma-\int_{\Omega}p^{\mathrm{h}}(\nabla\cdot\hat{\mathbf{u}}^{\mathrm{h}})\,\mathrm{d}\Omega-\int_{\Omega}\hat{p}^{\mathrm{h}}(\nabla\cdot\mathbf{u}^{\mathrm{h}})\,\mathrm{d}\Omega\\&+\sum_{e=1}^{n_{\mathrm{el}}}\int_{\Omega^{e}}\tau_{\mathrm{GLS}}(\nabla\hat{p}^{\mathrm{h}}\cdot\nabla p^{\mathrm{h}})\,\mathrm{d}\Omega=\mathbf{0}\end{aligned}\tag{7}$$

where n_{el} is the number of elements and Ω^{e} the domain for element e. The boundary term is zero since Γ_{out} is a free boundary cf. Equation (6). Here the stabilization parameter is chosen as

$$\tau_{\mathrm{GLS}}=\alpha_{0}\frac{\rho h_{e}^{2}}{4\mu}\tag{8}$$

where h_e is the element size and $\alpha_0=\frac{1}{3}$ as this appears to be the optimal value for linear elements [24]. Moreover, for the Stokes problem ($\rho=0,\alpha=0$) with linear velocity interpolation, this stabilization scheme is consistent since it yields a zero residual for an exact solution to the Stokes equations. The GLS stabilization deals with the LBB condition, but it does not fix the problems arising due to high flow speeds [24, 25]. In addition, in the very low permeability (Darcy) limit, stabilization may be required [26] also in the context of topology optimization [8]. However, since our scope is the transport in low speed laminar flow rather than high speed flows or transport in Darcy flows, both these stabilization techniques have been left out of this study.

In order to model convection dominated transport the transport problem is also stabilized to avoid using an extremely fine mesh resulting in large computation times. The weak form of Equation (3) including SUPG stabilization [21] yields

Find $\phi^{\mathrm{h}}\in\mathscr{J}_{\phi}^{\mathrm{h}}$ such that $\forall\hat{\phi}^{\mathrm{h}}\in\mathscr{V}_{\phi}^{\mathrm{h}}$:

$$\begin{aligned}&\int_{\Omega}\hat{\phi}^{\mathrm{h}}(\mathbf{u}^{\mathrm{h}}\cdot\nabla\phi^{\mathrm{h}})\,\mathrm{d}\Omega+\frac{1}{Pe}\int_{\Omega}\nabla\hat{\phi}^{\mathrm{h}}\cdot\nabla\phi^{\mathrm{h}}\,\mathrm{d}\Omega-\frac{1}{Pe}\int_{\Gamma_{\mathrm{wall}}\cup\Gamma_{\mathrm{out}}}\hat{\phi}^{\mathrm{h}}\nabla\phi^{\mathrm{h}}\cdot\mathbf{n}\,\mathrm{d}\Gamma\\&+\sum_{e=1}^{n_{\mathrm{el}}}\int_{\Omega^{e}}\tau_{\mathrm{SUPG}}\mathbf{u}^{\mathrm{h}}\cdot\nabla\hat{\phi}^{\mathrm{h}}\underbrace{\left(\mathbf{u}^{\mathrm{h}}\cdot\nabla\phi^{\mathrm{h}}-\nabla\cdot\left(\frac{1}{Pe}\nabla\phi^{\mathrm{h}}\right)\right)}_{\text{Strong form residual}}\mathrm{d}\Omega=0\end{aligned}\tag{9}$$

DOI: 10.1002/fld

where the boundary term is zero due to the boundary conditions imposed on ϕ. Notice, that for linear elements the second contribution in the residual is zero, thus large concentration gradients in the streamwise direction are penalized. Here the stabilization parameter τ_{SUPG} is determined as described in [27]

$$\tau_{\mathrm{SUPG}} = \left(\frac{4}{h_e^2 Pe} + \frac{2|\mathbf{u}^{\mathrm{h}}|}{h_e} \right)^{-1} \tag{10}$$

4. TOPOLOGY OPTIMIZATION

The optimization problems considered are mixing problems with the aim of determining the optimal material layout. The procedure is that a given spatial domain is divided into small (finite) elements where each of these can be either solid(black) or fluid(white). This yields an integer problem, which is difficult to solve computationally due to its non-differentiable nature. In order to deal with this, the optimization problem is relaxed by introducing continuous design variables, which can take any value between 0 (no flow) and 1 (fluid). The design variables enter the flow equation through the inverse permeability function $\alpha(\xi)$, cf. Equation (1). The optimization problem can then be stated as

$$\begin{aligned}
\min_{\boldsymbol{\xi}} \quad & \Phi = \frac{1}{\langle\phi\rangle_{\mathrm{in}}^2 \int_{\Gamma_{\mathrm{in}}} 1 \,\mathrm{d}\Gamma} \int_{\Gamma_{\mathrm{out}}} (\phi^{\mathrm{h}} - \langle\phi\rangle_{\mathrm{in}})^2 \,\mathrm{d}\Gamma \\
\text{s.t.} \quad & \text{Governing equations (7), (9)} \\
& \Delta p \leqslant \beta \Delta p_{\mathrm{ref}} \\
& \alpha_e(\xi_e) = \overline{\alpha} + (\underline{\alpha} - \overline{\alpha}) \xi_e \frac{1+q}{\xi_e + q} \quad \text{for } e = 1, \ldots, n_{\mathrm{el}} \\
& 0 \leqslant \xi_e \leqslant 1 \quad \text{for } e = 1, \ldots, n_{\mathrm{el}}
\end{aligned} \tag{11}$$

where $\boldsymbol{\xi} \in \mathbb{R}^{n_{\mathrm{el}}}$ is a vector of element design variables, which parameterizes the design variable field ξ^{h}, n_{el} is the number of elements and Φ is the cost function, which measures the mixing performance. The mixing performance is defined as the difference between the concentration at the outlet and the average inlet concentration $\langle\phi\rangle_{\mathrm{in}} = \int_{\Gamma_{\mathrm{in}}} \phi^{\mathrm{h}} \,\mathrm{d}\Gamma / \int_{\Gamma_{\mathrm{in}}} 1 \,\mathrm{d}\Gamma$ normalized with respect to the average inlet concentration, such that an ideal mixer will have the performance $\Phi_{\mathrm{ideal}} = 0$ due to conservation of mass, see Figure 2. The governing equations enter as constraints in the optimization problem and in order to control the pressure drop $\Delta p = \int_{\Gamma_{\mathrm{in}}} p^{\mathrm{h}} \,\mathrm{d}\Gamma$ between the inlet and the outlet, another constraint is imposed which limits it to a factor β times the pressure drop of the initial and empty straight pipe corresponding to $\boldsymbol{\xi} = \mathbf{1}$. The absolute pressure is fixed at zero at the outlet and therefore it does not enter into the constraint. The interpolation function α was first introduced by Borrvall and Petersson [6] and it plays an important role in topology optimization. The optimal material distribution for Stokes flow problems in terms of minimum pressure drop is black–white, i.e. as opposed to the interpolation used in e.g. topology optimization of solid structures [4], intermediate values of ξ (gray elements) are not favorable. Thus the minimum pressure drop problem in Stokes flow is self-penalized and the α function ensures that gray elements can appear in the problem. Gray elements are important in order to prohibit an integer nature of the optimization problem during the early design process. Moreover, from a physical point of

DOI: 10.1002/fld

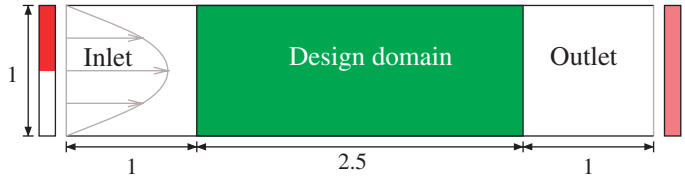

Figure 2. General problem definition for mixing problems. The modeling domain is divided into three subdomains: inlet, outlet and design domain. Flow field: The inlet velocity profile is parabolic in order to model fully developed pipe flow. The horizontal walls have a no slip condition $\mathbf{u}=0$ and the outlet is free such that normal stress $(\mu(\nabla\mathbf{u}+(\nabla\mathbf{u})^{\mathrm{T}})-p\mathbf{I})\cdot\mathbf{n}=\mathbf{0}$ and $p=0$. The concentration field: Heaviside profile at the inlet, no flux conditions at the horizontal walls $\nabla\phi\cdot\mathbf{n}=0$ and free at the outlet where the performance of the mixer is computed. The concentration is illustrated by the Heaviside function illustrated at the inlet and a uniform distribution at the outlet.

view the term $\alpha\mathbf{u}$, cf. Equation (1), penalizes large velocities in regions with low permeability. Even though the mixing problem is not a minimum pressure drop problem, the same interpolation function is used as it appears to work well, which we attribute to the pressure drop constraint. The bound values on $(\underline{\alpha},\overline{\alpha})=(0,10^4)$, are the minimum and maximum inverse permeabilities, q is a penalization parameter, here $q=1$. The zero lower bound on the inverse permeability is motivated from a physical point of view since the free stream is governed by the Navier–Stokes equations and the well posedness of the optimization problem for $\underline{\alpha}=0$ was considered in [7]. The last line in (11) defines box constraints on the design variables.

The optimization problem is solved using the method of moving asymptotes (MMA) [28], which works well for optimization problems with many design variables but few constraints. It is a gradient-based optimization algorithm that solves several convex and separable subproblems by an interior point method for each design iteration. In order to use the pressure drop constraint with the MMA algorithm it is turned into a function yielding a negative value if feasible and positive if violated. The pressure drop constraint is expressed as

$$g=\frac{\Delta p}{\beta\Delta p_{\mathrm{ref}}}-1\leqslant 0 \tag{12}$$

In the field of topology optimization a volume constraint is often imposed. However, for mixer design problems a volume constraint, limiting the amount of solid material, is hardly relevant since material weight is not an issue. Instead we impose the pressure drop constraint, which has obvious physical relevance.

4.1. Adjoint sensitivity analysis

In order to achieve consistent sensitivities the adjoint sensitivity analysis method [20, 29–31] is utilized resulting in new linear partial differential equations (PDEs) that need to be solved in order to compute the sensitivities. This is done by forming the Lagrangian, the sum of the objective function and the weak expressions for the state Equations (7)–(9) evaluated with the state solution $(\mathbf{u}^{\mathrm{h}},p^{\mathrm{h}},\phi^{\mathrm{h}})$ and with Lagrange multiplier fields $(\boldsymbol{\lambda}_{\mathbf{u}}^{\mathrm{h}},\lambda_p^{\mathrm{h}},\lambda_\phi^{\mathrm{h}})$ instead of the test functions $(\hat{\mathbf{u}}^{\mathrm{h}},\hat{p}^{\mathrm{h}},\hat{\phi}^{\mathrm{h}})$, and differentiating it with respect to the design variables. By rearranging the resulting expression, adjoint problems arise which when solved eliminate the direct computations of $\mathrm{d}\mathbf{u}^{\mathrm{h}}/\mathrm{d}\boldsymbol{\xi}$, $\mathrm{d}p^{\mathrm{h}}/\mathrm{d}\boldsymbol{\xi}$ and $\mathrm{d}\phi^{\mathrm{h}}/\mathrm{d}\boldsymbol{\xi}$, which are computationally expensive due to the large number of design

DOI: 10.1002/fld

variables. The result is an adjoint transport problem, where $\lambda_\phi^{\mathrm{h}}$ is the adjoint concentration field:

Find $\lambda_\phi^{\mathrm{h}} \in \mathscr{J}_\phi^{\mathrm{h}}$ such that $\forall \hat{\lambda}_\phi^{\mathrm{h}} \in \mathscr{V}_\phi^{\mathrm{h}}$

$$\int_\Omega \left(\lambda_\phi^{\mathrm{h}} (\mathbf{u}^{\mathrm{h}} \cdot \nabla \hat{\lambda}_\phi^{\mathrm{h}}) + \frac{1}{Pe} \nabla \lambda_\phi^{\mathrm{h}} \cdot \nabla \hat{\lambda}_\phi^{\mathrm{h}} \right) \mathrm{d}\Omega + \int_\Omega (\mathbf{u}^{\mathrm{h}} \cdot \nabla \lambda_\phi^{\mathrm{h}}) \tau_{\mathrm{SUPG}} \left(\mathbf{u}^{\mathrm{h}} \cdot \nabla \hat{\lambda}_\phi^{\mathrm{h}} - \frac{1}{Pe} \nabla^2 \hat{\lambda}_\phi^{\mathrm{h}} \right) \mathrm{d}\Omega$$
$$+ \frac{2}{\langle \phi \rangle_{\mathrm{in}}^2 \int_{\Gamma \mathrm{in}} 1 \, \mathrm{d}\Gamma} \int_{\Gamma_{\mathrm{out}}} \hat{\lambda}_\phi^{\mathrm{h}} (\phi - \langle \phi \rangle_{\mathrm{in}}) \, \mathrm{d}\Gamma = 0 \tag{13}$$

Having solved the adjoint transport problem, the adjoint flow problem (with unknowns $\boldsymbol{\lambda}_{\mathbf{u}}^{\mathrm{h}}$ and λ_p^{h}) can be solved where the adjoint concentration appears on the right-hand side:

Find $\boldsymbol{\lambda}_{\mathbf{u}}^{\mathrm{h}} \in \mathscr{J}_{\mathbf{u}}^{\mathrm{h}}$ and $\lambda_p^{\mathrm{h}} \in \mathscr{J}_p^{\mathrm{h}}$ such that $\forall \hat{\boldsymbol{\lambda}}_{\mathbf{u}}^{\mathrm{h}} \in \mathscr{V}_{\mathbf{u}}^{\mathrm{h}}$ and $\forall \hat{\lambda}_p^{\mathrm{h}} \in \mathscr{V}_p^{\mathrm{h}}$:

$$\int_\Omega [\nabla \boldsymbol{\lambda}_{\mathbf{u}}^{\mathrm{h}} \cdot \mu (\nabla \hat{\boldsymbol{\lambda}}_{\mathbf{u}}^{\mathrm{h}} + (\nabla \hat{\boldsymbol{\lambda}}_{\mathbf{u}}^{\mathrm{h}})^{\mathrm{T}}) - \lambda_p^{\mathrm{h}} (\nabla \cdot \hat{\boldsymbol{\lambda}}_{\mathbf{u}}^{\mathrm{h}}) + \boldsymbol{\lambda}_{\mathbf{u}}^{\mathrm{h}} \cdot (\hat{\boldsymbol{\lambda}}_{\mathbf{u}}^{\mathrm{h}} \cdot \rho \nabla \mathbf{u}^{\mathrm{h}} + \mathbf{u}^{\mathrm{h}} \cdot \rho \nabla \hat{\boldsymbol{\lambda}}_{\mathbf{u}}^{\mathrm{h}})$$
$$+ \boldsymbol{\lambda}_{\mathbf{u}}^{\mathrm{h}} \cdot \alpha(\xi) \hat{\boldsymbol{\lambda}}_{\mathbf{u}}^{\mathrm{h}}] \, \mathrm{d}\Omega - \int_\Omega \hat{\lambda}_p^{\mathrm{h}} (\nabla \cdot \boldsymbol{\lambda}_{\mathbf{u}}^{\mathrm{h}}) \, \mathrm{d}\Omega + \sum_{e=1}^{n_{\mathrm{el}}} \int_{\Omega^e} \tau_{\mathrm{GLS}} (\nabla \lambda_p^{\mathrm{h}} \cdot \nabla \hat{\lambda}_p^{\mathrm{h}}) \, \mathrm{d}\Omega$$
$$= - \int_\Omega \lambda_\phi^{\mathrm{h}} (\hat{\boldsymbol{\lambda}}_{\mathbf{u}}^{\mathrm{h}} \cdot \nabla \phi^{\mathrm{h}}) \, \mathrm{d}\Omega - \int_\Omega \left(\frac{\partial \tau_{\mathrm{SUPG}}}{\partial \mathbf{u}^{\mathrm{h}}} \cdot \hat{\boldsymbol{\lambda}}_{\mathbf{u}}^{\mathrm{h}} \right) \mathbf{u}^{\mathrm{h}} \cdot \nabla \lambda_\phi^{\mathrm{h}} \left(\mathbf{u}^{\mathrm{h}} \cdot \nabla \phi^{\mathrm{h}} - \frac{1}{Pe} \nabla^2 \phi^{\mathrm{h}} \right) \mathrm{d}\Omega$$
$$- \int_\Omega \tau_{\mathrm{SUPG}} \left[\hat{\boldsymbol{\lambda}}_{\mathbf{u}}^{\mathrm{h}} \cdot \nabla \lambda_\phi^{\mathrm{h}} \left(\mathbf{u}^{\mathrm{h}} \cdot \nabla \phi^{\mathrm{h}} - \frac{1}{Pe} \nabla^2 \phi^{\mathrm{h}} \right) + \mathbf{u}^{\mathrm{h}} \cdot \nabla \lambda_\phi^{\mathrm{h}} (\hat{\boldsymbol{\lambda}}_{\mathbf{u}}^{\mathrm{h}} \cdot \nabla \phi^{\mathrm{h}}) \right] \mathrm{d}\Omega \tag{14}$$

where

$$\frac{\partial \tau_{\mathrm{SUPG}}}{\partial \mathbf{u}^{\mathrm{h}}} = - \frac{2 \mathbf{u}^{\mathrm{h}}}{h_e |\mathbf{u}^{\mathrm{h}}|} \left(\frac{4}{{h_e}^2 Pe} + \frac{2 |\mathbf{u}^{\mathrm{h}}|}{h_e} \right)^{-2} \tag{15}$$

Inserting the adjoint solutions in the expression for the sensitivities of the Lagrangian results in the following simple expression:

$$\frac{\mathrm{d}\Phi}{\mathrm{d}\boldsymbol{\xi}} = \int_\Omega \hat{\xi}^{\mathrm{h}} \boldsymbol{\lambda}_{\mathbf{u}}^{\mathrm{h}} \cdot \frac{\partial \alpha}{\partial \xi} \mathbf{u}^{\mathrm{h}} \, \mathrm{d}\Omega \tag{16}$$

where $\hat{\xi}^{\mathrm{h}}$ is the test function (shape function) for the design variable field ξ^{h}. It should be noted though, that the introduction of this test function is only a very convenient way to introduce the design variable field and thereby sensitivities in COMSOL and the variable is newer being solved for cf. [11].

Finally, the sensitivity of the constraint function g needs to be computed. This can be done analogously, but with the difference that no adjoint transport problem appears for this case since the pressure only appears in the flow equations. The right-hand side of Equation (14) then becomes

$$\mathrm{RHS} = \frac{-1}{\beta \Delta p_{\mathrm{ref}}} \int_{\Gamma_{\mathrm{in}}} \hat{\lambda}_p^{\mathrm{h}} \, \mathrm{d}\Gamma \tag{17}$$

where β and Δp_{ref} are fixed constants cf. Equation (11).

4.2. Density filter

It is common to use regularization techniques to ensure well-posed topology optimization problems [32]. The density filter approach used in this work was introduced by Bruns and Tortorelli [33],

DOI: 10.1002/fld

its convergence was proven by Bourdin [34] and it has recently been reviewed and extended by Sigmund [35]. The density filter has some attractive properties. Apart from removing mesh dependency by ensuring a minimum length scale in the optimized topology, it also tends to convexify the optimization problem leading to better convergence. Contrary to creeping flow problems where mesh dependency is not an issue cf. [6], the optimized topologies for mixing problems seem to exhibit some mesh dependency when the Péclet and Reynolds numbers are increased.

For the second example problem, presented later, the filter has been imposed from the beginning. After convergence it has been turned off and the optimization has been continued in order to increase the contrast in the permeability.

5. IMPLEMENTATION

For the implementation of the finite element method COMSOL Multiphysics 3.4, a high level PDE toolbox that can be integrated with Matlab, is utilized. The package includes routines for all parts of the analysis; meshing, assembling, solving and plotting. This leaves the main focus on the formulation of the objective function, formulation of interpolation functions, implementation of the sensitivity analysis and the communication with the optimization algorithm. The adjoint sensitivity analysis is performed on the same mesh as the original problem, and the sensitivities, Equation (16), are obtained by formulating an artificial problem and retrieving the right-hand side using the assembly procedure in a manner similar to Olesen *et al.* [11]. Moreover, a correct implementation of the sensitivity calculation was confirmed by a finite difference check. To solve the optimization problem the MMA [28] is used.

The initial conditions for the design field is a random uniform distribution, such that unsymmetries in the final design can be triggered if they are desired, which might be a problem if the initial distribution is uniform. The high level programming language approach makes it possible to implement and test different methods and approaches easily on academic size problems. The following flowchart presents the optimization procedure:

1. Initialization
   Set up equation system, *compute reference values*, *filter-neighborhood*, *initialize iteration counter* $i=1$, *etc.*
2. Apply filter to design variables
3. Solve the state problems by FEM, Equations (7), (9)
4. Compute the objective and constraint value, Equations (11), (12)
5. Compute sensitivities (Φ', g') by the adjoint method, Equations (13)–(14), (16)–(17)
6. Apply filter to sensitivities (chain rule)
7. Update design variables ξ by MMA call
8. Check for convergence $\|\xi^i - \xi^{i-1}\|_\infty \ll 1\%$
   If convergence is not reached, *go to 2 and increase iteration counter* $i=i+1$
   else continue
9. Post processing

DOI: 10.1002/fld

As it is seen from the flowchart, the state and adjoint problems will be solved several times, therefore some effort has been invested in representing and solving the equation system as efficiently as possible. This is the reason for choosing a first-order velocity–pressure pair and to compensate by stabilizing the formulation instead of using the LBB stable Taylor–Hood pair (second-order velocity, first-order pressure). In order to solve the equation systems, the *Pardiso* solver implemented in COMSOL is used, as it is a fast direct solver that to some extent is able to make use of multiple processors. An iterative solver (*GMRES*) has also been tested and performs well, though it cannot outperform the direct solver for the problem sizes used in this paper.

The computational environment used was a double dual-core Intel Xeon 5160 3.00 GHz with 16 GB RAM running GNU/Linux 2.6.9-55.ELsmp, COMSOL 3.4 and Matlab 7.4 (R2007a). With this configuration the total execution time was approximately 92 and 136 h for the two micromixer examples, having approx. 160.000 and 340.000 state dofs in each of the flow problems, respectively.

6. DESIGN EXAMPLES

6.1. Micromixer with prescribed pressure drop

As a first test case a channel with square cross-section as seen in Figure 3 is considered. Only the middle section of the channel is included as a design domain in order to avoid boundary effects influencing on the optimized design. The design variables are initially given random values and as the optimization progresses the material is redistributed and an optimized topology is achieved which is shown in Figure 4, and a plot of the concentration along the channel is shown in Figure 5. The performance of the optimized mixer is $\Phi_{\text{opt}} = 0.2051$ compared with the $\Phi_{\text{empty}} = 0.6786$ of the empty pipe, which is an improvement of 70% at the cost of a 2.5 fold increase in the pressure drop compared with the empty straight pipe (enforced via the pressure drop constraint with $\beta = 2.5$). It is seen that even though there is a great improvement in the mixing, the solute still has regions of high and low concentrations. By allowing a larger pressure drop the mixing can be further improved (see below). The stretching and folding that occurs in the mixer is visualized in Figure 5. It is interesting to note that the optimized topology does not have any unattached solid elements

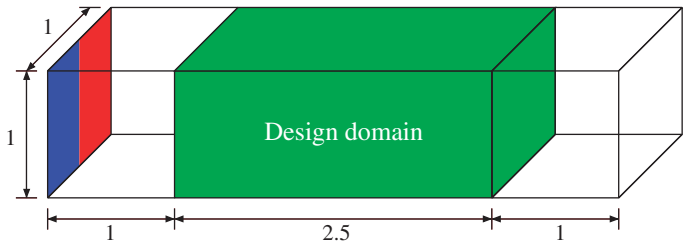

Figure 3. Pipe with square cross-section having outer measures $1 \times 1 \times 4.5$ and a design domain of length 2.5 in order to avoid influence from boundary conditions on the design. Parabolic inflow profile to the left with a Heaviside concentration distribution. No slip at horizontal faces and free outlet at the right vertical face.

DOI: 10.1002/fld

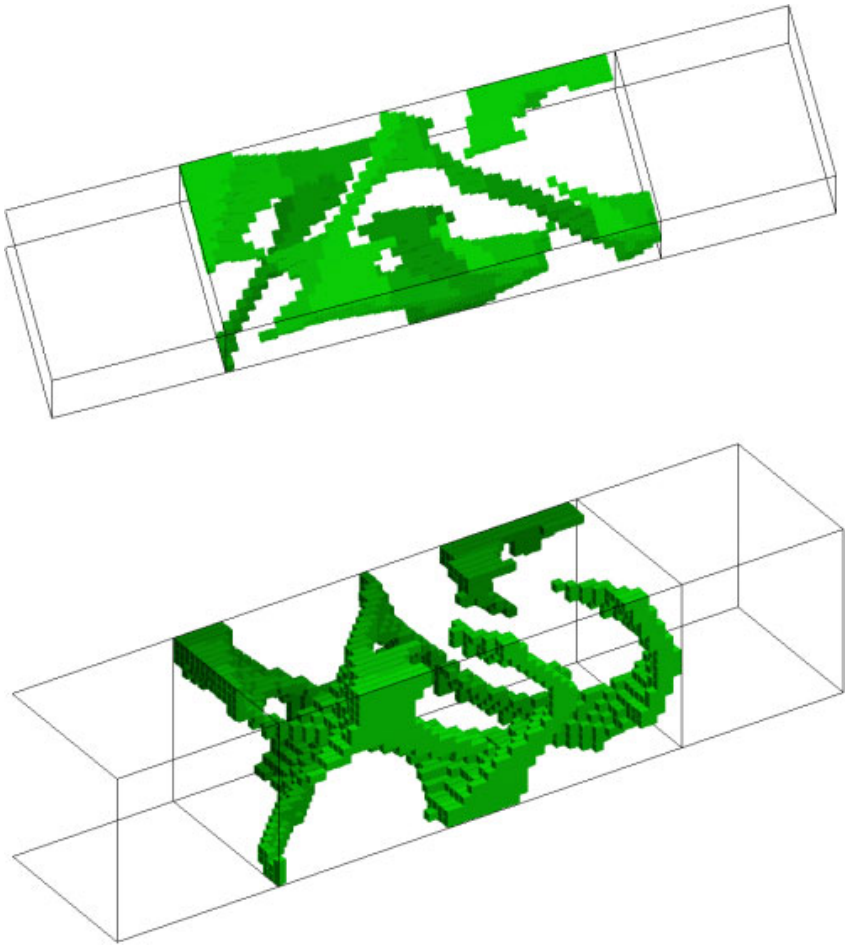

Figure 4. Optimized topology for Stokes flow ($\rho=0, \mu=1$) with $Pe=1000$ in the square cross-sectioned pipe. Design variables plotted with threshold $\xi<0.5$, colored by depth. Design variable distribution: $\xi<0.1:10\%$, $\xi>0.9:89\%$. Problem details: 20 000 ($20\times20\times50$) design variables. Final objective $\Phi_{\text{final}}=0.2051$, reference objective $\Phi_{\text{empty}}=0.6786$. Allowed pressure drop $\beta=2.5$. Computation time approx. 92 h. Iterations: 1041 without filter.

even though this was not implemented as a constraint. Most probably isolated solid regions would cause too much pressure loss compared with their mixing performance.

In order to study the influence of the allowed pressure drop β, several optimizations were conducted and in Figure 6 the relation between the optimized mixer performance and the allowed pressure drop is shown. It is seen from the curve that the performance vs pressure drop relation is a monotonically decreasing function that approaches 0 for a large pressure drop. From the related design plots it can be seen that the topology is changing and is getting more entangled as the pressure drop is increased, yielding more complex mixing patterns.

A design with this complexity would be difficult if not impossible to obtain with traditional shape optimization techniques. The basic design principle is that 'propeller blades' are connected to the pipe wall to enhance mixing without violating the pressure drop constraint. If manufacturing

DOI: 10.1002/fld

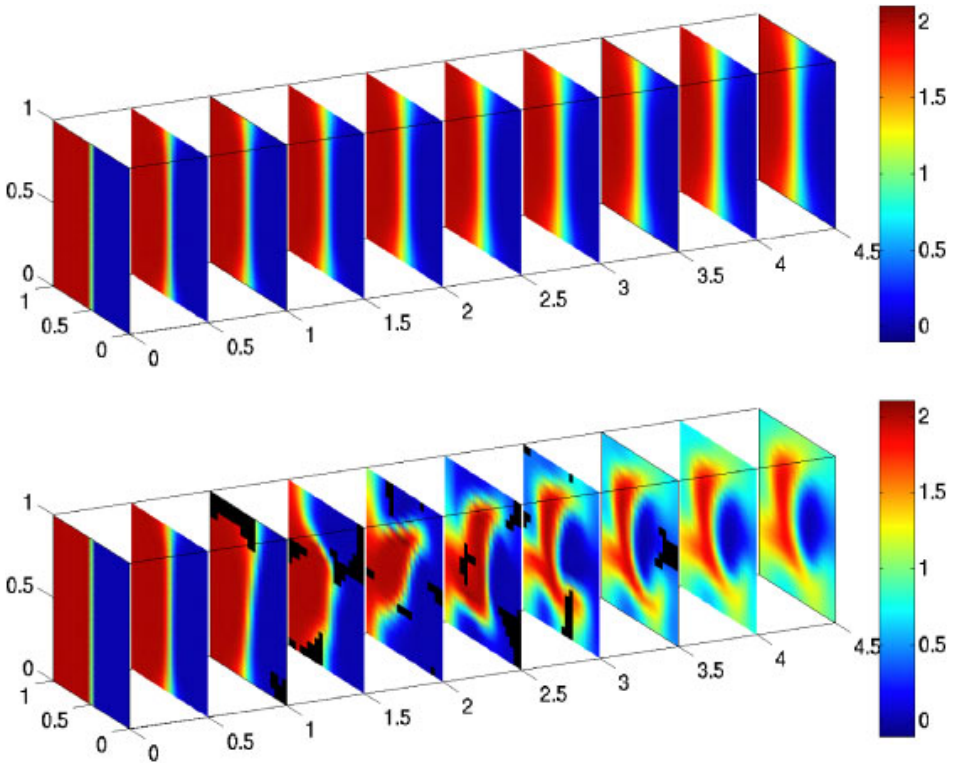

Figure 5. Concentration ϕ in several cross-sections showing the mixing progress of the unoptimized straight pipe mixer (upper) and the optimized mixer shown in Figure 4 (lower). Solid material ($\xi < 0.5$) in the cross-sections is colored black.

abilities prevent the realization of this complicated design, geometrical constraints like casting constraints could be added to the problem. In the following example, we ensure manufacturability by limiting the size of the design domain.

6.2. *Micromixer with bottom layer design domain*

Many different micromixer designs have been presented in the literature having widely different performances [2, 36, 37]. This motivates the use of a general and systematic approach like topology optimization to optimize mixing performance. In order to do this a reference geometry, a section of a channel with the same dimensions as the staggered herringbone mixer by Stroock *et al*. [2], is introduced in Figure 7. The bottom part of the geometry is defined as the design domain. This subdomain consists of material with a low permeability, acting as a no-slip boundary. Letting the topology optimization procedure redistribute the material in the design domain, a new and optimized design appears as shown in Figure 8. As it is not possible for the optimizer to block the main fluid path the pressure constraint is no longer necessary and therefore deactivated. In Figure 8 the optimized topology for $Re = 0.01$ flow is shown. The topology includes well-known details from other micromixers. At the inlet 45° inclined grooves appear transitioning to herring bone-like structures at the center part of the channel and finally transforming back toward inclined grooves in the other direction. The performance of the optimized mixer is $\Phi_{\text{opt}} = 0.5594$ compared

DOI: 10.1002/fld

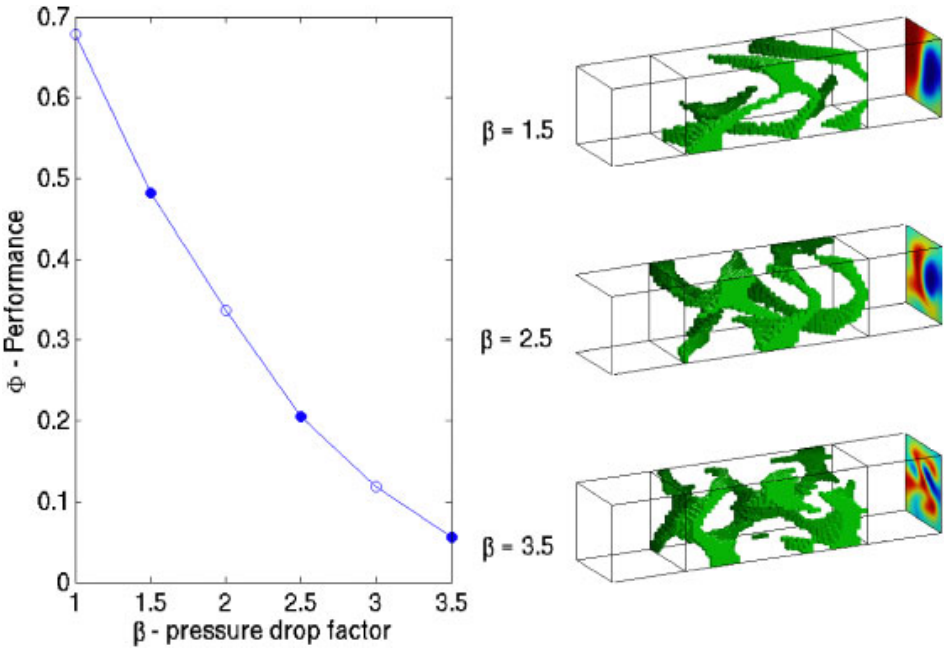

Figure 6. Variation of the allowed pressure drop factor β for the straight pipe mixer. Left: performance vs pressure drop. Right: selected optimized mixers and the concentration distribution on the outlet face (Same coloring as in Figure 5, $\phi \in [0; 2]$).

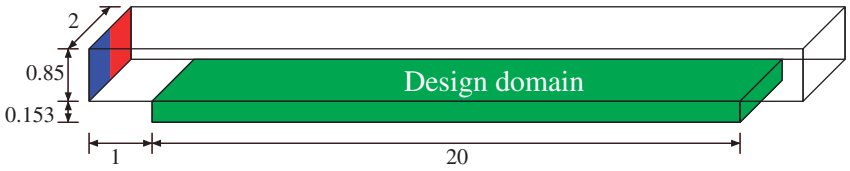

Figure 7. Problem figure showing the reference micromixer. The inlet velocity profile is parabolic in order to mimic fully developed laminar flow and the concentration profile is a Heaviside function. The total channel length is 22 ($\approx$12.9 times the hydraulic diameter) and the outlet is constructed similar to the inlet. The design domain is for the reference filled with material with a low permeability.

with the $\Phi_{\text{ref}} = 0.8114$ of the reference channel (see Figure 7), which is an improvement of 31% at the cost of 1.27 fold increase in pressure drop. The length of the modeled mixer is restricted due to limitations in computer time of our COMSOL implementation and therefore the mixer cannot be as long as those experimentally investigated in Stroock *et al.* [2]. Using the lowest Re/Pe number from Stroock *et al.* [2], it is only possible to compute the performance of the mixer after one segment. Comparing the mixing performance it is seen that the reference performs better, but this is surely due to the limited resolution of the model. Many of those entanglements shown on the intensity pictures in the reference will definitely not be possible to resolve with the current COMSOL-based implementation.

DOI: 10.1002/fld

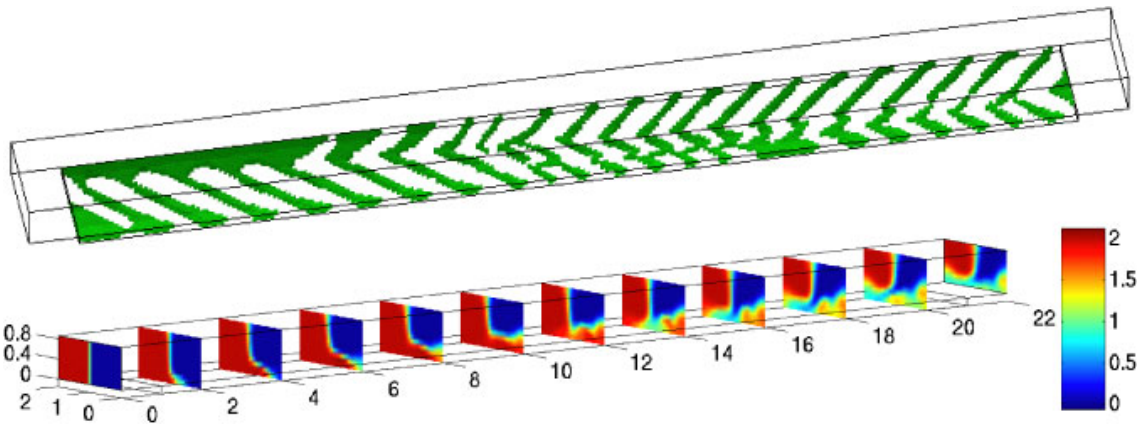

Figure 8. Optimized topology for the micromixer with bottom layer design domain having $Re=0.01$, $Pe=2000$. Top: design variables thresholded by $\xi<0.5$ and colored by depth. Design variable distribution: $\xi<0.1:20\%$, $\xi>0.9:73\%$. Bottom: concentration ϕ plotted in several cross-sections along the mixer. Computed using $u1p1\phi1$ elements and by using 11520 design variables ($240\times24\times2$) in the bottom layer. Optimized performance $\Phi_{\text{final}}=0.5594$, compared with $\Phi_{\text{ref}}=0.8114$ improvement of 31% by the cost of a 1.27 fold increase in pressure drop. $\Delta p_{\text{final}}=732.5$, $\Delta p_{\text{ref}}=575.9$. Iterations: 641 with filter (radius $=0.1167$) succeeded by 748 without filter. Total computation time was approx. 165 h.

Although this example suffers from a rough geometry description (known as the 'Duplo-syndrome' in the topology optimization community), it supports a combination of herringbones and slanted groves as optimal geometric shapes in micromixers, provided that manufacturing constraints only permit geometric variation in a bottom layer of the pipe cf. Figure 7. In addition, this study demonstrates that mixing performance is improved by varying the geometric pattern throughout the mixer. Hence, the topology optimization methodology goes beyond more traditional optimization studies using a parameter sweep on a fixed geometry, see e.g. Li and Chen [38] who also studied the mixer by Stroock *et al.* [2]. Also, it is concluded that periodically repeated mixers may be suboptimal.

7. DISCUSSION AND CONCLUSIONS

This study shows that topology optimization provides a systematic general approach for the design of microfluidic mixers. The first example presented shows that the method is capable of optimizing in-line mixers subjected to a constraint on the allowable pressure drop. The second example shows that design details such as staggered herring bones and slanted grooves appear when using this general and systematic approach. The designs are very similar to the ones experimentally investigated by Stroock *et al.* [2] exhibiting chaotic advection.

The examples considered have been run at Péclet numbers of $Pe=\{1000, 2000\}$ for low Reynolds number flows, hence, a gap remains in the experimental conditions reported in Stroock *et al.* [2]. From a computational point of view the larger the *Pe* number, the larger the domain needed in order to model say 50% mixing, which in turn increases the problem sizes beyond our computational capabilities with the present COMSOL implementation. Nevertheless, apart from verifying the

DOI: 10.1002/fld

approach, our simulations in the chosen parameter regime may help to improve the understanding of the basic design principles, which enhance micromixer performance.

To provide more practical results, the effect of imposing manufacturing constraints, such as symmetry in a cross-section of the pipe, would be a relevant direction of research as it would give the possibility of enhancing the geometric complexity while staying within the limits of available manufacturing technologies.

ACKNOWLEDGEMENTS

The authors thank the TopOpt group (www.topopt.dtu.dk) at the Technical University of Denmark for fruitful discussions related to this paper.

REFERENCES

1. Ottino JM, Wiggins S. Introduction: mixing in microfluidics. *Philosophical Transactions of the Royal Society A*: *Mathematical*, *Physical and Engineering Sciences* 2004; **362**(1818):923–935. DOI: 10.1098/rsta.2003.1355.
2. Stroock AD, Dertinger SKW, Ajdari A, Mezic I, Stone HA, Whitesides GM. Chaotic mixer for microchannels. *Science* 2002; **295**(5555):647–651. DOI: 10.1126/science.1066238.
3. Bendsøe MP, Kikuchi N. Generating topologies in structural design using a homogenization method. *Computer Methods in Applied Mechanics and Engineering* 1988; **71**:197–224. DOI: 10.1016/0045-7825(88)90086-2.
4. Bendsøe MP, Sigmund O. *Topology Optimization—Theory*, *Methods and Applications* (2nd edn). Springer: Berlin, 2003.
5. Pironneau O. On optimum profiles in Stokes flow. *Journal of Fluid Mechanics* 1973; **59**:117–128.
6. Borrvall T, Petersson J. Topology optimization of fluids in Stokes flow. *International Journal for Numerical Methods in Fluids* 2003; **41**(1):77–107. DOI: 10.1002/fld.426.
7. Evgrafov A. The limits of porous materials in the topology optimization of Stokes flows. *Applied Mathematics and Optimization* 2005; **52**(3):263–277. DOI: 10.1007/s00245-005-0828-z.
8. Guest JK, Prévost JH. Topology optimization of creeping fluid flows using a Darcy–Stokes finite element. *International Journal for Numerical Methods in Engineering* 2006; **66**(3):461–484. DOI: 10.1002/nme.1560.
9. Wiker N, Klarbring A, Borrvall T. Topology optimization of regions of Darcy and Stokes flow. *International Journal for Numerical Methods in Engineering* 2007; **69**(7):1374–1380. DOI: 10.1002/nme.1811.
10. Gersborg-Hansen A, Sigmund O, Haber R. Topology optimization of channel flow problems. *Structural and Multidisciplinary Optimization* 2005; **30**:181–192. DOI: 10.1007/s00158-004-0508-7.
11. Olesen LH, Okkels F, Bruus H. A high-level programming language implementation of topology optimization applied to steady-state Navier–Stokes flow. *International Journal for Numerical Methods in Engineering* 2006; **65**(7):975–1001. DOI: 10.1002/nme.1468.
12. Evgrafov A. Topology optimization of slightly compressible fluids. *ZAMM* 2006; **86**(1):46–62. DOI: 10.1002/zamm.200410223.
13. Thellner M. Multi-parameter topology optimization in continuum mechanics. *Ph.D. Thesis*, Department of Mechanical Engineering, Linköping University, 2005. ISBN-10 91-8529-71-2.
14. Gersborg-Hansen A. Topology optimization of flow problems. *Ph.D. Thesis*, Department of Mathematics and Department of Mechanical Engineering, Solid Mechanics, Technical University of Denmark, DCAMM Special Report S96, 2007. ISBN-10 87-90416-23-6.
15. Okkels F, Bruus H. Scaling behavior of optimally structured catalytic microfluidic reactors. *Physical Review E* 2007; **75**(1):016301. DOI: 10.1103/PhysRevE.75.016301.
16. Pingen G, Evgrafov A, Maute K. Topology optimization of flow domains using the lattice Boltzmann method. *Structural and Multidisciplinary Optimization* 2007; **34**(6):507–524. DOI: 10.1007/s00158-007-0105-7.
17. Evgrafov A, Pingen G, Maute K. Topology optimization of fluid domains: kinetic theory approach. *ZAMM* 2008; **88**(2):129–141. DOI: 10.1002/zamm.200700122.
18. Aage N, Poulsen TH, Gersborg-Hansen A, Sigmund O. Topology optimization of large scale Stokes flow problems. *Structural and Multidisciplinary Optimization* 2008; **35**:175–180. DOI: 10.1007/s00158-007-0128-0.

19. Guest JK, Prévost JH. Optimizing multifunctional materials: design of microstructures for maximized stiffness and fluid permeability. *International Journal of Solids and Structures* 2006; **43**:7028–7047. DOI: 10.1016/j.ijsolstr.2006.03.001.
20. Othmer C. A continuous adjoint formulation for the computation of topological and surface sensitivities of ducted flows. *International Journal for Numerical Methods in Fluids* 2008; Published on-line. DOI: 10.1002/fld.1770.
21. Brooks AN, Hughes TJR. Streamline upwind/Petrov–Galerkin formulations for convection dominated flows with particular emphasis on the incompressible Navier–Stokes equations. *Computer Methods in Applied Mechanics and Engineering* 1982; **32**(1–3):199–259. DOI: 10.1016/0045-7825(82)90071-8.
22. Hughes TJR, Franca LP. A new finite element formulation for computational fluid dynamics: VII. The Stokes problem with various well-posed boundary conditions: symmetric formulations that converge for all velocity/pressure spaces. *Computer Methods in Applied Mechanics and Engineering* 1987; **65**(1):85–96. DOI: 10.1016/0045-7825(87)90184-8.
23. Zienkiewicz OC, Taylor RL. *The Finite Element Method—Volume 3*: *Fluid Dynamics*. Butterworth Heinemann: London, 2000.
24. Donea J, Hureta A. *Finite Element Methods for Flow Problems*. Wiley: West Sussex, 2003.
25. Tezduyar TE, Ramakrishnan S, Sathe S. *International Journal for Numerical Methods in Fluids* 2008; Published on-line. DOI: 10.1002/fld.1743.
26. Masud A, Hughes TJR. A stabilized mixed finite element method for Darcy Flow. *Computer Methods in Applied Mechanics and Engineering* 2002; **191**:4341–4370. DOI: 10.1016/S0045-7825(02)00371-7.
27. Codina R. Comparison of some finite element methods for solving the diffusion–convection–reaction equation. *Computer Methods in Applied Mechanics and Engineering* 1998; **156**:185–210. DOI: 10.1016/S0045-7825(97)00206-5.
28. Svanberg K. The method of moving asymptotes—a new method for structural optimization. *International Journal for Numerical Methods in Engineering* 1987; **24**:359–373. DOI: 10.1002/nme.1620240207.
29. Vidal CA, Lee HS, Haber RB. The consistent tangent operator for design sensitivity analysis of history-dependent response. *Computing Systems Engineering* 1991; **2**:509–523.
30. Michaleris P, Tortorelli DA, Vidal CA. Tangent operators and design sensitivity formulations for transient non-linear coupled problems with applications to elastoplasticity. *International Journal for Numerical Methods in Engineering* 1994; **37**(14):2471–2499. DOI: 10.1002/nme.1620371408.
31. Choi K, Kim NH. *Structural Sensitivity Analysis and Optimization*. vols 1 and 2. Springer: Berlin, 2005. ISBN 03872-3336-9.
32. Sigmund O, Petersson J. Numerical instabilities in topology optimization: a survey on procedures dealing with checkerboards, mesh-dependencies and local minima. *Structural Optimization* 1998; **16**(1):68–75. DOI: 10.1007/BF01214002.
33. Bruns TE, Tortorelli DA. Topology optimization of non-linear elastic structures and compliant mechanisms. *Computer Methods in Applied Mechanics and Engineering* 2001; **190**(26–17):3443–3459. DOI: 10.1016/S0045-7825(00)00278-4.
34. Bourdin B. Filters in topology optimization. *International Journal for Numerical Methods in Engineering* 2001; **50**:2143–2158. DOI: 10.1002/nme.116.
35. Sigmund O. Morphology-based black and white filters for topology optimization. *Structural and Multidisciplinary Optimization* 2007; **33**:401–424. DOI: 10.1007/s00158-006-0087-x.
36. Liu RH, Stremler MA, Sharp KV, Olsen MG, Santiago JG, Adrian RJ, Aref H, Beebe DJ. Passive mixing in a three-dimensional serpentine microchannel. *Journal of Microelectromechanical Systems* 2000; **9**:190–197. DOI: 10.1109/84.846699.
37. Yang JT, Huang K, Tung KY, Hu IC, Lyu PC. A chaotic micromixer modulated by constructive vortex agitation. *Journal of Micromechanics and Microengineering* 2007; **17**:2084–2092. DOI: 10.1088/0960-1317/17/10/021.
38. Li C, Chen T. Simulation and optimization of chaotic micromixer using lattice Boltzmann method. *Sensors and Actuators B* 2005; **106**(2):871–877. DOI: 10.1016/j.snb.2004.09.006.

Publication [P5]

An explicit parameterization for casting constraints in gradient driven topology optimization

Struct Multidisc Optim
DOI 10.1007/s00158-011-0632-0

BRIEF NOTE

An explicit parameterization for casting constraints in gradient driven topology optimization

Allan Roulund Gersborg · Casper Schousboe Andreasen

Received: 8 June 2010 / Revised: 13 December 2010 / Accepted: 31 January 2011

Abstract From a practical point of view it is often desirable to limit the complexity of a topology optimization design such that casting/milling type manufacturing techniques can be applied. In the context of gradient driven topology optimization this work studies how castable designs can be obtained by use of a Heaviside design parameterization in a specified casting direction. This reduces the number of design variables considerably and the approach is simple to implement.

Keywords Topology optimization · Casting constraint · MBB-problem

1 Introduction

The fundamental concept of the density based topology optimization method (Bendsøe and Kikuchi 1988; Bendsøe and Sigmund 2004) is to represent the geometry as a digital image where the color of each pixel corresponds to the value of a physical parameter, e.g. the density. This approach gives a very rich set of candidate designs, and naturally control strategies for the end design have been a hot research topic since the beginning of the topology optimization era.

Eurohorcs/ESF European Young Investigator Award: "Synthesis and topology optimization of optomechanical systems". DCAMM Research School via the Danish Agency for Science, Technology and Innovation. Danish Center for Scientific Computing (DCSC).

A. R. Gersborg (✉) · C. S. Andreasen
Section for Solid Mechanics, Department of Mechanical Engineering, Technical University of Denmark, 2800, Kgs. Lyngby, Denmark
e-mail: agersborg.hansen@gmail.com

C. S. Andreasen
e-mail: csan@mek.dtu.dk

Image processing techniques (filters) have been the main theme for controlling the design. Early studies focused on how to ensure a well posed problem and how to obtain physically meaningful designs, cf. the references in Bendsøe and Sigmund (2004). Lately the imposition of minimum length scales (Guest 2009) and manufacturing tolerant designs (Sigmund 2009; Wang et al. 2010) have been investigated.

In connection with casting constraints Harzheim and Graf (2006) reviewed non-smooth techniques and Zuo et al. (2006) formulated a smooth method using wavelets. Also, commercial software from e.g. FE-design GmbH (Pedersen and Allinger 2006) and Altair (Schramm and Zhou 2006) allow for casting and other manufacturing constraints, however, to the authors best knowledge the underlying methods are not broadly available.

The addition of casting constraints to a topology optimization problem has the consequence that the problem becomes a fixed-grid shape optimization problem for which a pixel based design representation may seem inappropriate. Despite this subtlety, we find it valuable to study a method which at a small coding effort ensures castable designs in a standard topology optimization context. We believe that this is relevant when, e.g. collaborating with experimentalists who request simple topology designs for preliminary proof of principle studies, model calibration experiments etc.

These considerations motivate the present note which has its focus on ensuring an optimized end design which can be manufactured by casting, milling or modern additive manufacturing techniques. It contributes with a method for ensuring castable designs in a gradient driven topology optimization context based on a finite element solution. The classical 2D MBB-problem (Olhof 1991; Sigmund 2001) on a regular mesh is considered since this benchmark may encompass the main difficulties of casting constraints, it is well-known and available to the community.

Published online: 01 March 2011

2 Topology optimization

2.1 Preliminaries

The classical MBB problem (Olhof 1991; Sigmund 2001) is taken as the point of reference, i.e., the goal is to minimize the compliance of a structure subject to a volume constraint and the conditions seen in Fig. 1. The corresponding nested topology optimization problem is

$$\min_{\rho\in\mathbb{R}^m} \quad c = \mathbf{u}^{\mathrm{T}}\mathbf{f} \tag{1a}$$

$$\text{subject to} \quad \widetilde{\rho} = \mathscr{F}(\rho), \qquad \widetilde{\rho} \in \mathbb{R}^n \tag{1b}$$

$$\mathbf{K}(\widetilde{\rho})\mathbf{u} = \mathbf{f} \tag{1c}$$

$$g \leq 0 \tag{1d}$$

$$0 \leq \rho_i \leq 1 \quad \text{for } i = 1, ..., m \tag{1e}$$

where ρ is a vector with m non-dimensional design variables and c is the compliance objective function. In order to ensure mesh independent designs and a well posed optimization problem a density filter (Bruns and Tortorelli 2001; Bourdain 2001) denoted by $\mathscr{F}(\cdot)$ is employed. It is constructed such that $0 \leq \rho_i \leq 1 \Rightarrow 0 \leq \widetilde{\rho}_i \leq 1$ as described in detail in Bourdain (2001). Typically, ρ and $\widetilde{\rho}$ have the same number of entries, i.e., $n = m$. The equations of linear elasticity are discretized using bilinear quadrilateral elements such that $\mathbf{K}$ is the stiffness matrix, $\mathbf{u}$ the displacement vector and $\mathbf{f}$ the external load vector. The material density is the design field and taken to be element wise constant, i.e., $n = N$ where N is the number of elements. Moreover, it is interpolated using SIMP (Solid Isotropic Material with Penalization cf. Bendsøe 1989; Zhou and Rozvany 1991) in order to get 0–1 designs and a lower bound to avoid a singular matrix i.e., the stiffness matrix is assembled as

$$\mathbf{K}(\widetilde{\rho}) = \sum_{i=1}^{N} \left(\underline{\rho} + \left(\overline{\rho} - \underline{\rho}\right)\widetilde{\rho}_i^{\,p}\right)\mathbf{K}_e \tag{2}$$

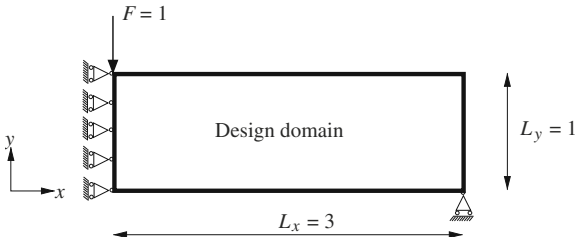

Fig. 1 Boundary conditions for the MBB problem. The x displacement is fixed at the left side of the domain and the y displacement is fixed in the lower right corner. A unit load is applied in the upper left corner and the aspect ratio of the design domain is $L_x/L_y = 3$. To simplify the exposition we place the design domain in the 1st quadrant such that $0 \leq x \leq L_x$ and $0 \leq y \leq L_y$

where $\underline{\rho}$ is the lower bound on the density, $\overline{\rho}$ the upper bound, $p > 1$ is the penalty power and $\mathbf{K}_e$ is the element stiffness matrix. The volume constraint is measured by

$$g = \frac{\sum_{i=1}^{N}\widetilde{\rho}_i v_i}{\gamma V} - 1 \tag{3}$$

where v_i is the element volume, γ the allowed solid volume fraction and V the volume of the design domain. Using this measure the volume constraint enters in the optimization problem in (1d). Finally, (1e) defines box constraints on the design variables.

For the compliance objective function the sensitivity analysis is simple since no adjoint system of equations needs to be solved. The sensitivities become (cf. Bendsøe and Sigmund 2004; Sigmund 2009)

$$\frac{\mathrm{d}c}{\mathrm{d}\widetilde{\rho}_i} = -\mathbf{u}^{\mathrm{T}} p\widetilde{\rho}_i^{\,p-1}\mathbf{K}_e\,\mathbf{u}, \qquad \frac{\mathrm{d}c}{\mathrm{d}\rho_i} = \frac{\mathrm{d}c}{\mathrm{d}\widetilde{\rho}_j}\frac{\mathrm{d}\widetilde{\rho}_j}{\mathrm{d}\rho_i}. \tag{4}$$

For the state independent volume constraint one finds

$$\frac{\mathrm{d}g}{\mathrm{d}\widetilde{\rho}_i} = \frac{v_i}{\gamma V}, \qquad \frac{\mathrm{d}g}{\mathrm{d}\rho_i} = \frac{\mathrm{d}g}{\mathrm{d}\widetilde{\rho}_j}\frac{\mathrm{d}\widetilde{\rho}_j}{\mathrm{d}\rho_i}. \tag{5}$$

The optimization problem (1) is solved using the gradient driven MMA algorithm (Svanberg 1987). Figure 2 displays a standard non-castable design for a 60×20 mesh. In the following n_x denotes the number of elements in the x-direction and n_y denotes the number of elements in the y-direction.

2.2 Casting constraint

Now we pose the additional constraint in the MBB problem that the design should be castable in the x-direction. This corresponds to having a monotonically decreasing $\widetilde{\rho}$ field $\left(\frac{\partial\widetilde{\rho}}{\partial x} \leq 0\right)$. For small problems, i.e., problems with $N \sim 1{,}000$, a strategy is to introduce linear constraints in the standard problem (1) i.e.

$$\widetilde{\rho}\left(x_{i+1}, y_j\right) - \widetilde{\rho}\left(x_i, y_j\right) \leq 0 \tag{6}$$

Fig. 2 Optimized topology design for the MBB problem on a 60×20 mesh with a volume constraint of 50%, density filter with radius $r = 1.4/20$ and fixed $p = 3$. The graybar shows the value of the physical density $\widetilde{\rho}$, $c = 2.16 \cdot 10^2$, $g = -8.15 \cdot 10^{-6}$ and the design is obtained in $j = 232$ iterations. $m = n = N = 1{,}200$

where $i = 1, \ldots, n_x - 1$, $j = 1, \ldots, n_y$ and (x_i, y_j) denotes the coordinates of the center of each element. However, for large meshes this strategy makes the optimization problem very costly to solve which motivates to ensure a castable design a priori by changing the design parameterization.

The basic idea of the parametrization (cf. Fig. 3) is to represent the densities in a row of elements by a single design value controlling the position of the interface between solid and void. For a non-uniform mesh one may map the density to strips of elements in the non-uniform mesh.

By choosing a smooth approximation to a Heaviside function we ensure a monotone and differentiable density along the row as well as a 0–1 design when the steepness of the approximating function increases. Below the parametrization is explained in detail starting from a non-smooth Heaviside function and ending with a pseudo-code ready for implementation.

Using a standard Heaviside function of the form

$$H(t) = \begin{cases} 1, & t \leq 0 \\ 0, & t > 0 \end{cases}, \qquad t \in \mathbb{R} \tag{7}$$

one may define the density in the j'th row of elements as

$$\widetilde{\rho}(x) = H(s(x) - \rho_j) \tag{8}$$

where $s = x/L_x \in [0; 1]$ is a normalized x-coordinate and ρ_j defines the position of the solid-void interface. Differentiability of the parametrization is obtained by use of a smooth approximation of the Heaviside function in (7) such that

$$\widetilde{\rho}(x) = H_s(s(x), \rho_j; \beta) \tag{9}$$

with $H_s(s(x), \rho_j; \beta)$ given by

$$\left.\begin{aligned} &\textbf{If} \quad \rho_j \leq s(x) \\ &\quad H_s = 1 - \rho_j \left[e^{-\beta(1 - s(x)/\rho_j)} - \left(1 - s(x)/\rho_j\right) e^{-\beta} \right] \\ &\textbf{else} \\ &\quad H_s = 1 - (1 - \rho_j) \left[1 - e^{-\beta(s(x) - \rho_j)/(1 - \rho_j)} \right. \\ &\qquad\qquad \left. + \left(s(x) - \rho_j\right) e^{-\beta}/(1 - \rho_j) \right] - \rho_j \end{aligned}\right\} \tag{10}$$

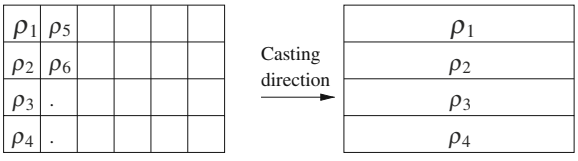

Fig. 3 *Left* Standard design parametrization, one design variable per element. *Right* New casting parametrization. One design variable defines the densities in a row of elements in the casting direction

where $\beta > 0$ controls the steepness of the approximation (Xu et al. 2010). In the top of Fig. 4 the resulting parametrization is shown where the normalized x-coordinate refers to the center of the element. This natural choice implies that $0 < s(x) < 1$ and the formulation does not allow for elements at the left/right boundary to be void/solid unless very large β values are used. Large β values would worsen the conditioning of the formulation and instead a stretched formulation with a new variable $\widehat{\rho}$ is introduced. This stretches the smooth approximation of the Heaviside function from the interval $\rho \in [0; 1]$ to $\widehat{\rho} \in [-b; a]$ where a and $-b$ are the new limits. This is illustrated in the bottom plot of Fig. 4 where it is seen that with this stretched variable it is possible to obtain either solid or void at left and right boundaries.

The proposed parametrization reduces the number of design variables to $m = n_y$ and the procedure can be interpreted as a filter $\widetilde{\rho}\left(x_i, y_j\right) = \mathcal{H}\left(\rho\left(y_j\right)\right)$. The procedure for computing the density field $\widetilde{\rho}(x_i, y_j)$ from the design field $\rho(y_j)$ can be summarized in three steps for every element:

$$\left.\begin{aligned} &1.\ \text{Compute the normalized } x\text{-coordinate} \\ &\quad s_i = x_i/L_x \\ &2.\ \text{Compute the stretched variable} \\ &\quad \widehat{\rho} = (a + b)\rho(y_j) - b, \quad b < a,\ \widehat{\rho} \in [-b; a] \\ &3.\ \text{Compute the density of the element} \\ &\quad \widetilde{\rho}\left(x_i, y_j\right) = H_s(s_i, \widehat{\rho}; \beta) \end{aligned}\right\} \tag{11}$$

where (x_i, y_i) is the center coordinate of the i'th element and $\widehat{\rho}$ the stretched coordinate. Note that the design variables ρ define the location of the solid-void interface (cf. Fig. 5).

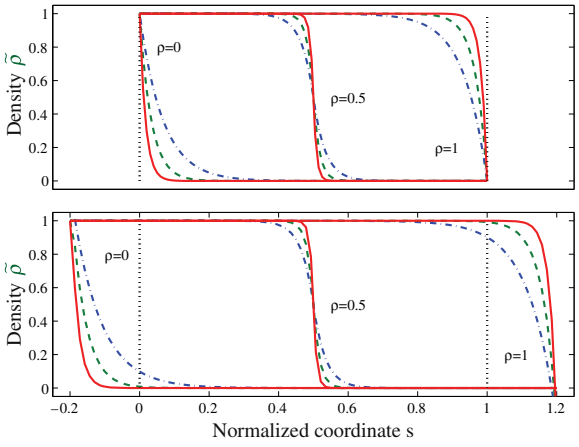

Fig. 4 Step function parametrization (cf. (10)) shown for $\rho = \{0, 0.5, 1\}$ and with varying steepness $\beta = \{15, 30, 60\}$ indicated by {.-, - -, –}, respectively. $s = x/L_x$ is the normalized x-coordinate and $\widetilde{\rho}$ is the density. *Top* Using the definition in (9). *Bottom* The definition using a stretched variable (cf. (11)) with $b = 0.2$ and $a = 1.2$

Fig. 5 Illustration of a castable field $\widetilde{\rho} = \mathscr{K}(\rho(y))$ on a 60×20 mesh with $\beta = 30$, $\rho = (0, 1/19, 2/19, \ldots, 1)^{\mathrm{T}}$, $a = 1.2$, $b = 0.2$

The flexibility of the stretched variable is, however, problematic for large values of β and unstable convergence behavior is observed if a and b are chosen too large. To avoid this we have used $b < 0$, i.e. a solid wall is enforced at the left boundary, which makes physical sense since it corresponds to assigning the force to a solid element, cf. Fig. 1, and allows for intermediate densities at the right boundary by selecting a slightly larger than one.

Having introduced the casting parameterization the complete procedure can be summarized in terms of pseudo code including a continuation of the steepness β:

1. Initialization. $j = 1$, $k = 1$, $l = 1$
   Initialize design $\rho = \mathbf{1}$. *Set up system of equations, filter neighbourhood, etc.*
2. Compute density $\widetilde{\rho}$ from design variables ρ, (11)
3. Solve the elastic problem, (1c)
4. Evaluate objective and constraint, (1a), (3)
5. Compute sensitivities, (4), (5)
6. Update design variables ρ by MMA call
7. Stopping criterion: max $\|\rho^{j+1} - \rho^{j}\| < 10^{-2}$, $l > 5$ and a feasible design $g \leq 0$. *If fulfilled continue, else* $j = j + 1$, $l = l + 1$ *and go to 2*
8. Continuation. *If* $k > k_{\max}$ *continue, else adjust continuation variable* (β), $k = k + 1$, $l = 1$, *restart MMA and go to 2*
9. Post processing

in which the counters j, k, l refer to iteration number, continuation step and iterations since last continuation step, respectively. The number of different β-values is given by $k_{\max}$.

2.2.1 Two solid-void interfaces

Since it is often of interest to model two solid parts separated by void we define a parameterization which allows for two material interfaces.

The idea is to combine one Heaviside function of the above type defined by the design variables $\rho_1(y_j)$ with a flipped Heaviside function defined by the design variables $\rho_2(y_j)$, i.e. the number of design variables is doubled $m = 2n_y$ and $\rho = [\rho_1^{\mathrm{T}} \ \rho_2^{\mathrm{T}}]^{\mathrm{T}}$ (cf. Fig. 6). Using the definition of $\mathcal{H}$ in (11) we define the parameterization $\widetilde{\rho} = \mathcal{H}_2(\rho) = \mathcal{H}_2\left(\rho_1(y_j), \rho_2(y_j)\right)$ as

$$\left.\begin{array}{ll} 1. & \breve{\rho}_1\left(x_i, y_j\right) = \mathcal{H}\left(\rho_1\left(y_j\right)\right) \\ 2. & \breve{\rho}_2\left(x_i, y_j\right) = 1 - \mathcal{H}\left(\rho_2\left(y_j\right)\right) \\ 3. & \widetilde{\rho}\left(x_i, y_j\right) = \breve{\rho}_1 + (1 - \breve{\rho}_1)\,\breve{\rho}_2 \end{array}\right\} \tag{12}$$

where the second step flips the Heaviside function and the last step ensures that $\widetilde{\rho} \in [0; 1]$.

Fig. 6 A design field $\widetilde{\rho} = \mathcal{H}_2(\rho)$ which has two castable solid parts. 60×20 mesh using $\beta = 30$, $a = 1 - 1/n_x$, $b = -1/n_x$, $\rho = (0, 1/76, 2/76, \ldots, 19/76, \ 57/76, 58/76, \ldots, 76/76)^{\mathrm{T}}$. This choice of (a, b) ensures black elements along the left and right boundaries

3 Numerical examples

3.1 One material interface

The classical MBB example with a 50% volume constraint is considered with $\left(\underline{\rho}, \overline{\rho}\right) = \left(10^{-9}, 1\right)$ using the parameterization $\widetilde{\rho} = \mathcal{H}(\rho)$ from (11). Figure 7 displays the resulting

Fig. 7 Optimized design for the MBB problem subject to a 50% volume constraint and the parameterization $\widetilde{\rho} = \mathcal{H}(\rho)$ (cf. (11)). The value of $\widetilde{\rho}$ is displayed in the graybar. Continuation on $\beta = \{15, 30, 35, 40\}$ is performed. **a** 240×80 elements obtained in 34 iterations with $c = 6.12 \cdot 10^2$ and **b** 480×160 elements obtained in 34 iterations with $c = 6.15 \cdot 10^2$. The constraint g is negative and of the order $10^{-5} - 10^{-4}$

Fig. 8 Comparison of the design in Fig. 7b with an analytic estimate of the height (*white line*) given by $h(x) = 0.43\sqrt{L_x - x}$. The estimate is obtained using Bernoulli–Euler beam theory (Pedersen and Pedersen 2009) and a surprisingly good agreement with the design is observed despite the aspect ratio of $L_x/L_y = 3$. See the Pedersen and Pedersen (2009) for further details on analytical solutions also using Timoshenko beam theory

designs for two meshes which are obtained in relatively few optimization iterations. The design differs completely from the MBB beam in Fig. 2 due to the casting parameterization. Unlike the original solution no void can be placed along the left boundary as this would make the structure unstable. Hence the only location in which it is possible to place void is the upper right corner. This of course yields a somewhat *simple* and expected design but it meets the required manufacturability condition. The result can be compared with an analytical solution to an equivalent beam problem. By using slender beam theory and optimality criterion techniques (uniform strain energy density) Pedersen and Pedersen (2009) presented an optimal shape which is compared in Fig. 8. The main difference occurs at the upper left boundary where a small vertical bar is inserted to transfer the force to the larger horizontally oriented solid with a smoothly varying height.

From a physical perspective it is desirable to place solid material at the support in the lower right corner, which motivates $a > 1$ (cf. Fig. 5). Experience shows, however, that this leads to unstable convergence behavior, which may be explained as follows. The main contribution to the sensitivity $\mathrm{d}c/\mathrm{d}\rho_i$ is from the gray elements(transition region) which cause the sensitivity for large β effectively to vanish for $a \gg 1$. This motivates a large update of ρ_i by the MMA which does not check if the update is advantageous for the objective thus oscillatory and non-convergent behavior is

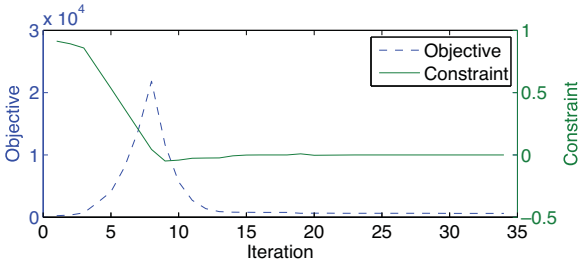

Fig. 9 Iteration history for the design seen in Fig. 7a

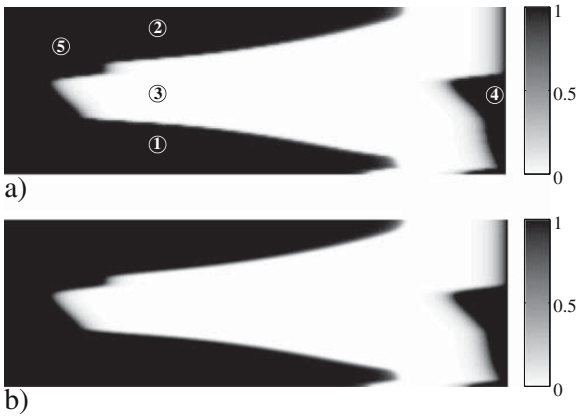

Fig. 10 Optimized design for the layout of a soft inclusion (*white*) in a strong material (*black*). The physical densities $\widetilde{\rho}$ are shown and both designs are feasible with a maximum constraint value of approximately -10^{-5}. Continuation on $\beta = \{20, 30, \ldots, 60\}$ is employed. **a** 240×80 elements $j = 35$ and $c = 1.43 \cdot 10^2$ and **b** 480×160 elements $j = 35$ and $c = 1.45 \cdot 10^2$

observed. To avoid this we allowed intermediate densities at the right boundary by selecting $(a, b) = (1.0521, -1/480)$ and employed continuation on $\beta = \{15, 30, 35, 40\}$. This value of a yields a density of $\widetilde{\rho} \approx 0.86$ for $\beta = 40$ in the lower right corner which seems acceptable from a practical point of view. In order to compensate for the weaker material at the right boundary more solid material is placed around it which may explain the deviation from the analytical result.

The iteration history is seen in Fig. 9 and despite the continuation approach a smooth convergence behavior is observed. The initial design is infeasible which explains the increase in the objective in the first iterations.

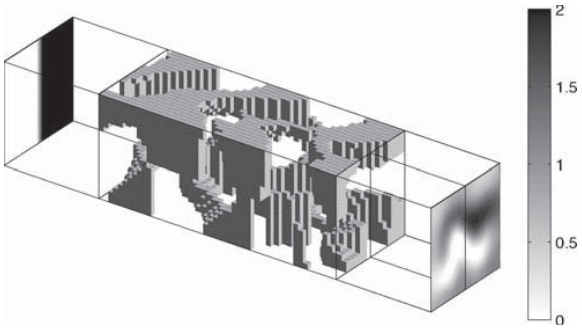

Fig. 11 Inline microfluidic mixer optimized using the explicit parameterization of Section 2.2.1. *Left face* Fully developed velocity profile and discontinuous concentration profile. *Right face* Free outlet conditions (zero pressure) and concentration profile (cf. graybar). Creeping flow conditions and convection dominated transport. Allowed pressure drop is 5 times the one for a corresponding empty pipe

3.2 Two material interfaces

In order to illustrate how the methodology works without changing the physical problem setting we consider the academic distribution problem of a soft material in a stronger material by letting $(\underline{\rho}, \overline{\rho}) = (\frac{1}{2}, 1)$. In order to ensure two material interfaces $(a, b) = (1 - 1/480, -1/480)$ is used, allowing only solid material at the vertical boundaries. Furthermore the length of the soft material is subjected to box constrains $0.2 \leq L_{\text{soft}}/\left(L_x - 2/480\right) \leq 0.8$, where L_{soft} denotes the horizontal length of the soft material strip and L_x the horizontal dimension of the design domain (cf. Fig. 1). To avoid layer-wise instabilities in the design we have added density filtering (Bruns and Tortorelli 2001; Bourdain 2001) of the design variables ρ with a radius of $r = 1.4/240$ such that the box constraints translate to $2n_y$ constraints which are added to the standard problem (1)

$$g_I(i) = \hat{\rho}(i) - \hat{\rho}(i + n_y) + 0.2 \leq 0 \tag{13a}$$

$$g_{II}(i) = \hat{\rho}(i + n_y) - \hat{\rho}(i) - 0.8 \leq 0 \tag{13b}$$

where $i = 1, ..., n_y$ and $\hat{\rho} = [\mathscr{F}(\rho_1)^{\mathrm{T}} \ \mathscr{F}(\rho_2)^{\mathrm{T}}]^{\mathrm{T}}$ (for coarse meshes this 1D filtering is not critical). If the manufacturability was ensured by linear constraints as in (6) such a filtering might also be necessary to avoid single rows of solid elements.

For all meshes an outer (2D) density filter was added such that the overall parameterization becomes $\widetilde{\rho} = \mathscr{F}\left(\mathcal{H}_2\left(\hat{\rho}\right)\right)$.

The result of the optimization is seen in Fig. 10 which may be explained in physical terms as follows: The main design principle is to maximize the bending stiffness with strong outer material ① & ② and soft core material ③, i.e. a composite beam. Note that the shape of ② is similar to the shape of the design in the previous example. The first separation constraint (13a) limits the length of the upper branch ② and prohibits that the lower branch ① connects to the support in the lower right corner. The combination of a poor material utilization in the center of the beam ③ and the second constraint (13b) yields that the thickness of the strong material to the right of the domain increases. The right material interface has the shape of a stool ④ which efficiently transfers the load to the support. Moreover, the second constraint (13b) causes the sharp edges to the left ⑤ and is also responsible for the shape difference between the upper ① and lower ② branch in the right hand side of the design domain.

4 Perspectives

This parameterization method is intended and developed for ensuring manufacturability of general 3D topology optimized designs of e.g. microfluidic mixers. Such micro devices do not allow for very intricate designs and are often an assembly of two machined parts. Following the method described in Andreasen et al. (2009) and imposing the explicit parameterization of Section 2.2.1 an optimized castable inline microfluidic mixer can be obtained. An example of such a design using 20,000 design elements is shown in Fig. 11. The manufacturability is ensured by the parameterization, the number of design variables is reduced to 2,000 and the consideration of 18,000 linear constraints can be avoided.

5 Conclusions

The proposed explicit Heaviside parameterization provides a way of obtaining castable designs in gradient driven topology optimization at a small coding effort. This option is useful as a means to reduce the complexity of topology designs e.g. when collaborating with experimentalists.

Acknowledgments The authors thank Ole Sigmund and the TopOpt group at DTU for fruitful discussions related to the present work.

References

Andreasen CS, Gersborg AR, Sigmund O (2009) Topology optimization of microfluidic mixers. Int J Numer Methods Fluids 61:498–513

Bendsøe MP (1989) Optimal shape design as a material distribution problem. Struct Multidisc Optim 4(1):193–202

Bendsøe MP, Kikuchi N (1988) Generating optimal topologies in structural design using a homogenization method. Comput Methods Appl Mech Eng 71(2):197–224

Bendsøe MP, Sigmund O (2004) Topology optimization: theory, methods and applications, 2nd edn. Springer, Berlin

Bourdin B (2001) Filters in topology optimization. Int J Numer Methods Eng 50(9):2143–2158

Bruns TE, Tortorelli DA (2001) Topology optimization of non-linear elastic structures and compliant mechanisms. Comput Methods Appl Mech Eng 190(26–27):3443–3459

Guest JK (2009) Topology optimization with multiple phase projection. Comput Methods Appl Mech Eng 199:123–135

Harzheim L, Graf G (2006) A review of optimization of cast parts using topology optimization II—topology optimization with manufacturing constraints. Struct Multidisc Optim 31:388–399

Olhoff N, Bendsøe MP, Rasmussen J (1991) On CAD-integrated structural topology and design optimization. Comput Methods Appl Mech Eng 89:259–279

Pedersen CBW, Allinger P (2006) Industrial implementation and applications of topology optimization and future needs. In: IUTAM symposium on topological design optimization of structures, machines and materials: status and perspectives. Solid mechanics and its applications, vol 137. Springer, pp 229–238. ISBN 1-4020-4729-00

Pedersen P, Pedersen NL (2009) Analytical optimal designs for long and short statically determinate beam structures. Struct Multidisc Optim 39:343–357

Schramm U, Zhou M (2006) Recent developments in the commercial implementation of topology optimization. In: IUTAM symposium on machines and materials: status and perspectives. Solid mechanics and its applications, vol 137. Springer, pp 239–248. ISBN 1-4020-4729-0

Sigmund O (2001) A 99 line topology optimization code written in Matlab. Struct Multidisc Optim 21(2):975–1001

Sigmund O (2009) Manufacturing tolerant topology optimization. Acta Mech Sin 25:227–239

Svanberg K (1987) The method of moving asymptotes—a new method for structural optimization. Int J Numer Methods Eng 24:359–373

Wang F, Lazarov BS, Sigmund O (2010) On projection methods, convergence and robust formulations in topology optimization. Struct Multidisc Optim. doi:10.1007/s00158-010-0602-y

Xu, S, Cai, Y, Cheng, G (2010) Volume preserving nonlinear density filter based on heaviside functions Struct Multidisc Optim 41:495–505

Zhou M, Rozvany GIN (1991) The COC algorithm, part II: topological, geometry and generalized shape optimization. Comput Methods Appl Mech Eng 89:197–224

Zuo K-T, Chen L-P, Zhang Y-Q, Yang J (2006) Manufacturing- and machining-based topology optimization. Int J Adv Manuf Technol 27:531–536

DTU Mechanical Engineering
Section of Solid Mechanics
Technical University of Denmark

Nils Koppels Allé, Bld. 404
DK- 2800 Kgs. Lyngby
Denmark
Phone (+45) 45 25 42 50
Fax (+45) 45 93 14 75
www.mek.dtu.dk
ISBN: 978-87-90416-59-1

DCAMM
Danish Center for Applied Mathematics and Mechanics

Nils Koppels Allé, Bld. 404
DK-2800 Kgs. Lyngby
Denmark
Phone (+45) 4525 4250
Fax (+45) 4593 1475
www.dcamm.dk
ISSN: 0903-1685